

# **ACOUSTIC TRANSDUCTION – MATERIALS AND DEVICES**

**Period 1 January 1998 to 31 December 1998**

**Annual Report**

**VOLUME III**

**OFFICE OF NAVAL RESEARCH  
Contract No: N00014-96-1-1173**

**APPROVED FOR PUBLIC RELEASE –  
DISTRIBUTION UNLIMITED**

**Reproduction in whole or in part is permitted for any  
purpose of the United States Government**

**Kenji Uchino**

**PENNSTATE**



**THE MATERIALS RESEARCH LABORATORY  
UNIVERSITY PARK, PA**

**Reproduced From  
Best Available Copy**

19990427 043

# REPORT DOCUMENTATION PAGE

Form Approved  
OMB No. 0704-0188

Public reporting burden for this collection of information is estimated to average 1 hour per response, including the time for reviewing instructions, searching existing data sources, gathering and maintaining the data needed, and completing and reviewing the collection of information. Send comments regarding this burden estimate or any other aspect of this collection of information, including suggestions for reducing this burden, to Washington Headquarters Services, Directorate for Information Operations and Reports, 1215 Jefferson Davis Highway, Suite 1204, Arlington, VA 22202-4302, and to the Office of Management and Budget, Paperwork Reduction Project (0704-0188), Washington, DC 20503

1. AGENCY USE ONLY (Leave blank)		2. REPORT DATE 04/05/99	3. REPORT TYPE AND DATES COVERED ANNUAL REPORT 01/01/98-12/31/98	
4. TITLE AND SUBTITLE ACOUSTIC TRANSDUCTION -- MATERIALS AND DEVICES			5. FUNDING NUMBERS ONR CONTRACT NO: N00014-96-1-11173	
6. AUTHOR(S) KENJI UCHINO				
7. PERFORMING ORGANIZATION NAME(S) AND ADDRESS(ES) Materials Research Laboratory The Pennsylvania State University University Park PA 16802			8. PERFORMING ORGANIZATION REPORT NUMBER	
9. SPONSORING/MONITORING AGENCY NAME(S) AND ADDRESS(ES) Office of Naval Research ONR 321SS Ballston Centre Tower One 800 N Quincy Street Arlington VA 22217-5660			10. SPONSORING/MONITORING AGENCY REPORT NUMBER	
11. SUPPLEMENTARY NOTES				
12a. DISTRIBUTION / AVAILABILITY STATEMENT			12b. DISTRIBUTION CODE	
13. ABSTRACT (Maximum 200 words)				
14. SUBJECT TERMS			15. NUMBER OF PAGES	
			16. PRICE CODE	
17. SECURITY CLASSIFICATION OF REPORT	18. SECURITY CLASSIFICATION OF THIS PAGE	19. SECURITY CLASSIFICATION OF ABSTRACT	20. LIMITATION OF ABSTRACT	

## ABSTRACT

This report documents work performed over the period 1 January 1998 to 31 December 1998 on a MURI under the Office of Naval Research Contract N00014-96-1-1173. The topic "Acoustic Transduction Materials and Devices" brings together groups in the Materials Research Laboratory (MRL), the Applied Research Laboratory (ARL), and the Center for Acoustics and Vibrations (CAV) at Penn State.

Research on the program is adequately represented in the 80 technical appendices.

Outstanding accomplishments include:

Exploration of several new relaxor ferroelectric perovskite solid solution with morphotropic phase boundaries. New evidence of the onset of nonlinearity in soft donor doped PZTs at surprisingly low (1V/cm) fields. Confirmation of the relaxor phase induced by electron irradiation in PVDF:TrFE copolymers, and a processing method which permits very high (4%) electrostrictive strain in the transverse direction, vital for the practical use in actuator systems. In composite transducer, "first fruits" of the cooperative program are cymbal arrays which form most effective acoustic projectors, and a new "dog bone" design which permits deeper submergence for the cymbal. Agile transducers, the 3-D acoustic intensity probe and high force high strain torsional and step and repeat systems continue to make excellent progress. In actuator studies true acoustic emission is proving to be an excellent tool in reliability studies and a new design of small-scale (mini) piezoelectric motor shows outstanding performance. Thick thin film studies and are now "gearing up" for the development of the mini tonpilz arrays. New combinations of ultrasonic and resonance methods appear to offer unique capability for complete characterization of ferroelectric piezoelectric materials.

The mode of presentation of the report emphasizes the outstanding progress made in published research. It is important to also document that the slower and more painstaking development of practical transducer systems in the cymbal and mini tonpilz arrays is progressing very favorably.

# **ACOUSTIC TRANSDUCTION – MATERIALS AND DEVICES**

**Period 1 January 1998 to 31 December 1998**

**Annual Report**

**VOLUME III**

**OFFICE OF NAVAL RESEARCH  
Contract No: N00014-96-1-1173**

**APPROVED FOR PUBLIC RELEASE –  
DISTRIBUTION UNLIMITED**

**Reproduction in whole or in part is permitted for any  
purpose of the United States Government**

**Kenji Uchino**



## APPENDICES

### VOLUME I

#### GENERAL SUMMARY PAPERS

1. Cross, L.E., "Recent Developments in Piezoelectric Ferroelectric Materials and Composites," Proceedings of the 4<sup>th</sup> European Conference on Smart Structures and Materials in Conjunction with the 2<sup>nd</sup> International Conference on Micromechanics, Intelligent Materials and Robotics, Harrogate, UK (6-8 July 1998).
2. Newnham R.E., "Functional Composites for Sensors and Actuators," Chapter in *The Era of Materials*, edited by S. Majumdar, R. Tressler, and E. Miller, 259-275, Pennsylvania Academy of Science (1998).
3. Uchino, K., "Piezoelectric Ultrasonic Motors: Overview," *Smart Mater. Struct.* **7**, 273-285 (1998).
4. Newnham, R.E., "Phase Transformations in Smart Materials," *Acta Cryst. A* **54**, 729-737 (1998).

#### 2.0 MATERIALS STUDIES

##### 2.1 Polycrystal Perovskite Ceramics

5. Liu, S.F., I.R. Abothu, S. Komarneni, P. Poosanaas, D.S. Paik, Y. Ito, and K. Uchino, "PLZT Ceramics from Conventional and Microwave Hydrothermal Powders," Proceedings in Asian Meeting on Ferroelectrics (AMF2), Singapore (December 8-11, 1998).
6. Abothu, I.R., P. Poosanaas, S. Komarneni, Y. Ito, and K. Uchino, "Nanocomposite Versus Monophasic Sol-Gel Processing of PLZT Ceramics," Proceedings in Asian Meeting on Ferroelectrics (AMF2), Singapore (December 8-11, 1998).
7. Kim, J.S., Y.H. Chen, and K. Uchino, "Dielectric and Piezoelectric Properties of Fe<sub>2</sub>O<sub>3</sub>-Doped 0.57PSN-0.43PT Ceramics," *J. Korean Phys. Soc.* **32** [2], S1248-1250 (1998).
8. Alberta, E.F. and A.S. Bhalla, "Electrical Property Diagram and Morphotropic Phase Boundary in the Pb(In<sub>1/2</sub>Ta<sub>1/2</sub>)O<sub>3</sub>-PbTiO<sub>3</sub> Solid Solution System," *Ferroelectric Letters* (1998). [accepted]
9. Meng, J.F., Z-Y. Cheng, B.K. Rai, R.S. Katiyar, E. Alberta, R. Guo, and A.S. Bhalla, "Photoluminescence in PbMg<sub>1/3</sub>Nb<sub>2/3</sub>O<sub>3</sub>-PbIn<sub>1/2</sub>Nb<sub>1/2</sub>O<sub>3</sub> Systems," *J. Mater. Res.* **13** (7), 1861 (1998).
10. Alberta, E.F. and A.S. Bhalla, "Investigation of the Lead Indium Niobate-Lead Magnesium Niobate Solid Solution," *Materials Letters* (1998). [accepted]
11. Alberta, E.F., A.S. Bhalla, and T. Takenaka, "Large Hydrostatic Piezoelectric Constant and Temperature Dependence of the Piezoelectric Properties of Bi(NiTi)<sub>1/2</sub>O<sub>3</sub>:PbTiO<sub>3</sub> Ceramics," *Ferroelectrics Letters* (1998). [accepted]
12. Zhang, Q.M. and J. Zhao, "Electromechanical Properties of Lead Zirconate Titanate Piezoceramics Under the Influence of Mechanical Stress, IEEE Trans. UFFFC (accepted).
13. Kugel, V.D. and L.E. Cross, "Behavior of soft Piezoelectric Ceramics under High Sinusoidal Electric Fields," *J. Appl. Phys.* **84** (5), 2815-2830 (1998).

## VOLUME II

### 2.0 MATERIALS STUDIES

#### 2.1 *Polycrystal Perovskite Ceramics* (continued)

14. Du, X.-H., Q.M. Wang, U. Belegundu, and K. Uchino, "Piezoelectric Property Enhancement in Polycrystalline Lead Zirconate Titanate by Changing Cutting Angle," J. Ceram. Soc. Jpn. (1999). [accepted]
15. Mueller, V. and Q.M. Zhang, "Nonlinearity and Scaling Behavior in Donor Doped Lead Zirconate Titanate Piezoceramic," Appl. Phys. Lett. **72**, 2692 (1998).
16. Uchino, K and H. Aburatani, "Field Induced Acoustic Emission in Ferroelectric Ceramics," Proc. IEEE Ultrasonic Symp., Sendai, Japan (October 1998). [in press]
17. Newnham, R.E. and S. Trolier-McKinstry, "Size Effects in Ferroics" Integrated Ferroelectrics **20**, 1-13, Gordon & Breach Science Publishers (March 1998).

#### 2.2 *Relaxor Ferroelectric Single Crystal Systems*

18. Uchino, K., "High Electromechanical Coupling Piezoelectrics: Relaxor and Normal Ferroelectric Solid Solutions," Solid State Ionics **108**, 43-52 (1998).
19. Wada, S. S.E. Park, L.E. Cross, and T.R. Shrout, "Domain Configuration and Ferroelectric Related Properties of Relaxor Based Single Crystals," J. Korean Phys. Soc. **32**, S1290-S1293 (1998).
20. Belegundu, U., X. H. Du, and K. Uchino, "In-Situ Observation of Domain Orientation in  $\text{Pb}(\text{Zn}_{1/3}\text{Nb}_{2/3})\text{O}_3\text{-PbTiO}_3$  Single Crystals," Proc. 5<sup>th</sup> Intl. Symp. Ferroic Domains and Mesoscopic Structures, University Park, PA (April 1998).
21. Du, X.H., J. Zheng, U. Belegundu, and K. Uchino, "Crystal Orientation Dependence of Piezoelectric Properties of Lead Zirconate Titanate Near the Morphotropic Phase Boundary," J. Appl. Phys. Ltrs. **72** (19), 2421-2423 (1998).
22. Rehrig, P.W., S.-E. Park, S. Trolier-McKinstry, G.L. Messing, B. Jones, and T.R. Shrout, "Piezoelectric Properties of Zirconium-Doped Barium Titanate Single Crystals Grown by Templated Grain Growth," submitted to J. Appl. Phys.
23. Du, X., Q.M. Wang, U. Belegundu, A. Bhalla, and K. Uchino, "Crystal Orientation Dependence of Piezoelectric Properties of Single Crystal Barium Titanate," Mat. Ltr. (1999) [accepted].
24. Guo, R., H.T. Evans, Jr., and A.S. Bhalla, "Crystal Structure Analysis and Polarization Mechanisms of Ferroelectric Tetragonal Tungsten Bronze Lead Barium Niobate," Ferroelectrics **206/207**, 123-132 (1998).

#### 2.3 *New High Strain Polymer Materials*

25. Zhao, X., V. Bharti, Q.M. Zhang, T. Ramotowski, F. Tito, and R. Ting, "Electromechanical Properties of Electrostrictive P(VDF-TrFE) Copolymer," Appl. Phys. Ltrs. **73**, 2054 (1998).
26. Bharti, V., G. Shanthi, H. Xu, Q.M. Zhang, and K. Liang, "Evolution of Transitional Behavior and Structure of Electron Irradiated Poly(vinylidene fluoride-trifluoroethylene) Copolymer Films," Appl. Phys. Ltrs. [accepted].
27. Cheng, Z.-Y., V. Bharti, T.B. Xu, S. Wang, and Q.M. Zhang, "Transverse Strain Responses in Electrostrictive Poly (vinylidene fluoride-trifluoroethylene) Films and Development of a Dilatometer for the Measurement," J. Appl. Phys. [accepted]

### VOLUME III

#### 2.0 MATERIALS STUDIES

##### 2.3 *New High Strain Polymer Materials* (continued)

28. Bharti, V., X.Z. Zhao, Q.M. Zhang, T. Ramotowaski, F. Tito, and R. Ting, "Ultrahigh Field Induced Strain and Polarized Response in Electron Irradiated Poly(vinylidene fluoride-trifluoroethylene) Copolymer," *Mat. Res. Innovat.* **2**, 57-63 (1998).
29. Su, J., P. Moses, and Q.M. Zhang, "A Bimorph Based Dilatometer for Field Induced Strain Measurement in Soft and Thin Free Standing Polymer Films," *Rev. Sci. Instruments* **69** (6), 2480 (1998).

#### 3.0 TRANSDUCER STUDIES

##### 3.1 *Composite Structures*

30. Hughes, W.J., "Transducers, Underwater Acoustic," *Encyclopedia of Applied Physics*, Vol. 22, 67 (1998).
31. Tressler, J.F., W.J. Hughes, W. Cao, K. Uchino, and R.E. Newnham, "Capped Ceramic Underwater Sound Projector."
32. Zhang, J., W.J. Hughes, A.C. Hladky-Hennion, and R.E. Newnham, "Concave Cymbal Transducers."
33. Wang, Q.M., X.-H. Du, B. Xu, and L.E. Cross, "Theoretical Analysis of the Sensor Effect of Cantilever Piezoelectric Benders," *J. Appl. Phys.* **85** (3), 1702-1712 (1998).
34. Fernandez, J.F., A. Dogan, J.T. Fielding, K. Uchino, and R.E. Newnham, "Tailoring the Performance of Ceramic-Metal Piezocomposite Actuators, 'Cymbals'," *Sensors and Actuator A65*, 228-237 (1998).
35. Wang, Q.M. and L.E. Cross, "A Piezoelectric Pseudoshear Multilayer Actuator," *Appl. Phys. Ltrs.* **72** (18), 2238 (1998).
36. Geng, X. and Q.M. Zhang, "Resonance Modes and Losses in 1-3 Composites for Ultrasonic Transducer Applications," *J. Appl. Phys.* **85** (3), 1342 (1999).

##### 3.2 *Frequency Agile Transducers*

37. Hebert, C.A. and G. A. Lesieutre, "Flexural Piezoelectric Transducers with Frequency Agility Obtained Via Membrane Loads," *J. Intel. Mat. Sys. & Str.* (1998). [accepted].
38. Davis, C.L. and G.A. Lesieutre, "An Actively Tuned Solid State Vibration Absorber Using Capacitive Shunting of Piezoelectric Stiffness," *J. Sound & Vibration* (1998). [accepted]
39. Bernard, J., G.A. Lesieutre, and G.H. Koopmann, "Active Broadband Force Isolation using a Flexural Piezoelectric Inertial Actuator," *J. Sound & Vibration* (1999). [submitted]

## VOLUME IV

### 3.0 TRANSDUCER STUDIES

#### 3.3 *3-D Acoustic Intensity Probes* (continued)

40. Lauchle, G.C. and A.R. Jones, "Unsteady Lift Force on a Towed Sphere," *J. Fluids and Structures* **112** (1998).
41. Lauchle, G.C., A.R. Jones, J.J. Dreyer, and J. Wang, "Flow-Induced Lift Forces on a Towed Sphere," *Proc. Of ASME Noise Control and Acoustics Division ASME 1998, NCA-28*, 103-111 (1998).
42. Brungart, T.A. G.C. Lauchle, S. Deutsch, and E. Riggs, "Outer-Flow Effects on Turbulent Boundary Layer Wall Pressure Fluctuations," *J. Acoust. Soc. Am.* **105** (4) (April 1999).
43. Brungart, T.A., G.C. Lauchle, and R.K. Ramanujam, "Installation Effects of Fan Acoustic and Aerodynamic Performance," *Noise Control Eng. J.* **47** (January/February 1999).

### 4.0 ACTUATOR STUDIES

#### 4.1 *Materials : Designs : Reliability*

44. Uchino, K., "New Trend in Ceramic Actuators," *Proc. 6<sup>th</sup> Intl. Aerospace Symp. '98*, Nagoya, Japan, p. S1-2, 1-10 (July 14-15, 1998).
45. Uchino, K., "Materials Issues in Design and Performance of Piezoelectric Actuators: An Overview," *Acta. Mater.* **46** (11), 3745-3753 (1998).
46. Yao, K., W. Zhu, K. Uchino, Z. Zhang, and L.C. Lim, "Design and Fabrication of a High Performance Multilayer Piezoelectric Actuator with Bending Deformation."
47. Aburatani, H. and K. Uchino, "Acoustic Emission in Damaged Ferroelectric Lead Zirconate Titanate Ceramics," *Jpn. J. Appl. Phys.* **37**, L553-L555 (1998).
48. Atherton, P.D. and K. Uchino, "New Developments in Piezo Motors and Mechanisms," *Proc. 6<sup>th</sup> Intl. Conf. On New Actuators (Actuator 98)*, Bremen, Germany, p. 164-169 (June 17-19, 1998).
49. Uchino, K. and B. Koc, "Compact Piezoelectric Ultrasonic Motors," *2<sup>nd</sup> Asian Meeting on Ferroelectrics (AMF-2)*, Singapore (December 7-11, 1998).
50. Koc, B., Y. Xu, and K. Uchino, "Ceramic/Metal Composite Piezoelectric Motors," *IEEE Ultrasonic Symposium*, Sendai, Japan (October 1998).
51. Koc, B., Y. Xu, and K. Uchino, "Roto-Linear Ultrasonic Motors," *Proc. 6<sup>th</sup> Intl. Conf. On New Actuators (Actuator 98)*, Bremen, Germany, p. 349-352 (June 17-19, 1998).
52. Koc, B., A. Dogan, Y. Xu, R.E. Newnham, and K. Uchino, "An Ultrasonic Motor Using a Metal-Ceramic Composite Actuator Generating Torsional Displacement," *Jpn. J. Appl. Phys.* **37**, 5659-5662 (1998).

#### 4.2 *Photostrictive Actuators*

53. Poosanaas, P. and K. Uchino, "Photostrictive Effect in Lanthanum-Modified Lead Zirconate Titanate Ceramics Near The Morphotropic Phase Boundary," *J. Mat. Chem. & Phys.* (October 1998). [submitted]
54. Uchino, K. and P. Poosanaas, "Photostriction in PLZT and Its Applications," *Proc. CIMTEC '98*, Florence, Italy (June 14-19, 1998).

## VOLUME V

### 4.0 ACTUATOR STUDIES

#### 4.3 *Torsional and High Force Actuators (continued)*

- 55. Glazounov, A.E., Q.M. Zhang, and C. Kim, "Torsional Actuator Based on Mechanically Amplified Shear Piezoelectric Response," *Sensors and Actuators* (1998). [submitted]
- 56. Frank, J., G.H. Koopmann, W. Chen, and G.A. Lesieutre, "Design and Performance of a High Force Piezoelectric Inchworm Motor."

### 5.0 MODELING and CHARACTERIZATION

#### 5.1 *Finite Element and Other Methods*

- 57. Qi, W. and W. Cao, "Finite Element and Experimental Study of Composite and 1-D Array Transducers," *SPIE* **3341** (1998).
- 58. Wang, H., W. Jiang, and W. Cao, "Characterization of Lead Zirconate Titanate Piezoceramic Using High Frequency Ultrasonic Spectroscopy," *J. Appl. Phys.* (1998). [accepted]
- 59. Zhu, S.N., B. Jiang, and W. Cao, "Characterization of Piezoelectric Materials Using Ultrasonic and Resonant Techniques," *Proceedings of SPIE Imaging '98*, **3341**, 154-162 (1998).
- 60. Cao, W., "Virtual Design of Medical Transducers," *Proceedings of SPIE Imaging '98*, **3341**, 56-63 (1998).
- 61. Cao, W., "Elastic Property Characterization in Thin Samples of Sub-Wavelength in Thickness," *Ferroelectrics* **206/207**, 355-363 (1998).
- 62. Cao, W., S.N. Zhu, and B. Jiang, "Analysis of Shear Modes in A Piezoelectric Resonator," *J. Appl. Phys.* **83**, 4415-4420 (1998).

#### 5.2 *Relaxor Ferroelectrics*

- 63. Giniewicz, J.R., A.S. Bhalla, and L.E. Cross, "Variable Structural Ordering in Lead Scandium Tantalate-Lead Titanate Materials," *Ferroelectrics* **211**, 281-297 (1998).
- 64. Pan, X., W.D. Kaplan, M. Rühle, and R.E. Newnham, "Quantitative Comparison of Transmission Electron Microscopy Techniques for the Study of Localized Ordering on a Nanoscale," *J. Am. Ceram. Soc.* **81** (3), 597-605 (1998).
- 65. Zhao, J., A.E. Glazounov, and Q.M. Zhang, "Change in Electromechanical Properties of 0.9PMN:0.1PT Relaxor Ferroelectric Induced by Uniaxial Compressive Stress Directed Perpendicular to the Electric Field," *Appl. Phys. Ltrs.* **74**, 436 (1999).
- 66. Zhao, J., V. Mueller, and Q.M. Zhang, "The Influence of the External Stress on the Electromechanical Response of Electrostrictive 0.9Pb(Mg<sub>1/3</sub>Nb<sub>2/3</sub>)O<sub>3</sub>-0.1PbTiO<sub>3</sub> in the dc Electrical Field Biased State," *J. Mat. Res.* **14**, 3 (1999).

## VOLUME VI

### 5.0 MODELING and CHARACTERIZATION

#### 5.3 *Thin and Thick Thin Films*

67. Maria, J.P., W. Hackenberger, and S. Trolier-McKinstry, "Phase Development and Electrical Property Analysis of Pulsed Laser Deposited  $\text{Pb}(\text{Mg}_{1/3}\text{Nb}_{2/3})\text{O}_3\text{-PbTiO}_3$  (70/30) Epitaxial Films," *J. Appl. Phys.* **84** (9), 5147-5154 (1998).
68. Shepard, J.F., Jr., P.J. Moses, and S. Trolier-McKinstry, "The Wafer Flexure Technique for the Determination of the Transverse Piezoelectric Coefficient ( $d_{31}$ ) of PZT Thin Films," *Sensors and Actuators A* **71**, 133-138 (1998).
69. Zavala, G. J.H. Fendler, and S. Trolier-McKinstry, "Stress Dependent Piezoelectric Properties of Ferroelectric Lead Zirconate Titanate Thin Films by Atomic Force Microscopy," *J. Korean Phys. Soc.* **32**, S1464-S467 (1998).
70. Wasa, K., Y. Haneda, T. Satoh, H. Adachi, I. Kanno, K. Setsune, D.G. Schlom, S. Trolier-McKinstry, C.-B. Eom, "Continuous Single Crystal  $\text{PbTiO}_3$  Thin Films Epitaxially Grown on Miscal (001)  $\text{SrTiO}_3$ ," *J. Korean Phys. Soc.* **32**, S1344-S1348 (1998).
71. Xu, B., Y. Ye, L.E. Cross, J.J. Bernstein, and R. Miller, "Dielectric Hysteresis from Transverse Electric Fields in Lead Zirconate Titanate Thin Films," *Appl. Phys. Ltrs.* (1998). [submitted]
72. Xu, B., N.G. Pai, Q.-M. Wang, and L.E. Cross, "Antiferroelectric Thin and Thick Films for High Strain Microactuators," *Integrated Ferroelectrics* **22**, 545-557 (1998).

#### 5.4 *Domain Studies*

73. Erhart, J. and W. Cao, "Effective Material Properties in Twinned Ferroelectric Crystals," *J. Appl. Phys.* (1999). [submitted]
74. Belegundu, U., M. Pastor, X.H. Du, L.E. Cross, and K. Uchino, "Domain Formation in  $0.90\text{Pb}(\text{Zn}_{1/3}\text{Nb}_{2/3})\text{O}_3\text{-}0.10\text{PbTiO}_3$  Single Crystals under Electric Field along [111] Direction," *IEEE '98*, Sendai, Japan (1998).
75. Zhu, S.N. and W. Cao, "Pyroelectric and Piezoelectric Imaging of Ferroelectric Domains in  $\text{LiTaO}_3$  by Scanning Electron Microscopy," *Phys. Status Solidi* (1998). [submitted]
76. Hatch, D.M. and W. Cao., "Determination of Domain and Domain Wall Formation at Ferroic Transitions," *Ferroelectric* (1998). [submitted]
77. Mueller, V. and Q.M. Zhang, "Threshold of Irreversible Domain Wall Motion in Soft PZT-Piezoceramic. *Ferroelectrics* **206/207**, 113-122 (1998).
78. Aburatani, H., J.P. Witham, and K. Uchino, "A Fractal Analysis on Domain Related Electric Field Induced Acoustic Emission in Ferroelectric Ceramics," *Jpn. J. Appl. Phys.* **37**, 602-605 (1998).

### 5.5 Electrostriction

79. Newnham, R.E., V. Sundar, R. Yimnirun, J. Su, and Q.M. Zhang, "Electrostriction in Dielectric Materials," in *Advances in Dielectric Ceramic Materials*, eds. K. Nair and A. Bhalla. Ceramic Trans. **88**, 154-39 (1998).
80. Sundar, V., R. Yimnirun, B.G. Aitken, and R.E. Newnham, "Structure Property Relationships in the Electrostriction Response of Low Dielectric Permittivity Silicate Glasses," Mat. Res. Bull. **33**, 1307-1314 (1998).

# **APPENDIX 28**



## ORIGINAL ARTICLE

Vivek Bharti · Xing-Zhong Zhao · Q.M. Zhang  
T. Romotowski · F. Tito · R. Ting

## Ultrahigh field induced strain and polarization response in electron irradiated poly(vinylidene fluoride-trifluoroethylene) copolymer

Received: 10 June 1998 / Accepted: 30 July 1998

**Abstract** The influence of electron dosage on the field induced strain, dielectric constant, and polarization response has been investigated in electron irradiated poly(vinylidene fluoride-trifluoroethylene) (P(VDF-TrFE)) 50/50 copolymer. It was found that under suitable electron dosage an ultrahigh electrostrictive strain can be achieved. Interestingly, material after irradiation exhibits many features resembling those of relaxor ferroelectrics, suggesting that the electron irradiation breaks up the coherent polarization domain in normal ferroelectric P(VDF-TrFE) copolymer into nano-polar regions that transform the material into a relaxor ferroelectric. In addition, many of the material properties including the field induced polarization, the electrostrictive strain, and elastic modulus exhibit irregular change (non-monotonical) with electron dosage, indicating a complex relation among the crosslinking density, crystallinity, crystallite size, and molecular conformation in determining the material responses.

**Key words** Polymers · PVDF-TrFE · Electron irradiation · Dielectric constant · Vogel-Fulcher law · Strain · Polarization · Electrostriction · Elastic modulus · Elastic energy density

### Introduction

Ferroelectric polymers, because of their flexibility, low weight, easy processibility, have attracted a great deal of attention and effort for a broad range of device applica-

tions [1, 2]. However, in comparison with other existing functional materials such as ceramics, current ferroelectric polymers suffer low electric field sensitivity (low dielectric constant, low piezoelectric coefficients, low field induced strain, etc.) which severely limits the application range of these materials [3–5]. In order to overcome the shortcomings of ferroelectric polymers, in the past several decades, there is a constant effort in searching new ferroelectric polymers and improving the existing materials. When considering improving the electric field sensitivity of these materials, there are several possible approaches one can take, including to make use of the instability of the material near a phase transformation and to introduce defects in the crystal structure to increase the compliance of the material towards the external field. As has been observed recently in polyvinylidene fluoride-trifluoroethylene (P(VDF-TrFE)) copolymer, by high energy electron irradiation the material can be converted to exhibit many features very similar to a relaxor ferroelectric including a slim polarization hysteresis loop at temperatures near the dielectric peak which gradually evolves into a normal ferroelectric polarization hysteresis loop with reduced temperature and the dispersion of the broad dielectric peak with frequency which follows the Vogel-Fulcher law. In addition, the material exhibits a massive electrostriction, a relatively high dielectric constant, and high elastic energy density, which are highly desirable for high performance electromechanical devices.

PVDF and its copolymer P(VDF-TrFE) are the best known and most widely used ferroelectric polymers because of their relatively high polarization level and high electromechanical activity [1, 2]. In most cases, the material is in the semicrystalline form having a morphology of crystallites in an amorphous surrounding. The ferroelectricity of the material is from the crystalline region and however, analogous to other ferroelectric materials. However, the boundary conditions at the crystalline regions, i.e., the amorphous-crystalline interface and the amorphous phase, have a profound effect on the ferroelectric and electromechanical responses of the material.

V. Bharti · X.-Z. Zhao · Q. M. Zhang (✉)  
167 Materials Research Laboratory,  
The Pennsylvania State University, University Park,  
PA 16802, USA  
Fax: +1-814-865-2326, e-mail: QNZ1@PSU.EDU

T. Romotowski · F. Tito  
Naval Undersea Warfare Center, Newport, RI 02841, USA

R. Ting  
Department of Chemistry, University of Central Florida,  
Orlando, FL 328, USA

In the past several decades, there are many experiments conducted to investigate the influence of high energy electron or  $\gamma$ -ray irradiation on the chemical and structural changes in PVDF based copolymers [6–9]. It is well known that these irradiations will induce crosslinking and cause changes in the molecular conformation and crystallinity in fluoropolymers. More recent structural studies also revealed that high energy electron irradiation destroys the all trans conformation in the ferroelectric phase and transformed it into a paraelectric like phase [10]. Clearly, electron irradiation introduces several defects in P(VDF-TrFE) copolymers with the effect of breaking up the coherent macro-polar regions (all trans conformation) in normal ferroelectric phase and significantly increasing the amorphous-crystalline interface regions [7, 10].

In this paper, we report the dependence of various material responses, including the polarization hysteresis loop, the dielectric constant, the remanent polarization as a function of temperature obtained from the pyroelectric coefficient, and the field induced strain, of P(VDF-TrFE) 50/50 on the electron irradiation dosage in the range from 80 to 120 Mrad. The irradiation was carried out at room temperature with 3 MeV electron source under nitrogen atmosphere.

## Experimental

The results presented here were obtained from P(VDF-TrFE) 50/50 (50 mol% of VDF) which has a relatively low F-P transition temperature (70°C) and small polarization hysteresis compared with the higher VDF mol% compositions [11]. The copolymer was from Solvay & Cie of Bruxelles. The film used in this investigation was fabricated by melt pressing powder at 225°C and then cooling slowly to room temperature. The films thickness were between 25 to 40  $\mu\text{m}$ . For the electric measurement, gold electrodes sputtered onto the film surfaces were used.

We characterized the electric field induced strain with a bimorph-based strain sensor designed specifically for the polymer film [12] and the measurement was carried out at room temperature. The polarization hysteresis loops were measured by a Sawyer-Tower circuit [13] in the temperature range from –25 to 50°C. At each temperature, the samples were allowed to equilibrate for 15 min before measuring the polarization hysteresis loop. The frequency range for the polarization and strain measurement is from 1 to 10 Hz.

The dielectric constant was evaluated by HP multi-frequency LCR meter (HP4274 A) equipped with a temperature chamber. The frequency range is from 50 Hz to 1 MHz. In each measurement, the sample was first heated to 125°C and then the measurement was performed for both cooling and heating cycles in the temperature interval from –63 to 125°C at a rate of 2°C/min. The elastic modulus was measured by a Dynamic Mechanical Analyzer (TA Instruments, Model No. 2890) [14] in the frequency range from 1 to 100 Hz and temperature from –60 to 80°C.

The pyroelectric coefficient was measured using the Byer-Roundy technique. For the data reported here, the sample was first poled by applying a DC field of about 30 MV/m at 80°C and then slowly cooled down to –125°C under the field. The field was switched off at –125°C and the pyroelectric coefficient was measured at a heating rate of 2°C/min using a HP 4140B pico-ammeter. The polarization of the sample was then determined by the integration of the obtained current data. It was observed that for non-irradiated samples, the polarization obtained was not dependent on the applied DC field level for a field above 30 MV/m. On

the other hand, the polarization obtained here for samples after irradiation increases with increased DC bias field, reflecting that there is no well defined coercive field and a broad distribution of polarization activation energy in the material. Because of the limit of the current experimental set-up on the allowed DC bias field level, we could not systematically examine the dependence of the polarization on DC bias field to higher field level. Further improvement on the experimental set-up will be made to increase the DC bias field level.

## Results and discussions

### Dielectric response

The temperature and frequency dependence of the small signal dielectric constant for P(VDF-TrFE) 50/50 films with different irradiation dosages is shown Fig. 1. For the comparison, the dielectric constant of unirradiated sample is also presented in Fig. 2. Apparently the dielectric constant peak of these irradiated samples is quite broad. The data also shows that the maximum dielectric constant decreases monotonically with electron dosage. In addition, there is a strong frequency dispersion and the peak temperature ( $T_m$ ) of the dielectric constant moves to higher temperature with increase in frequency. These features seem resembling those observed in the relaxor ferroelectric ceramic materials [15]. Hence, in analogous to the relaxor in ceramic systems, we also attempted to fit the data with the Vogel-Fulcher law, which is an empirical relation observed in many systems which undergo freezing below certain temperature,  $T_f$  [16–18].

$$\epsilon' = \epsilon_\infty \exp\left[\frac{-U}{k(T_m - T_f)}\right] \quad (1)$$

where  $U$  is a parameter describing the distribution width of relaxation time (or energy). Hence, for a system with narrow distribution of relaxation time such as in normal ferroelectrics,  $U$  will approach to zero. A typical result of the fitting is shown in Fig. 3 and the fitting of the data with Eq. (1) yields:  $U=2\times 10^{-3}$  eV and  $T_f=317$  K for 80 Mrad,  $U=2.4\times 10^{-3}$  eV and  $T_f=318$  K for 100 Mrad, and  $U=1.3\times 10^{-3}$  eV and  $T_f=320.3$  K for 120 Mrad. While for unirradiated samples, the fitting yields  $U=5.5\times 10^{-4}$  eV,  $T_f=339$  K. It was observed that in all the materials examined the dielectric peak and  $T_f$  move to lower temperature after irradiation. However, there exist a threshold dosage and beyond that, the peak and  $T_f$  show slight increase in temperature. Since the peak position and  $T_f$  are directly related to the activation energy, the results suggest that the electron irradiation breaks up the ferroelectric macro-domains which significantly reduces the activation energy of the polar groups. Upon further electron irradiation, the increased amorphous phase and crosslinking density may impose constraints on the activation of the polar groups, resulting in a slight increase of  $T_f$  as observed.

It should also be noted that there are two peaks observed in the low frequency dielectric loss data, one is

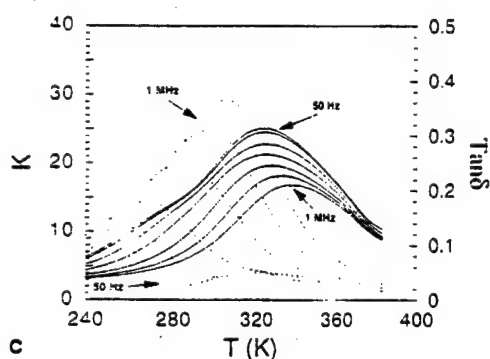
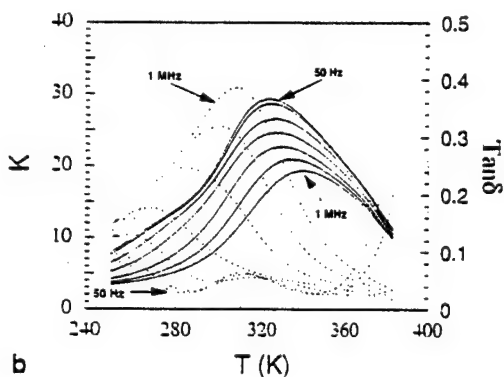
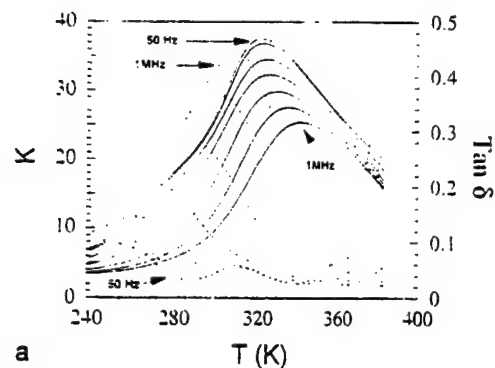


Fig. 1a-c The dielectric constant (solid lines) and dielectric loss (dashed lines) as a function of temperature for P(VDF-TrFE) 50/50 copolymer after a) 80, b) 100 and c) 120 Mrad irradiation dosages. The measuring frequency: (from top to bottom for dielectric constant and from bottom to top for dielectric loss) 50 Hz, 100 Hz, 1 KHz, 10 KHz, 0.1 MHz, 0.4 MHz and 1 MHz

near  $-20^{\circ}\text{C}$  whose peak temperature moves up with frequency and the other is much weaker and occurs at a temperature near  $40^{\circ}\text{C}$ . This weak higher temperature peak merges with the shoulder of the low temperature loss peak at high frequencies. To identify these peaks, we compare the data with unirradiated sample whose dielectric data is relatively well understood [19, 20]. As shown in Fig. 2, there is three peaks in the low frequency dielectric loss of unirradiated samples, the broad low temperature loss peak near  $-20^{\circ}\text{C}$  and moving up in temperature with frequency is from the glass transition in the amorphous phase, the relatively sharp peak at near  $67^{\circ}\text{C}$  whose position does not change with frequency is due to the ferroelectric-paraelectric (F-P) transition. In addition,

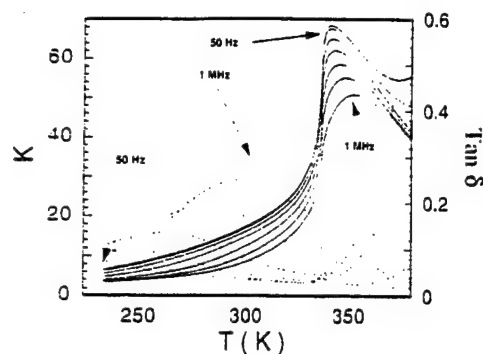


Fig. 2 Variation of dielectric constant (solid lines) and dielectric loss (dashed lines) with temperature for unirradiated copolymer film at 50 Hz, 100 Hz, 1 KHz, 10 KHz, 0.1 MHz, 0.4 MHz and 1 MHz frequencies

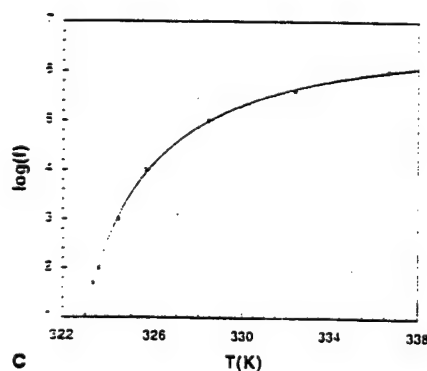
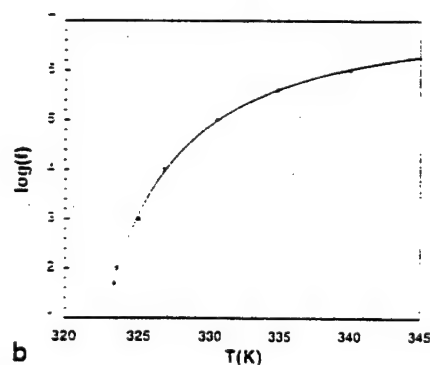
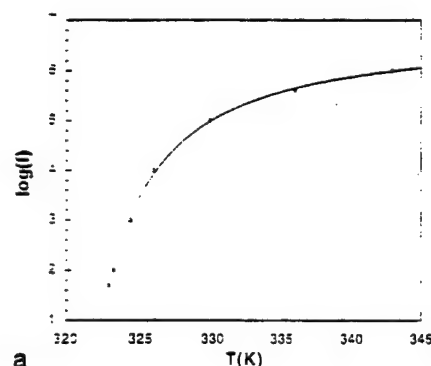


Fig. 3a-c Fitting of Vogel-Folcher law for a) 80, b) 100 and c) 120 Mrad irradiated copolymer films. The solid line is the fitting and circles are the data obtained from the Fig. 1

there is a weak shoulder at a temperature near  $40^{\circ}\text{C}$  which is believed to be due to the defects at the crystalline-amorphous interface. The data in Fig. 2 also reveals that the main contributor to the dielectric loss in the material is from the glass transition in the amorphous region and on the other hand, the real part of the dielectric constant in the unirradiated samples shows very little sign of the glass transition of the amorphous phase, indicating that the glass transition does not affect the real part of the dielectric constant.

Hence, the dielectric data reveals that the irradiated samples do not possess the loss peak due to the F-P transition, while the peaks from the two other processes are still present in the samples. In addition, the peak near  $40^{\circ}\text{C}$  seems to be enhanced after the irradiation, possibly caused by the increase of the amorphous-crystalline interface. In analogous to the situation in the unirradiated samples, the glass transition in the amorphous phase does not affect the real part of the dielectric constant in any significant manner, however, it is still the main contributor to the dielectric loss. It can be seen that at temperatures below  $80^{\circ}\text{C}$ , the dielectric loss is relatively low at frequencies below 1 kHz. At higher frequencies, the dielectric loss due to the glass transition becomes quite high at near room temperature.

#### Polarization response

Figure 4 presents the polarization hysteresis loops measured at room temperature for P(VDF-TrFE) 50/50 films before and after irradiation. The sample before irradiation exhibits a well defined ferroelectric polarization hysteresis loop with a coercive field at  $45\text{ MV/m}$  (the field level at  $P=0$  in the hysteresis loop) and a remanent polarization of  $6.4\text{ mC/cm}^2$  (the polarization level at  $E=0$  in the hysteresis loop). In contrast, the samples irradiated with dosages from 80 to 120 Mrad exhibit slim hysteresis loops and the polarization level of the samples are also reduced. These results indicate that the large polarization hysteresis can be removed by irradiation and are inconsistent with the dielectric constant data where the sharp F-P transition is removed.

It is interesting to note that although the polarization level  $P_s$  at  $160\text{ MV/m}$  for irradiated samples reduced drastically compared with unirradiated ones, the change of this polarization with electron dosage is not monotonical. For unirradiated samples,  $P_s$  is  $8.7\text{ mC/cm}^2$ . While for samples with 80 Mrad dosage,  $P_s$  is reduced to  $5.5\text{ mC/cm}^2$ . However, further increasing the dosage to 100 Mrad raises  $P_s$  to  $6.5\text{ mC/cm}^2$ . At even higher dosage (120 Mrad),  $P_s$  is again dropped to  $4.5\text{ mC/cm}^2$ . The drop of  $P_s$  with irradiation can be understood by assuming that there is an increase of amorphous phase after the irradiation, which is consistent with the dielectric constant and elastic modulus data to be presented. The reason for the raise of  $P_s$  with dosage from 80 to 100 Mrad is not clear. There are several possibilities which could be responsible to this anomalous change including the

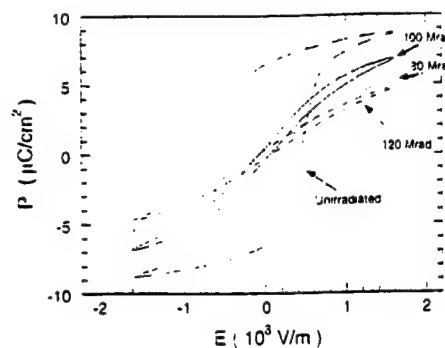


Fig. 4 The polarization hysteresis loops of P(VDF-TrFE) 50/50 copolymer measured at room temperature before and after irradiation

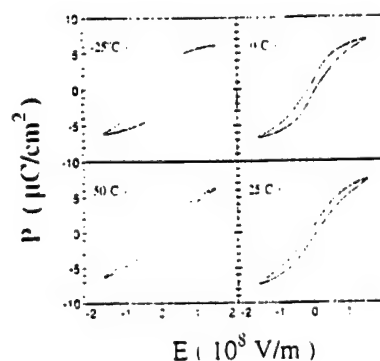


Fig. 5 Change in polarization hysteresis loop with temperature for P(VDF-TrFE) 50/50 copolymer films irradiated (100 Mrad) at room temperature

motions of crystalline-amorphous interface which will depend on the interface area, crystallite size, and cross-linking density, and the rotation of the polar clusters.

As the temperature is lowered to below room temperature, we observed a gradual appearance of the polarization hysteresis, i.e., an gradual increase in the remanent polarization. The data presented in Fig. 5 is for samples irradiated with 100 Mrad. The re-appearance of the polarization hysteresis with reduced temperatures suggests that the material after these irradiation treatments is still a ferroelectric.

The pyroelectric coefficient of both irradiated and unirradiated samples is presented in Figs. 6 and 7 and the polarization as a function of temperature obtained from integration of the pyroelectric current is shown in Fig. 8. The data from the unirradiated samples exhibit a sharp drop of polarization (a sharp pyroelectric peak) at a temperature near  $70^{\circ}\text{C}$ , the F-P transition temperature. While for irradiated samples, the change of polarization with temperature is more gradual. Moreover, in contrast to the unirradiated samples, the data from the irradiated samples exhibits two major broad pyroelectric peaks. The one at temperature near  $-25^{\circ}\text{C}$  is apparently associated with the glass transition, indicating increased amorphous phase due to the irradiation and increased influence of the amorphous phase on the polarization response in the material. And the one at higher temperature

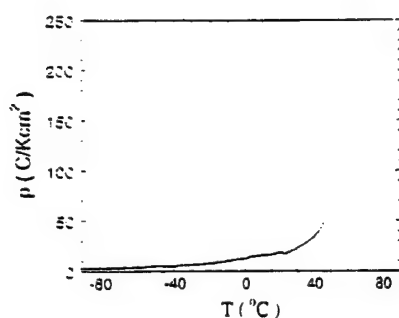


Fig. 6 Change in the pyroelectric current with temperature before irradiation

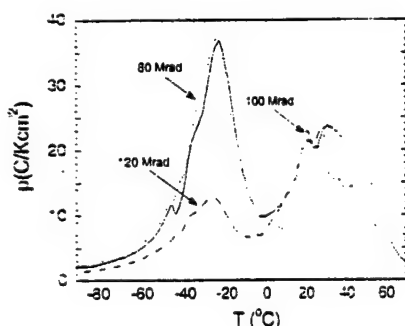


Fig. 7 Pyroelectric current with temperature for irradiated copolymer films

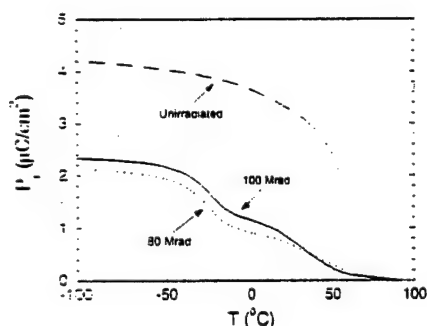


Fig. 8 Variation of remanent polarization with temperature obtained from the integration of the pyroelectric current shown in Figs. 6 and 7

(above 20°C) seems to be associated with the polarization freezing process, consisting with the dielectric constant data.

The results presented show that the P(VDF-TrFE) 50/50 copolymer after irradiation exhibits many features resembling those of relaxor ferroelectrics in ceramic systems [15], that is, the slim polarization hysteresis loop at temperature near the dielectric peak which gradually evolves into a normal ferroelectric polarization hysteresis loop with reduced temperature and the dispersion of the broad dielectric peak which follows the V-F law. However, unlike ceramic systems, the polymeric material we are dealing here is much more complicated due to the existence of the amorphous phase which should have significant effect on the polarization responses in the crys-

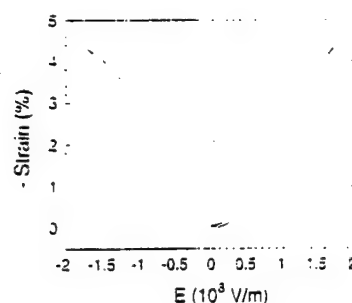


Fig. 9 Electric field induced strain versus electric field measured at room temperature for irradiated (100 Mrad) copolymer film

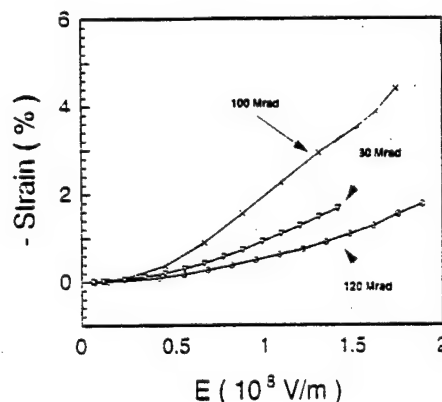


Fig. 10 The dependence of the induced strain amplitude on electric field for copolymer films irradiated with different irradiation doses. The symbols here are the data points and solid lines are drawn to grid points

talline region and the material as a whole. On the other hand, the amorphous matrix may also provide an extra-parameter which can be used to adjust the material properties.

#### The electrostrictive strain and elastic response

More interestingly, the copolymer after irradiation produces an ultrahigh strain as shown in Fig. 9 which is the strain along the thickness direction (longitudinal strain) from sample irradiated with 100 Mrad. Again, the induced strain level for the three irradiation conditions, 80, 100, and 120 Mrad, shows an irregular change with dosage as summarized in Fig. 10. The sample with 100 Mrad generate the highest strain, which is about  $-4.4\%$  under a field of 174 MV/m, while the sample with 120 Mrad exhibit the lowest strain level. This trend seems quite similar to the polarization behavior presented in the previous section.

Combined with the polarization data (Fig. 3), one can obtain the electrostrictive coefficient  $Q_{11}$  from the relation  $S=QP^2$ , where  $S$  is the longitudinal strain and  $P$  the is polarization [21]. The electrostrictive coefficient  $Q_{11}$  for samples under the three irradiation dosages is:  $-8.7 \text{ m}^2/\text{C}^2$  for 100 Mrad,  $-6.6 \text{ m}^2/\text{C}^2$  for 80 Mrad, and

Fig. 11a, b The change in the elastic modulus (a) and (b) mechanical loss as a function of temperature for unirradiated and irradiated copolymer films

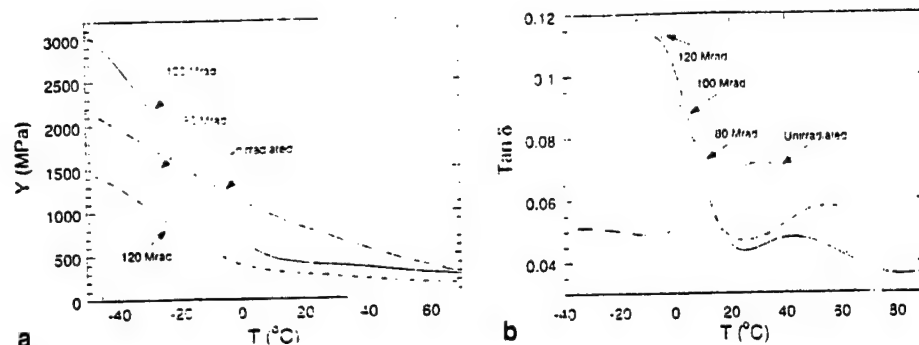


Table 1 Comparison of the strain and strain energy density

Materials	Y (GPa)	Typical $S_m$	$YS_m^2/2$ (J/cm <sup>3</sup> )	$YS_m^2/2\rho$ (J/kg)
Piezoceramic (1)	64	0.2%	0.13	4.25
Magnetostrictor (2)	100	0.2%	0.2	21.6
PZN-PT single crystal (22)	7.7	1.7%	1.0	131
P(VDF-TrFE) irradiated (100 Mrad)	0.45	4.4%	0.43	230

$-5.9 \text{ m}^2/\text{C}^2$  for 120 Mrad. The results indicate that in addition to lower polarization level, the lower strain response in 80 Mrad and 120 Mrad irradiated samples are also a consequence of lower electrostrictive coefficients.

Nevertheless, the results here show that under a proper electron irradiation, a large electrostrictive strain can be achieved in P(VDF-TrFE) copolymers. Materials with such high electrostrictive strain are attractive for actuator, sensor, and transducer applications [15, 22]. However, in very soft polymers the Maxwell stress effect, originating from the Coulomb force of the charges, can deform the material to a high strain level [23, 24]. Hence, other parameters such as the strain energy density are also used to evaluate an actuator material [25]. To evaluate the strain energy of the irradiated polymers, the elastic modulus of these materials was measured. Figure 11 present the elastic modulus and dissipation factor ( $\tan\delta$ ) as a function of temperature at 10 Hz. In most of the temperature region, the elastic modulus of irradiated samples is reduced compared with unirradiated samples, indicating an increase of the amorphous phase and breaking up of the crystalline region into smaller size. For irradiated samples, over a relatively broad temperature range (above  $10^\circ\text{C}$ ), the elastic modulus shows a very weak temperature dependence. Interestingly, the elastic modulus also exhibits an irregular change with electron dosage. That is, the modulus for samples irradiated with 100 Mrad is higher than those of 80 Mrad and 120 Mrad, indicating a complicated relationship of the elastic modulus with the defects structure introduced by irradiation.

From the elastic modulus, the elastic energy density of these materials is determined. In Table 1, we compare the irradiated P(VDF-TrFE) copolymer (100 Mrad) with several currently known materials, including the ferro-

electric relaxor single crystal PZN-PT, which has been shown to possess an ultrahigh strain response [26, 27]. Both the volumetric energy density, which is proportional to  $YS_m^2/2$  and related to the device volume, and gravimetric energy density, which is proportional to  $YS_m^2/2\rho$  and related to the device weight, are included in this table, where Y is the elastic modulus,  $S_m$  is the strain level, and  $\rho$  is the density of the material [25]. Apparently, in terms of the strain and strain energy density, the electrostrictive P(VDF-TrFE) copolymer reported here exhibits a significantly improved performance compared with traditional piezoceramic and magnetostrictive materials and is on a par with the PZN-PT single crystal.

## Summary

The influence of the electron dosage (from 80 Mrad to 120 Mrad) on the field induced strain, the polarization response, the dielectric constant, and elastic modulus of P(VDF-TrFE) 50/50 copolymer irradiated at room temperature has been investigated. It was found that the samples with 100 Mrad exhibit a strain of  $-4.4\%$  under a field of 175 MV/m and a strain energy density much higher than those of the conventional piezoceramic and magnetostrictive materials. Many irregular changes of the responses with dosage were observed. Although in general, the irradiation lowers the dielectric constant peak temperature and increases the dispersion in the peak position (relaxor behavior). It was observed that the dielectric peak temperature moves up slightly at higher dosage, accompanied with a decrease in the frequency dispersion in the peak position. Among the three dosages examined (80, 100, and 120 Mrad), the samples with 100 Mrad exhibit the highest field induced polarization, the strain, and the elastic modulus. In addition, it was also observed that the smaller strain response in the 80 Mrad and 120 Mrad samples compared with the 100 Mrad sample is caused by both a reduction in the polarization level and the electrostrictive coefficient.

**Acknowledgements** The authors would like to thank L. E. Cross, J. Lindberg and G. Kavarnos for stimulating discussions. This work was supported by ONR through Grant No. N00014-97-1-0900 and NSF through Grant No. ECS-9710459.



## References

1. Lovinger AJ (1983) *Science* 220:1115
2. Tashiro K (1995) *Ferroelectric Polymers*. In: Nalwa HS (ed) Marcel Dekker, New York, p 43
3. Cross LE (1996) *Ceramic Trans* 68:15; the data in Table 1 is for PST-4
4. Hathaway KB, Clark Arthur E (1993) *MRS Bulletin* 18:34; the data in Table 1 is for Terfenol-D
5. Wayman SM (1993) *MRS Bulletin* 18:49
6. Daudin B, Dubus M, Legrand JF (1987) *J Appl Phys* 62:994
7. Odajima A, Takasa Y, Ishibashi T, Yuasa K (1985) *Jpn J Appl Phys* 24:381
8. Lyons BJ (1995) *Radiat Phys Chem* 45:159
9. Macchi F, Daudin B, Hillairer J, Lauzier J, NiGoma JB, Cavaillie JY, Legrand JF (1990) *Nucl Instr Phys Res B* 46:334
10. Lovinger AJ (1985) *Macromolecules* 18:910
11. Furukawa T (1989) *Phase Transition* 18:143
12. Su J, Moses P, Zhang QM (1998) *Rev Sci Instruments* (in press)
13. Sinha JK (1965) *R Sci Instrum* 42:696
14. DMA 2980, TA Instruments, Inc., New Castle, DE 19720
15. Cross LE (1987) *Ferroelectrics* 76:241
16. Vogel H (1921) *Z Phys* 22:645; Fulcher GS (1925) *J Am Ceram Soc* 8:339
17. Tagantsev AK (1994) *Phys Rev Lett* 72:1100
18. Mattsson J, Jonsson T, Nordblad P, Aruga H, Ito A (1995) *Phys Rev Lett* 74:4305
19. Furukawa T, Tajitsu Y, Zhang X (1992) *Ferroelectrics* 135:401
20. Davis GT, Furukawa T, Lovinger AJ, Broadhurst MG (1982) *Macromolecules* 15:329
21. Sundar V, Newnham RE (1992) *Ferroelectrics* 135:431
22. Haertling GH (1987) *Ferroelectrics* 75:25
23. Zhang QM, Su J, Kim C, Ting R, Capps R (1997) *J Appl Phys* 81:2770
24. Pelrine R, Kornbluh RD, Joseph JP (1998) *Sensors and Actuators A* 64:77
25. Giurgiutiu V, Rogers C (1996) *J Intel Mater Syst and Struct* 7:656
26. Park Seung-Eek, Shrout T (1997) *J Appl Phys* 82:1804
27. Service RF (1997) *Science* 275:1878

# **APPENDIX 29**



# A bimorph based dilatometer for field induced strain measurement in soft and thin free standing polymer films

J. Su and P. Moses

*Materials Research Laboratory, Pennsylvania State University, University Park, Pennsylvania 16802*

Q. M. Zhang<sup>a)</sup>

*Materials Research Laboratory and Department of Electrical Engineering, Pennsylvania State University, University Park, Pennsylvania 16802*

(Received 19 February 1997; accepted for publication 27 March 1998)

A bimorph based dilatometer has been developed which enables one to characterize the electric field induced strain response in the out-of-plane direction in thin and soft free standing polymer film samples conveniently over a relatively wide frequency range (1 Hz to 1 kHz). The test results demonstrate that the newly developed dilatometer is capable of detecting displacement down to sub-angstrom range. The agreement between the test results from the bimorph dilatometer, the results from a laser dilatometer, and the model analysis indicates that the device can indeed be used reliably for these measurement with high sensitivity. © 1998 American Institute of Physics. [S0034-6748(98)03706-X]

## I. INTRODUCTION

Polymeric materials have many attractive and unique features for electronic and electromechanical transduction applications. In these applications, how the material behaves under an external electric field is of prime concern in the material selection. Because of the softness of samples to be characterized, currently it is still a great challenge to reliably determine the strain induced by an external electric field in thin polymer films without imposing constraint.

In general, the existing techniques for characterizing the electric field induced strain response in a polymer film can be grouped into two categories: the contact methods and noncontact methods. The contact methods such as the one making use of the change in capacitance between two parallel plates to measure the dimensional change of a polymer film are typically difficult to be used on routine bases.<sup>1,2</sup> In addition, the contacts from the capacitor plates in the capacitance method may impose mechanical constraints in the sample which could be significant for a soft and thin sample and introduce large error in the measurement. For the noncontact measurements, where the laser dilatometer is the one most frequently used, in order to determine the field induced strain in the out-of-plane direction in thin films, two laser beams on the opposite faces of the sample are required. However, again because of the thinness and softness of the films, it is quite easy to excite the flexure motion in the sample which causes severe errors in the results.<sup>3</sup> It appears to us that currently there exists no suitable technique to characterize the electric field induced strain in thin and soft polymeric samples reliably and conveniently.

The recent development of the atomic force microscope has demonstrated the high sensitivity of a cantilever beam in detecting small force, which implies that the similar principle

may be transplanted to measure the displacement of soft polymer films without imposing large stress or mechanical constraints in the sample.<sup>4,5</sup> In an even more traditional area, i.e., displacement sensor in a phonograph cartridge, the demands of audiophiles have been forcing the constant improvement of the sensor head and as a result, phonograph cartridges are well developed high sensitivity transducers which require a very small contact force and can be operated over a wide frequency range. Inspired by these advancements, we attempted to develop a high sensitivity displacement sensor to characterize the electric field induced strain in soft and thin polymeric samples based on the piezoelectric bimorph cantilever beam, which in the current device was modified from a phonograph pick-up cartridge, and the results are reported in this article.

## II. EXPERIMENT

The schematic of the setup is shown in Fig. 1. The one end of the piezoelectric bimorph is clamped at a solid support and at the other end, a stainless steel (ss) pin which is in contact with the sample is attached using a thin layer of epoxy glue. Under an external electric field, the sample expands and contracts in the  $z$  direction and generates a corresponding motion in the sensor head. Consequently, a bending in the piezoelectric bimorph is produced. Through the direct piezoelectric effect, an electrical output which is proportional to the sensor head displacement is generated. After the calibration, this output signal can be used to quantitatively measure the displacement. In the current setup, a well aged PZT-4 piezoceramic is used as the displacement standard, whose piezoelectric  $d_{33}$  value was measured by both a laser dilatometer and a Berlincourt  $d_{33}$  meter.<sup>6,7</sup> By applying a fixed voltage to this standard, typically in the range between 1 and 10 V, a displacement in the range of 2–20 Å is generated to calibrate the device. A typical calibration curve thus obtained is shown in Fig. 2 where the measured current

<sup>a)</sup> Author to whom correspondence should be addressed.

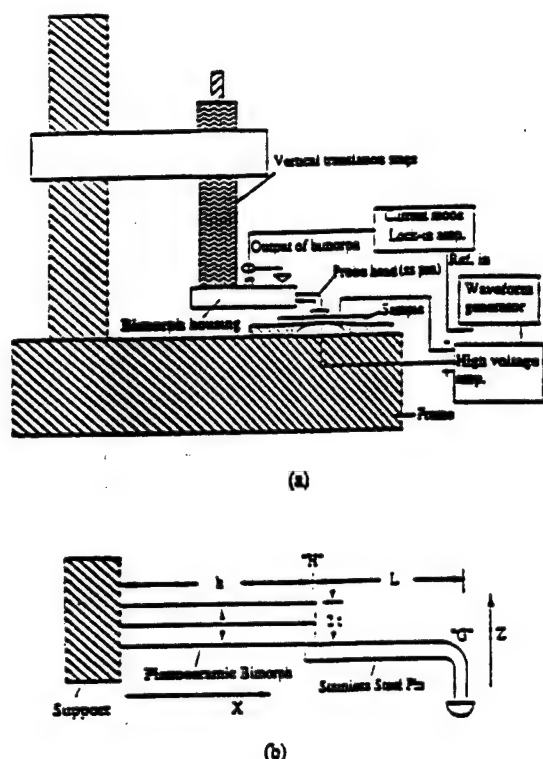


FIG. 1. (a) Schematic of the newly developed high resolution displacement sensor and the electric driving and detection circuit. (b) schematic of the sensor head consisting of a piezoelectric bimorph and a stainless steel pin. The bending in the bimorph generates an electric output which is proportional to the displacement at the point  $G$ .

from a lock-in amplifier versus the displacement in the PZT-4 standard is presented against the measuring frequency. Since the stability of the bimorph sensor is crucial to the device, a bimorph in a commercial phonograph cartridge made by RCA is used here. The dimensions of the bimorph are:  $r=0.3$  mm, the width  $w=1.5$  mm, and the length  $h$  is approximately 10 mm. The dimensions of the PZT-4 standard is  $5 \times 5 \times 5$  mm<sup>3</sup>. The lock-in amplifier used is Model SR830 from Stanford Research Systems having a current sensitivity down to the fA range.

To assess the performance of this newly developed bimorph based dilatometer in characterizing the field induced

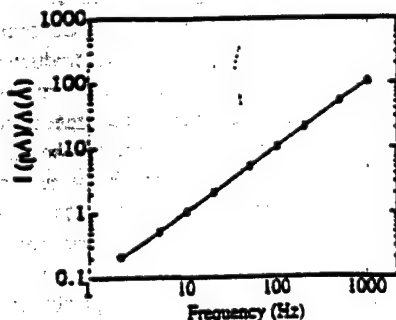


FIG. 2. The calibration curve of the displacement sensor which shows that the sensitivity of the device is proportional to the frequency. Open circles are the experimental data and solid line is a linear fitting curve. The time constant of the lock-in amplifier is 1 s for signals at 1 KHz and 10 s at frequencies below 20 Hz.

strain in soft polymer films, the relationship between the sample surface displacement and charge output of the bimorph is analyzed based on a static model and results are compared with the experiment. In addition, a direct comparison of the experimental results from a laser dilatometer, which is a well established technique in displacement characterization, and from the new bimorph based dilatometer will also be made.

### III. ANALYSIS OF THE PERFORMANCE

In the analysis, the bimorph and ss pin are treated as a cantilever system with one end clamped. In the analysis, the displacement  $\delta$  and the slope  $\alpha$  at the piezobimorph end  $H$  are derived first and then the displacement at the tip  $G$  of the ss pin is evaluated. For a force applied at the tip  $G$  (Fig. 1) along the  $z$  direction, the moment  $M$  in the beam is

$$M = F(h + L - x), \quad (1)$$

where  $x=0$  is at the boundary between the support and the bimorph. From the theory of cantilever beam,  $YK\delta^2 = \int_0^L M^2 dx = \int_0^L F^2(h + L - x)^2 dx = FL^3/3$ , where  $Y$  is the Young's modulus,  $K$  is the moment of inertia, and for the bimorph beam  $K=2\pi r^4/3$ , the slope at the bimorph end  $H$  is

$$\alpha = \frac{F}{2YK} (h^2 + 2hL), \quad (2)$$

and the displacement at  $H$  is

$$\delta^b = \frac{F}{2YK} [(L+h)^2 h + \{L^3 - (L+h)^3\}/3]. \quad (3)$$

The bending in the piezoceramic bimorph will also produce a displacement at the point  $G$  of the ss pin, which can be shown through the geometric consideration:

$$\delta' = \delta^b - \alpha L, \quad (4)$$

where the second term on the right hand side of the equation is just a geometric amplification effect. In addition, the force  $F$  will also produce a displacement (from the bending of the ss pin) at the point  $G$  of the ss pin according to<sup>8</sup>

$$\delta'' = \frac{4L^3}{3\pi Y^s r^4}, \quad (5)$$

where  $r$  is the radius and  $Y^s$  is the Young's modulus of the ss pin, respectively. Combining Eqs. (4) and (5) yields the relationship between the force  $F$  and displacement  $\Delta$  at the sensor head (point  $G$ ):

$$\Delta = \delta' + \delta'' = BF, \quad (6)$$

where

$$B = \frac{4L^3}{3\pi Y^s r^4} + \frac{3h}{2\pi r^4 Y} (hL + L^2 + 2h^2/3).$$

The charge output  $q$  is evaluated using the energy function of a piezoelectric bimorph of length  $h$  when subjected to a moment  $M = F(L + h - x)$  as outlined in the Ref. 9, which yields

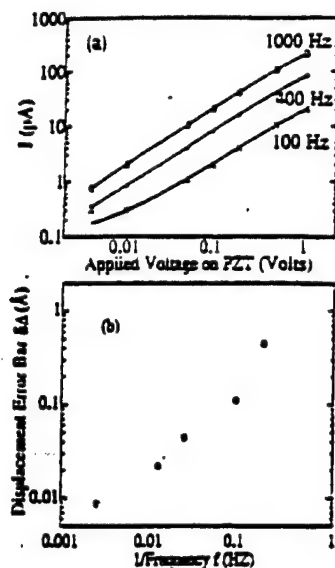


FIG. 3. (a) The current measured by a lock-in amplifier vs the displacement in a PZT-4 standard (the displacement in PZT-4 =  $2.20 \text{ \AA} \times \text{applied voltage}$ ) which shows a linear relationship between the displacement and the current output. The sensitivity of the device increases at low frequency. Open circles, black dots, and crosses are the data points and solid lines are drawn to guide eyes. (b) The displacement error bar vs frequency. Apparently, the error bar increases faster than  $1/f$ . The time constant of the lock-in amplifier was adjusted at each frequency to obtain the maximum sensitivity (from 1 s at 1 kHz to 30 s at 5 Hz).

$$C = -\frac{3d_{31}(h^2 - 2Lh)}{8r} F \quad (7)$$

and

$$C = -\frac{3d_{31}(h^2 - 2Lh)}{8rB} \Delta. \quad (8)$$

In our setup,  $L$  is approximately the same as  $h$  and hence,  $B$  in Eq. (6) is proportional to  $h^3$ .

#### IV. EXPERIMENTAL RESULTS

Presented in Fig. 3(a) is the relationship between the current output of the sensor head and driving electric field applied to the PZT-4 standard (the displacement of PZT-4 is linearly proportional to the driving field), where 1 V corresponds to a displacement of  $2.2 \text{ \AA}$ . The data shown are at 100 Hz, 400 Hz, and 1 kHz. The time constant of the lock-in amplifier is 10 s. Since for a given displacement  $\Delta$  at the sensor head  $G$ , the charge output  $q$  is fixed and for a sinusoid signal, the current output  $I$  from the bimorph is equal to  $q\omega$ , where  $\omega$  is the angular frequency. The sensitivity of the system which is defined as  $I/\Delta$ , hence, will be directly proportional to the frequency, as shown in Fig. 2 where for a given applied voltage,  $I$  increases linearly with frequency. On the other hand, the environmental noises such as the vibration and air turbulence, which in the current system are the major source limiting the probe sensitivity, become severe at low frequencies. Due to this reason, the measured error bar  $\delta\Delta$  of the displacement ( $\Delta = \delta\Delta$ ) versus frequency, as shown in Fig. 3(b), deteriorates faster than  $1/f$ , where  $\delta\Delta$  is evaluated from the half width at half maximum of the

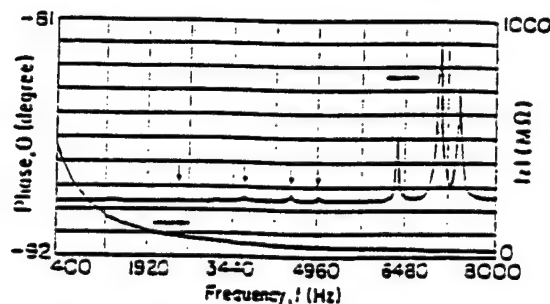


FIG. 4. The electric impedance curve measured from the piezoelectric bimorph when the probe head was in contact with a sample. There is no noticeable resonance at frequencies below 2 kHz (the weak resonances are indicated by arrows). Hence, the current device can be used up to 1 kHz without the interference of the resonance. The resonant frequency in the device can be raised by reducing the lengths of the bimorph and ss pin.

displacement data for a given applied voltage. To reduce these noises, the setup was placed inside a closed chamber during the measurement. It should be noted that when using a lock-in amplifier in signal detection, the sensitivity of the system can be improved by increasing the time constant of the lock-in sampling time. For that reason, the time constant of the lock-in amplifier was adjusted at each measuring frequency to obtain the maximum sensitivity of the system at that frequency. The data in Fig. 3 show that the probe has a sub-angstrom sensitivity over a relatively wide frequency range. For instance, at 100 Hz, it can detect a displacement of about  $0.03 \text{ \AA}$ .

The data at 100 Hz were also used to make a comparison between the test result and the performance prediction based on the static model presented in the preceding section. Since in the construction of the sensor head, the exact dimensions such as  $h$  and  $L$  cannot be controlled precisely, the approximate values of  $h = 10$  and  $L = 10 \text{ mm}$  are used in the calculation. The other parameters are: for the piezoceramic bimorph,  $r = 0.3 \text{ mm}$ ,  $w = 1.5 \text{ mm}$ ,  $Y = 6.06 \times 10^{10} \text{ N/m}^2$ , and  $d_{31} = -274 \text{ pC/N}$ , and for the ss pin,  $r = 0.32 \text{ mm}$ ,  $Y^{\text{ss}} = 1.92 \times 10^{11} \text{ N/m}^2$ . Using these parameters, we obtain the charge output  $2.2 \times 10^{-13} \text{ C}$  for a displacement at the sensor head of  $11.04 \text{ \AA}$ , while the experimentally measured value is  $1.59 \times 10^{-13} \text{ C}$  [data in Fig. 3(a)]. Considering the approximations made in the model analysis where the joint between

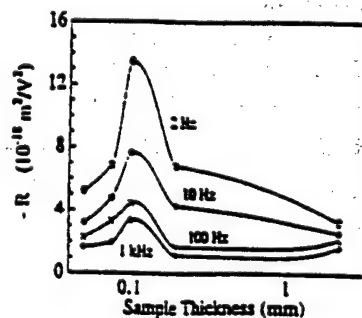


FIG. 5.  $R$  of a polyurethane elastomer (DOW 2103-30AE) as a function of the sample thickness at different frequencies. The negative sign of  $R$  coefficient indicates that the film contracts when a voltage is applied. The thinnest sample measured is  $20 \text{ \mu m}$  thick. Data points are shown on the figure and the solid curves are drawn to guide eyes.

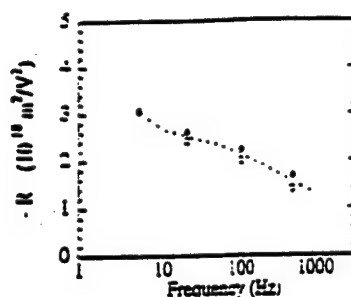


FIG. 6. Comparison of  $R$  coefficient of a polyurethane sample (2 mm thick) measured from a double beam laser dilatometer (solid circles) and the newly developed bimorph dilatometer (open circles) as a function of frequency.

the ss pin and the bimorph was assumed to be rigid with zero length, the agreement between the experiment and theoretical model is satisfactory, indicating that the probe functions properly with a high sensitivity.

One of the concerns in operating this new instrument is its operational frequency range. At the low frequency end, the frequency limit is mainly caused by the decrease of the sensitivity as the frequency is lowered. On the other hand, on the high frequency end, it is the resonant frequency of the system which limits how high the probe can be operated. For a cantilever beam, the resonant frequency is inversely proportional to the square of the length ( $h$  and  $l$  for the system discussed here).<sup>1,10</sup> Shown in Fig. 4 is the electric impedance of the probe head (the impedance is from the piezoelectric bimorph) versus frequency for the system tested where the probe head is in contact with a sample as in the measurement situation. As seen, the first resonance mode appears at a frequency above 2 kHz. From the fixed boundary condition at the two ends, this resonance corresponds to a half-wave length resonance. Hence, the device can be used at frequencies up to 1 kHz without the interference from the resonant mode, which was also confirmed by direct experimental results.

After the calibration and evaluation of the device, a series of polyurethane elastomers (DOW 2103-80AE) was characterized as to their field induced strain responses. It is well known that in this type of material, because of the central symmetry, the strain  $S$  is proportional to the square of the applied electric field  $E$ , i.e.,  $S = RE^2$ , where  $R$  is a coefficient describing the sensitivity of strain change in the material to the external electric field. For a sinusoidal applied electric field  $E = E_0 \cos \omega t$ , it is the  $2f$  component of the strain response that is measured by the lock-in amplifier.

$$S = R(E_0 \cos \omega t)^2 = RE_0^2(1 - \cos 2\omega t)/2 \quad (9)$$

which indicates the displacement amplitude  $\Delta$  measured at the probe head at  $2f$  frequency is

$$\Delta = -t_p RE_0^2 \cos(2\omega t)/2 \quad (10)$$

because  $S = \Delta/t_p$ , where  $t_p$  is the sample thickness. From the calibration curve,  $\Delta$  can be determined and from Eq. (10),  $R$  can be obtained. Shown in Fig. 5 is the  $R$  coefficient for polyurethane films versus thickness at different frequencies measured at room temperature. The samples are made from solution casting and the electrode is sputtered gold film of about 300 Å thickness. The negative sign of  $R$  coefficient indicates that the film contracts as an electric field is applied. The device is quite convenient in measuring the electric field induced strain in thin film samples and the thinnest film measured here is 20 μm. From the basic principle of the device and the analysis presented, it is clear that the probe can be used to characterize the strain response in even thinner films. The dependence of  $R$  with thickness has been investigated earlier using a laser dilatometer and due to the limitation of the measuring technique, the thinnest sample examined was 0.15 mm.<sup>3,11</sup> In the thickness range overlapped, the results from the two measurements are consistent with each other. The dependence of  $R$  with film thickness implies that measured strain response contains significant contributions from surface or interface effect which was discussed in another publication.<sup>12</sup> Figure 6 presents a comparison between the result measured from the current device and that from a double beam laser dilatometer on polyurethane sample of 2 mm thickness. Apparently, the results from the two agree with each other quite well. The agreement of the results between the two dilatometers and between the experimental results and the model analysis indicate that the device can be used reliably for the strain measurement in polymeric films.

## ACKNOWLEDGMENT

This work was supported by the Office of Naval Research.

- <sup>1</sup> M. Zhenyi, J. L. Scheinbeim, J. W. Lee, and B. A. Newman, *J. Polym. Sci., Part B: Polym. Phys.* **32**, 3731 (1994).
- <sup>2</sup> R. F. Sami, H. Tong, T. W. Poon, B. D. Silverman, P. S. Ho, and A. R. Rossi, *J. Appl. Polym. Sci.* **46**, 1329 (1992).
- <sup>3</sup> H. Wang, Q. M. Zhang, L. E. Cross, R. Ting, C. Coughlin, and K. Rittenmyer, *Proceedings of the 9th IEEE International Symposium on Applications of Ferroelectrics 1994*, p. 182.
- <sup>4</sup> G. L. Miller, J. E. Griffith, E. R. Wagner, and D. A. Grigg, *Rev. Sci. Instrum.* **62**, 705 (1991).
- <sup>5</sup> T. Inoh and T. Suga, *J. Vac. Sci. Technol. B* **12**, 1581 (1994).
- <sup>6</sup> PZT-4 is the trademark of Morgan Marce Inc. OH for its piezoceramic.
- <sup>7</sup> Q. M. Zhang, S. J. Jang, and L. E. Cross, *J. Appl. Phys.* **65**, 2307 (1989).
- <sup>8</sup> Landau and E. M. Lifshitz, *Theory of Elasticity* (Pergamon, Oxford, 1986).
- <sup>9</sup> J. G. Smith, S. I. Dalke, and T. K. Cooney, *Sens. Actuators A* **28**, 41 (1991).
- <sup>10</sup> J. M. Herbert, *Ferroelectric Transducers and Sensors* (Gordon and Breach Science, New York, 1982).
- <sup>11</sup> H. Wang, Ph.D. thesis, The Pennsylvania State University, 1994.
- <sup>12</sup> J. Su, Q. M. Zhang, and R. Ting, *Appl. Phys. Lett.* **71**, 350 (1997).

# **TRANSDUCER STUDIES**

**Composite Structures**

# **APPENDIX 30**

# TRANSDUCERS, UNDERWATER ACOUSTIC

W. JACK HUGHES, *Applied Research Laboratory, Pennsylvania State University, State College, Pennsylvania, U.S.A.*

	<b>Introduction</b> .....	67	4.4	Mechanical Transducer .....	77
1.	<b>Operating Environment</b> .....	68	4.5	Electromagnetic, Moving-Coil Transducers .....	77
2.	<b>Materials</b> .....	68	4.6	Resonant Bubble Transducer .....	78
2.1	Piezoelectric Materials .....	68	4.7	Helmholtz Resonator .....	78
2.2	Piezoelectric Ceramics .....	69	4.8	Hydroacoustic Projector .....	78
2.3	Composite Ceramics .....	70	4.9	Spherical-Shell Transducer ....	78
2.4	Piezoelectric Polymers .....	70	4.10	Impulsive Transducer .....	78
2.5	Magnetostrictive Materials .....	70	5.	<b>Longitudinal Vibrator Transducers (3 kHz to &gt;100 MHz)</b> .....	79
3.	<b>Testing of Underwater Transducers</b> .....	70	5.1	Tonpiz Transducers .....	79
3.1	Calibration Formulas .....	71	5.2	Thickness Vibrators .....	81
3.2	Calculated Parameters .....	73	5.3	Shaped Ceramic Transducers .....	82
3.3	Cavitation .....	74	6.	<b>Other Transducers</b> .....	83
4.	<b>Low-Frequency Transducers (10–5000 Hz)</b> .....	75		<b>Works Cited</b> .....	84
4.1	Flexural Disk .....	75		<b>Further Reading</b> .....	84
4.2	Flexensional Transducer (300–3000 Hz) .....	76			
4.3	Free-Flooded Ring .....	77			

## INTRODUCTION

A transducer is a device that converts energy from one form to another. An electroacoustic transducer transforms electrical energy into acoustic energy, or vice versa. An electromechanical transducer transforms electrical energy to mechanical energy or movement, which then may transmit energy. These are the energy transformations that will be involved in the transducers mentioned in this article. Understanding and design of transducers is multidisciplinary and involves a knowledge of materials, physics, acoustics, electrical engineering, mechanical engineering, and chemistry. Fortunately, there are many guidelines that can be followed in which the beginner can understand the various disciplines involved. Some people call the successful fabrication of transducers a "black art." This is an overworked term; transducer design and fabrication follow a well thought-out path, but do require a broad knowledge in the sciences and engi-

neering. They also require learning how acoustics interacts with different materials and their acoustic impedances. Baffles, housings, and resonant structures typically surround the transducer and can have a major impact on its performance. Just like in most fields, the "bugs" need to be "worked out" from the design for the transducer to be an integral part of a measuring system.

Landmarks in the history of electroacoustics were Bell's invention of the telephone (1876) and Edison's work on the carbon microphone and the phonograph. Langevin and others used steel-quartz-steel resonator plates, which form a composite underwater projector transducer for the detection of submarines. Equivalent circuits that describe the action of piezoelectric resonators were developed by Van Dyke (1928) and Mason (1934, 1948), and good introductions can be found in Wilson (1985), Stansfield (1990), Hunt (1982), Berlincourt *et al.* (1964), Kinsler *et al.* (1982), and Bobber (1988). The discovery of



the large piezoelectric effects in ceramics (e.g., barium titanate, 1946) led to the development of the technology of modern piezoelectric ceramics, and to the improvement in the performance of electromechanical transducers.

There are many different types of transducers that can be discussed. A good list of the different types of transducers used in the field of acoustics can be seen in the *Journal of the Acoustical Society of America* index under the listing 43.38, "Transduction; Acoustical devices for the generation and reproduction of sound." The transducer types from this list that are generally used in underwater acoustics are magnetostrictive transducers, electromagnetic and electrodynamic transducers, piezoelectric and ferroelectric transducers; transducer arrays, acoustic interaction effects in arrays, hydroacoustic and hydraulic transducers, and impulse transducers. Acoustic transducers of various types must satisfy the application needs over a frequency range of seven decades. In Fig. 1 is shown a convenient comparison of the large acoustic frequency range, the application, and devices and materials. This article is devoted mostly to describing underwater transducers, how they are tested, and how they operate. An excellent introduction to underwater electroacoustics can be found in Wilson (1985) and in Kinsler *et al.* (1982).

## 1. OPERATING ENVIRONMENT

Operating a transducer in an underwater environment is dramatically different from operating in air, and significantly affects how the transducer is designed and the types of materials used in the design. To gather an understanding of the difference, the relative

pressure for a given particle displacement in air and water is now determined. The ratio of acoustic pressure  $p$  to particle velocity  $v$  is equal to the specific acoustic impedance of the medium  $\rho c$ , where  $\rho$  is the density and  $c$  is the sound velocity. The particle displacement is given by

$$\chi = v/\omega = (p/\omega)\rho c, \quad (1)$$

where  $\omega = 2\pi f$  is the angular frequency and  $f$  is the frequency. The acoustic impedance  $\rho c$  for water is  $1.5 \times 10^6$  Rayls (Rayl = kg/m<sup>2</sup>·sec) and for air is 415 Rayls. For a given pressure and frequency, the ratio of the particle velocities is equal to the ratio of the medium impedances; hence, 3600 times more motion is needed in air than in water to create the same pressure level. From this it is obvious that a transducer in air must be much more compliant than in water (e.g., a compliant loudspeaker versus a stiff ceramic).

## 2. MATERIALS

Materials typically used in an underwater environment undergo a length or volume change when an alternating electric or magnetic field is applied to the material. They can be generally grouped into piezoelectrics, ceramics, composites, polymers, and magnetostrictive materials.

### 2.1 Piezoelectric Materials

The piezoelectric effect arises because of the asymmetries in the crystal structure, which create an electric dipole moment in the crystal lattice that is sensitive to both elastic strain and applied electric field.

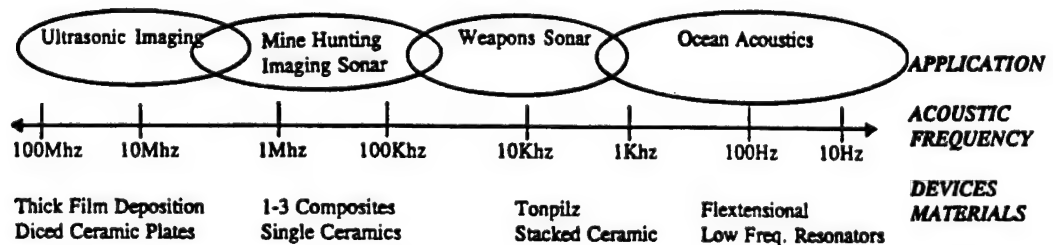


FIG. 1. Acoustic frequency range for transducers.



Quartz is one of the earliest materials discovered with the piezoelectric effect. It is rarely used for underwater projectors; however, its very low internal losses and very high mechanical  $Q$  lead to the use of quartz in stable resonant circuits in the communication and electronics fields. Rochelle salt, an extremely active piezoelectric material, was used for early underwater projectors and hydrophones, and as phonograph pickups and microphones. It is very sensitive to moisture, which can dissolve the crystal, and hence was replaced by more environmentally stable materials for underwater transducers. Ammonium dihydrogen phosphate (ADP) replaced Rochelle salt in the 1940s. Modern transducers use piezoelectric ceramics, which are sintered polycrystalline materials polarized by large electrical fields while they are cooling from temperatures near or above the Curie point (typically 200–400 °C), a characteristic temperature above which a ceramic element shows no sign of piezoelectric activity. In practice, the operating temperature should be limited to about half of the Curie point. Ceramics can have their properties tailored to fit specific applications. In addition to the ceramics, piezorubber and piezoelectric polymers such as polyvinylidene fluoride (PVDF) have come into use. Also, a matrix material called "1-3 composites" (because of the orientation direction of its small PZT rods) is coming into use for large transducer systems.

Other piezoelectric materials that are sometimes used are these: Lithium sulfate ( $\text{LiSO}_4 \cdot \text{H}_2\text{O}$ ) is used for hydrophones; tourmaline has been used in the calibration of hydrostatic pressure devices and in the measurement of blast wave pressures; lead metaniobate ( $\text{PbNb}_2\text{O}_6$ ) has a very high Curie temperature and a low mechanical  $Q$ , and is used for deep submergence hydrophones; lead titanate ( $\text{PbTiO}_3$ ) has a large hydrostatic piezoelectric constant, which allows this material to be used as a volume expander. A volume expander means that all surfaces of the material expand in phase, allowing simple hydrophone mounting materials to be used.

## 2.2 Piezoelectric Ceramics

The most widely used ceramics for underwater transducers are made from lead zirconate titanate (PZT). The materials used for

ceramics are polycrystalline, which have Curie temperatures between about 200 and 400 °C. Ceramic materials are quite variable in their properties, are difficult to maintain consistency between batches and manufacturers, and have nonlinear properties, and their properties change with age. Even with these problems, ceramics are the predominant type of piezoelectric material used today. A good description of the properties of piezoelectric materials can be found in Wilson (1985). The technology of barium titanate (B) and lead zirconate titanate (PZT) has been relatively stable so that their physical properties can be listed with some degree of confidence. A list can be obtained from any manufacturer or from many of the references given above.

Because the U.S. Navy procures ceramics for their sonar systems, a standard was developed for obtaining reproducibility of transducer characteristics from one manufacturer to another. The military specification is known as MIL-STD-1376(SHIPS), and classifies ceramics in this way:

*Classification.* The ceramic shall be of the following types:

*Type I*—Hard lead zirconate-titanate, such as PZT-4, with a Curie temperature equal to or greater than 310 °C.

*Type II*—Soft lead zirconate-titanate, such as PZT-5, with a Curie temperature equal to or greater than 330 °C.

*Type III*—Very hard lead zirconate-titanate, such as PZT-8, with a Curie temperature equal to or greater than 290 °C.

*Type IV*—Barium titanate with additives and a Curie temperature equal to or greater than 100 °C.

*Type V*—A high dielectric constant material similar to type II.

*Type VI*—An extremely high dielectric constant material, such as PZT-5H, similar to type II.

The type I compositions are hard materials developed for high-power projectors. Type I has a high electric field, high coupling coefficient, and low dielectric loss properties under high drive fields. The low dielectric loss is important so that heating effects are minimal. Type III materials provide high stability for high drive levels and very low dielectric losses. Types II, V, and VI are soft materials developed for hydrophones and

have high dielectric constants with high sensitivity, but also have high dielectric losses. Type VI has an extremely high dielectric constant and is often used in very high-frequency medical transducers.

The words hard and soft refer to how difficult it is to depolarize the ceramic. Unless the manufacturing process is well controlled, the values for a particular ceramic may vary as much as 10%. A solution to the varying properties from different batches and manufacturers is to purchase all of the ceramic that will be needed, plus spares, from a single batch.

The piezoelectric constant  $d$  expresses the ratio of the field developed along an axis to the applied stress. It quantifies the movement (motion) of the ceramic when a voltage is applied. A high value of  $d$  is looked for in ceramic used for a high-power projector. The piezoelectric constant  $g$  expresses the ratio of strain developed along an axis to the applied field. It quantifies the output voltage of the ceramic when a motion, or pressure, is applied. The product of the two piezoelectric strain coefficients,  $g$  and  $d$ , is a very useful measure of "goodness" per unit volume of a piezoelectric material when minimization of the hydrophone internal noise is a major design criterion. Lists of piezoelectric properties can be obtained from any manufacturer or in Wilson (1985).

### 2.3 Composite Ceramics

Considerable effort has been directed to the development of new composite configurations of the PZT ceramics with nonactive materials. Piezorubber is composed of ceramic particles imbedded into a rubber matrix. It is very flexible, is used as hydrophones, and is called a 0-3 composite material. The 0 means that the ceramic particles do not touch one another, and the 3 means that it is used in the thickness mode. Another new material is composed of many small parallel ceramic rods imbedded vertically in a matrix material. These are called 1-3 composites because the ceramic is connected in one direction, and it is used in the thickness direction. This 1-3 composite is available in large sheets and can be used as a projector as well as a hydrophone. Large-area sensors can be used because of the minimal planar vibration modes and the capability

to electroplate the surfaces. This material is finding many applications in underwater transducers.

### 2.4 Piezoelectric Polymers

Large piezoelectric effects are present in the polymer material polyvinylidene fluoride (PVDF or PVF<sub>2</sub>). When the material is stretched along one axis and polarized, it becomes a very useful sensor. It is available in sheets with electrodes on the surfaces. For hydrophone uses, thicknesses of the order of 500  $\mu\text{m}$  are used. PVDF has the advantages of flexibility, an impedance close to that of water, and a high hydrophone sensitivity relative to thickness. It is a poor transmitter and can be used only up to a temperature of about 100 °C. PVDF can be used where a very thin sensor is needed and where complex shapes can be etched into its surface. There are many other applications where a continuous sensor material that does not have any significant planar vibration modes can be used.

### 2.5 Magnetostrictive Materials

The magnetostrictive effect occurs when a magnetic field is applied to a material and causes a strain that is a nonlinear function of the applied field. The most important magnetostrictive materials are nickel and Terfenol-D. Nickel was used in the 1930s and 1940s in the construction of sonar projectors and hydrophones. Its use diminished because of its low electromechanical coupling coefficient, which relates the amount of kinetic energy available in the material to its total energy. Recently, the development of Terfenol-D by Clark (1980) has made available a high electromechanical coupling coefficient and a high electromagnetic strain. This material appears to have a chance to replace ceramics in some sonar transducers, especially in low-frequency projectors. A combination of Terfenol-D and ceramics in a single transducer has some interesting properties as described by Butler *et al.* (1990).

## 3. TESTING OF UNDERWATER TRANSDUCERS

To be able to use transducers properly, certain characteristics of the transducer and arrays of transducers must be measured and

Table 1. Calibration formulas.

Calibration test	Abbr.	Eq. No.	Formula	Units
Free-field voltage sensitivity	FFVS, $M$	2	$M_s - E_s + E_x$ $E_x - E_t - \text{TVR}_s + 20 \log D$	dB re 1 V/ $\mu$ Pa
Transmitting voltage response	TVR, $S$	3	$E_s - M_s - E_t + 20 \log D$	dB re $\mu$ Pa/V @ 1 m
Transmitting current response	TCR	6	$E_s - M_s - I_t + 20 \log D$ $\text{TVR} + 20 \log( Z )$	dB re $\mu$ Pa/A @ 1 m
Transmitting power response	TWR	7 8 14	$E_s - M_s + 20 \log D - 10$ $\log(e_t i_t \cos \phi)$ $\text{TVR} + 10 \log(R_p)$ $170.8 + \text{DI} + 10 \log(\mu)$	dB re $\mu$ Pa/W @ 1 m
Source level	SL	12 13 15	$\text{TWR} + 10 \log(P_t)$ $\text{TVR} + E_t$ $170.8 + 10 \log(P_t) + \text{DI} + 10 \log(\mu)$	dB re $\mu$ Pa @ 1 m
Equivalent hydrophone thermal noise	$\text{SPL}_n$	24	$10 \log(R) - M - 198$	dB re 1 V/ $\mu$ Pa
Equivalent parallel resistance of projector	$R_p$	9	$Z/\cos \phi$	Ohms
Efficiency	$\mu$		$10 \log(P_t/P_0)$	
Beamwidth (-3 dB)	BW (-3 dB)	16 18	Circular piston $60 \lambda/d$ Continuous line $50 \lambda/d$	Degrees
	BW (-10 dB)	20	$1.8 \text{ BW} (-3 \text{ dB})$	
	BW (null)	21	$2.3 \text{ BW} (-3 \text{ dB})$	
Directivity index	DI	17 19	Circular piston $10 \log(4\pi \times \text{area}/\lambda^2)$ Continuous line $10 \log(2L/\lambda)$	
Cavitation threshold intensity	$I_c$	27	$0.15[P_c(0) + h/33]^2$	W/cm <sup>2</sup>
Cavitation threshold pressure at zero depth	$P_c(0)$	26	$0.000 25f^2 + 0.045f + 1$	Atmospheres

understood. Equally important is knowing the various tests that can be performed on transducers and how to calculate the transducer parameters; see ANSI (1972). The term "transducer" as presented here implies that the device can be used either as a projector (transmitter) or as a hydrophone (receiver). When the term "projector" or "hydrophone" is mentioned, the characteristic being discussed will only apply to that type of device. For example, the directivity pattern of a transducer will be the same whether it is used as a projector or as a hydrophone. Efficiency is only associated with a projector. For quick reference, a tabulation of calibration formulas is presented in Table 1, and a definition of variables is listed in Table 2.

### 3.1 Calibration Formulas

The *free-field voltage sensitivity* (FFVS) of a hydrophone (or receiver) is the open-circuit electrical output of the hydrophone per

Table 2. Definition of variables used in Table 1.

$E_s$	Measured open-circuit voltage of standard hydrophone (dB)
$E_x$	Measured open-circuit voltage of test hydrophone (dB)
$E_t$	Transmit voltage (dB)
$e_t$	Transmit voltage (V)
$M_s$	FFVS of standard hydrophone (dB)
$D$	Separation distance (m)
$I_t$	Transmit current (dB)
$i_t$	Transmit current (A)
$\phi$	Voltage/current phase angle (deg)
DI	Directivity index (dB)
$P_t$	Input power (W)
$P_0$	Output acoustic power (W)
$R$	Equivalent series resistance of hydrophone ( $\Omega$ )
$d$	Diameter of piston (m)
$L$	Length of line source (m)
$\lambda$	Wavelength in water (m)
$h$	Depth
$f$	Frequency (kHz)

unit free-field pressure. The symbol  $M$  is typically used and was derived from the word "microphone," the air equivalent of a hydrophone. The open-circuit voltage measurement is made with a preamplifier with a high input impedance. The free-field pressure is what would exist at a given location without the presence of reflections. The easiest method to obtain the FFVS is by comparing the unknown hydrophone with a standard hydrophone when placed into the same acoustic field (usually a pure tone burst of sufficient time). A standard hydrophone will typically have a table of decibel signal level versus frequency. The signal level received by the hydrophone is determined by measuring the level within a time-gated portion of the signal that corresponds to the direct path. This way, interference due to reflected pulses are ignored, and a high signal-to-noise ratio is obtained. The FFVS,  $M$ , is given by

$$\text{FFVS(dB)} = M_x(\text{dB}) = M_s - E_s - E_x, \quad (2)$$

where  $M_s$  is the FFVS (in dB) of the standard hydrophone,  $E_s$  is the measured open-circuit voltage (in dB) of the standard hydrophone, and  $E_x$  is the measured open-circuit voltage (in dB) of the hydrophone being calibrated. The subscript  $x$  denotes the unknown or test hydrophone, and the subscript  $s$  the standard hydrophone. All units are decibels referenced to 1 V per micropascal (dB re 1 V/ $\mu$ Pa). Sometimes this is called the receive voltage sensitivity (RVS).

The *transmitting voltage response* (TVR) of a projector is the transmitted free-field pressure produced for a 1-V signal applied across the electrical terminals of the transducer and referenced to a distance of 1 m. The symbol  $S$  is commonly used and stands for "speaker." The measurement is made by monitoring the output voltage of a standard hydrophone placed in the acoustic far field (defined below) of the projector. The TVR,  $S$ , is given by

$$\begin{aligned} \text{TVR(dB)} &= S_x(\text{dB}) \\ &= E_s - M_s - E_t + 20 \log D, \end{aligned} \quad (3)$$

where  $E_s$  is the measured open-circuit voltage (in dB) of the standard hydrophone,  $M_s$  is the FFVS (in dB) of the standard hydrophone,  $E_t$  is the projector transmit voltage (in dB), and  $D$  is the separation distance in

meters. The units are decibels referenced to 1 micropascal per volt at 1 meter (dB re  $\mu$ Pa/V @ 1 m).

The *far-field distance*  $x$  from a square or circular transducer is conservatively defined as

$$x = \text{area}/\lambda, \quad (4)$$

where  $\lambda$  is the wavelength in water. The far-field distance  $x$  from a line or thin cylinder is conservatively defined as

$$x = L^2/\lambda, \quad (5)$$

where  $L$  is the line length.

The *transmitting current response* (TCR) of a projector is the transmitted free-field pressure produced for a 1-A signal applied to the electrical terminals of a projector and referenced to a distance of 1 m. The measurement is made by monitoring the output voltage of a standard hydrophone placed in the far field of the projector. The TCR is given by

$$\text{TCR}_x(\text{dB}) = E_s - M_s - I_t + 20 \log D, \quad (6)$$

where  $E_s$  is the measured open-circuit voltage (in dB) of the standard hydrophone,  $M_s$  is the FFVS (in dB) of the standard hydrophone,  $I_t$  is the projector transmit current (in dB), and  $D$  is the separation distance in meters. The units are decibels referenced to 1 micropascal per ampere at 1 meter (dB re  $\mu$ Pa/A @ 1 m).

The *transmitting power response* (TWR) of a projector is the transmitted free-field pressure produced for a signal of 1 W applied to the electrical terminals of a transducer and referenced to a distance of 1 m. The TWR is given by

$$\begin{aligned} \text{TWR} &= E_s - M_s + 20 \log D \\ &\quad - 10 \log(e, i, \cos \phi), \end{aligned} \quad (7)$$

where  $E_s$  is the measured open-circuit voltage (in dB) of the standard hydrophone,  $M_s$  is the FFVS (in dB) of the standard hydrophone,  $D$  is the separation distance in meters,  $e$ ,  $i$  is the projector transmit voltage,  $i$ , is the projector transmit current, and  $\phi$  is the voltage/current phase angle. The units are decibels referenced to 1 micropascal per watt at 1 meter (dB re  $\mu$ Pa/W @ 1 m).

Using Eqs. (3) and (7), the TWR can be written as a function of TVR as

$$\text{TWR} = \text{TVR} + 10 \log(R_p), \quad (8)$$

where  $R_p$  is the equivalent parallel resistance of the projector and is given by

$$R_p = |z|/\cos \phi. \quad (9)$$

It is evident that either a standard hydrophone or a calibrated projector is required to obtain the transmit or receive response of an unknown transducer. Hydrophones that have calibration response data can be purchased, or can be sent to a calibration facility.

An absolute method to calibrate transducers without the need of a standard is called a *reciprocity* calibration. The reciprocity calibration allows an absolute calibration without the need of a transducer with a known response (see ACOUSTICAL INSTRUMENTS). It requires three transducers, one of which is a projector, one a hydrophone, and one which is reciprocal. A reciprocal transducer has the ratio of its receiving sensitivity  $M$  (when acting as a hydrophone) to its transmitting current response  $S$  (when acting as a projector) equal to a constant called the *reciprocity parameter*,  $J$ :

$$J = \frac{M_r}{S_t} = \frac{\text{FFVS}}{\text{TCR}}. \quad (10)$$

For spherical waves,

$$J_s(\text{dB}) = 20 \log(2/\rho c) = 354 + 20 \log f, \quad (11)$$

where  $\rho = 1000 \text{ kg/m}^3$  is the density of water,  $c = 1500 \text{ m/s}$  is the sound velocity, and  $f$  is the frequency. All units are MKS. Fortunately, most ceramic transducers are reciprocal. Details of this calibration method will not be presented here, as there are several excellent discussions available; see Albers (1965) or Bobber (1988).

The phase response of a projector is not of concern in most calibrations. When measuring phase response, the best reference is a standard, omnidirectional hydrophone having a constant sensitivity and operating well below its resonance frequency. In this region the phase of its transduction is constant and well suited as a reference. Comparison phase

measurements are obtained by reference to the phase of the drive voltage.

The *source level* (SL) of a projector is the transmitted free-field pressure produced by a signal of the applied power or applied voltage to the electrical terminals of a projector and referenced to a distance of 1 m. The SL is given by

$$\text{SL}(\text{dB}) = \text{TWR} - 10 \log P_i, \quad (12)$$

$$\text{SL}(\text{dB}) = \text{TVR} + E_r, \quad (13)$$

where  $P_i$  is the projector input power (in watts) and  $E_r$  is the projector input voltage (in dB). The units are decibels referenced to 1 micropascal at 1 meter (dB re  $\mu\text{Pa}$  @ 1 m).

The power delivered to a projector is dissipated in either the electrical or the mechanical resistance within the transducer, or it is radiated into the water. The *efficiency* ( $\eta$ ) of a projector is the ratio of the total acoustic output power to the total electrical input power. The TWR, Eq. (7), and SL, Eq. (12), can also be written as functions of efficiency,

$$\text{TWR}(\text{dB}) = 170.8 + \text{DI} + 10 \log \eta, \quad (14)$$

$$\text{SL}(\text{dB}) = 170.8 + 10 \log P_i + \text{DI} + 10 \log \eta. \quad (15)$$

where  $P_i$  is the input power, DI is the directivity index (see Sec. 3.2), and the quantity 170.8 dB accounts for the  $\rho c$  of the medium and the reference of 1  $\mu\text{Pa}$ . The directivity index is very difficult to measure because it involves the total power radiated and requires the measurement of directivity patterns in several planes (Sec. 3.2 shows the calculation of DI). The DI needs to be accurate to 0.1 dB for a good efficiency calculation, which for most projectors ranges from 50% to 80%.

### 3.2 Calculated Parameters

One of the major parameters of a transducer or transducer array is the directivity pattern (often called beam pattern), which is the response level of the transducer as a function of the incident angle of the sound. A transducer will have the same directivity pattern whether operating as a projector or a hydrophone. It is a function of the aperture

and frequency and is used to calculate the power and efficiency parameters of the transducer. A high directivity indicates that the acoustic power of a projector is concentrated into a small region, and for a hydrophone high directivity allows high imaging resolution and reduces the influence of ocean isotropic noise. The *directivity index*, DI, of a transducer is a very important parameter that quantifies the sharpness, or directionality, of the pattern and is closely associated with the beamwidth. Approximate equations (Stansfield, 1990) for the half-power ( $-3$  dB) beamwidth BW and directivity index DI of a circular piston in an infinite baffle are

$$BW \approx 60\lambda/d, \quad (16)$$

$$DI = 10 \log(4\pi \times \text{area}/\lambda^2). \quad (17)$$

The approximate equations for the half-power ( $-3$  dB) beamwidth BW and directivity index DI of a continuous line are

$$BW \approx 50\lambda/L, \quad (18)$$

$$DI = 10 \log(2L/\lambda). \quad (19)$$

The beamwidth of a square radiating surface uses Eq. (18), where  $L$  will be the side of the square, and Eq. (17) for the DI. Parameters for rectangular and elliptical radiating surfaces can be found in Albers (1965) or Stansfield (1990). The beamwidths at the  $-10$ -dB level and between the first nulls can be obtained by using a multiplying factor:

$$BW(-10 \text{ dB}) \approx 1.8BW(-3 \text{ dB}), \quad (20)$$

$$BW(\text{btwn. nulls}) \approx 2.3BW(-3 \text{ dB}). \quad (21)$$

These equations apply for dimensions greater than one wavelength of sound in water.

The *equivalent thermal-noise pressure level* is important in determining the lowest signal that can be developed in a hydrophone. This noise level of the hydrophone can be associated with an equivalent sound-pressure level in the ocean. The open-circuit voltage  $E_n$  developed by thermal agitation in a 1-Hz band is called the Johnson noise,

$$E_n = \sqrt{4KTR}, \quad (22)$$

where  $K$  is the Boltzmann gas constant ( $1.38 \times 10^{-23}$  J/K),  $T$  is the absolute temperature in kelvins, and  $R$  is the equivalent series resistance of the electrical impedance of the transducer in ohms (in general, this is a function of frequency). The equivalent noise sound-pressure level,  $SPL_n$ , is

$$SPL_n = E_n/M, \quad (23)$$

and written in decibel form for a temperature of  $15^\circ\text{C}$  is

$$SPL(\text{dB}) = 10 \log(R) - M - 198. \quad (24)$$

For example, a  $1000\text{-}\Omega$  impedance hydrophone with a FFVS of  $-200$  dB re  $1 \text{ V}/\mu\text{Pa}$  will have an equivalent thermal-noise sound-pressure level of  $20$  dB re  $1 \text{ V}/\mu\text{Pa}$ .

### 3.3 Cavitation

The onset of cavitation occurs when the motion of the radiating face creates a partial vacuum that is greater than the vapor pressure of the water. The cavitation threshold is the point where the power applied to the projector is sufficient to start the formation of bubbles at its face. An empirical curve (Urlick, 1975) that shows the frequency dependence of the cavitation threshold  $P_c$ , using continuous-wave (cw) data in fresh water at atmospheric pressure, is

$$P_c(0) = 0.00025f^2 + 0.045f - 1 \quad (\text{atmospheres}), \quad (25)$$

where  $P_c(0)$  is the cavitation threshold at zero depth and  $f$  is the frequency in kHz. This is approximately valid up to frequencies of a few hundred kilohertz. As the depth of operation is increased, the cavitation threshold increases as

$$P_c(h) = P_c(0) + h/10 \quad (\text{atmospheres}), \quad (26)$$

where  $P_c(h)$  is the cavitation threshold at depth  $h$  and  $h$  is the depth in meters. The cavitation threshold can be approximately expressed as occurring when the acoustic intensity at the radiating face of the transducer is equal to

$$I_c = 0.15[P_c(0) + h/10]^2 \text{ W/cm}^2. \quad (27)$$

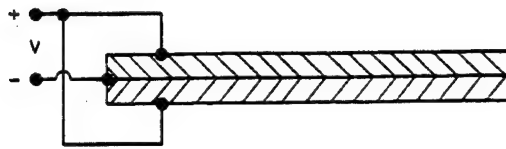


FIG. 2. Schematic of a basic bilaminar flexural disk transducer (Wilson, 1985).

In practice the intensity can be 2 to 3 times higher before cavitation will affect the source level. A value of 0.3 is used by Wilson (1985). The intensity at the surface of a transducer or array can be calculated by multiplying the acoustic output power by the area of the transducer. The cavitation threshold is sensitive to temperature, dissolved-air content, frequency, acoustic pulse length, depth, and acoustic hot spots on the transducer face. Quantifying the onset of cavitation is difficult and, if important, should be determined experimentally. See Urick (1975) and Stansfield (1990) for more information.

#### 4. LOW-FREQUENCY TRANSDUCERS (10-5000 Hz)

The design of transducers and arrays capable of radiating power at frequencies less than about 1 kHz has the basic requirement of producing large displacements efficiently. The size and weight of the transducer becomes an important issue at these low frequencies, since the source level depends upon the amount of volume of water that is moved. Radiation loading, which determines the amount of sound radiated, is also typically small because the size of the transducer is small relative to a wavelength. At 1 kHz the wavelength of sound in water is 5 ft; at 100 Hz it is 50 ft. Fortunately, for most low-frequency active transducers, the output

power requirements are not as high as those for transducers operating at higher frequencies. To design high-power transducers at low frequencies in a moderate size, they need to be less stiff than a ceramic thickness vibrator. To accomplish this more compliant transducer design, use is made of a mechanical amplification such as a lever. This provides a mechanical impedance transformer resulting in a lower stiffness. One technique for doing this is to use flexural motion of plates and shells that have a lower stiffness and a lower mechanical resonance frequency for the same overall dimensions of the structure. Other methods involve the use of a gas-filled enclosure as the stiffness element of electromagnetic or hydraulic systems. The general characteristics of these designs are discussed in the following.

##### 4.1 Flexural Disk

An example of a transducer that involves flexure is the flexural plate transducer; see Fig. 2. The basic principal of a flexural disk is that if a force is applied to one face of a thin metal disk, it will be displaced at the center, or flex, putting one side into compression and the other side into tension. A bilaminar disk will have two piezoelectric ceramic disks bonded together. An electrical field across the ceramics will result in an expansion in the ceramic disk that has the field and the polarization in the same direction, and a compression in the ceramic that has the field and the polarization in the opposite direction. The result is to cause a bending of the pair of disks converting a small displacement in the ceramic into a larger displacement of the surface radiating into water. For more efficiency, a double bilaminar disk transducer can be used, which has two faces radiating in opposite directions to act as a volume expander. Fig. 3. Basic design pa-

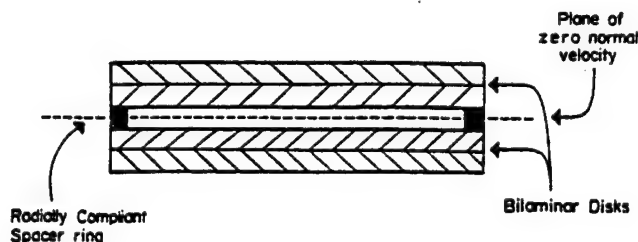


FIG. 3. Double bilaminar disk (Wilson, 1985).



rameters were derived by Woollett (1960) and can serve as further reading.

A metal plate can be inserted between the two ceramic disks, a trilaminar design, or one of the ceramic disks can be replaced with a metal plate. Typically, the ceramic is placed on the outside of the metal so that under a hydrostatic load the ceramic will be in compression so that it will not fracture. Limitations on hydrostatic pressure can be overcome by providing air pressure compensation. This, however, adds complexity and affects performance.

Flexural disk transducers are good as small, modest-power sources at low frequencies. Mechanical values of  $Q$  typically range between 10 and 15. They are relatively low cost because of their simple construction, and hence will be an economical and compact solution for not too demanding an application. Flexural disks are extensively used as low-frequency hydrophones because of their low cost and high sensitivity.

#### 4.2 Flextensional Transducer (300–3000 Hz)

This device also utilizes flexure motion, but instead of using the ceramic itself in flexural motion, it uses a mechanical gain to transform the thickness-mode vibration in the ceramic into a larger displacement. The basic features of the flextensional transducer are illustrated schematically in Fig. 4. A

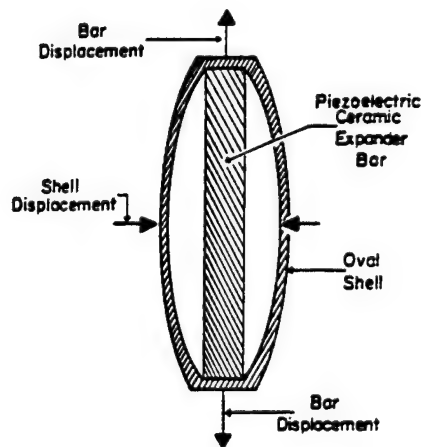


FIG. 4. Schematic of a flextensional transducer (Wilson, 1985).

stack of ceramics operates in the thickness mode and is connected to a surrounding shell. When the stack expands, the major axis of the shell moves outward, and the minor axis moves inward. This produces a large volume displacement, transforming the high-impedance, small motion of the stack into a lower-impedance, larger movement of the shell. Several different types of design use this mechanism and are divided into classes of flextensional transducers. Flexural transducers primarily are designed to resonate in the frequency range of 300 to 3000 Hz, and generally have higher power outputs than the flexural disks, although at a higher cost (Stansfield, 1990).

A Class I flextensional transducer is a three-dimensional structure created by rotating about an axis along the stack; see Fig. 5. If it is rotated about an axis normal to the stack, a ring-shell projector is obtained, a Class V flextensional. The ceramic in a Class V flextensional is also extended in the third dimension and forms either a disk, which drives the shell by radial stress in the disk, or a ring around the circumference joining the two half shells.

Another configuration is an elliptical cylinder generated by extending the figure out of the plane of the sketch and capping it on both top and bottom. This is called a Class IV flextensional transducer and has been studied more thoroughly than other classes. Design characteristics have been calculated by analytical and by finite-element analysis; however, the design depends on a number of parameters and does not lead to any simple design equations. The resonance frequency and the maximum hydrostatic pressure that an elliptical shell can withstand depend on the major and minor axis, wall thickness, and material properties of the shell, with the stack having a lesser influence. A rule of thumb is that eccentricity should not be greater than about 3. The use of a glass-reinforced plastic shell helps achieve a low resonance frequency and wide bandwidth.

The size of flextensional transducers is generally much less than a wavelength in water at their resonance frequency; hence, they tend to have an omnidirectional directivity pattern in the plane perpendicular to their axis. Values of mechanical  $Q$  down to 2 are achievable. Compared to a flexural disk of the same size, the  $Q$  of a flextensional



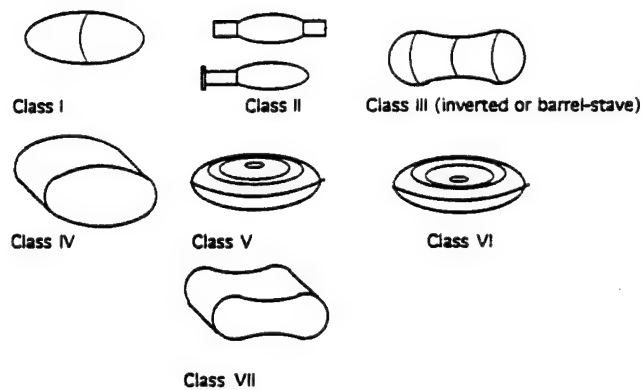


FIG. 5. Flextensional transducer classes (McCollum *et al.*, 1992).

transducer can be lower by a factor of 2–4. Also, a flextensional can be smaller than a flexural disk when hydrostatic pressure is the limiting requirement.

A compressive prestress must be applied to the stack in order to achieve high power output. It is usually accomplished by squeezing the minor axis, which expands the major axis, then inserting the stack into the shell. The relaxation of the shell applies the proper preload needed for the stack. It must also be realized that the hydrostatic pressure, which applies force to the shell, will also compress the minor axis and reduce the preload on the stack. The preload must be sufficiently designed so that hydrostatic pressure does not adversely affect its performance. Finite-element analysis is needed to detail the static stresses in the shell under hydrostatic pressures. Material fatigue during high-power operation must also be taken into account.

In summary, flextensional transducers constitute useful sources within the band of about 300–3000 Hz. They can provide significant power from a compact size, can operate at high hydrostatic pressures, and have wide bandwidths, especially when compared to other designs such as the air-backed flexural disk. The cost, however, is higher. The design process needs considerable care, using finite-element analysis to account for the complex interactions between parameters.

#### 4.3 Free-Flooded Ring

A cylindrical ring that is open to the water (a free-flooded ring) can be used for low-frequency projectors that are independent of hydrostatic pressure. This transducer oper-

ates in the ring, or circumferential, mode of vibration. The radiation from the inner and end surfaces of the ring oppose that from the outer surface and can lead to partial cancellation of the radiation. It is possible, however, to design the height of the ring such that cancellation effects are not too great. Because it can be free flooded, no pressure compensation mechanisms are required. Since the resonance frequency is dependent on the diameter of the ring, a resonance of 1000 Hz would result in a ring of about 1 m diameter, which is impractical. The free-flooded ring can be typically used for frequencies above about 4000 Hz.

#### 4.4 Mechanical Transducer

In the frequency range of 1–50 Hz an electric motor can be used to drive pistons to sufficiently large amplitudes of vibration. The frequency can be changed by varying the speed of the motor; however, it is not easy to change the amplitude of the oscillation, which limits the versatility of this approach. They are very useful when high power is required at frequencies below about 20 Hz.

#### 4.5 Electromagnetic, Moving-Coil Transducers

Moving-coil electromagnetic transducers can be considered at audio frequencies. They are used as loudspeakers in air because large displacements are easily generated. In water they can be used as low-power, wide-bandwidth sources from 40 Hz to 20 kHz. The J9 transducer is a standard projector that has a moving coil mounted on a very compliant

suspension system. It is necessary to balance the air pressure within the transducer to the external water pressure by means of an air-filled collapsible rubber bag. Beyond a depth of about 25 m an air compensation device is needed. The maximum power for the J9 is 20 W at frequencies above 200 Hz, but the efficiency is less than 1%. This device requires careful handling so that the suspension is not damaged. Also, the calibrated response may vary with drive level. It should be calibrated every time it is used.

#### 4.6 Resonant Bubble Transducer

A gas-filled bag can be placed at the face of a moving-coil transducer to increase the radiation loading and increase the efficiency near resonance. The broadband low efficiency of a moving-coil transducer is transformed into a narrower-bandwidth, higher-efficiency transducer. The compliance in the bubble, or bag, provides a compact low-frequency source of modest power, narrow bandwidth, and a resonance frequency that varies with depth.

#### 4.7 Helmholtz Resonator

The Helmholtz resonator is another resonant device that can be used as a low-frequency source. This resonator uses a rigid enclosed volume with a short neck of specified length and cross-sectional area. The outer end of the neck is exposed to the medium. The compliance of the cavity volume resonates with the mass of the fluid in the neck to form a simple mass-spring system. A transducer is placed in the wall of the cavity to excite the resonance. The resonance frequency is not dependent on density but is proportional to the sound velocity of the medium. Therefore, the resonance frequency of a Helmholtz resonator in water is about four times higher than in air. The mechanical  $Q_M$  is typically well above 20. The best way to reduce the resonance frequency is to maximize the cavity volume to a limit where the dimensions remain less than  $\lambda/4$ . One method of exciting the cavity is to place a flexural disk at one end of the cavity; another is to use ceramic rings in the wall of a cylindrical cavity. Cavitation can occur within the cavity at high source levels.

The Helmholtz resonator is a potential solution for a compact low-frequency projector

that can operate down to great depths. In practice, to achieve rigid walls in a water environment requires thick walls, hence extra weight, and the narrow bandwidth and low efficiency have limited their usefulness. The use of this device, some specific design parameters, and their effects on the acoustic performance are addressed by Henriquez and Young (1980) and Kinsler *et al.* (1982).

#### 4.8 Hydroacoustic Projector

The hydroacoustic projector, developed by Bouyoucos (1975), is a device that uses hydraulic fluid at high pressure to drive a flexing disk or a piston and is capable of large amplitudes of motion. A high-pressure hydraulic fluid flow is controlled by an electromechanical shuttle valve that causes the pressure oscillations in the acoustic drive cavity. This, in turn, exerts pressure oscillations on the flexural disks, which then radiate into the water. The electromechanical valve is typically a ceramic stack and provides control for the transducer. Power is derived from the high-pressure hydraulic fluid. The flexural disks, plus the various components, are designed to resonate over a fractional bandwidth of about 20%. It is an effective high-power source at low frequencies where weight and size are not critical. It is best used at frequencies below a few kilohertz and is not suitable for use as a hydrophone.

#### 4.9 Spherical-Shell Transducer

A spherical shell composed of piezoelectric ceramic is another design for achieving a low-resonance frequency with a reasonable value of  $Q$ . One approach is to fabricate a large sphere with a number of triangular-shaped ceramic plates. These plates are cemented together into a mosaic to form a spherical shape, which radiates an omnidirectional pattern. A 30-in. diameter sphere has been fabricated with a usable frequency range from 0.5 to 2.0 kHz and a minimum efficiency of 75%.

#### 4.10 Impulsive Transducer

Explosive sources are the most common impulsive source. Urlick (1975) gives a good description of their use as underwater sound sources. These are commonly small charges of explosive materials ranging from a few

grains to a few pounds. High velocity of detonation explosives such as TNT ( $>15\,000$  ft/s) are preferred over other materials such as black powder (0.1–1 ft/s), which has an explosion process called deflagration, or burning. The detonation introduces a shock wave normally followed by a series of pressure "bubble" pulses. Only one or two bubble oscillations are of practical significance. About 40% of the total chemical energy is radiated as acoustic energy. Most of the acoustic energy is concentrated between 5 and 1000 Hz. Explosive charges are easily portable and yield a short, omnidirectional, high-power, broadband pulse. The disadvantage is that explosives cannot be made repeatable, give a high background of reverberation, and cannot be coded for sonar applications.

The *sonar thumper* is an impulsive source generated by the repulsion of an aluminum plate by a large coil imbedded in a plastic matrix; see Albers (1965). A pulse of current in the coil induces eddy currents in the aluminum plate, causing it to be repelled by the coil. A large pulse of short duration (a capacitive discharge) needs to be passed through the coil. Although the pressure pulses are smaller than using an explosive, the thumper can be triggered and synchronized with a recorder system.

An *underwater spark source* acts as a small impulsive source but can be repeated for a number of pulses. A capacitive discharge across a gap between a pair of electrodes in the water generates the acoustic noise. It is a very simple transducer but has the disadvantage that the condition of the electrodes changes with use, which varies the pressure level of successive sparks. Peak pressures of 240 dB re  $1\,\mu\text{Pa}$  at 1 m are possible. An *air gun* impulse source is created when high-pressure air is momentarily vented to the surrounding water to produce an air-filled cavity, which then collapses and radiates a transient pulse.

## 5. LONGITUDINAL VIBRATOR TRANSDUCERS (3 kHz to $>100$ MHz)

Longitudinal vibrators represent the standard transducer type used for a broad frequency range from about 3 kHz to above 100 MHz. *Tonpilz* transducers, which are a composite of ceramic and "head" and "tail"

masses, predominate up to a frequency of about 100 kHz. Near the lower frequency of 3 kHz, the length and mass of the transducer becomes very large and other types become useful. Near 100 kHz the *tonpilz* transducer becomes very small, and it is more convenient simply to use the thickness vibration mode of a ceramic. The frequency range of 5–50 kHz is mainly used for weapon and detection sonars. From about 50 to 600 kHz, transducers are used for mine hunting, ocean bottom profiling, and fish finders. Frequencies from 600 kHz to 3 MHz are used for in-water high-resolution imaging arrays. Above about 3 MHz, transducers are used for medical ultrasound imaging and nondestructive testing. Ultrasonic microscopes operate up to the gigahertz frequency range.

### 5.1 Tonpilz Transducers

The *tonpilz* transducer is a longitudinal vibrator and gets its name from a composition of two German words, "sound" and "mushroom" or "singing mushroom." It is named, as can be seen, from its shape as shown in Fig. 6. These transducers are operated near resonance and typically are combined into arrays of many elements. Since arrays are often electrically phased to steer their directivity patterns to angles away from the normal to the plane of the array, the size of the radiating face needs to be about half of a wavelength in water. The *tonpilz* transducer has head and tail masses and a central ceramic (or magnetostrictive) motor section that are bonded together and put into compression by a central bolt. This creates a mass-spring-mass system that is a very efficient vibrator and radiator. The face of the head couples into water, and the tail has as light an acoustic load (such as air) as possible. A large radiated sound power can be achieved by this design.

There are four basic approaches to the *tonpilz* transducer design. The first approach is mentioned by Wilson (1985), who treats the transducer as a mass-spring-mass system. A second approach uses equivalent circuits or four-port networks as discussed by many authors. This is the most common method of *tonpilz* transducer design and requires electrical circuit programs or special codes to handle the complex, coupled equations. A third design approach is from Mc-

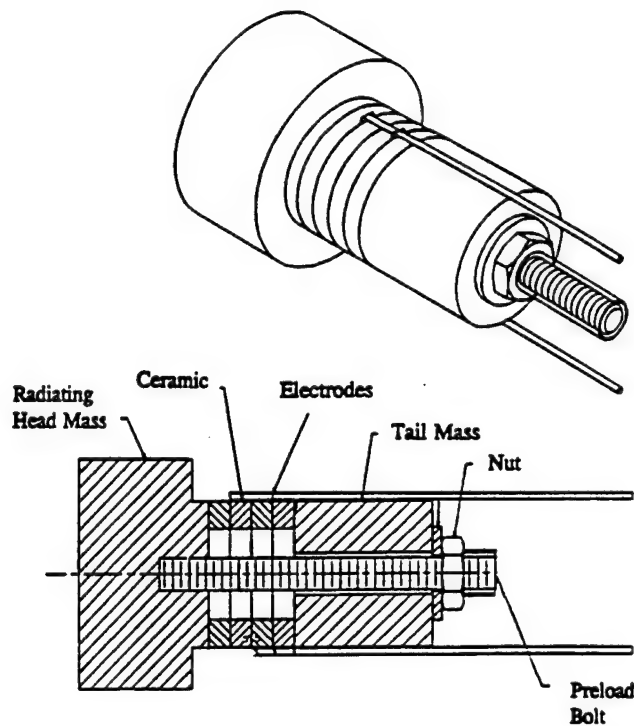


FIG. 6. Schematic of a tonpilz longitudinal vibrator.

Cammon and Thomson (1980), who treat the tonpilz transducer from an energy and waveguide basis, and a fourth approach uses finite-element analysis, which gives a very detailed vibration characterization, but is very time-consuming. Often the design is made by using a combination of the second and fourth approaches to generate an approximate design (within 10%) and then to detail the design. The first approach is not used very often but is more illustrative.

A tonpilz transducer can be used for frequencies from about 3 kHz to about 100 kHz. At frequencies above about 100 kHz, a thickness vibrator can be used. At 100 kHz a ceramic thickness vibrator made of a PZT-4 rod would have a length of 2 cm, and it would be less expensive. A tonpilz transducer, being a composite element, is used to reduce the overall length, make the stresses in the active material more uniform, make use of the piezoelectric material more effective, and reduce the mechanical  $Q$ . The radiating face typically has a larger area than the ceramic in order to increase the power output for a given strain in the ceramic and to obtain a better impedance match between water and the active transducer material.

The head/ceramic area ratio is limited to about 3–10 by the need to avoid flexural resonances in the tonpilz head and to have a sufficient volume of ceramic.

It is typically assumed that all components of the element are small compared to a wavelength. The desire is to have the element face dimension be half of a wavelength in water so that multiple-element arrays can be phased for beam steering. The head mass should be kept light by using a low-density metal, such as aluminum or magnesium, and a minimal thickness determined by setting its flexural resonance at about twice the fundamental resonance. The ceramic stack design must consider the number of ceramics, dimensions, compliance, electric field limits, power-handling capability, electrical impedance, electromechanical coupling coefficient, and cost. For most cases the ceramic used for transducers that both transmit and receive is PZT-4 (Navy type I). If high acoustic fields are required, then projectors use PZT-8 (Navy type III) to minimize high-power heating effects. Designs typically use multiple stacked rings of 4 to 6 ceramics for low-impedance, high-power applications where the transducer must also receive. An

even number of rings is used so that they can be connected in parallel with alternating polarity and electric fields. The maximum usable electrical field limit of ceramics is often a limit for the operation of the transducer. For PZT-4 (Navy type I), the maximum field is about 2400 V/cm (6 V/mil), and for PZT-8 (Navy type III) it is about 4000 V/cm (10 V/mil). The maximum voltage that can be applied to a transducer is equal to the field limit times the thickness of a single ceramic. For more information on the power-handling capabilities of ceramics, see Berlincourt *et al.* (1964).

To maximize the displacement of the head, the tail mass should be made as large as possible and have a mass 3 to 5 times that of the head. Typically a high-density metal such as tungsten, stainless steel, or brass is used. The in-water mechanical  $Q$  will typically have a value of 5 to 7; however, when assembled into an array, the  $Q$  will drop to a value of 2 to 5. A bolt is typically used between the head and tail to place a compressive load of 2000 to 6000 lb/in.<sup>2</sup> on the ceramic so that high drive levels do not place the ceramics into tension. Placing the ceramics into tension may result in creating microcracks that will lead to failure.

The tonpilz transducer is capable of very high source levels, has an efficiency of (80–90)%, and is typically formed into arrays, which can form patterns capable of being steered to different angles. These arrays are used for imaging and locating objects. The cavitation threshold for the transducer or the array is calculated using Eq. (25). The intensity times the array face area gives a cavitation limited maximum power.

## 5.2 Thickness Vibrators

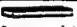

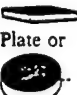






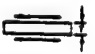






At frequencies higher than 100 kHz, solid ceramic shapes are typically used. These transducers can become a significant portion of a wavelength in size, and it is often necessary to account for vibration modes set up in the ceramic. The mathematics of analysis may become more complex, but the design itself has less flexibility than the low-frequency designs. It is at these frequencies that the broad-area transducers such as PVDF and the 1-3 PZT composites are becoming popular. These newer materials have greatly reduced or eliminated unwanted

structural vibrations, allowing single transducers with a size of many wavelengths.

A *thickness vibrator* is a thin plate in which both the electrical field and the polarization are in the thickness direction. A *length expander* is a long thin bar with the electrical field parallel to the length. The polarization is also in the same direction as the electric field. To determine the fundamental resonance frequency for these vibration modes as well as for others, the equations are presented in Table 3 as a function of the *frequency constant* and the controlling dimension of the vibrator. This is a very useful table for determining the ceramic dimensions needed for a particular design. Fish finders, mine-hunting transducers, bottom profilers, ultrasonic medical transducers, and nondestructive testing transducers are typically fabricated by starting with a ceramic plate, dicing it into small elements, and then filling the gaps with a polymer. These are, in essence, 1-3 composite materials that have a specific design and application. Complex shape transducers using injection-molded 1-3 composite materials have been fabricated by the author using electroplating techniques. Complete arrays and large-area projector/hydrophone transducers are possible because of the mode decoupling achieved in a 1-3 composite.

When an air-backed transducer is excited by a pulse, little energy is lost and it rings at its resonance frequency. This impedance mismatch at the back of the transducer is desirable for continuous-wave operation; however, it is very undesirable for medical ultrasonic transducers. Lateral resolution in ultrasonic imaging is dependent on the transducer reproducing a pulse with little ringing present. Ringing can be reduced by using absorptive backings such as a tungsten-loaded epoxy. The penalty with using an absorptive backing to reduce ringing is a reduction in the sensitivity. A more current approach is to apply matching layers of suitable thickness (approximately quarter wavelength) and characteristic impedance between the ceramic and the medium. These layers permit efficient power transfer from the ceramic to water (the human body) without much loss in sensitivity. Typically a light acoustic backing will also be used. The use of matching layers to reduce ringing also results in a broader bandwidth. See Shung (1992) for more detail.

**Table 3.** Vibration modes for common transducer configurations.

Shape and electrode position	Vibration mode	Type of coupling	Direction of polarization	Controlling dimension	Frequency constant in kHz-m (kHz-in)			
					Type I PZT-4	Type III PZT-8	Type IV BaTiO <sub>3</sub>	Type VI PZT-5H
 Long, thin bar or strip	 Longitudinal mode Length varies	$k_{31}$	↓	$L$	1.60 (63)	1.75 (69)	2.34 (92)	1.41 (56)
 Plate or Thin disc	 Thickness mode Thickness varies	$k_{33}$	↓	$T$	2.03 (80)	2.13 (84)	2.87 (113)	1.75 (69)
 Thin disc	 Radial mode Radius varies	$k_p$	↓	$D$	2.16 (85)	2.36 (93)	3.18 (125)	1.98 (78)
 Thin walled tube	 Radial mode Mean diameter varies	$k_{31}$	↖ ↗ ↘ ↙	$D$	1.02 (40)	1.07 (42)	1.47 (58)	0.89 (35)
 Shear plate	 Thickness shear mode rectangular cross-section is distorted into a rhombus	$k_{15}$	—	$T$	1.32 (52)	1.33 (57)	1.59 (62)	1.10 (43)
 Thin walled sphere	 Radial mode Mean diameter varies	$k_p$	↖ ↗ ↘ ↙	$D$	1.72 (68)	1.83 (72)	2.46 (97)	1.47 (58)
 Hemisphere	 Radial mode Mean diameter varies	$k_p$	↖ ↗ ↘ ↙	$D$	2.08 (82)	2.26 (89)	3.02 (119)	1.85 (73)
 Bender transducer	 Flexural mode Free end moves at right angle to beam axis	$k_{31}$	↓ or ↑ ↑ or ↓	$\frac{L^2}{t}$	0.51 (20)	0.56 (22)	0.74 (29)	0.46 (18)

### 5.3 Shaped Ceramic Transducers

Ceramic piezoelectric materials can be fabricated into a wide variety of shapes and sizes, and they lend themselves to designs

for specific applications that would be difficult for single ceramic pieces. The shapes shown in Table 3 are an example.

*Spherical transducers* are typically the choice for omnidirectional patterns. Com-

plete omnidirectionality can be obtained by using a spherical transducer that has a diameter smaller than a wavelength. One of the problems of a sphere is attaching leads to the inner electrode. For this reason two hemispheres are used, with the wires being attached prior to bonding the two pieces together. Small *cylindrical transducers* will also produce omnidirectional patterns and are often easier to fabricate. When used as a hydrophone, the cylinder dimensions are determined by the frequency range over which a flat response is desired. The upper limit of the flat range is slightly below the lowest resonance frequency. When operating as a projector, the fundamental resonance mode will produce the peak acoustic pressure level. There are three fundamental modes of vibration: length mode (a half-wavelength resonator), radial mode (the breathing mode, calculated using the mean diameter), and wall-thickness mode. Some coupling is present between these various modes of vibration. The coupling between the length and radial modes becomes very strong when the length is approximately three times the mean radius, and results in distorted patterns and frequency responses. This ratio is a design "forbidden zone" and should be avoided. See Hueter and Bolt (1955) for more detail. The cylindrical ceramic typically has its ends capped to shield the inner cylindrical surface from the acoustic medium. Since the outside and inside surfaces are electroded, and the polarization is radial, the electrical impedance is low. Also, the cylinder has a large radiating area in relation to the cross section of the ceramic, resulting in the mechanical impedance of the element being much lower than a solid ceramic of the same dimension. This permits a better acoustic match between the ceramic and the water.

A *bimorph* is a bender transducer (see Table 3), which flexes and has the capability for handling larger motions and smaller forces than single piezoelectric plates. This transducer is fabricated by bonding two shear-mode plates or two longitudinal-mode plates together in such a manner that when a voltage is applied, the plates will deform in opposite directions, resulting in a bending or twisting action. One example is the low-frequency flextensional transducer discussed earlier. The bimorph is typically a high-frequency transducer operating in air and is of-

ten used for ac and dc relays, audio alarms, tweeters, and micromanipulators. A shear-mode transducer has been used in shear accelerometers and for generating surface waves on structures.

## 6. OTHER TRANSDUCERS

*Parametric transducers* are used to create very narrow beamwidths at low frequencies. They rely on the nonlinear properties of water at high source levels. When two frequencies are generated at high amplitudes, intermodulation products are produced in the nonlinear medium such that the column of fluid in front of the transducer acts as a thin line array radiating in the direction of propagation. This characteristic is equivalent to an end-fire acoustic array. The low-frequency difference beam, called the secondary frequency component, has nearly the same beamwidth as at the primary frequency. The narrow beamwidth is achieved by use of a transducer that has a much smaller aperture than a conventional transducer. Even though the narrow beamwidth is very attractive, the parametric array is not typically used because the process is very inefficient.

In *fiber optic sensors* the variation in pressure in acoustic waves affects the optical properties of thin fiber optic cables. Compared to other hydrophones, it has high sensitivity and is insensitive to electromagnetic interference. In almost all of the standard configurations the sensing of the acoustic wave is accomplished in an optical detector that is sensitive to phase differences between light that has traveled a distance in fiber exposed to the sound and light that has traveled about the same distance but was not exposed to the sound. Mechanical noise pickup is a problem.

*Chemical acoustic sensors* result from phenomena in electrolytes that permit sensing acoustic pressure by measuring electrochemical potential. An acoustic wave that strikes an electrode where gas is being liberated by electrolysis causes an alternating component of the electrical potential. In another phenomenon, when a layer of electrolyte-filled nonconducting fiber surrounds an electrode, an electrokinetic effect in the fiber changes the electrode potential relative to the surrounding electrolyte. A microphone for low-



## 84 Transducers, Underwater Acoustic

frequency sounds called the solion infrasonic microphone uses a chemical reaction that depends on the flow of ions through an acoustic resistance placed in the electrolyte between the electrodes.

### Works Cited

Albers, V. M. (1965), *Underwater Acoustics Handbook—II*, University Park: The Pennsylvania State Univ. Press.

ANSI (1972), *Procedures for Calibration of Underwater Electroacoustic Transducers*, New York: American National Standards Institute.

Berlincourt, D. A., Curran, D. R., Jaffe, H. (1964), "Piezoelectric and Piezomagnetic Materials and Their Function in Transducers," in: Warren P. Mason (Ed.), *Physical Acoustics*, Vol. 1A. New York: Academic, Chap. 3, p. 250.

Bobber, R. J. (1988), *Underwater Electroacoustic Measurements*, Los Altos, CA: Peninsula Publishing.

Bouyoucos, J. V. (1975), "Hydroacoustic Transduction," *J. Acoust. Soc. Am.* **57**, 1341-1351.

Butler, J. L., Butler, S. C., Clark, A. E. (1990), "Unidirectional Magnetostrictive Piezoelectric Hybrid Transducer," *J. Acoust. Soc. Am.* **88**, 7-11.

Clark, A. E. (1980), "Magnetostrictive Rare Earth-Fe<sub>2</sub> Compounds," in: E. P. Wohlfarth (Ed.), *Ferromagnetic Materials*, Vol. 1, Amsterdam: North-Holland Chap. 7.

Henriquez, T. A., Young, A. M. (1980), "The Helmholtz Resonator as a High-Power Deep-Submergence Source for Frequencies below 500 Hz," *J. Acoust. Soc. Am.* **65**, 1556-1558.

Hueter, T. F., Bolt, R. H. (1955), *Sonics*, New York: Wiley.

Hunt, Frederick V. (1982), *Electroacoustics*, Cambridge, MA: Harvard Univ. Press. Reprinted by the Acoustical Society of America. New York.

Kinsler, L. E., Frey, A. R., Coppens, A. B., Sanders, J. V. (1982), *Fundamentals of Acoustics*, 3rd ed., New York: Wiley.

Mason, Warren P. (1934), "Electrical Wave Filters Employing Quartz Crystals as Elements," *Bell Syst. Tech. J.* **13**, 405-452.

Mason, Warren P. (1948), *Electromechanical Transducers and Wave Filters*, 2nd ed. New York: Van Nostrand.

McCammon, D. F., Thomson, W. Jr., (1980), "The Design of Tonpilz Piezoelectric Transducers Using Nonlinear Goal Programming," *J. Acoust. Soc. Am.* **68**, 754-757.

McCollum, D. F., Hamonic, B. F., Wilson, O. B. (1992), *Transducers for Sonics and Ultrasonics, Proceedings of the Third International Workshop*, Lancaster, PA: Technomic Publishing Co., Inc.

Shung, K. K., Smith, M. B., Tsui, B. M. W.

(1992), *Principles of Medical Imaging*, New York: Academic Press, Inc.

Stansfield, D. (1990), *Underwater Electroacoustic Transducers*, Bath Univ. Press and Institute of Acoustics.

Urick, R. J. (1975), *Principles of Underwater Sound*, 2nd ed., New York: McGraw-Hill.

Van Dyke, K. S. (1928), "The Piezoelectric Resonator and Its Equivalent Network," *Proc. I.R.E.* **16**, 742-764.

Wilson, O. B. (1985), *An Introduction to the Theory and Design of Sonar Transducers*, Washington DC: U.S. Government Printing Office.

Woollett, R. S. (1960), Theory of the Piezoelectric Flexural Disk Transducer with Applications to Underwater Sound, USL Research Report No. 490, U.S. Navy Underwater Sound Laboratory, New London CT.

### Further Reading

Beranek, Leo L. (1954), *Acoustics*, New York: McGraw-Hill.

Bouyoucos, J. V. (1975), "Hydroacoustic Transduction," *J. Acoust. Soc. Am.* **57**, 1341-1351.

Brigham, G., Glass, B. (1980), "Present Status in Flexensional Transducer Technology," *J. Acoust. Soc. Am.* **64**, 1046-1052.

Butler, J. L., Cipolla, J. R., Brown, W. D. (1981), "Radiating Head Flexure and Its Effect on Transducer Performance," *J. Acoust. Soc. Am.* **70**, 500-503.

Cady, W. G. (1964), *Piezoelectricity*, Rev. Ed., Vol. 1, New York: Dover.

Firestone, F. A. (1933), "A New Analogy between Mechanical and Electrical Systems," *J. Acoust. Soc. Am.* **4**, 249-267.

Groves, Ivor V. (Ed.) (1981), *Acoustic Transducers*, Benchmark Papers in Acoustics No. 14, Stroudsburg, PA: Hutchinson Ross.

Kinsler, L. E., Frey, A. R., Coppens, A. B., Sanders, J. V. *Fundamentals of Acoustics*, 3rd ed., New York: Wiley.

Martin, G. E. (1964), "On the Theory of Segmented Electromechanical Systems," *J. Acoust. Soc. Am.* **36**, 1366-1370.

Mason, Warren P. (1981), "Piezoelectricity, Its History and Applications," *J. Acoust. Soc. Am.* **70**, 1561-1566.

Olson, Harry F. (1943), *Dynamic Analogies*, New York: Van Nostrand.

Sims, C. S. (1963), "Bubble Transducer for Radiating High-Power Low-Frequency Sound in Water," *J. Acoust. Soc. Am.* **32**, 1305-1308.

Woollett, R. S. (1977), *Underwater Helmholtz Resonator Transducers: General Design Principles*, NUSC Technical Rept. 5633, Naval Underseas Systems Center, New London, CT.



# **APPENDIX 31**

# Capped Ceramic Underwater Sound Projector

James F. Tressler, W. Jack Hughes<sup>1</sup>, Wenwu Cao, Kenji Uchino, and Robert E. Newnham

Materials Research Laboratory, <sup>1</sup>Applied Research Laboratory  
The Pennsylvania State University  
University Park, PA 16802 USA

**Abstract** -- A new type of transducer has been developed for use as a shallow water sound projector at frequencies from 5 kHz to 50 kHz. Dubbed the 'cymbal', it is similar to the more commonly known 'moonie' or class V ring/shell flextensional designs. Prototype cymbal arrays with a radiating area of 14.5 cm<sup>2</sup> have been developed and tested. Two mounting schemes were examined: unpotted and potted in a 5 mm thick layer of stiff polyurethane. In both cases, a transmitting response comparable to the more widely used tonpilz transducer is attainable. When tested under hydrostatic pressures, the cymbal can withstand pressures of at least 2.5 MPa (which corresponds to 250 m of water depth) without a degradation in its performance.

## I. INTRODUCTION

Sound transmission is the single most effective means of directing energy transfer over large distances underwater [1]. The number of applications which utilize some form of acoustic energy is quite large, with frequencies ranging anywhere between 10<sup>-3</sup> Hz to 10<sup>9</sup> Hz. There is currently a great interest in the development of shallow water acoustic projectors that operate in the frequency range from 1 kHz to 100 kHz. Ideally, these transducers should be thin, lightweight, exhibit medium to high acoustic output power, be able to conform to a curved surface, and be of simple design such that they are easy and inexpensive to mass produce.

Currently, the predominant underwater projector systems that operate in the 1 kHz to 100 kHz frequency range are the tonpilz transducers and 1-3 composites. The tonpilz transducer consists of a stack of piezoceramic (typically PZT) rings connected mechanically in series and electrically in parallel. The ring stack is sandwiched between two metal masses: a heavy tailmass and a light, flared headmass which serves to transmit the generated acoustic energy into the surroundings. Tonpilz transducers are characterized by their very large acoustic output power, are typically tens of centimeters in thickness, and are designed to operate at frequencies below 100 kHz.

The 1-3 type composites consist of a number of piezoceramic rods separated by a 3-D interconnected polymer matrix. These composites have been manufactured in a number of ways [2]. The current state of the art fabrication method is by injection molding [3]. The performance of 1-3 composites is strongly affected by the elastic properties of both the ceramic and polymer phases, the volume fraction of piezoceramic rods, and most importantly, the aspect ratio of the ceramic rods [4]. Typical 1-3 composites designed for use below 100 kHz are at least 1 cm thick.

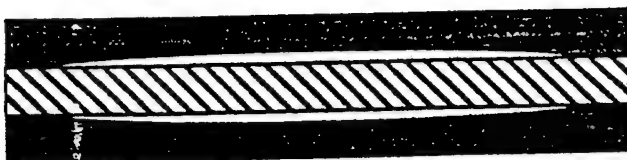
A third type of underwater projector that is seeing a resurgence in interest is the so-called flextensional transducer. Flextensionals have been in existence since the 1920s and have seen use as underwater projectors since the late 1950s [5]. Flextensionals consist of a piezoceramic drive element encapsulated by a metal shell. The shape of the shell has become quite diverse over the years and so a classification system has been established to group the common designs together [6]. Flextensional transducers typically range in size from several centimeters to several meters in length and can weigh up to hundreds of kilograms.

A miniaturized version of the class V flextensional transducer was developed in the late 1980s at the Materials Research Laboratory at The Pennsylvania State University for use as an underwater pressure sensor [7]. This transducer was named the 'moonie' due to the crescent moon shaped cavity on the inner surface of the caps. A second generation moonie-type transducer has recently been developed which consists of a thinner cap with a slightly different shape. This transducer has been dubbed the 'cymbal' due to the similarity in shape of its caps to that of the musical instrument of the same name. The moonie and cymbal designs are compared in Fig. 1.

The moonie and cymbal transducers consist of a piezoceramic (usually PZT) disk poled in the thickness direction which is sandwiched between and mechanically coupled to two metal caps, each of which contains a shallow cavity on its inner surface. The presence of these cavities allows the caps to convert and amplify the small radial displacement and vibration velocity of the piezoceramic disk into a much larger axial displacement and vibration velocity normal to the surface of the caps. This enhanced displacement and vibration velocity from the caps contribute to a much larger acoustic pressure output than would occur in the uncapped ceramic. The dimensions of the standard-size moonie and cymbal transducers are presented in TABLE I.

*This work was funded by the Office of Naval Research*

(a) moonie structure



(b) cymbal structure



Fig. 1. Cross-sectional views of the (a) moonie-type, and (b) cymbal-type transducers. The dark areas represent the caps and the cross-hatched areas the PZT disk.

TABLE I  
DIMENSIONS OF THE STANDARD MOONIE AND CYMBAL TRANSDUCERS

Moonie Parameter	Dimension
cap diameter	12.7 mm
cap thickness	1.0 mm
cavity depth	0.25 mm
cavity diameter	9.0 mm
PZT thickness	1.0 mm
PZT diameter	12.7 mm
Cymbal Parameter	
cap diameter	12.7 mm
cap thickness	0.25 mm
cavity depth	0.30 mm
cavity diameter	9.0 mm
dimple diameter	3.0 mm
PZT thickness	1.0 mm
PZT diameter	12.7 mm
weight	= 2 grams

## II. PARAMETERS TO MEASURE

Among the relevant parameters that need to be reported in order to fully characterize an underwater projector, the most important are resonance frequency, mechanical  $Q$ , electroacoustic efficiency, electromechanical coupling coefficient ( $k_{ep}$ ), transmitting voltage response (TVR), source level (SL), and beam patterns. Transmitting voltage response is equal to the sound pressure produced by the projector

referenced (re:) to a distance of one meter from the acoustic center of the transducer when unit voltage is applied across its electrical terminals. It is reported in terms of dB re:  $1 \mu\text{Pa}/\text{V}$  @ 1 m, or as  $1 \mu\text{Pa}\cdot\text{m}/\text{V}$ . Source level is the intensity of the radiated sound (i.e. radiated power) relative to the intensity of a plane wave of rms pressure  $1 \mu\text{Pa}$  referred to a point one meter from the acoustic center of the projector. Source level is related to the transmitting voltage response through the applied input voltage as:

$$\text{SL} = \text{TVR} + 20 \cdot \log V_{\text{in,rms}} \quad (1)$$

Thus, this parameter has the same units as TVR. In general, a source level of greater than 200 dB re:  $1 \mu\text{Pa}/\text{V}$  @ 1 m is desirable. The beam pattern describes the response of the transducer relative to its main acoustic axis.

## III. COMPUTER MODELING

The ANSYS® finite element software program (version 5.1) was used to model the behavior of the cymbal transducer both in-air as well as when it was water-loaded. Modal analysis of a two-dimensional axisymmetric model was performed to obtain vibration mode shapes, resonance frequencies, and the stress distribution within the structure at resonance. Harmonic analysis was utilized to calculate admittance versus frequency curves, from which a theoretical effective coupling coefficient could be derived.

## IV. EXPERIMENTAL PROCEDURE

Single element cymbal transducers were fabricated by first simultaneously cutting and shaping the caps in a die press. The caps were then adhered to a poled PZT disk using a very thin layer of epoxy. The bonding quality after curing was characterized by measuring the admittance spectra of the transducer.

Single element cymbal transducers were incorporated into 9-element square arrays, where the single elements were wired together electrically in parallel. Two mounting schemes were investigated: unpotted and potted in a stiff layer of polyurethane approximately 5 mm thick.

Underwater calibration tests were performed in the anechoic water tank at the Applied Research Laboratory at Penn State. The tank measures 5.5 m in depth, 5.3 m in width, and 7.9 m in length. A pure tone sinusoidal pulse signal of 2 msec duration was applied to the test transducer and its acoustic output was subsequently measured by a standard F33 hydrophone. The test transducer and the standard are positioned so that they are at a depth of 2.74 m and separated by a distance of 3.16 m.

## V. RESULTS AND DISCUSSION

TABLE II provides some typical experimentally measured values for the parameters described in section II. These are all values for standard-size single element brass-capped cymbals except where otherwise noted. The large shift in the fundamental resonance frequency is due to the mass loading effect of the water. The  $d_{33}$  coefficient is really an effective  $d_{33}$  coefficient (since it is reported for a device). The PZT type in parenthesis is the type used as the active element in the transducer.

TABLE II  
TYPICAL AIR- AND WATER-LOADED CHARACTERISTICS OF THE STANDARD-SIZE BRASS-CAPPED CYMBAL TRANSDUCER

	air-loading	water-loading
$f_r$	23.4 kHz	15.9 kHz
$Q_m$	0.20	0.25
efficiency	200	30
$d_{33}$ (PZT-552)	12000 pC/N	90%
$d_{33}$ (PZT-5A)	8000 pC/N	
$d_{33}$ (PZT-4)	6000 pC/N	
$d_{33}$ (PZT-8)	5000 pC/N	

Fig. 2. shows the first resonance frequency of standard-size cymbal transducers with different cap materials as calculated by FEA both in-air and in-water. The first resonance frequency in-air is proportional to the sonic velocity of the cap material,  $\sqrt{E/\rho(1-\sigma)}$ , where  $E$  is the cap Young's modulus,  $\rho$  its density, and  $\sigma$  its Poisson's ratio. When the resonance frequency is measured in-water, the linear trend in the data is no longer observed. This is due to the difference in the density of the caps. Cymbals which have caps with densities closer to that of water, such as titanium, will exhibit a much more marked change in its resonance frequency in going from air to water than cymbals with caps of higher density. e.g. tungsten.

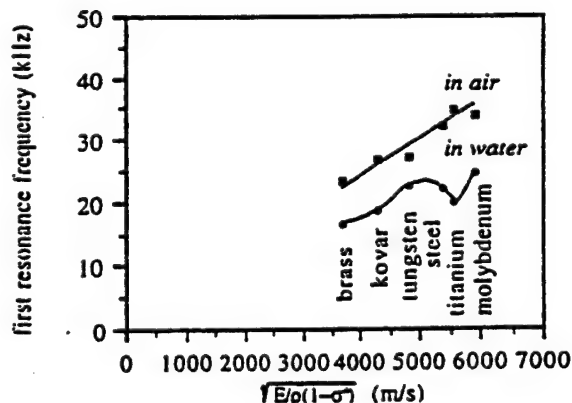


Fig. 2. First resonance frequency of standard-size cymbal transducers with different endcaps measured in-air and in-water.

The transmitting voltage response in the neighborhood of the first resonance frequency for same-size single element brass-capped cymbal transducers utilizing different PZT types is shown in Fig. 3. The transmitting response correlates with the effective  $d_{33}$  coefficient of the device, as seen from TABLE II. Single element cymbals are characterized by a relatively high  $Q_m$  ( $\approx 20$ ) and consequently a narrow bandwidth.

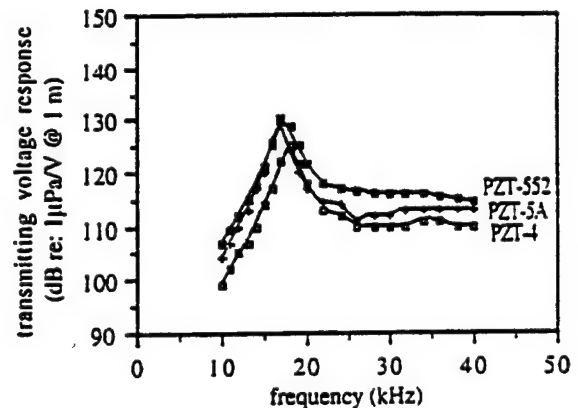


Fig. 3. Transmitting voltage response of a standard-size brass-capped cymbal utilizing different PZT types.

The transmitting voltage response of nine-element arrays of standard-size brass-capped cymbals, both potted and unpotted, are compared in Fig. 4. The fundamental resonance frequency is now strongly damped in both cases, resulting in wideband behavior. This is in part due to the array more closely approaching the idealized 'pc' loading conditions as compared to the single element.

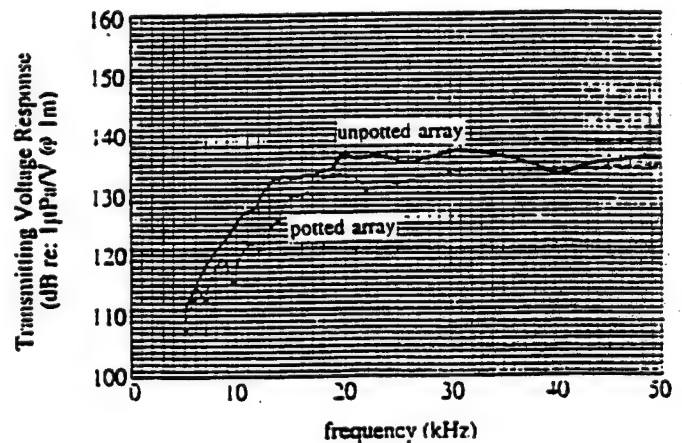


Fig. 4. Comparison of the transmitting voltage response of nine element potted and unpotted arrays of standard-size brass-capped cymbals utilizing PZT-552 driving elements.

A representative beam pattern for the nine-element arrays at 50 kHz is shown in Fig. 5. At frequencies below 50 kHz, the array exhibits near omnidirectionality. Above 50 kHz, the side lobes become more pronounced and grating lobes appear. Thus, 50 kHz is taken to be the upper use frequency for the arrays.

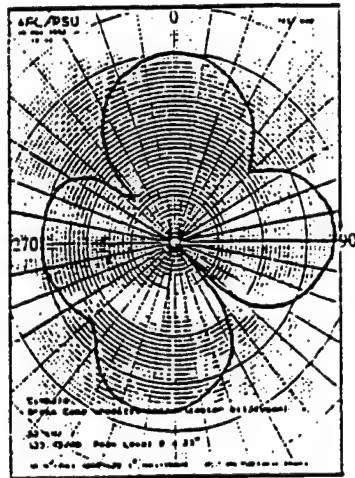


Fig. 5. Beam pattern of the array of brass-capped cymbals at 50 kHz.

Fig. 6. shows the source level as measured for the unpotted array when driven at 52 dBV both before and after failure. A source level of greater than 190 dB is generated by the array between about 18 kHz and at least 25 kHz. Although this is still less than the desired 200 dB, it is important to keep in mind that this is for an array of radiating area of only 14.5 cm<sup>2</sup>. Increasing the radiating area by incorporating more single elements into the array will enhance the source level by a factor of  $20 \cdot \log A$ , where A is equal to the increase (i.e. multiplication factor) in radiating area.

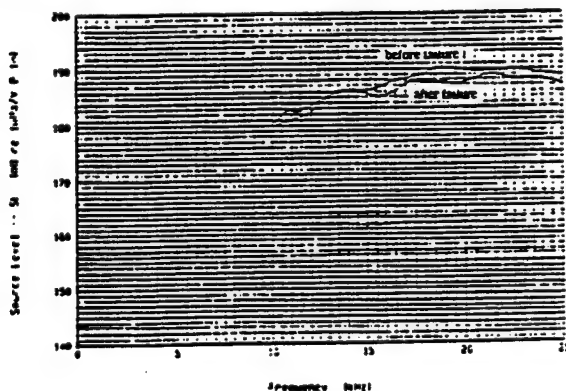


Fig. 6. Source level of the unpotted cymbal array as measured both before and after failure.

Fig. 7. shows the measured pressure dependence of the effective  $d_n$  and  $g_n$  coefficients of single-element brass-capped

cymbal transducers with different cavity depths. The standard-size cymbal can withstand up to 2.5 MPa without a significant degradation in its properties.

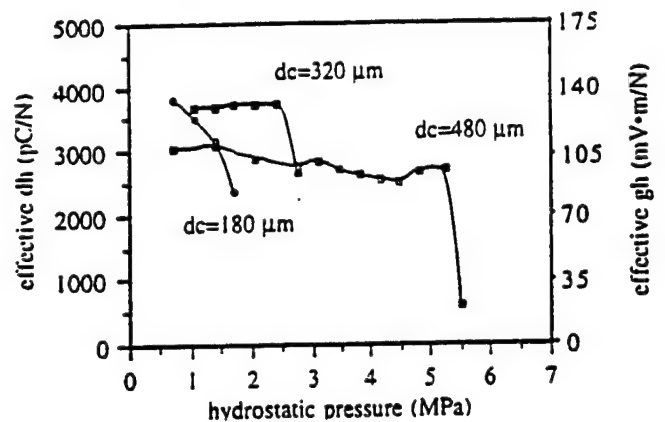


Fig. 7. Measured pressure dependence of the effective  $d_n$  and  $g_n$  coefficients for standard-size brass-capped single element cymbal transducers.

## VI. CONCLUSIONS

The cymbal transducer appears to be a viable candidate for medium- to high-power shallow water acoustic projector applications. Its thin profile when incorporated into arrays makes it ideal for attaching to a curved surface. In addition, its simple design renders it easy and inexpensive to mass produce.

## ACKNOWLEDGMENTS

The authors would like to thank Ender Kuntsal of ITC in Santa Barbara, CA. and Robert Dashem of the Applied Research Laboratory at Penn State for their contributions.

## REFERENCES

- [1] R.F.W. Coates, *Underwater Acoustic Systems*, Macmillan New Electronics Series, Hong Kong, 1990.
- [2] T.R. Gururaja, A. Safari, R.E. Newnham, and L.E. Cross, "Piezoelectric ceramic-polymer composites for transducer applications," in *Electronic Ceramics: Properties, Devices, and Applications*, L.M. Levinson, Ed., New York: Marcel Dekker, Inc., 1988, pp. 92-145.
- [3] L. Bowen, R. Gentilman, D. Fiore, H. Pham, W. Serwatka, C. Near, and B. Pazol, "Design, fabrication, and properties of Sonopanel 1-3 piezocomposite transducers," *Ferroelectrics*, vol. 187, pp. 109-120, 1996.
- [4] W. Cao, Q.M. Zhang, and L.E. Cross, "Theoretical study on the static performance of piezoelectric ceramic-polymer composites with 1-3 connectivity," *J. App. Phys.*, vol. 72, pp. 5814-5821, 1992.
- [5] K.D. Rolt, "History of the flexensional electroacoustic transducer," *J. Acoust. Soc. Am.*, vol. 87, pp. 1340-1349, 1990.
- [6] E.F. Rynne, "innovative approaches for generating high power, low frequency sound," in *Transducers for Sonics and Ultrasonics*, M.D. McCollum, B.F. Hamonic, and O.B. Wilson, Eds., Lancaster, PA: Technomic, 1993, pp. 38-49.
- [7] Q.C. Xu, S. Yoshikawa, J.R. Belsick, and R.E. Newnham, "Piezoelectric composites with high sensitivity and high capacitance for use at high pressures," *IEEE Trans. UFFC*, vol. 38, pp. 634-639, 1991.

# **APPENDIX 32**

## Concave Cymbal Transducers

Jindong Zhang, W. Jack Hughes<sup>1</sup>, A.C. Hladky-Hennion<sup>2</sup>, and Robert E. Newnham  
Materials Research Laboratory, The Pennsylvania State University, University Park, PA 16802

<sup>1</sup>Applied Research Laboratory, The Pennsylvania State University, University Park, PA 16802

<sup>2</sup>IEMN-Departement I. S. E. N., 41 Boulevard Vauban, 59046 LILLE, France

### ABSTRACT

A new type of cymbal transducer, called the concave cymbal, has been developed to increase the pressure tolerance and reliability of the transducer under high hydrostatic pressure. The main feature of the new design is a lead zirconate titanate ceramic ring sandwiched between two concave metal endcaps. It shows much improved pressure performance and can withstand a pressure of up to 6 MPa while maintaining high effective hydrostatic piezoelectric coefficients. When incorporated into a planar array with a radiating area of  $5.5 \text{ cm} \times 5.5 \text{ cm}$  and weight of only 30 g, a transmitting voltage response of around 125 dB re  $1 \mu\text{Pa/V @ 1m}$  was obtained over a frequency range between 20 and 50 kHz.

## Introduction

Flextensional transducers were first developed in the 1920s and have been used as underwater transducers since the 1950s[1]. They consist of a piezoelectric or magnetostrictive drive element and a mechanical shell structure. The shell is used as a mechanical transformer which transforms the high impedance, small extensional motion of the ceramic into low impedance, large flexural motion of the shell. According to the shape of the shell, flextensional transducers are divided into five classes [2]. Flextensional transducers range in size from several centimeters to several meters in length and can weigh up to hundreds of kilograms. They are commonly used in the frequency range of 300 to 3000 Hz [3]. They can operate at high hydrostatic pressures, and have wide bandwidths with high power output. The fabrication process is labor intensive and not easy to control due to the application of pre-stress, therefore its cost is quite high.

A new type of high performance flextensional transducer, called the "moonie," was developed at the Materials Research Laboratory at the Pennsylvania State University in the late 1980's [4]. Its basic structure is similar to a Class V flextensional transducer, but its bonding and fabrication process are very simple, which makes it very easy and inexpensive to mass-produce.

A second-generation moonie type transducer, which has a thinner cap with a slightly different shape, was also developed [5]. It was named the cymbal because of the similarity in shape of its cap to that of the musical instrument of the same name.

The moonie and cymbal transducers consist of a piezoelectric disk (poled in the thickness direction) sandwiched between two metal end caps. The caps contain a shallow cavity on their inner surface. The presence of the cavities allows the caps to convert and amplify the small radial displacement of the disk into a much larger axial displacement normal to the surface of the caps, which contributes to a much larger acoustic pressure output than would occur in the uncapped ceramic.



The standard cymbal is intended for shallow water use (no deeper than 200 m water) due to its convex structure and thin caps. If the hydrostatic pressure exceeds a certain threshold, the metal caps deform permanently and the cavity collapses, thus destroying the amplification effect [6]. A new type of cymbal transducer, which is called the concave cymbal, or double-dipper cymbal, was developed to improve the pressure tolerance. In this new design, a ceramic ring is used instead of a disk. The ring is sandwiched between two inverted metal caps. One advantage of this design is that it greatly improves the pressure tolerance of the cymbal transducers. Another advantage is that the ceramic and the metal caps vibrate in phase, eliminating any out-of-phase component of the radiating field. Schematic drawings of a standard and a double-dipper cymbal transducer are shown in Figure 1.

## Experimental Procedure

### A. Fabrication

Brass caps were punched from a metal foil of 0.25 mm thickness and shaped using a special die. The shaped caps had a diameter of 12.7 mm. The cavity diameter was 9.0 mm at the bottom and 3.2 mm at the top. The cavity depth was 0.2 mm. The caps were then bonded to a piezoelectric ceramic ring (PKI 552, Piezokinetics Inc., Bellefonte, PA) having a thickness of 1 mm, outer diameter of 12.7 mm, and inner diameter of 9.0 mm. The PZT rings were poled in the thickness direction. The bonding material is an Emerson and Cuming insulating epoxy. A ratio of three parts 45 LV epoxy resin to one part 15LV hardener was used. The thickness of the epoxy bonding layer was approximately 20  $\mu\text{m}$ . The entire assembly was kept under uniaxial stress in a special die for 24 hours at room temperature to allow the epoxy time to cure.

Single element cymbal transducers were incorporated into a 9-element square planar array. The nine cymbals were sandwiched between two copper-clad PC boards each 1.5 mm thick. Holes 11 mm in diameter were drilled equidistant from one another through the boards. Each element has a center-to-

center spacing of 13.5 mm. Plastic posts 1.5 mm thick were used to maintain a uniform distance between the upper and lower panels, which were screwed together tightly to keep the transducers in place. The elements are electrically in parallel because of the PC board. After assembly, the array had a dimension of 5.5 cm  $\times$  5.5 cm and a thickness of 0.4 cm. Its weight was around 30 g.

Underwater calibration tests of single cymbals and arrays were performed at the Applied Research Laboratory at Penn State. The tank measures 5.5 m in depth, 5.3 m in width and 7.9 m in length. A pure tone sinusoidal pulse signal of 2 msec duration was applied to the test transducer and its acoustic output was monitored with a standard F33 hydrophone. The test transducer and the standard were positioned at a depth of 2.74 m and separated by a distance of 3.16 m. The parameters measured for these underwater devices were resonance frequency, mechanical Q, Transmitting Voltage Response (TVR), Free-Field Voltage Sensitivity (FFVS), and beam pattern.

## B. Finite Element Analysis

The Finite Element Analysis code ATILA was used in the evaluation and further improvement of our cymbal transducer designs. ATILA was developed at the Acoustics Department at Institut Supérieur d'Electronique du Nord (ISEN) to model underwater transducers[7]. A static analysis was performed to provide information concerning pre-stresses and the transducer's response under hydrostatic pressure. Modal analysis was carried out to determine the vibration modes, their resonance and antiresonance frequencies, and associated coupling factors. Through harmonic analysis, the in-air and in-water impedance and displacement field can be computed as a function of frequency, together with the Transmitting Voltage Response, Free Field Voltage Sensitivity and the directivity patterns. In this study, ATILA was used to estimate the TVR and FFVS of several cymbal transducer designs.

## Results and Discussions

It has previously been shown for standard cymbals that the flextensional resonance frequency can be tailored easily by changing the cap material and geometry [8]. The concave cymbal utilizes the same amplification mechanism as the standard cymbal, but its flextensional resonance frequency is slightly lower than its standard counterpart as is shown in Table I, and it is also easily tailored. Other in-air characteristics of concave cymbal transducers are also shown and compared with standard cymbal transducers in Table I. The effective  $d_{33}$  and capacitance of concave cymbal transducers are smaller than those of standard cymbal transducers due to less piezoelectric material used in the device.

Figure 2 shows a representative admittance spectrum of a concave cymbal transducer. The first peak, at 22 kHz, is associated with the flextensional mode of the composite transducer. The higher resonance peaks comes from the coupling between the radial mode of the ceramic ring and high order flextensional modes. Fig.2 also shows the admittance spectrum of a nine-element concave cymbal array. Its resonance is damped and broadened due to element interactions and the fact that the individual elements have slightly different frequencies.

Fig.3 shows the pressure dependence of the effective  $d_h$  of double-dipper and standard cymbals. Effective  $d_h$  for bulk PZT as a function of pressure is also shown and compared. Both standard and concave cymbals have effective  $d_h$  values over fifty times larger than that of bulk piezoelectric material. The standard cymbal can withstand 2 MPa, but when the pressure increases over 2 MPa, it fails catastrophically. In the case of the concave cymbal, it has a slightly lower  $d_h$  than the standard cymbal but it survives up to 6 MPa without significant degradation in its properties. The concave cymbal exhibits much improved pressure tolerance under hydrostatic loading. Under some certain higher pressures, the concave cymbal may fail due to the meeting of the two brass end caps which causes a short circuit. But it

can be avoided by applying a thin insulating layer between the brass caps and its pressure tolerance can be further improved.

The TVR and FFVS of a single concave cymbal are shown in Figure 4. Like the standard cymbal, the concave cymbal shows narrow band characteristics with a mechanical  $Q$  around 9. The TVR and FFVS calculated with the ATILA code are also shown for comparison with the experimental results. Fairly good agreement is obtained indicating that ATILA adequately models the cymbal behavior in water. The small discrepancies between the calculated and the experimental results may arise from imperfections in the ring, from stresses in the metal caps, or from the fact the contribution of the epoxy bonding layer and the fixtures used to hold the sample were not taken into account in modeling.

Since individual concave cymbals are not powerful enough, and are not sufficiently broad-band for practical use, the incorporation of single elements into arrays is necessary to improve underwater performance. The TVR and FFVS of a nine-element array of concave cymbal transducers are illustrated in Figure 5. The array shows broader band characteristics in both TVR and FFVS. It has a TVR of around 125 dB re  $1\mu\text{Pa/V}$  @ 1m and is rather flat over the frequency range from 20-50 kHz. Its FFVS is not as flat as the TVR, but a wider bandwidth can be obtained by incorporating more cymbal elements into the array and by precisely controlling and arranging the resonance frequencies and position of the array elements. Modeling studies are under way to optimize the performance of a double-dipper array.

The use of PZT rings allows the drive elements to be poled in different directions. The ring can be poled through its thickness as in this experiment, or it can also be poled radially, in which case  $d_{33}$  can be used and the electromechanical coupling coefficient is expected to be higher.

### Potential Applications

Concave cymbal transducers demonstrate a much improved pressure tolerance over standard cymbals and can go much deeper underwater, extending the range of operation for cymbal transducers. The simple fabrication process makes it easy to mass-produce these transducers which will greatly reduce

its cost. The thin profile, light weight and low cost makes it possible to assemble a very large array of cymbals, either in a planar or conformal array. It is expected that the array can be further optimized to work as well as a standard Tonpilz array when a high source level is bit required. The cymbal transducers may be a good transducer for conformal arrays where drastically reducing the vehicle's weight and cost is important. Hard, PZT4, instead of soft, PZT5, piezoelectric drive elements can be used to achieve a high source level.

The low-cost concave cymbal array can also be used as a receiver for acoustic imaging. The most useful frequency range for underwater imaging appears to be the 5-50 kHz band [9] where the concave cymbal transducer excels. When fully optimized, an array of cymbal hydrophones may serve as a multi-element receiver capable of functioning as an acoustic camera. Phased arrays of a thousand or more hydrophones are feasible using these small low-cost, mass-produced components with high hydrostatic piezoelectric coefficients. The improved pressure performance allows the concave cymbal transducer array to work both in shallow water and in deep submergence.

### Conclusion

The concave, or double-dipper cymbal, is shown to have a much higher pressure tolerance than the standard cymbal. Its thin profile and small size make it easy to mount in a planar or curved array. When incorporated into a planar nine-element array, it shows medium output power and broad band characteristics combined with a small radiating area and light weight. The double-dipper cymbal is a promising candidate as an underwater sound projector and receiver.

### Acknowledgments

The authors would like to thank Dr. Kenji Uchino, Dr. J. F. Tressler, Sedat Alkoy, Rattikorn Yimnirun and Jayne Giniewicz for their helpful discussions, and Greg Granville and Bob Dashem at

Applied Research Laboratory of Penn State for their assistance. This work is funded by the Office of Naval Research.

## References

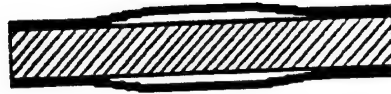
- [1] K. D. Rolt, "History of the flextensional electroacoustic transducers," *J. Acoust. Soc. Am.*, vol. 87, pp. 1340-1349, 1990.
- [2] E. F. Rynne, "Innovative Approaches for Generating High Power, Low Frequency Sound," in *Transducers for Sonics and Ultrasonics*, M. D. McCollum, B. F. Hamonic, and O. B. Wilson, Eds., Lancaster, PA: Technomic, 1993, pp.38-49.
- [3] W. Jack Hughes, *Encyclopedia of Applied Physics*, Vol.22, WILEY-VCH Verlag GmbH, 1998, pp67-84
- [4] Q. C. Xu, S. Yoshikawa, J. R. Belsick, and R. E. Newnham, "Piezoelectric composites with High Sensitivity and High Capacitance for Use at High Pressures," *IEEE Trans. UFFC*, vol 38, pp. 634-639, 1991
- [5] Aydin Dogan, Kenji Uchino, and Robert E. Newnham, "Composite Piezoelectric Transducers with Truncated Conical Endcaps 'Cymbals'," *IEEE Trans. UFFC*, vol. 44 , No3, pp. 597-605, May 1997.
- [6] J. F. Tressler, A. Dogan, J. F. Fernandez, J. T. Fielding, K. Uchino, and R. E. Newnham, "Capped Ceramic Hydrophones," in *1995 IEEE Ultrasonics Proceedings*, 1995, pp. 897-900.
- [7] A. C. Hladky-Hennion and J. N. Decarpigny, "Finite element modeling of active periodic structures: application to 1-3 piezocomposites," *J. Acoust. Soc. Am.*, vol. 94, pp. 621-635, 1993
- [8] J. F. Tressler, *PhD Thesis*, Penn State University, 1997.
- [9] R. J. Urick, *Principles of Underwater Sound*, McGraw Hill Book Co., NY, 1967.

Table I Typical in-air characteristics of standard and concave cymbal transducers

---

	standard cymbal	concave cymbal
flextensional frequency	24 kHz	23 kHz
coupling coefficient	20%	15%
effective $d_{33}$	12000 pC/N	4000 pC/N
capacitance	2.9 nF	1.2 nF

---



(a)



(b)

Figure 1 Cross-sectional views of the (a) standard cymbal, and (b) double-dipper cymbal transducers



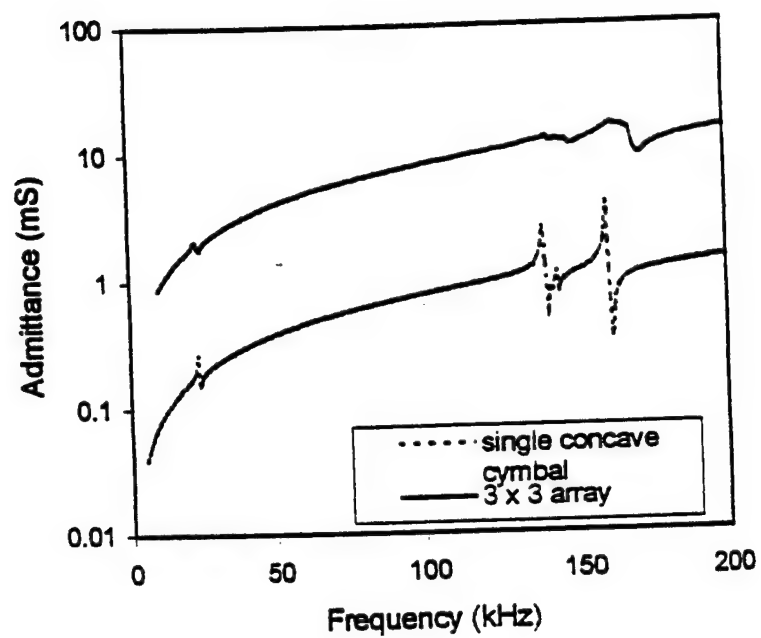


Figure 2 Admittance spectrum of a single concave cymbal transducer and a nine-element array

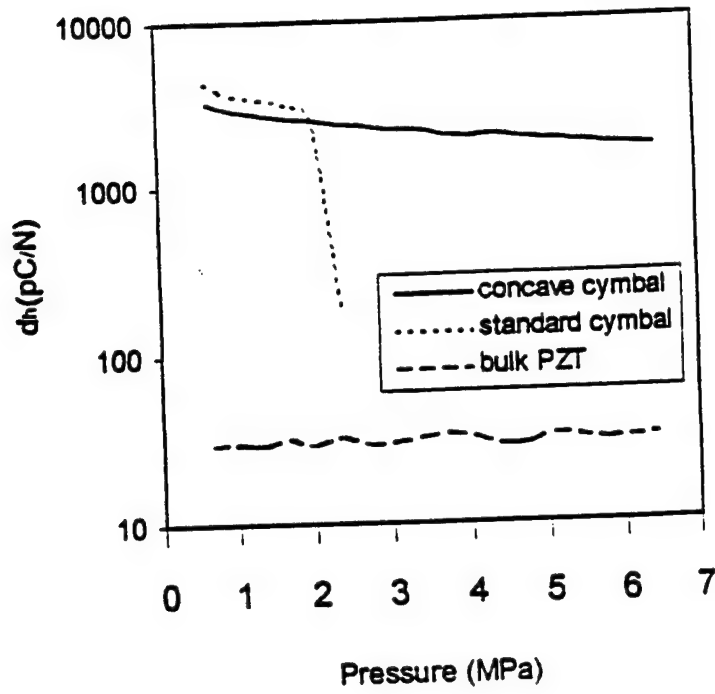
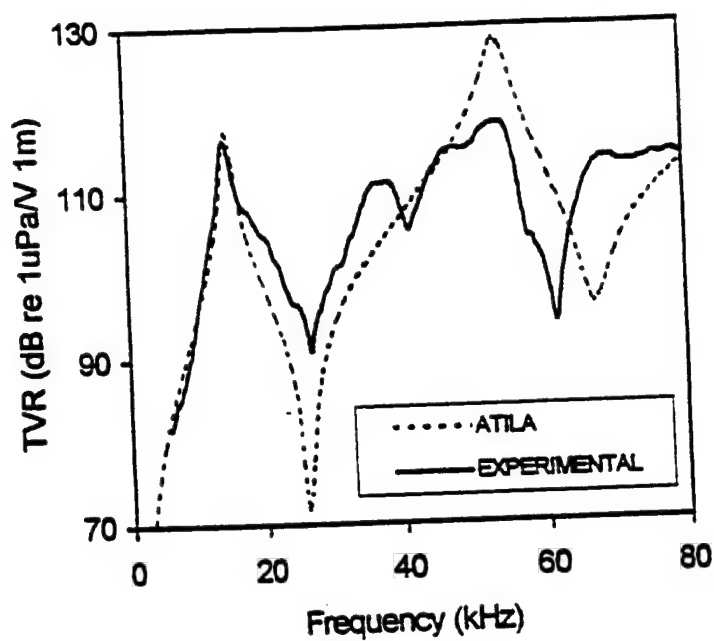
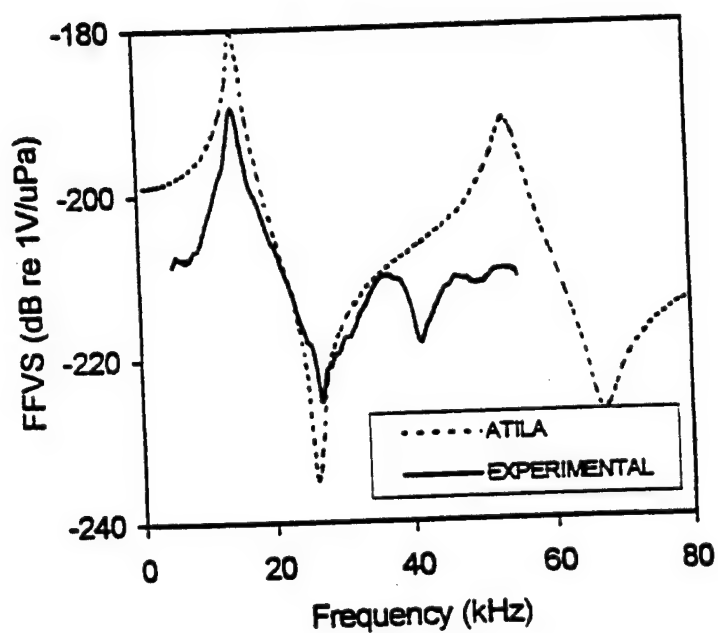


Figure 3 Pressure dependence of the effective  $d_h$  coefficients for the standard and concave cymbal transducers

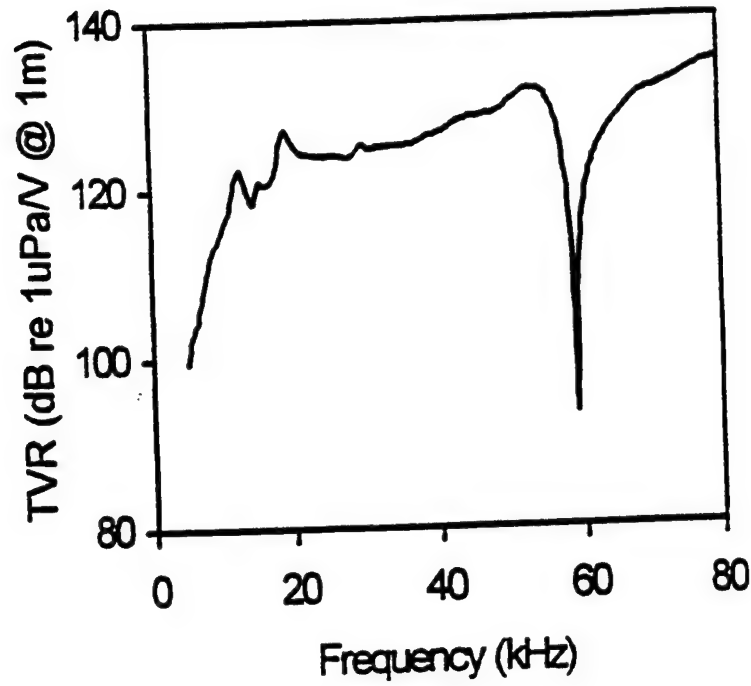


(a)

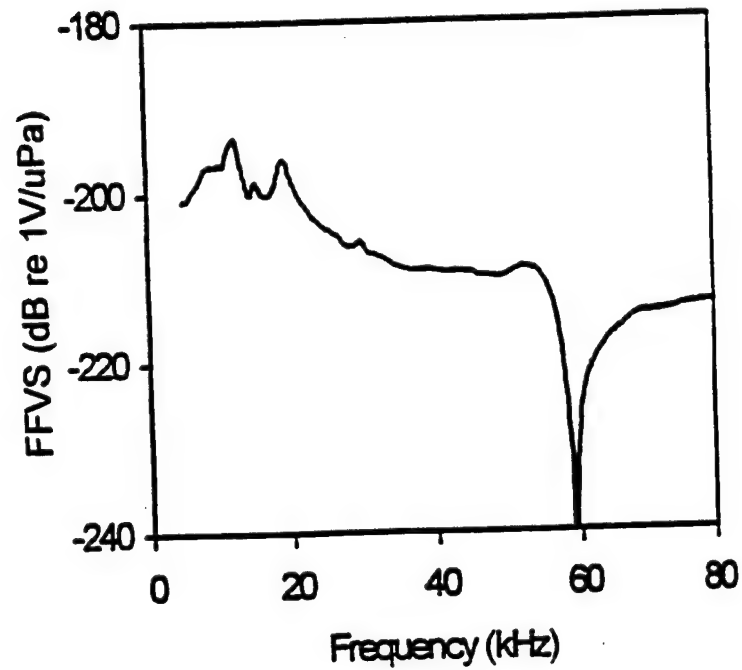


(b)

Figure 4 Measured and calculated (ATILA) (a)TVR and (b) FFVS of a concave cymbal transducer



(a)



(b)

Figure 5 Measured (a) TVR and (b) FFVS of a nine-element array of concave cymbal transducers

# **APPENDIX 33**

# Theoretical analysis of the sensor effect of cantilever piezoelectric benders

Qing-Ming Wang,<sup>a)</sup> Xiao-hong Du, Baomin Xu, and L. Eric Cross  
*Intercollege Materials Research Laboratory, The Pennsylvania State University,  
 University Park, Pennsylvania 16802-4801*

(Received 26 May 1998; accepted for publication 13 October 1998)

Piezoelectric bending mode elements such as bimorph and unimorph benders can be used as both actuation and sensing elements for a wide range of applications. As actuation elements, these devices convert electric input energy into output mechanical energy. As sensing elements, they convert external mechanical stimuli into electrical charge or voltage. In this article, the sensing effect of cantilever mounted piezoelectric bimorph unimorph and triple layer benders subjected to external mechanical excitations are discussed. General analytical expressions relating generated electric voltage (or charge) to the applied mechanical input excitations (moment  $M$ , tip force  $F$ , and body force  $p$ ) are derived based on the constitutive equations of these bending devices. It is found that the clamping effect of each component in the bender devices decreases the dielectric constant. The bimorph bender has a higher voltage sensitivity than the unimorph or triple layer bender with the same geometrical dimensions. The dependence of voltage and charge sensitivities on the thickness ratio and the Young's modulus ratio of the elastic layer and piezoelectric layer under different conditions are discussed and compared for the unimorph and triple layer benders. © 1999 American Institute of Physics. [S0021-8979(99)05302-5]

## I. INTRODUCTION

Many novel solid state devices based on piezoelectric materials have been developed in recent years for a wide range of electromechanical applications.<sup>1-3</sup> These devices can perform either actuator or sensor functions by utilizing the direct or converse piezoelectric effect. Two classical examples of piezoelectric devices are bimorph and unimorph configurations, which have been widely used for acoustic sensing, loudspeaker, relay, micropumps, micropositioners, and many other applications. With simple structures, the unimorph and bimorph are capable of producing large strokes under low electric voltage as actuation elements or providing high mechanical force/load sensitivity as sensory devices.

As schematically shown in Figs. 1(a) and 1(b), a bimorph bender consists of two piezoelectric thin plates with polarization normal to the interface. The application of electric field forces one plate to expand and the other to contract. Since there is constraint at the interface of these two plates, bending deformation occurs in the whole structure. Similarly, bending can be produced in the unimorph where the transverse deformation of the piezoelectric plate is constrained by the nonpiezoelectric elastic plate [Fig. 1(c)]. Therefore, bimorphs and unimorphs can be used as actuation elements. Two types of connections are commonly used in bimorph design and fabrication: one is a series connection and the other is a parallel connection. In the series connection, the two piezoelectric layers have opposite polarization directions, and an electric field is applied across the total thickness of the bimorph. While connected in parallel, the two piezoelectric layers have the same polarization direc-

tions and the electric field is applied across each individual plate with opposite polarity. In both cases, the applied electric field is parallel to the polarization direction in one plate but antiparallel in the other plate so that the transverse strain can be converted into bending deformation. The driving voltage for a bimorph actuator in the parallel connection can be reduced to half the value for a bimorph in the series connection while remaining the same electric strength and keeping the same actuation capability. However, since the dielectric capacitance in the parallel case is four times that in the series case, power consumption,  $P = 1/2 CV^2$  is the same in both cases. With the same driving voltage, the actuation capability of a parallel bimorph is twice that of a series bimorph. For actuator applications, low driving voltage is usually desirable, therefore a bimorph in parallel connection can be used.

On the other hand, the unimorph and bimorph benders can be used as mechanical sensing elements since electric charge or voltage can be generated on the electrodes of the bimorph or unimorph devices when an external mechanical moment, force or load is applied. As an example, if a force  $F$  is acting perpendicularly on the tip of a cantilever mounted series bimorph, bending deformation occurs, thus tensile stresses are induced in the upper plate while compressive stresses are induced in the lower plate in the direction of the length of the beam. The distribution of these stresses is non-uniform with a maximum value at the top surface (positive) and the bottom surface (negative) and zero at the interface (neutral plane) [Fig. 1(a)]. Consequently, negative charges are produced at the top electrode while positive charges are at the bottom electrode, since at the top surface,

$$P_3 = d_{31}T_1, \quad (1)$$

where  $P_3$  is polarization in the thickness direction in units of

<sup>a)</sup> Author to whom correspondence should be addressed; electronic mail: qmwang@lexmark.com

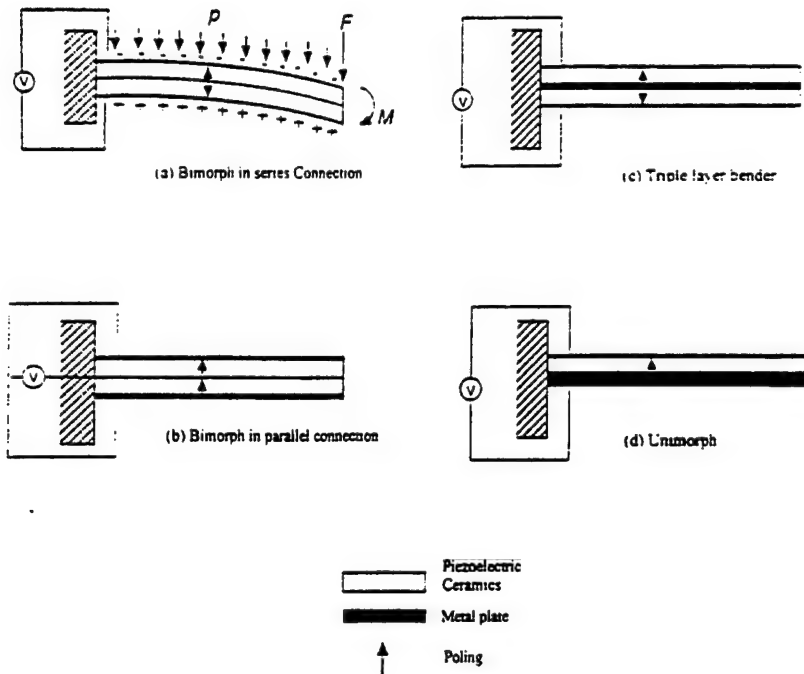


FIG. 1. Structure of bimorph, unimorph and triple layer benders: (a) bimorph bender in series connection, (b) bimorph bender in parallel connection, (c) triple layer bender, (d) unimorph bender, and (e) the RAINBOW device.

$C/m^2$ ,  $T_1$  is stress in the length direction in units of  $N/m^2$ , and  $d_{31}$  is the transverse piezoelectric coefficient (C/N); at the bottom surface,

$$P_3 = d_{31}(-T_1). \quad (2)$$

$d_{31}$  is a negative value for piezoelectric ceramics such as barium titanate  $BaTiO_3$  and lead zirconate titanate  $Pb(Zr_xTi_{1-x})O_3$  (PZT). Therefore, a voltage difference is built up across the top and bottom electrodes. For a parallel connected bimorph, electric charges with the same sign are generated on the top and bottom electrodes. Electric voltage is built up between the surface electrodes and the interface electrode of the bimorph. With the same external force, the electric charges generated by a parallel bimorph is twice the value generated by a series bimorph. However the generated electric voltage in the parallel bimorph is half the value produced by a series bimorph, since the capacitance of the parallel bimorph is four times that of the series bimorph,

$$V_{para} = \frac{Q_{para}}{C_{para}} = \frac{2Q_{series}}{4C_{series}} = \frac{1}{2} V_{series}. \quad (3)$$

For sensory applications, high generated voltage is frequently desired, therefore the bimorph in series connection is preferred.

However, since bimorphs are composed of two thin piezoelectric ceramic plates, and ceramic is fragile in general, reliability is of concern in practical applications. Triple layer benders, which consist of two piezoelectric layers and a sandwiched central elastic layer [Fig. 1(d)], can be used to improve the mechanical reliability. However, in any case, the interfaces in the bimorph, unimorph or triple layer benders are mechanically weak locations. Delamination may occur after being driven for a period of time under periodic excitations due to the relaxation, debonding of the epoxy bonding materials.

Recently, a new piezoelectric bending mode device, the so-called reduced and internally biased oxide wafer (RAINBOW) was developed by Haertling at Clemson University.<sup>4,5</sup> This device consists of a piezoelectric active layer and a chemically reduced nonpiezoelectric layer formed by a special high temperature processing. Basically the RAINBOW device is a modified unimorph bender. When the piezoelectric layer is driven under electric field, bending deflection will be generated due to the constraint of the chemically reduced piezoelectric inactive layer. On the other hand, when an external force or load is applied to the RAINBOWs, electric charges (or voltage) will be generated in the piezoelectric layer due to direct piezoelectric effect. One of the advantages of the RAINBOW device over other bending mode piezoelectric devices is that RAINBOW has a monolithic structure. Moreover, compared with bimorph and unimorph devices, large thermal stresses exist in RAINBOW devices. These internal stresses are formed when the RAINBOW is cooled down to room temperature after the high temperature treatment, since the chemically reduced layer and the remaining piezoelectric layer have different thermal expansion coefficients. These residual thermal stresses are believed to be beneficial to the electromechanical performance of RAINBOW devices.

Although bimorph, unimorph and triple layer benders have been widely used in many applications and there is a significant amount of literature available detailing their operational principles and applications, it is found, however, there is a lack of analysis of the sensing performance of these devices; for example, no systematic comparison has been made on these devices. Most previous research has focused on actuator applications. In this article, the sensing effects of the above mentioned devices subjected to external mechanical excitations are discussed based on their constitutive equations. Comparison is made between these devices by taking

into account their geometrical dimensions and the elastic and electromechanical properties of their components.

## II. SENSOR PERFORMANCE ANALYSIS OF A CANTILEVER BIMORPH

The constitutive relations for the cantilever mounted bimorph have been derived by Smits *et al.*,<sup>6</sup> and they describe the behavior of the bimorph under static conditions. For a series connected bimorph bender subjected to the following excitations: an electric voltage  $V$  across its thickness, a uniformly distributed external body load  $p$ , an external tip force  $F$  perpendicular to the beam, and an external moment  $M$  at the free end, the generated electrical charge then can be expressed by the following equation:

$$Q = \frac{3d_{31}L}{t^2}M + \frac{3d_{31}L^2}{2t^2}F + \frac{d_{31}wL^3}{2t^2}p - \frac{\epsilon_{33}^X Lw(1-k_{31}^2/4)}{t}V, \quad (4)$$

where  $L$ ,  $w$ , and  $t$  are the bimorph length, width and thickness, respectively;  $\epsilon_{33}^X$  is the dielectric constant of the piezoelectric material under a free condition;  $d_{31}$  is the transverse piezoelectric coefficient;  $k_{31}^2$  is the transverse piezoelectric coupling coefficient, and  $k_{31}^2 = d_{31}^2/s_{11}^E\epsilon_{33}^X$ . The total capacitance of the bimorph bender can be obtained by

$$C = \frac{\partial Q}{\partial V}, \quad (5)$$

i.e.,

$$C = \frac{\epsilon_{33}^X Lw(1-k_{31}^2/4)}{t}. \quad (6)$$

Therefore, the dielectric constant of the bimorph bender as a whole is

$$\epsilon_b = \epsilon_{33}^X(1-k_{31}^2/4), \quad (7)$$

which is smaller than the free dielectric constant of piezoelectric material since in a bimorph bender two pieces of piezoelectric material are mechanically bonded together. The clamping effect exists in the bimorph actuator because of the constraint of the two piezoelectric layers at the interface. This clamping effect reduces the dielectric constant of the bimorph bender.

When only an external moment is applied on the free end of the bimorph, the generated electric charge becomes

$$Q = \frac{3d_{31}L}{t^2}M. \quad (8)$$

The open circuit electric voltage generated between the top and bottom electrodes of the bimorph can be calculated as

$$V = \frac{Q}{C} = \frac{3d_{31}}{\epsilon_{33}^X w t(1-k_{31}^2/4)}M. \quad (9)$$

When only an external tip force is acting on the tip of the bimorph bender, the generated electric charge in the bimorph becomes

$$Q = \frac{3d_{31}L^2}{2t^2}F. \quad (10)$$

Therefore, the open circuit electric voltage generated in the bimorph bender by the applied external tip force is

$$V = \frac{3d_{31}L}{2\epsilon_{33}^X w t(1-k_{31}^2/4)}F. \quad (11)$$

Therefore, the bimorph bender can be used as a force sensor. If the dielectric constant  $\epsilon_{33}^X$ , piezoelectric constant  $d_{31}$  and coupling coefficient  $k_{31}^2$  of the piezoelectric material and the dimensions of the bimorph are known, by measuring the electric voltage generated across the bimorph bender, the acting external tip force can be calculated by Eq. (11). Obviously, from Eq. (11), to increase the sensitivity ( $V/F$ ), a bimorph with a large  $L/t$  ratio is preferred.

The external tip force can be related to the tip deflection  $\delta$  by<sup>7,8</sup>

$$F = \frac{3E_p I \delta}{L^3}, \quad (12)$$

where  $E_p I$  is the flexural rigidity of the bimorph bender. It should be noted that here  $E_p$  is the Young's modulus of the piezoelectric material under the open circuit condition ( $E_p = 1/s_{11}^D$ ), and  $I$  is the moment of inertia of the bimorph bender. For beam structure, the moment of inertia is<sup>7</sup>

$$I = \frac{wt^3}{12}. \quad (13)$$

Substituting Eqs. (12) and (13) into Eq. (11), we have

$$V = \frac{3t^2}{8L^2} \frac{d_{31}}{\epsilon_{33}^X s_{11}^D} \frac{1}{1-k_{31}^2/4} \delta. \quad (14)$$

Therefore, the bimorph bender can also be used as a displacement sensor.

Similarly, when only an external load  $p$  is applied to the bimorph bender, the generated electric charge in the bimorph is

$$Q = \frac{d_{31}wL^3}{2t^2}p, \quad (15)$$

and the open circuit electric voltage generated in the bimorph bender in this case becomes

$$V = \frac{d_{31}L^2}{2\epsilon_{33}^X t(1-k_{31}^2/4)}p. \quad (16)$$

Therefore, a bimorph bender can be used for acoustic sensor applications. A bimorph with a large  $L^2/t$  ratio, high  $k_{31}$ , and a large  $d_{31}/\epsilon_{33}^X$  ratio has a high sensitivity to the external load  $p$ .

By combining Eqs. (9), (11) and (16), the voltage generated in the bimorph bender under various external mechanical excitations can be expressed as



TABLE I. Comparison of piezoelectric materials properties for bending mode sensor applications.

Materials	$K_3^X$	$d_{31} (\times 10^{-12} \text{ C/N})$	$k_{31}$	Figure of merit $S (\times 10^{-3})$
BaTiO <sub>3</sub>	1900	-79	0.21	-4.746
Soft PZT 3203HD	3800	-320	0.44	-10
Soft PZT 5A	1700	-171	0.34	-11.74
Undoped PZT	730	-93	0.31	-14.75
Hard PZT 4	1300	-122	0.33	-10.90
Hard PZT 3	1000	-97	0.30	-11.21

$$^X \epsilon_{33}^X = \epsilon_0 K_3^X \text{ and } \epsilon_0 = 8.85 \times 10^{-12} \text{ F/m.}$$

$$V = \frac{3d_{31}}{\epsilon_{33}^X w t (1 - k_{31}^2/4)} M + \frac{3d_{31}L}{2\epsilon_{33}^X w t (1 - k_{31}^2/4)} F - \frac{d_{31}L^2}{2\epsilon_{33}^X t (1 - k_{31}^2/4)} p. \quad (17)$$

Obviously, to have high sensitivities (which can be defined as  $V/M$ ,  $V/F$ , or  $V/p$ ) for the bimorph bender to external mechanical excitations, piezoelectric materials with a high piezoelectric coefficient  $d_{31}$ , high electromechanical coupling coefficient  $k_{31}$ , and low dielectric constant  $\epsilon_{33}^X$  should be used for fabricating bimorph displacement, force or pressure sensors. A figure of merit

$$S = \frac{d_{31}}{\epsilon_{33}^X (1 - k_{31}^2/4)} \quad (18)$$

can be defined for materials selection for bimorph mechanical sensor design and fabrication. The properties and the figure of merit of several commercially available piezoelectric materials are listed and compared in Table I. For ferroelectric ceramics such as PZTs, an increase of piezoelectric properties is accompanied by a dielectric constant increase, and improvement of the electromechanical coefficient  $k_{31}$  then becomes more critical in increasing the figure of merit.

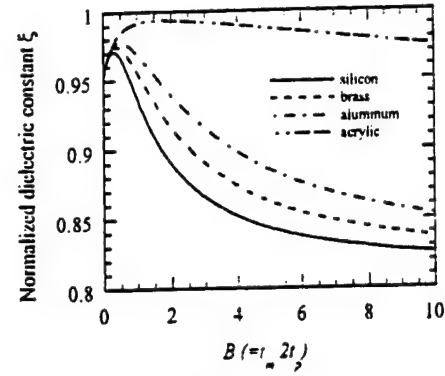
### III. SENSOR PERFORMANCE ANALYSIS OF CANTILEVER TRIPLE LAYER BENDERS

The constitutive equations for a symmetrical triple layer bender have been derived by Wang and Cross<sup>9</sup> recently. For a series connected symmetrical triple layer bender, when it is subjected to the above mentioned excitations, the electric charge generated can be expressed as

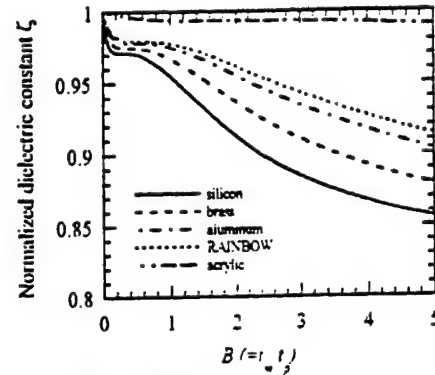
$$Q = \frac{6s_{11}^m d_{31}(t_m + t_p)L}{D} M + \frac{3s_{11}^m d_{31}(t_m + t_p)L^2}{D} F - \frac{s_{11}^m d_{31}(t_m + t_p)L^3 w}{D} p + \frac{Lw}{2t_p} \epsilon_{33}^X \times \left( 1 - \frac{D - 6s_{11}^m t_p(t_m + t_p)^2}{D} k_{31}^2 \right) V, \quad (19)$$

where  $D = 2s_{11}^m(3t_m^2 t_p + 6t_m t_p^2 + 4t_p^3) + s_{11}^E t_m^3$ . The total thickness of the triple layer bender is  $t = 2t_p + t_m$ . As a special case, if  $t_m = 0$ , Eq. (19) becomes Eq. (4).

The capacitance of the triple layer bender is dependent on the thickness of the piezoelectric and elastic layers,



(a) Triple layer benders



(b) Unimorph benders

FIG. 2. (a) Normalized dielectric constant  $\xi$  plotted as a function of elastic/ceramic thickness ratio for different triple layer benders; (b) normalized dielectric constant  $\xi$  plotted as a function of elastic/ceramic thickness ratio for different unimorph benders.

$$C_{\text{triple}} = \frac{Lw}{2t_p} \epsilon_{33}^X \left( 1 - \frac{D - 6s_{11}^m t_p(t_m + t_p)^2}{D} k_{31}^2 \right). \quad (20)$$

For analyzing the dielectric property of the triple layer bender, we define

$$A = \frac{s_{11}^p}{s_{11}^m} = \frac{E_m}{E_p}, \quad B = \frac{t_m}{2t_p}, \quad (21)$$

where  $E_m$  and  $E_p$  are the Young's modulus of the elastic (metal) layer and the piezoelectric ceramic layer, i.e.,  $A$  is the Young's modulus ratio of these two layers and  $B$  is the thickness ratio of the elastic layer and the piezoelectric layer. The capacitance and dielectric constant of the triple layer bender can be written as

$$C_{\text{triple}} = \frac{Lw}{2t_p} \epsilon_{33}^X \left[ 1 - \left( 1 - \frac{3}{4} \frac{(2B+1)^2}{AB^3 + 3B^2 + 3B + 1} \right) k_{31}^2 \right], \quad (22)$$

$$\epsilon_{\text{triple}} = \epsilon_{33}^X \left[ 1 - \left( 1 - \frac{3}{4} \frac{(2B+1)^2}{AB^3 + 3B^2 + 3B + 1} \right) k_{31}^2 \right]. \quad (23)$$

To visualize the variation of the dielectric constant of the triple layer bender with the properties of its components, we define a nondimensional parameter,

$$\xi = 1 - \left( 1 - \frac{3}{4} \frac{(2B+1)^2}{AB^3 + 3B^2 + 3B + 1} \right) k_{31}^2. \quad (24)$$

In Fig. 2(a),  $\xi$  is plotted as a function of thickness ratio  $B$  for

a series of triple layer benders made from soft PZT and different elastic layers: silicon, brass, aluminum and acrylic. The Young's modulus ratios of these materials to a soft PZT ceramic are listed in Table II.  $k_{31} = 0.44$  of soft PZT 3203HD (Motorola, Albuquerque, NM) is used in the calculation.  $\xi$  is actually the normalized dielectric constant of the triple layer bender compared with the free dielectric constant of the piezoelectric component. The dielectric constant of the triple layer bender is always lower than that of the piezoelectric material in the free condition due to the partial clamping effect of each component. A maximum dielectric constant is observed at a certain thickness ratio for the triple layer bender. The thickness ratio for maximum dielectric constant can be found by

$$\frac{d\xi}{dB} = 0. \quad (25)$$

If  $1 \leq A < \infty$ , the thickness ratio for maximum dielectric constant is given by

$$B_{\max} = \cos \left[ \frac{1}{3} \arccos \left( \frac{2}{A} - 1 \right) \right] - \frac{1}{2}, \quad (26)$$

and if  $A \leq 1$ ,

$$B = \frac{1}{2} \sqrt{\frac{2}{A} - 1 + \sqrt{\left(\frac{2}{A} - 1\right)^2 - 1}} - \frac{1}{2} \sqrt{\frac{2}{A} - 1 - \sqrt{\left(\frac{2}{A} - 1\right)^2 - 1}} - \frac{1}{2}. \quad (27)$$

The use of a stiffer elastic layer leads to a lower dielectric constant for the triple layer bender. For comparison purposes, the normalized dielectric constant  $\xi$  of a unimorph bender, which will be discussed in Sec. IV, is shown in Fig. 2(b). It is found that at the same thickness ratio  $B$ , the triple layer bender has a lower dielectric constant than the unimorph bender.

Substituting Eq. (21) into Eq. (19), we have

$$\begin{aligned} Q &= \frac{3d_{31}L}{4t_p^2} \frac{(2B+1)}{AB^3+3B^2+3B+1} M \\ &+ \frac{3d_{31}L^2}{8t_p^2} \frac{(2B+1)}{AB^3+3B^2+3B+1} F \\ &+ \frac{d_{31}L^3w}{8t_p^2} \frac{(2B+1)}{AB^3+3B^2+3B+1} p + \frac{Lw}{2t_p} \epsilon_{33}^x \\ &\times \left[ 1 - \left( 1 - \frac{3}{4} \frac{(2B+1)^2}{AB^3+3B^2+3B+1} \right) k_{31}^2 \right] V. \end{aligned} \quad (28)$$

If only an external moment  $M$  is applied on the free end of the triple layer bender, the generated electric charge is

$$Q = \frac{3d_{31}L}{4t_p^2} \frac{(2B+1)}{AB^3+3B^2+3B+1} M. \quad (29)$$

and the electric voltage in the open circuit condition is

$$\begin{aligned} V &= \frac{Q}{C} \\ &= \frac{6d_{31}}{\epsilon_{33}^x w t_p} \\ &\times \frac{(2B+1)}{4(1-k_{31}^2)(AB^3+3B^2+3B+1)+3k_{31}^2(2B+1)^2} M. \end{aligned} \quad (30)$$

Similarly, if only an external tip force  $F$  is applied perpendicularly at the triple layer bender, the electric charge generated and open circuit voltage are

$$Q = \frac{3d_{31}L^2}{8t_p^2} \frac{(2B+1)}{AB^3+3B^2+3B+1} F, \quad (31)$$

and

$$\begin{aligned} V &= \frac{Q}{C} \\ &= \frac{3d_{31}L}{\epsilon_{33}^x w t_p} \\ &\times \frac{(2B+1)}{4(1-k_{31}^2)(AB^3+3B^2+3B+1)+3k_{31}^2(2B+1)^2} F. \end{aligned} \quad (32)$$

As in the case of the bimorph, the open circuit electric voltage of the triple layer bender generated can be related to the tip displacement. The flexural rigidity of a triple layer bender can be obtained by the transformed cross section method of the composite beam.<sup>7,8,10</sup>

$$E_p I_c = \frac{2wt_p^3 E_p}{3} (AB^3+3B^2-3B+1). \quad (33)$$

Substitution of Eqs. (12) and (33) into Eq. (32) leads to

$$\begin{aligned} V &= \frac{6d_{31}t_p^2}{\epsilon_{33}^x w L^2} \\ &\times \frac{(2B+1)(AB^3+3B^2+3B+1)}{4(1-k_{31}^2)(AB^3+3B^2+3B+1)+3k_{31}^2(2B+1)^2} \delta. \end{aligned} \quad (34)$$

Therefore, the voltage generated in the cantilever mounted triple layer bender is proportional to the tip displacement; by measuring the open circuit voltage, the displacement can be obtained.

If only uniform distributed external load  $p$  is applied, the electric charge and voltage generated in the triple layer bender become

$$Q = \frac{d_{31}L^3w}{8t_p^2} \frac{(2B+1)}{AB^3+3B^2+3B+1} p, \quad (35)$$

$$V = \frac{d_{31}L^2}{\epsilon_{33}^X t_p} \times \frac{(2B-1)}{4(1-k_{31}^2)(AB^3+3B^2+3B-1)+3k_{31}^2(2B+1)^2} P. \quad (36)$$

Therefore, to achieve high sensitivity, materials with high  $d_{31}/\epsilon_{33}^X$  and high  $k_{31}$  should be used to fabricate triple layer benders. i.e., the previously defined figure of merit  $S$  should be used for materials selection. To further clarify the sensing effect of the triple layer bender to external moment, force or load, the dependence of the generated electric charge and voltage on the geometrical dimension and elastic properties of each component will be discussed for the following three cases.

(1) We can compare the generated electric charge and electric voltage of a triple layer bender with a bimorph with the same geometrical dimensions. Since  $2t_p + t_m = t$  and  $t_m/2t_p = B$ , we have  $t_p = t/2(B+1)$ . Substituting  $t_p = t/2(B+1)$  into Eqs. (31) and (32), and comparing with Eqs. (10) and (11), we define the following normalized charge and voltage parameters:

$$q_{\text{triple}} = \frac{(2B-1)(B+1)^2}{AB^3+3B^2+3B+1}, \quad (37)$$

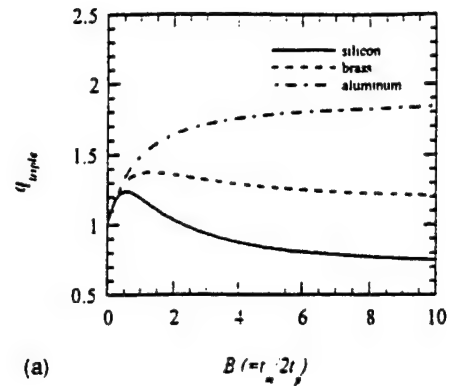
$$v_{\text{triple}} = \frac{4(2B+1)(B-1)(1-k_{31}^2/4)}{4(1-k_{31}^2)(AB^3+3B^2+3B-1)+3k_{31}^2(2B+1)^2}, \quad (38)$$

where  $q_{\text{triple}}$  and  $v_{\text{triple}}$  are the normalized electrical charge and voltage generated on the triple layer bender when external mechanical excitations are applied as compared with the bimorph bender. In Figs. 3(a) and 3(b),  $q_{\text{triple}}$  and  $v_{\text{triple}}$  are plotted against the variation of the thickness ratio  $B$  for a series of triple layer benders. It is found that if a stiff elastic layer (such as silicon) is used, the electrical charge generated increases with the thickness ratio  $B$  initially, reaches a maximum value and then decreases with the  $B$  value. However, if a less stiff elastic layer (such as aluminum) is used, the charge generated monotonically increases with the  $B$  value. When  $B$  becomes very large, the normalized charge parameter approaches a limiting value of  $2/A$ . The electrical voltage generated always decreases with the  $B$  values. Therefore, the voltage sensitivity of a triple layer bender is always lower than that of a bimorph bender if the dimensions are the same.

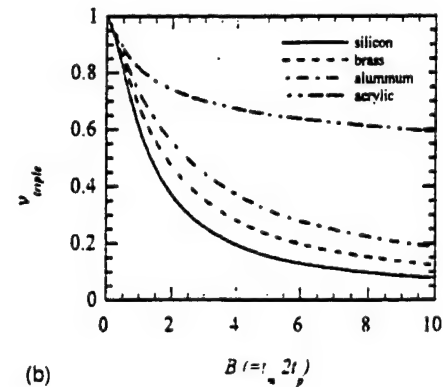
(2) If the piezoelectric layer thickness  $t_p$  is a constant whereas the center elastic layer is variable, from Eqs. (31) and (32) we can define two nondimensional charge and voltage parameters

$$q'_{\text{triple}} = \frac{(2B+1)}{AB^3+3B^2+3B+1}, \quad (39)$$

$$v'_{\text{triple}} = \frac{(2B+1)}{4(1-k_{31}^2)(AB^3+3B^2+3B-1)+3k_{31}^2(2B+1)^2}. \quad (40)$$



(a)



(b)

FIG. 3. (a) Normalized electrical charge as a function of the thickness ratio for different triple layer benders; (b) normalized electrical voltage as a function of the thickness ratio for different triple layer benders. (Here the total thickness of the triple layer bender is fixed.)

The variations of  $q'_{\text{triple}}$  and  $v'_{\text{triple}}$  with the thickness ratio  $B$  for different  $A$  values are plotted in Figs. 4(a) and 4(b). Both  $q'_{\text{triple}}$  and  $v'_{\text{triple}}$  decrease as the thickness ratio  $B$  increases.

(3) In some cases, the center elastic layer (substrate) thickness  $t_m$  is fixed, while the piezoelectric layer thickness is variable. The dependence of the generative charge and voltage of the triple layer bender on the thickness ratio and the Young's modulus ratio can be obtained by substituting  $t_p = t_m/2B$  into Eqs. (31) and (32),

$$Q = \frac{3d_{31}L^2}{8t_m^2} \frac{4B^2(2B+1)}{AB^3+3B^2+3B+1} F, \quad (41)$$

$$V = \frac{3d_{31}L}{\epsilon_{33}^X w t_m} \times \frac{2B(2B-1)}{4(1-k_{31}^2)(AB^3+3B^2+3B-1)+3k_{31}^2(2B+1)^2} F. \quad (42)$$

Similarly, we can define the following two nondimensional parameters:

$$q''_{\text{triple}} = \frac{4B^2(2B+1)}{AB^3+3B^2+3B+1}, \quad (43)$$

and

$$v''_{\text{triple}} = \frac{2B(2B-1)}{4(1-k_{31}^2)(AB^3+3B^2+3B-1)+3k_{31}^2(2B+1)^2}. \quad (44)$$

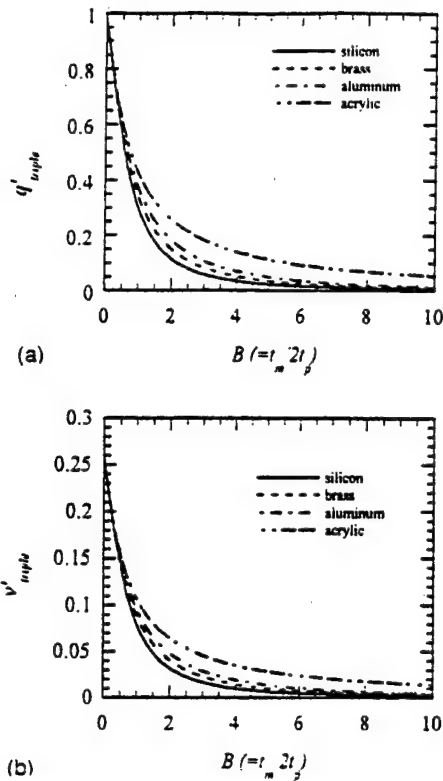


FIG. 4. (a) Nondimensional electrical charge parameter  $q'_{\text{triple}}$  as a function of the thickness ratio for different triple layer benders; (b) nondimensional electrical voltage parameter  $v'_{\text{triple}}$  as a function of the thickness ratio for different triple layer benders. (Here the piezoelectric layer thickness  $t_p$  is fixed.)

$q'_{\text{triple}}$  and  $v'_{\text{triple}}$  are plotted as functions of the thickness ratio for a series of triple layer benders, as is shown in Figs. 5(a) and 5(b). It is found that the charge parameter  $q'_{\text{triple}}$  increases with  $B$  very fast initially and then gradually becomes saturated when  $B$  becomes very large. In addition, a maximum voltage sensitivity can be obtained by adjusting the piezoelectric layer thickness. This is clear if we consider two limiting cases. (i) When the  $B$  value approaches zero, i.e., very thick piezoelectric layers are used in the triple layer bender, it becomes difficult to bend the device, and the deformation of piezoelectric layer will be very small. Therefore, the electric voltage generated will approach zero. (ii) When the  $B$  value becomes infinitely large, which means the piezoelectric layer thickness is infinitely thin, the capacitance of the piezoelectric layers will be infinitely large. Since the charges generated on the piezoelectric layers approach a certain value ( $8/A$ ) when  $B \rightarrow \infty$  [Eq. (43)], the voltage generated will then approach zero. Therefore, a maximum generated voltage can be observed between the two limiting cases. By a comparison of the different triple layer benders, it is observed that use of a less stiff elastic layer always leads to a higher charge or voltage sensitivity, since more bending deformation occurs in the piezoelectric layers for a given mechanical excitation.

#### IV. SENSOR PERFORMANCE ANALYSIS OF CANTILEVER UNIMORPH BENDERS

The actuation performance of a unimorph bender has been analyzed by Steel *et al.*<sup>11</sup> Later, the constitutive equa-

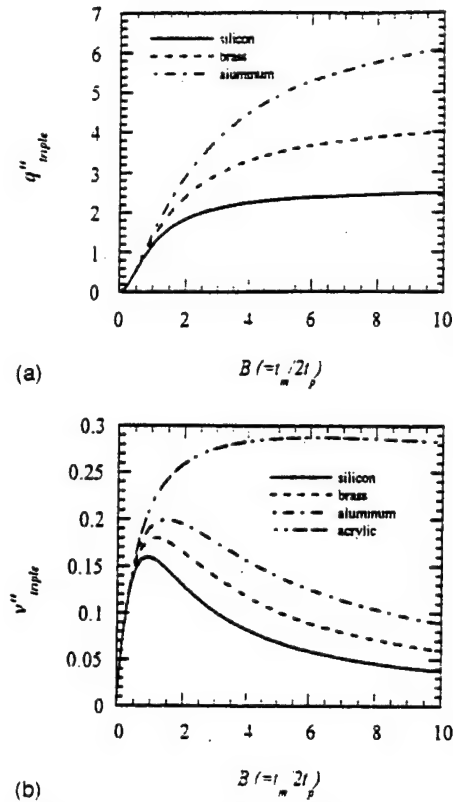


FIG. 5. (a) Nondimensional electrical charge parameter  $q''_{\text{triple}}$  as a function of the thickness ratio for different triple layer benders; (b) nondimensional electrical voltage parameter  $v''_{\text{triple}}$  as a function of the thickness ratio for different triple layer benders. (Here the center elastic thickness  $t_m$  of the triple layer bender is fixed.)

tions for a cantilever mounted unimorph have been derived by Smits and Choi,<sup>12</sup> and they describe the behavior of the unimorph under static conditions. If an external moment  $M$ , an external force  $F$ , a uniformly distributed load  $p$ , and an electric voltage  $V$  are applied to the unimorph, then the generated electrical charge can be expressed by the following equation:

$$Q = \frac{6d_{31}s_{11}^m s_{11}^p t_m(t_m + t_p)L}{K} M + \frac{3d_{31}s_{11}^m s_{11}^p t_m(t_m + t_p)L^2}{K} F + \frac{d_{31}s_{11}^m s_{11}^p t_m(t_m + t_p)L^3 w}{K} p + \frac{Lw}{t_p} \left( \epsilon_{33}^x - \frac{d_{31}^2 t_m (s_{11}^m t_p^3 + s_{11}^p t_m^3)}{K} \right) V, \quad (45)$$

where

$$K = (s_{11}^m)^2 (t_p)^4 + 4s_{11}^m s_{11}^p t_m(t_p)^3 + 6s_{11}^m s_{11}^p (t_m)^2 (t_p)^2 + 4s_{11}^m s_{11}^p t_p(t_m)^3 + (s_{11}^p)^2 (t_m)^4, \quad (46)$$

$s_{11}^m$  and  $s_{11}^p$  are elastic compliances of the elastic layer and the piezoelectric layer;  $t_m$  and  $t_p$  are the thickness of the elastic layer and the piezoelectric layer; and  $L$  and  $w$  are the length and width of the unimorph bender. The bonding layer thickness is usually very thin and its effect is ignored.

TABLE II. Materials properties used in the calculations.

Materials	$d_{31}$ (m/V)	Young's modulus (N/m <sup>2</sup> )	$A$ ( $=E_m/E_p$ )
Soft PZT ceramic	$320 \times 10^{-12}$	$6.2 \times 10^{10}$	...
Silicon	...	$19 \times 10^{10}$	3.05
Brass	...	$11 \times 10^{10}$	1.77
Aluminum	...	$6.5 \times 10^{10}$	1.05
Acrylic	...	$0.31 \times 10^{10}$	0.05

Similarly, for analyzing the effect of the elastic layer on the sensing performance of the unimorph bender, we define

$$A = \frac{s_{11}^p}{s_{11}^m} = \frac{E_m}{E_p}, \quad B = \frac{t_m}{t_p}, \quad (47)$$

and Eq. (45) can be rewritten as

$$Q = \frac{6d_{31}L}{t_p^2} \frac{AB(B+1)}{1+4AB+6AB^2+4AB^3+A^2B^4} M - \frac{3d_{31}L^2}{t_p^2} \frac{AB(B-1)}{1+4AB+6AB^2+4AB^3+A^2B^4} F - \frac{d_{31}L^3w}{t_p^2} \frac{AB(B-1)}{1+4AB+6AB^2+4AB^3+A^2B^4} P - \frac{Lw\epsilon_{33}^x}{t_p} \left( 1 - k_{31}^2 \frac{AB(1+AB^3)}{1+4AB+6AB^2+4AB^3+A^2B^4} \right) V. \quad (48)$$

The capacitance of the unimorph bender is

$$C = \frac{Lw\epsilon_{33}^x}{t_p} \left( 1 - k_{31}^2 \frac{AB(1+AB^3)}{1+4AB+6AB^2+4AB^3+A^2B^4} \right). \quad (49)$$

Therefore, the dielectric constant of piezoelectric layer in the unimorph bender becomes

$$\epsilon_u = \epsilon_{33}^x \left( 1 - k_{31}^2 \frac{AB(1+AB^3)}{1+4AB+6AB^2+4AB^3+A^2B^4} \right), \quad (50)$$

which is a function of the thickness ratio  $B$  and the Young's modulus ratio  $A$  of the elastic layer and the piezoelectric layers. Obviously, the dielectric constant of a unimorph bender is lower than the free dielectric constant of the piezoelectric materials because of the constraint of the elastic layer on the vibration of the piezoelectric layer.

To visualize the effect of the elastic layer on the dielectric constant of the unimorph bender, we can define

$$\zeta = 1 - k_{31}^2 \frac{AB(1+AB^3)}{1+4AB+6AB^2+4AB^3+A^2B^4}, \quad (51)$$

and plot  $\zeta$  against the thickness ratio  $B$  for a series of unimorphs made up of silicon, brass, aluminum, and acrylic layers with a soft PZT ceramic layer, as shown in Fig. 2(b). The calculated result for the cantilever RAINBOW bender is also included using the Young's modulus ratio of 0.85.<sup>13</sup> Obviously, the unimorph bender has a lower dielectric con-

stant than its free ceramic counterpart. The use of a stiffer elastic layer leads to larger decreases in the dielectric constant because the stiffer elastic layer can more effectively clamp the piezoelectric ceramic layer.

The clamping effect of the elastic layer on the dielectric property of piezoelectric materials in either a unimorph (monomorph) or a triple layer bender configuration is important in device design and performance evaluation. In recent years, PZT thin/thick films have been studied for microactuator and microsensor applications.<sup>14-19</sup> The above results are useful in considering the dielectric properties of thin/thick film PZT materials. Thin film PZTs usually have a lower dielectric constant than bulk ceramics with the same composition, which is often attributed to the grain size effect.<sup>20</sup> The size effect significantly affects the dielectric property of the PZT film. However, the clamping effect of the substrate on the piezoelectric film should also be taken into account. Thin/thick film PZTs are usually deposited on platinized silicon substrates. After deposition, the substrate is etched (by dry or wet etching techniques<sup>21,22</sup>) to a certain thickness. If the thickness ratio of the silicon layer and the PZT film is about 1:1 in a cantilever unimorph bender, a 5% reduction in dielectric constant can be expected. If the thickness is 5:1, the dielectric constant of the PZT layer will be decreased to about 80% of its free value due to the clamping effect of the silicon substrate, as shown in Fig. 2(b).

When only an external moment  $M$  is applied on the unimorph bender, the electric charge generated is

$$Q = \frac{6d_{31}L}{t_p^2} \frac{AB(B-1)}{1+4AB+6AB^2+4AB^3+A^2B^4} M, \quad (52)$$

and the electric voltage under the open circuit condition is

$$V = \frac{Q}{C} = \frac{6d_{31}}{\epsilon_{33}^x w t_p} \times \frac{AB(B+1)}{1+4AB+6AB^2+4AB^3+A^2B^4 - k_{31}^2 AB(1+AB^3)} M. \quad (53)$$

Similarly, when only an external tip force is acting on the tip of the unimorph bender, the electric charge generated on the unimorph becomes

$$Q = \frac{3d_{31}L^2}{t_p^2} \frac{AB(B+1)}{1+4AB+6AB^2+4AB^3+A^2B^4} F, \quad (54)$$

and the open circuit electric voltage produced due to the applied external tip force is

$$V = \frac{3d_{31}L}{\epsilon_{33}^x w t_p} \times \frac{AB(B+1)}{1-4AB+6AB^2+4AB^3+A^2B^4 - k_{31}^2 AB(1+AB^3)} F. \quad (55)$$

The generated open circuit electric voltage of a unimorph bender can also be related to the tip displacement by Eqs. (12) and (55). The flexural rigidity of a unimorph bender is given by<sup>10</sup>

$$E_p I_z = \frac{E_p w t_p^3}{12} \left( \frac{1 + 4AB + 6AB^2 + 4AB^3 + A^2B^4}{AB - 1} \right). \quad (56)$$

Substitution of Eqs. (12) and (56) into Eq. (55) leads to

$$V = \frac{3d_{31}t_p^2}{4\varepsilon_{33}^X D_{11} L^2} \frac{AB(B+1)}{R - k_{31}^2 AB(1+AB^3)} \frac{R}{AB+1} \delta, \quad (57)$$

where  $R = 1 + 4AB + 6AB^2 + 4AB^3 + A^2B^4$ . By measuring the electric voltage generated on the unimorph bender, the tip displacement can be obtained from the above equation.

When only an external load  $p$  is applied, the electric charge generated and the open circuit electric voltage in the unimorph are

$$Q = \frac{d_{31}L^3 w}{t_p^2} \frac{AB(B+1)}{1 + 4AB + 6AB^2 + 4AB^3 + A^2B^4} p, \quad (58)$$

$$V = \frac{d_{31}L^2}{\varepsilon_{33}^X t_p} \times \frac{AB(B-1)}{1 - 4AB + 6AB^2 + 4AB^3 - A^2B^4 - k_{31}^2 AB(1+AB^3)} p. \quad (59)$$

Therefore, to achieve high sensitivity, materials with high  $d_{31}/\varepsilon_{33}^X$  and high  $k_{31}$  should be used to fabricate unimorph benders. Following a similar procedure in discussing the triple layer bender to further clarify the sensing effect of unimorph benders to external excitations, the relationships between the electric signals generated and the physical properties of the unimorph bender are discussed in the following three cases.

(1) We can compare the electric charge generated and the electric voltage of unimorphs with a bimorph bender with the same geometrical dimensions. If the total thickness of the unimorph bender is  $t$ , i.e.,  $t_m + t_p = t$ . Since  $t_m/t_p = B$ , then  $t_p = t/(B+1)$ . Substituting  $t_p = t/(B+1)$  into Eqs. (54) and (55), we can define

$$q_{\text{uni}} = \frac{2AB(B+1)^3}{1 - 4AB + 6AB^2 + 4AB^3 + A^2B^4}, \quad (60)$$

$$v_{\text{uni}} = \frac{2AB(B+1)^2(1 - k_{31}^2/4)}{1 - 4AB + 6AB^2 + 4AB^3 + A^2B^4 - k_{31}^2 AB(1+AB^3)}, \quad (61)$$

where  $q_{\text{uni}}$  and  $v_{\text{uni}}$  are the ratios of the electric charge and voltage generated by the unimorph and bimorph benders. In Figs. 6(a) and 6(b),  $q_{\text{uni}}$  and  $v_{\text{uni}}$  are plotted against the thickness ratio  $B$  for a series of unimorph benders, including the cantilever RAINBOW device. It is found that if a stiff elastic layer (such as silicon) is used, the  $q_{\text{uni}}$  value increases with the thickness ratio  $B$  initially, reaches a maximum value and then decreases with the  $B$  value. However, if a less stiff elastic layer (such as aluminum) is used, the  $q_{\text{uni}}$  value

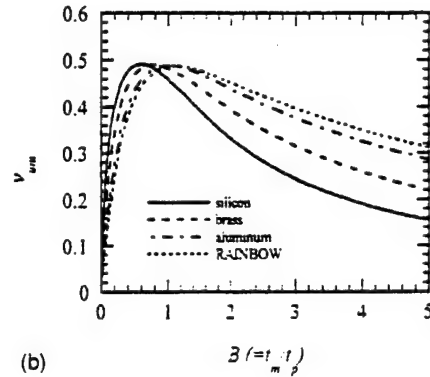
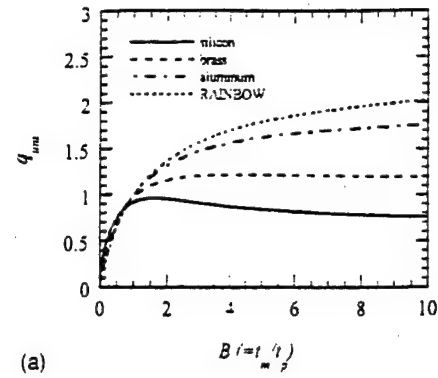


FIG. 6. (a) Nondimensional charge parameter  $q_{\text{uni}}$  plotted against the thickness ratio for different unimorph benders; (b) nondimensional voltage parameter  $v_{\text{uni}}$  plotted against the thickness ratio for different unimorph benders. (Here the total thickness of the unimorph bender is fixed.)

monotonically increases with the  $B$  value. When  $B$  becomes very large, the  $q_{\text{uni}}$  value approaches a limiting value of  $2/A$ .

From Fig. 6(b), a maximum charge parameter  $v_{\text{uni}}$  can be obtained for a unimorph bender at a suitable thickness ratio. This result is clear if we consider two limiting cases. (i) When the  $B \rightarrow 0$ , the structure becomes a single cantilever piezoelectric beam. If external mechanical excitations are applied, one half of the bender is subjected to tensile stress and the other half is subjected to compressive stress. Since the polarization of the piezoelectric plate is in the thickness direction from the bottom surface pointing toward the top surface, the same electric charge will be produced on the top surface and on the bottom surface. Therefore, the electric charge generated and the voltage become zero. (ii) When  $B \rightarrow \infty$ , the thickness of the piezoelectric layer is very small, hence its capacitance becomes very large. Since the electric charge generated approaches  $2/A$ , the electric voltage generated ( $V = Q/C$ ) approaches zero. Therefore, a maximum voltage sensitivity can be expected between these two limiting cases. The thickness ratio  $B$  for the maximum voltage sensitivity decreases as the Young's modulus ratio increases.

It has been demonstrated that for a cantilever mounted *unimorph actuator*, the maximum generative tip deflection and blocking force are half the value of that for a *bimorph actuator* if they have the same geometrical dimensions and are driven under the same magnitude of electric field.<sup>10</sup> The thickness ratio for the maximum generative tip deflection and blocking force is related to the Young's modulus ratio by a simple equation,



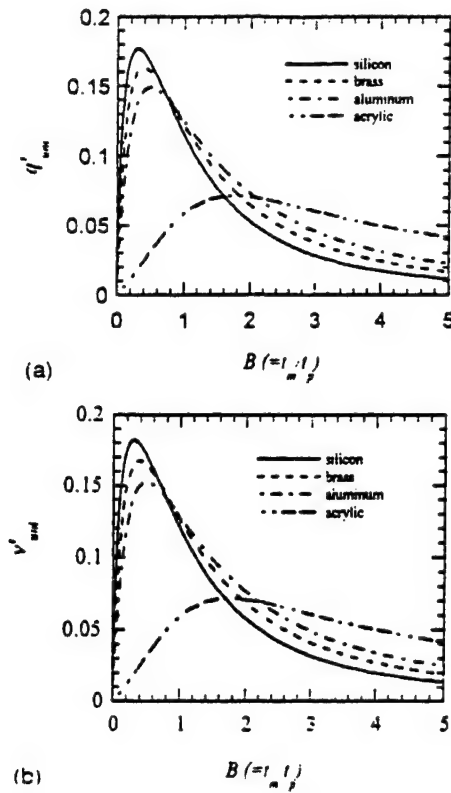


FIG. 7. (a) Nondimensional charge parameter  $q'_{uni}$  plotted against the thickness ratio for different unimorph benders; (b) nondimensional voltage parameter  $v'_{uni}$  plotted against the thickness ratio for different unimorph benders. (Here the thickness of the piezoelectric layer  $t_p$  is fixed.)

$$B_{max} = \sqrt{\frac{1}{A}}. \quad (62)$$

Here it is interesting to find that as a sensory element the maximum voltage sensitivity of the unimorph is close to but less than half the value of the bimorph bender. The thickness ratio  $B$  for maximum voltage sensitivity is very close to but higher than  $\sqrt{1/A}$ . The difference is very small and is negligible.

(2) If the piezoelectric layer thickness is fixed, while the elastic layer thickness is variable, in order to visualize the variation of the electric charge generated and the voltage with the thickness ratio  $B$  and the Young's modulus ratio  $A$  in the unimorph benders, we may define

$$q'_{uni} = \frac{AB(B+1)}{1+4AB+6AB^2+4AB^3+A^2B^4}. \quad (63)$$

$$v'_{uni} = \frac{AB(B+1)}{1+4AB+6AB^2+4AB^3+A^2B^4-k_{31}^2AB(1+AB^3)}. \quad (64)$$

In Fig. 7,  $q'_{uni}$  and  $v'_{uni}$  are plotted against the  $B$  values for a series of unimorph benders. Similarly, by choosing a suitable thickness ratio, a maximum sensitivity can be obtained. This result becomes clear by considering two extreme cases: (i) when  $B \rightarrow 0$ , the electric charge generated and the voltage will approach to zero, as discussed above for a single piezoelectric plate; (ii) when  $B \rightarrow \infty$ , i.e., a very thick elastic layer is used, it becomes difficult to bend the unimorph

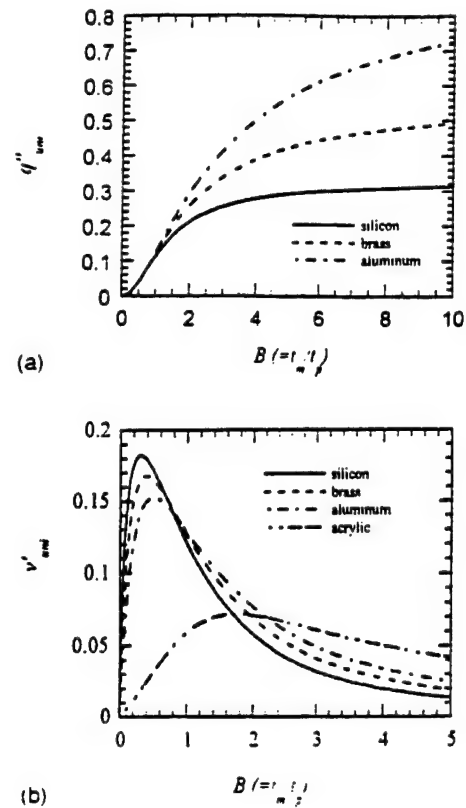


FIG. 8. (a) Nondimensional charge parameter  $q''_{uni}$  is plotted against the thickness ratio for different unimorph benders; (b) nondimensional voltage parameter  $v''_{uni}$  is plotted against the thickness ratio for different unimorph benders. (Here, the thickness of the elastic layer  $t_m$  is fixed.)

bender, and the deformation of the piezoelectric layer is therefore very small. The electric charge generated and the voltage will again approach zero. Therefore, a maximum generated voltage can be observed between the limiting cases. Also, it is seen that for a given piezoelectric layer thickness,  $t_p$ , the use of a stiffer elastic layer (such as silicon) can increase the maximum sensitivity ( $V/M$ ,  $V/F$ , or  $V/p$ ), and the thickness ratio  $B$  for the maximum sensitivity shifts to a lower value as  $A$  increases. The  $B$  values for maximum sensitivity are 0.29, 0.375, 0.5, 1.75, respectively, if silicon, brass, aluminum and acrylic are used as the elastic layers.

(3) In some cases such as in piezoelectric materials based on microelectromechanical system (MEMS) device fabrication, the elastic layer (substrate) thickness is fixed, while the piezoelectric layer is deposited (or bonded) to the substrate. The thickness of piezoelectric layer can vary. In these cases, substituting  $t_p = t_m/B$  into Eqs. (21) and (22), we may define

$$q''_{uni} = \frac{AB^3(B+1)}{1+4AB+6AB^2+4AB^3+A^2B^4}. \quad (65)$$

$$v''_{uni} = \frac{AB^2(B+1)}{1+4AB+6AB^2+4AB^3+A^2B^4-k_{31}^2AB(1+AB^3)}. \quad (66)$$

$q''_{uni}$  and  $v''_{uni}$  are plotted in Figs. 8(a) and 8(b) as functions of the thickness ratio for a series of unimorphs. The electric charge increases with the  $B$  values, and a maximum electric

voltage is found at a suitable thickness ratio. The use of a less stiff elastic layer leads to high sensitivity. The  $B$  values for maximum voltage sensitivity are 1.32, 1.68, and 2.1, respectively, if silicon, brass, and aluminum are used as the elastic layers.

## V. SUMMARY

The sensing effects of three piezoelectric cantilever benders subjected to various external mechanical excitations have been analyzed in this article based on their constitutive equations. The following conclusions are obtained.

- (1) Bimorph, unimorph, and triple layer benders have lower dielectric constants than the piezoelectric material itself due to the clamping effect of each component in these devices. For unimorph and triple layer benders, their dielectric constants also vary with the thickness ratio of the elastic and the piezoelectric layers. A maximum dielectric constant can be observed at certain thickness ratios for the triple layer bender, while for the unimorph bender, dielectric constant decreases with the thickness ratio monotonically. The use of a stiffer elastic layer leads to lower dielectric constant in both unimorph and triple layer benders.
- (2) A figure of merit is defined for the selection of piezoelectric materials for bending mode sensor design: materials with high  $d_{31}/\epsilon_{33}^X$  and high  $k_{31}$  are preferred for sensor design and fabrication.
- (3) Theoretical calculations demonstrate that the bimorph bender has the highest voltage sensitivity compared with unimorph and triple layer benders with the same geometrical dimensions. For the triple layer bender, voltage sensitivity decreases as the thickness ratio increases. For the unimorph bender, a maximum voltage sensitivity, close to half the value of a bimorph can be obtained at a thickness ratio of about  $\sqrt{1/A}$  [Figs. 3(b) and 6(b)].
- (4) With the piezoelectric layer thickness fixed, the voltage sensitivity of the triple layer bender decreases with the thickness ratio, while a maximum voltage sensitivity can be obtained at a certain thickness ratio [Figs. 4(b) and 7(b)].

- (5) With the substrate thickness fixed, maximum voltage sensitivities can be achieved by choosing a suitable thickness ratio for both the triple layer and unimorph benders [Figs. 5(b) and 8(b)].
- (6) The variation of charge sensitivities with the thickness ratio and the Young's modulus ratio of the elastic layer and the piezoelectric layer for both unimorph and triple layer benders at different conditions (constant  $t$ , constant  $t_m$  and constant  $t_p$ ) have also been compared and discussed.

- <sup>1</sup>J. M. Herbert, *Ferroelectric Transducers and Sensors* (Gordon and Breach Science, New York, 1982).
- <sup>2</sup>K. Uchino, *Ferroelectrics* **91**, 281 (1989).
- <sup>3</sup>K. Uchino, *Piezoelectric Actuator and Ultrasonic Motors* (Kluwer Academic, Boston, MA, 1996).
- <sup>4</sup>G. H. Haertling, *Am. Ceram. Soc. Bull.* **73**, 93 (1994).
- <sup>5</sup>G. H. Haertling, *Ferroelectrics* **154**, 101 (1994).
- <sup>6</sup>J. G. Smits, S. I. Dalke, and T. K. Cooney, *Sens. Actuators A* **28**, 41 (1991).
- <sup>7</sup>R. J. Roark and W. C. Young, *Formulas for Stress and Strain*, 5th ed. (McGraw-Hill, New York, 1975), pp. 113–115.
- <sup>8</sup>J. M. Gere and S. P. Timoshenko, *Mechanics of Materials*, 3rd ed. (PWS-Kent, Boston, MA, 1990), pp. 301–308.
- <sup>9</sup>Q.-M. Wang, and L. E. Cross, *IEEE Trans. Ultrason. Ferroelectr. Freq. Control* (submitted).
- <sup>10</sup>Q.-M. Wang, and L. E. Cross, *Ferroelectrics* (to be published).
- <sup>11</sup>M. R. Steel, F. Harrison, and P. G. Harper, *J. Phys. D* **11**, 979 (1978).
- <sup>12</sup>J. G. Smits and W.-s. Choi, *IEEE Trans. Ultrason. Ferroelectr. Freq. Control* **38**, 256 (1991).
- <sup>13</sup>Q.-M. Wang and L. E. Cross, *J. Appl. Phys.* **83**, 5358 (1998).
- <sup>14</sup>O. Yoko, M. Miyauchi, T. Tsurumi, and M. Daimon, *Jpn. J. Appl. Phys., Part 1* **32**, 4095 (1993).
- <sup>15</sup>M. Okuyama, *Bull. Ceram. Soc. Jpn.* **30**, 504 (1995).
- <sup>16</sup>M. Sakata, *Bull. Ceram. Soc. Jpn.* **31**, 927 (1996).
- <sup>17</sup>M. Sayer, *Proceedings of the IEEE Ultrasonics Symposium 1991*, 8–11 December, 1991, Orlando, FL, pp. 595–603.
- <sup>18</sup>W. P. Robbins, D. L. Polla, T. Tamagawa, D. E. Glumac, and W. Tjhen, *J. Micromech. Microeng.* **1**, 247 (1991).
- <sup>19</sup>R. E. Newnham, K. R. Udayakumar, and S. Trolier-McKinstry, in *Chemical Processing of Advanced Materials*, edited by L. L. Hench and J. K. West (Wiley, New York, 1992), p. 379.
- <sup>20</sup>D. L. Polla and L. F. Francis, *MRS Bull.* **21**, 59 (July 1996).
- <sup>21</sup>Lj. Ristic, H. Hughes, and F. Shemansky, in *Sensor Technology and Devices*, edited by Lj. Ristic (Artech House, Boston, 1994), Chap. 3.
- <sup>22</sup>E. W. Becker, W. Ehrfeld, P. Hagmann, A. Maner, and D. Mynchmeyer, *Microelectron. Eng.* **4**, 35 (1986).



# **APPENDIX 34**

# Tailoring the performance of ceramic–metal piezocomposite actuators, ‘cymbals’

J.F. Fernández \*, A. Dogan, J.T. Fielding, K. Uchino, R.E. Newnham

*International Center for Actuators and Transducers, Materials Research Laboratory, The Pennsylvania State University, University Park, PA 16802, USA*

Received 21 January 1997; accepted 19 August 1997

## Abstract

A unique design of metal–ceramic actuators exhibits very high displacement and large generative forces. This new metal–ceramic composite actuator design, the ‘cymbal’, consists of a piezoelectric disk sandwiched between two truncated conical metal endcaps. The radial motion of the piezoelectric ceramic is converted into flextensional and rotational motions in the metal endcap. Based on previous studies of ceramic–metal composites, a simplified model has been developed to evaluate the properties of cymbals and to aid in materials selection. The influence of the stiffness of the metal, the piezoelectric coefficients of the ceramics and the characteristics of the epoxy bond on actuator performance have been evaluated. It is found that the higher the transverse piezoelectric coefficient, the higher the displacement of the actuator. The stiffness of the metal reduces the displacement but allows the composite to support higher loads. There is a thermally induced displacement of the piezocomposite with the temperature that is related to the thermal expansion mismatch between the metal endcaps and the ceramic. By selecting appropriate materials, it is possible to avoid this thermally induced displacement. Very low or negligible temperature dependence of the displacement is attained by using PZT ceramics with temperature-independent properties together with metal caps having higher Young’s modulus and lower thermal expansion coefficients than the ceramics. © 1998 Elsevier Science S.A.

**Keywords:** Ceramic–metal actuators; Piezocomposites

## 1. Introduction

In recent years, piezoelectric and electrostrictive ceramics have been used in actuator applications such as displacement transducers, pressure sensors, shape controllers and precision micropositioners. When an electrical field is applied parallel to the polarization direction in a piezoelectric ceramic, an expansion takes place in the longitudinal direction accompanied by a contraction shrinkage in the transverse direction. There are two transducer designs which use these effects to enhance the displacement: multilayer ceramic actuators and bimorph actuators. The advantages of multilayer actuators are their large generative force and fast response, but the small displacements and high capacitance of multilayer actuators make them impractical for some applications. On the other hand, bimorph actuators show large displacements but only small generative forces. There is a need for reliable actuators with intermediate-level displacements and generative forces.

A new type of metal–ceramic composite actuator, which is based on the concept of a flextensional transducer, has been reported [1,2]. In this composite the PZT ceramic is sandwiched between two metallic endcaps with shallow cavities, giving a 2(0)–2–2(0) connectivity [3]. Since the shallow cavities have a moon shape, these composites have been called ‘moonies’. The radial motion of the piezoelectric ceramic is converted into a flextensional motion in the metal endcaps, giving a large displacement at the center of the cap in the direction perpendicular to the ceramic disk.

Due to the large difference in the thermal expansion coefficient between the metal (typically brass,  $20 \times 10^{-6} \text{ } ^\circ\text{C}^{-1}$ ) and the ceramic (lead zirconate titanate, PZT,  $6 \times 10^{-6} \text{ } ^\circ\text{C}^{-1}$ ) substantial thermally generated stress is produced in the composite during the cooling process when silver paste bonding is used. If no stress relaxation occurs below the glass softening temperature, typically  $400^\circ\text{C}$ , thermally induced compressive stresses are generated in the PZT, while tensile stresses are generated in the endcaps [4,5]. These prestresses help to maintain the PZT polarization during exposure to high hydrostatic pressure, which is required for hydrophone applications. However, this tensile stress concentration can easily

\* Corresponding author. Electroceramic Department, Instituto de Cerámica y Vidrio, CSIC, 28500 Arganda del Rey, Madrid, Spain. Tel.: +34 1 871 18 00. Fax: +34 1 870 05 50. E-mail: jfernandez@icv.csic.es

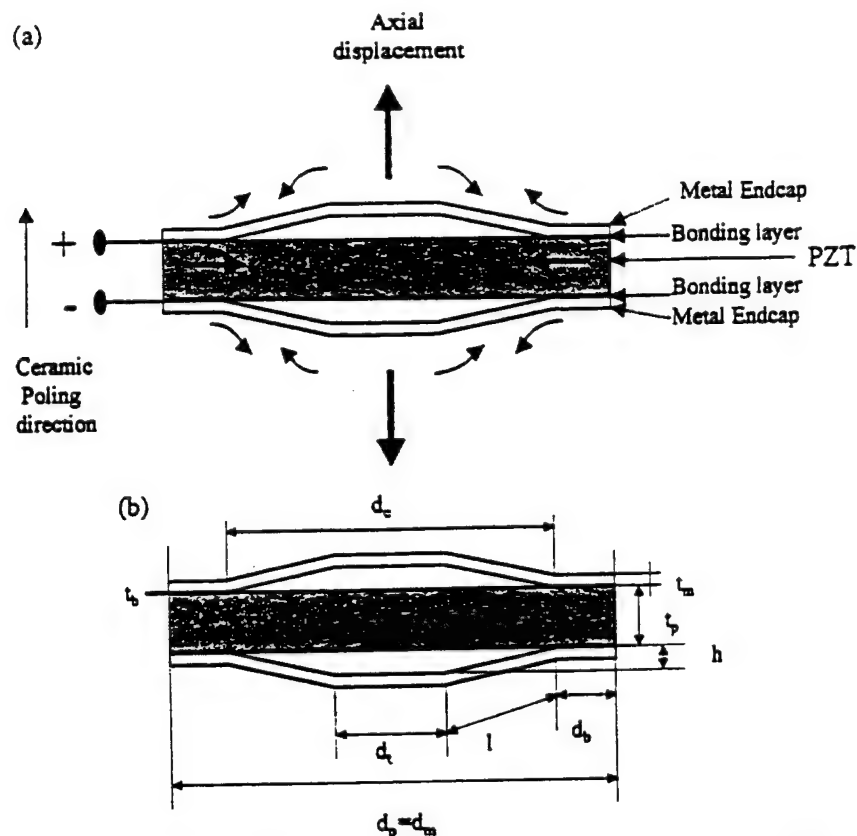


Fig. 1. (a) Geometry of the ceramic-metal composite actuator 'cymbal'. The solid arrows describe the displacement directions when the cymbal is driven by a field parallel to the poling direction of the ceramic. (b) Dimensions: endcap diameter  $d_m = 12.7$  mm; PZT diameter  $d_p = 12.7$  mm; cavity diameter  $d_c = 8.7$ ; endcap top part diameter  $d_t = 0.34$  mm; cavity depth  $h = 0.27$  mm; metal cap thickness  $t_m = 0.27$  mm; PZT thickness  $t_p = 1.0$  mm; bonding-layer thickness  $t_b = 0.01$  mm.

damage the outer edge of the PZT. The dimensional change produced during the poling process of the PZT increases this tensile stress concentration, reaching values close to the fracture strength of the ceramic.

As actuators, metal-ceramic composites need to achieve higher displacement and reduce the stress concentration in order to attain higher generative force and reliability. It was found that the introduction of a ring-shaped groove on the endcaps markedly enhanced the actuator displacement [6]. At the same time, assembly techniques using room-temperature-cured epoxies with prepoled ceramic were successfully developed. However, because the polymers have a low melting point, the epoxy bonding method is only useful for low-temperature applications. In addition, the temperature characteristics of the moonie are related to those of the ceramic elements [5]. The thermal expansion coefficient mismatch between the metal and the ceramic is the origin of a thermally induced displacement.

New metal-ceramic actuator designs using truncated conical metal endcaps, called 'cymbals' [3,6–9], Fig. 1, have demonstrated higher displacements, effective piezoelectric coefficients, generative forces, hydrophone characteristics and acceleration sensitivity. In cymbal actuators the radial motion of the piezoelectric ceramic is converted into flextensional and rotational motions in the metal endcap. By com-

parison with other high-displacement actuators, such as 'rainbows' [10], one of the big advantages of cymbal actuators is related to their composite nature, and thus to the ability of tailoring properties by adequate selection of the material properties.

In this paper a simplified calculation was used to aid in materials selection in order to understand the basic motion in cymbals-type actuators, and to evaluate the actuator properties of cymbals. The temperature dependence of the new metal-ceramic cymbal actuator design was also investigated.

## 2. Model

A simplified model of the cymbal was developed to help focus the research on the choice of materials. By optical microscopy examination of the polished cross sections of the punched brass cymbal endcaps, the existence of a curvature near the bonded region of the endcap was observed. This curvature leads to an undefined bonding area along with low load tolerance and low strength. It also causes the epoxy to leak into the cavity, creating spurious resonant peaks in the frequency response. Partial filling of the cavity also reduces the actuator displacement and leads to irreproducible results.

In order to avoid such problems, it is necessary to have a very good definition of the bonding area ring,  $d_b$ , of the metal

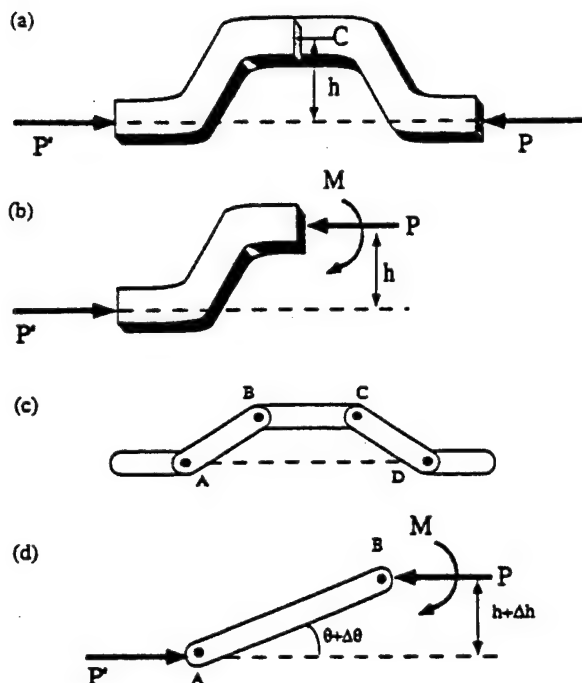


Fig. 2. Schematic view of the load applied in different approaches to the cymbal case. (a) Two force member is loaded axially, but eccentrically. (b) Portion of (a) showing that the internal forces in a given section must be equivalent to a force  $P$  applied at the centroid of the section  $C$ . (c) Ideal cymbal endcap formed with segments connected by pins. (d) Forces involved in segment  $AB$  of (c).

endcap, and at the same time to reduce as much as possible the deformation of metal that forms the cavity.

When the composite is driven electrically in the transverse direction, the piezoceramic disk shrinkage and therefore the endcaps are loaded eccentrically. Fig. 2 shows a schematic section of the circular endcap. The distribution of forces, and thus the corresponding stress distribution, cannot be uniform in the top part of the cavity. From the conditions of equilibrium of the portion of endcap shown in Fig. 2(b) it is found that the internal forces in the given section must be equivalent to a force  $P$  applied at the centroid of the section and a couple  $M$  of moment  $M = Ph$  [11], where  $h$  corresponds to the cavity depth. As a result, rotation or flexure or both will be produced, depending on the Young's modulus of the metal used and the geometry of the design.

Consider the structure shown in Fig. 2(c), in which the segments are pin connected. In that case, and if the structure is axially unloaded, the motion is purely rotational without mechanical loss. When the PZT is electrically driven by a field parallel to the polarization direction, the longitudinal shrinkage is transferred to the metal endcaps by the bonding. Compressive stresses are generated in the PZT while tensile stresses are generated in the endcaps. The bonding materials must be able to endure such stresses exerted in opposite directions, otherwise microcracks may form and debonding will occur. By increasing the bonding area it is possible to define a threshold area that prevents debonding. The highest efficiency in stress transfer is attained when the bonding area is

just large enough for the part of the endcap that forms the cavity to follow the shrinkage of the ceramic inside the cavity. However, if the bonding area is too much larger than the bonding-area threshold, a very high stress concentration will occur in the bonding area due to the piezoelectric shrinkage.

In order to simplify the calculations as much as possible, in a two-dimensional model it is helpful to consider the following approaches:

(a) The endcap motion is purely rotational, such that mechanical losses are not included, and the endcaps are rigid and free to rotate at the change points in topology.

(b) The transverse shrinkage of the ceramic,  $\Delta d_c$ , is completely compensated by a longitudinal displacement of the endcaps.

The total displacement is the sum of the longitudinal expansion of the ceramic plus the change of the cavity depth due to transverse shrinkage:

$$d = 2\Delta h + \Delta h_c \quad (1)$$

In this expression,  $\Delta h$  is the change in cavity depth and  $\Delta h_c$  is the longitudinal expansion of the ceramic under applied electrical field,  $E$ :

$$\Delta h_c = d_{33} E t_p \quad (2)$$

where  $d_{33}$  is the longitudinal piezoelectric coefficient and  $t_p$  is the thickness of the ceramic disk. The cavity depth change can be calculated from the expression

$$h + \Delta h = \{l^2 - [(d_c + \Delta d_c - d_i)/2]^2\}^{1/2} \quad (3)$$

where  $l$  is the lateral wall of the endcap and  $d_i$  is the diameter of the top part of the endcap. In Eq. (3) the shrinkage of the ceramic under applied field is

$$\Delta d_c = d_{31} E d_c \quad (4)$$

where  $d_{31}$  is the transverse piezoelectric coefficient, and  $d_c$  is the cavity diameter decrease. It is necessary to remark that  $d_{31}$  is negative, so  $\Delta d_c$  corresponds to a shrinkage of the ceramic in the transverse direction.

From Eq. (3) it is apparent that the larger the cavity diameter, the smaller the cavity depth; then a large piezoelectric coefficient will produce a higher displacement, with the ceramic-metal composite acting as a displacement amplifier.

The thermally induced displacement is a consequence of the thermal expansion mismatch between the ceramic and the metal. It is possible to calculate this thermally induced displacement from

$$\Delta h_{(T)} = t_p \Delta t_p + 2t_m \Delta t_m + 2\{[(\Delta t_m)^2 - ((d_c \Delta t_p - \Delta t_m \Delta d_i)/2)^2]^{1/2} - 2(h + t_m) - t_p\} \quad (5)$$

where  $\Delta t_p$  and  $\Delta t_m$  are the increases of ceramic thickness and metal thickness due to the dilatation with the temperature increase, as follows:

$$\Delta t_p = 1 + \alpha_p \Delta T \quad (6)$$

and

Table 1  
Piezoelectric properties of ceramics used as a drive element in cymbals

Ceramic	$\epsilon'$	$\lg \delta$	$d_{31}$ (pC N <sup>-1</sup> )	$d_{33}$ (pC N <sup>-1</sup> )
PZT 8D	1104	0.003	-107	289
PZT 5A	1802	0.016	-208	429
PZT 5H	3500	0.016	-285	581

Table 2  
Metal characteristics

Metal endcap	Density (g cm <sup>-3</sup> )	$\alpha$ (10 <sup>-6</sup> K <sup>-1</sup> )	$E$ (GPa)
Zirconium	6.49	5.9	77
Brass	8.53	19.9	110
Kovar	8.36	5.5	138
Low-carbon steel	7.86	11.7	207
Molybdenum	10.22	5.1	324
Tungsten	19.30	4.6	405

$$\Delta t_m = 1 + \alpha_m \Delta T \quad (7)$$

where  $\alpha_p$  and  $\alpha_m$  are the thermal expansion coefficients of the piezoceramic and the metal, respectively.  $\Delta d_t$  is the corresponding increase of the top part of the endcap with temperature in an analogue form of Eq. (7).

If the PZT is electrically driven, Eq. (3) can be rewritten including the thermal displacement dependence,

$$\begin{aligned} d_{(T)} = 2 \{ (l \Delta t_p)^2 - [(d_c \Delta t_p - \Delta t_m d_t)/2 \\ - (d_{31(T)} E d_c \Delta t_p / 2)^2]^{1/2} - 2 \{ (l \Delta t_p)^2 \\ - [(d_c \Delta t_p - d_t \Delta t_m) / 2]^2 \}^{1/2} + d_{33(T)} E t_p \Delta t_p \} \quad (8) \end{aligned}$$

where  $d_{31(T)}$  and  $d_{33(T)}$  are the corresponding piezoelectric coefficients at different temperatures. In this expression the thermally induced displacement was included. For  $\Delta T = 0$ , Eq. (8) transforms into Eq. (1). From this expression, it is clear that the temperature dependence of the ceramic-metal composites can be reduced by eliminating the mismatch between thermal expansion coefficients of ceramic and metal, and by reducing the temperature dependence of the piezoelectric coefficients.

### 3. Experimental procedure

Poled ceramic disks, 12.7 mm in diameter and 1 mm in thickness, of three different commercial ceramic composi-

tions were investigated. Table 1 summarizes the most important parameters of the piezoelectrics. Dielectric constant and dielectric loss were measured using an HP 4194A Impedance/Gain Phase Analyzer;  $d_{31}$  was measured by the resonance method [12] and  $d_{33}$  using a Berlincourt meter.

Several different cap metals were selected to test the importance of thermal expansion and Young's modulus. Molybdenum, tungsten, zirconium, brass (70% Cu–30% Zn), kovar (54% Fe–29% Ni–17% Co), and low-carbon steel (ASTM A 599 electroplated with tin) were selected. Table 2 lists the physical properties obtained from the technical literature [13,14]. Truncated-cone cymbals were obtained by punching and then pressing (up to 100 MPa) metal sheets approximately 250  $\mu$ m thick. Burrs generated during punching were carefully removed by grinding. The pressing process produces a well-defined ring-shaped bonding area of 2 mm and a cavity diameter of 8.7 mm. The bonding area was smoothed using SiC sandpaper of 400 mesh to remove oxide layers and to improve the surface for epoxy bonding. The cavity depth was determined by subtracting the metal thickness from the endcap thickness, both measured with a gage having an accuracy of  $\pm 2 \mu$ m.

The ceramic disk and the endcaps were bonded together around the circumference with two different epoxies. The epoxy was applied carefully to avoid filling the cavity, otherwise the properties are drastically changed. Bonding was performed under a small pressure over the bonding area using ring clamps. Details of the epoxies and the curing process are listed in Table 3. Both epoxies are two-component systems with similar lap tensile strengths. Eccobond is a black-colored epoxy that contains dispersed CaCO<sub>3</sub> particles. Masterbond is a light-brown pure epoxy phenolic with a wide temperature range of operation and needs to be cured at moderate temperatures.

The actuator was electrically driven at 0.1 Hz in frequency generated by a variable-phase digital function synthesizer (NF model D194) under an applied field of 1 kV mm<sup>-1</sup> supplied by a bipolar operational powder amplifier (Kepco model BOP100M), and then the axial displacement was measured using a linear voltage differential transducer, LVDT, Feinpruf 12021C Millitron displacement meter, or an MTI model 2000 photonic non-contact sensor. In both cases the resolution was 0.05  $\mu$ m. The displacement under load was monitored with an eddy-current sensor having a resolution of 0.2  $\mu$ m. Temperature-dependent experiments were performed in a specially designed temperature chamber over the range -5 to +95°C. Borosilicate Glass Standard

Table 3  
Characteristics of epoxies

Epoxy	Curing process	Temperature range (°C)	$\alpha$ (10 <sup>-6</sup> K <sup>-1</sup> )	Tensile lap strength (MPa)
Eccobond	24 h, 25°C	-55 to +95	55	16.4
Masterbond	20 h, 25°C + 4 h, 70°C	-55 to +228	35	17.4

Reference Material 731 from NIST [15], was used as a temperature standard.

#### 4. Results and discussion

Fig. 3 shows the metal sheet thickness and the cavity depth for the different metals selected. After pressing, the cavity depth of the endcap is approximately 270  $\mu\text{m}$  for zirconium, brass, low-carbon steel and kovar; 250  $\mu\text{m}$  for molybdenum and 175  $\mu\text{m}$  for tungsten. Before pressing, none of the endcaps shows a defined bonding-area ring because of the existence of a curvature near the bonding region that gives higher cavity depth, as pointed out in Fig. 3. The pressing process give more reproducible metal endcaps with defined cavity depth, cavity diameter and bonded regions, which is very important in order to get reliable composites.

Fig. 4 shows the effects of the Young's modulus of the metal endcaps and the hardness of the PZT ceramics on the displacement of composite cymbal actuators. For the same metal endcap, there is a marked dependence of the displacement on  $d_{31}$ , the piezoelectric coefficient of the ceramic. The model gave displacements from Eq. (3) of 26, 19 and 10  $\mu\text{m}$  for PZT 5H, PZT 5A and PZT 8D, respectively. These values are in relatively good agreement with the measured displacements of the cymbals built with the lower Young's modulus metal endcaps, i.e., zirconium endcaps. Increasing the Young's modulus of the metal endcaps reduces the displacement of the cymbal actuator. This reduction of the displacement is almost linear and the displacement of the higher Young's modulus metal endcaps is approximately 52–57% lower than that achieved using the least Young's modulus metal endcaps, and is practically independent of the ceramic type. The linear decrease of the displacement with the increase of the Young's modulus of the metal denotes the spring nature of the endcaps.

In the case of composites bonded with Masterbond, Fig. 4(b), a different behavior was exhibited, having differ-

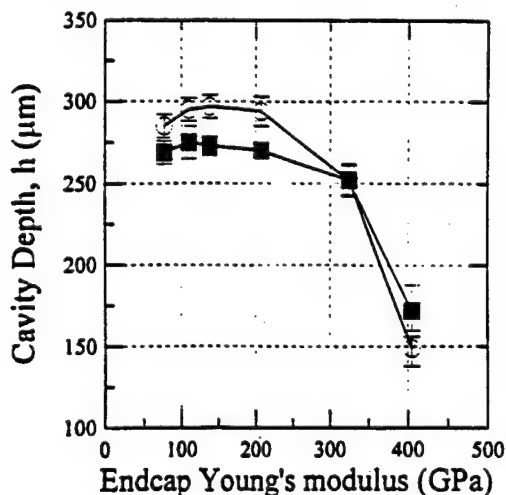


Fig. 3. Cavity depth of the cymbal endcap as punched (○) and after pressing (■) processes as a function of the metal Young's modulus.

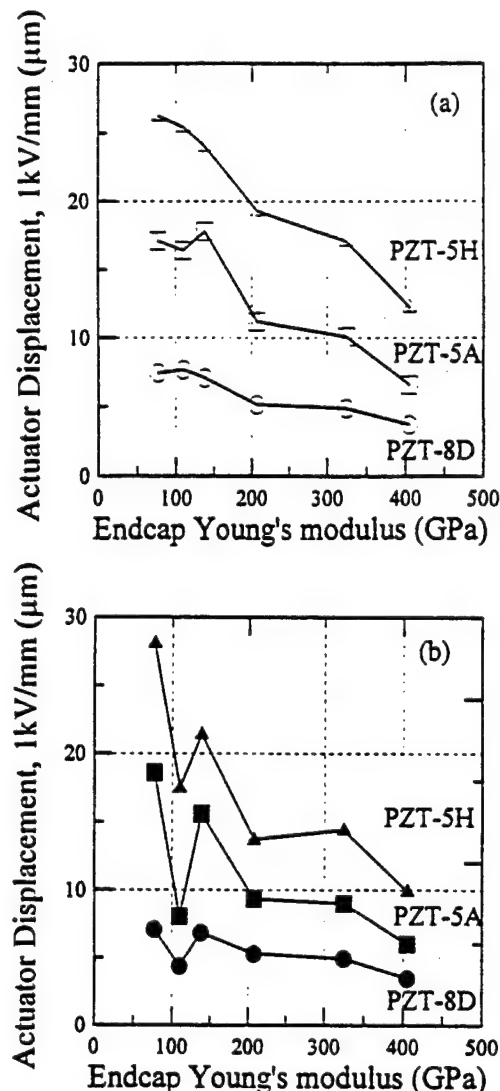


Fig. 4. Displacement of cymbal actuators for different base piezoceramics as a function of the metal Young's modulus for cymbals bonded with (a) Eccobond and (b) Masterbond.

ent displacement values, in general lower ones, than cymbals cured at room temperature. It seems that the displacement decrease is more pronounced for cymbals made with PZT 5H ceramics that have larger piezoelectric coefficients. The cymbals assembled with endcaps having larger thermal expansion coefficients than the ceramics generate stresses during the temperature epoxy curing, resulting in a marked decrease of the actuator displacements. The large thermal expansion coefficient mismatch between brass and the ceramic materials provokes a drastic reduction of the actuator displacements. In the case of PZT 5H ceramic-based composites, the higher dependence of the piezoelectric coefficients on temperature could be responsible for the larger decrease in the displacement characteristics. It is necessary to remark that the composite acts as a displacement amplification system of the piezoceramic, so the effect of stresses developed during curing is also amplified. It seems from the previous discussion that the zirconium endcaps are disappointing, but the Young's



modulus of this metal is slightly lower than that of the ceramics, so the stress could be transferred to the metal, and a possible deformation of the metal could occur.

The degree of hysteresis of the displacement is an important criterion for actuators that provides information about mechanical losses. It is defined [16] as

$$\Delta H\% = 100 \Delta X / X_{\max} \quad (9)$$

where  $X_{\max}$  is the displacement at maximum electric field, in the present case  $1 \text{ kV mm}^{-1}$ , and  $\Delta X$  is the difference in displacement between increasing and decreasing path at half maximum of the applied electric field. To eliminate walk off, the hysteresis data as well as the maximum displacement were recorded after 12 cycles. Fig. 5 shows the degree of hysteresis for the cymbal actuators plotted as a function of the endcap modulus of elasticity. There is a very little dependence of the hysteresis on the stiffness of the metal. The lowest hysteresis values were registered for ceramic-metal composites made from hard PZT, since the main cause of hysteresis losses is

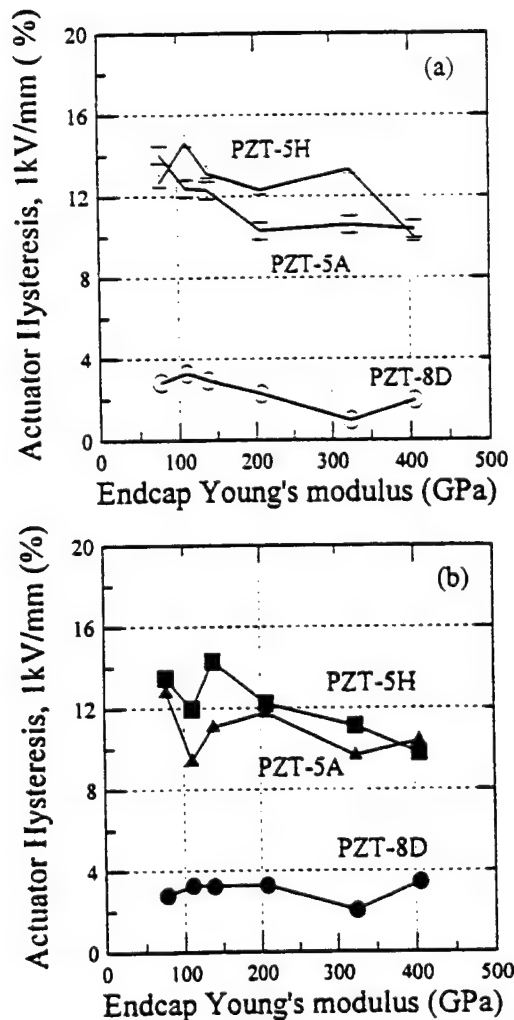


Fig. 5. Hysteresis of cymbal actuators for different base piezoceramics as a function of the metal Young's modulus for cymbals bonded with (a) Eccobond and (b) Masterbond.

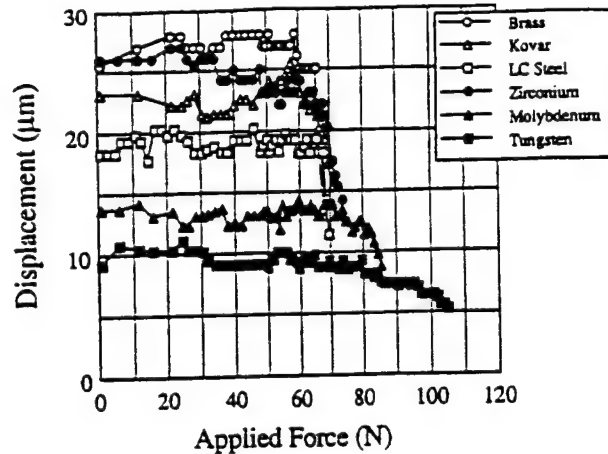


Fig. 6. Net displacement of the actuator axially loaded as a function of the applied load for different metal endcaps bonded with Eccobond using PZT-5H piezoceramic disks.

domain reversal. PZT-5A ceramic disks typically show 5–8% hysteresis losses.

Fig. 6 shows the net displacement under load. The net displacement is the displacement produced by the actuator when it is electrically driven. If the actuator is loaded a free deflection is produced and at each load the application of an electric field produced a net displacement. The free deflection of the composite is related to the spring characteristics of the composite. Metals with low modulus of elasticity show higher displacements and higher free deflection. On the contrary, the maximum load, defined as the load for which 90% of the initial net displacement is maintained, increased with the modulus of elasticity of the metal. Higher load than the maximum provokes a permanent deformation of the structure with loss of properties. Data were recorded before such a permanent deformation and debonding of the composite took place.

Fig. 7 collects the data for maximum load along with the free deflection for such a load for different metals endcaps. The values obtained for maximum load are significantly larger than those reported previously for the former cymbal-type actuator [7], ~25 N. The reason for such an improvement is related to a more efficient stress transmission of the endcaps. Low-carbon steel is the only metal studied that showed permanent deformation under maximum load. The other metals recovered their original net displacement after testing. Resonance spectra, which are very sensitive to symmetry changes, were recorded before and after the load test, up to the defined maximum load, with no variations except in the case of low-carbon-steel-based cymbals. On the other hand, the PZT piezoceramic type has very little influence on the maximum load, as shown in Fig. 8. For all three types of PZTs the maximum load is reached at approximately 67 N, for Kovar endcap cymbals bonded with Eccobond. The mechanical response of the cymbal-type piezocomposites is clearly related to the spring characteristics of the endcap.

For the composites made with Masterbond, debonding always takes place under a maximum load lower than that of

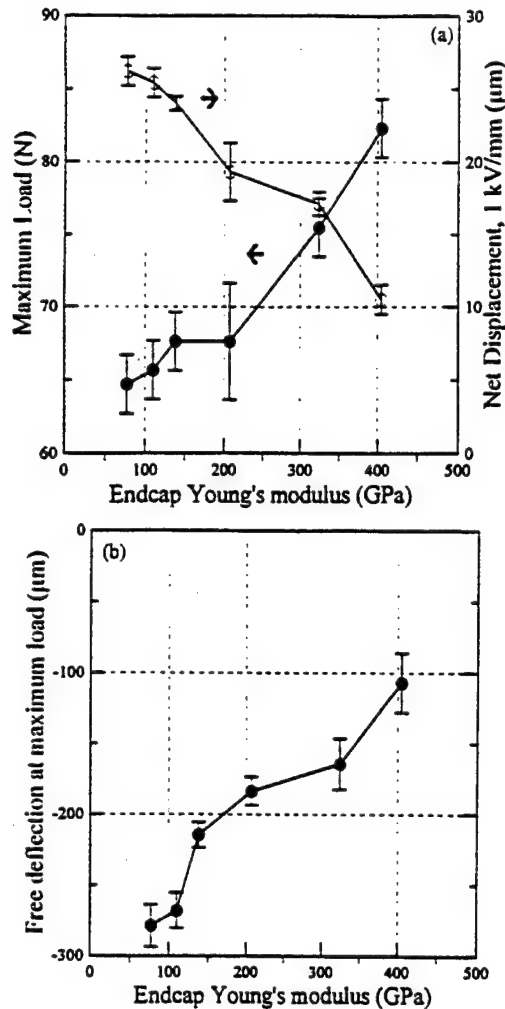


Fig. 7. (a) Maximum load and actuator net displacement and (b) free deflection vs. applied load as a function of the metal endcap Young's modulus. Cymbals bonded with Eccobond using PZT-5H ceramics.

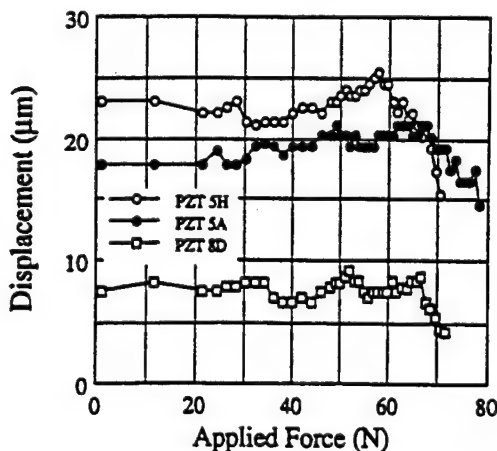


Fig. 8. Net displacement as a function of the applied load for different PZT-based piezoceramics bonded with Masterbond. The encaps were made of kovar.

the cymbals bonded with Eccobond, and the samples are destroyed. All the samples failed at the endcap face in contact with the load, leading to characteristic damage of the center

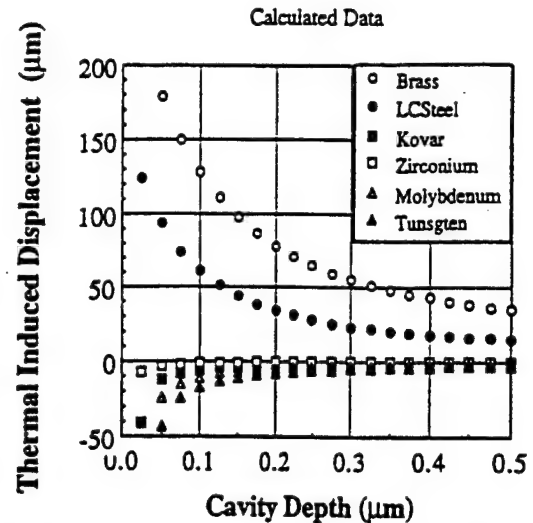


Fig. 9. Calculated thermally induced displacement for different metal endcaps as a function of the cavity depth of the actuator.  $\Delta T = 50^\circ\text{C}$ ,  $\alpha_p = 6 \times 10^{-6} \text{ } ^\circ\text{C}^{-1}$ .

of the PZT electrode. Although the tensile lap strength is similar for the two epoxies, the existence of particles in Eccobond confers higher flexibility. This provides more stress relief and a higher strength. Masterbond is a more crystalline epoxy because of its curing process. The calculated stress in the bonding-ring area of the endcap is 1.9 MPa for a load of 70 N. This is lower than the tensile lap strength of the epoxy. Nevertheless, small microcracks generated in the bonding by air bubbles, the free deflection of the endcap, the variations on the thickness of the epoxy, etc., could be the origin of a reduction of absorbed stress by the bonding. If the stress is concentrated in the upper endcap, bending of the ceramic could provoke the collapse of the structure, as observed. Additional new experimentation will be required to clarify this question, and may lead to improved designs for actuator applications.

Using Eq. (5) it is possible to calculate the thermally induced displacement of the cymbal actuators. The data calculated for the different metals (Fig. 9) show that it is possible to minimize and to avoid the thermally induced displacement. The measured data were somewhat smaller than the calculated values, Table 4. The discrepancies between the calculated data and the measured values are higher for large thermally induced displacements. This is attributed to the effect of the epoxy, which has a much higher thermal expansion coefficient than the ceramics and the metals, thus affecting the stress transfer. From the point of view of practical application, negative thermally induced displacements are very interesting because the metal produces a compressive stress on the ceramic that can reduce the depolarization caused by higher temperature.

Fig. 10 shows the thermal dependence of the net displacement for different endcap materials bonded to PZT 5H with Eccobond. There is a drastic decrease in displacement for temperatures higher than  $50^\circ\text{C}$ , which can be attributed to the bonding layer. The linear operation region of the actuator is



Table 4  
Thermally induced displacement ( $\mu\text{m}$ ) of different metal endcap PZT 5H cymbal actuators measured from  $-5$  to  $95^\circ\text{C}$ . The calculated data correspond to a  $\Delta T = 100^\circ\text{C}$

Epoxy	Tungsten	Molybdenum	Kovar	Zirconium	LC steel	Brass
Eccobond	-8.1	-0.5	-0.5	-0.5	4.8	48.9
Masterbond	-2.0	-2.0	-0.3	1.0	8.4	60.5
Calculated	-11.3	-6.8	-3.2	-0.1	50.0	118.4

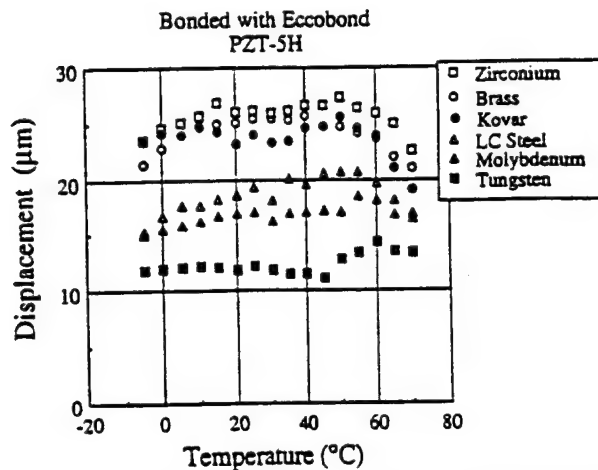


Fig. 10. Actuator net displacement as a function of the temperature for cymbals bonded with Eccobond using PZT 5H ceramics.

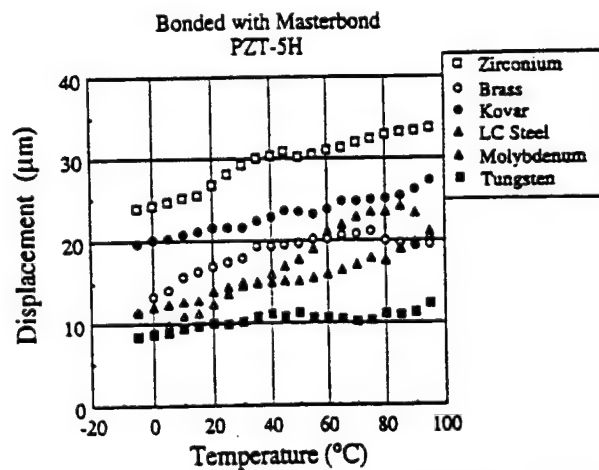


Fig. 11. Actuator net displacement as a function of the temperature for cymbals bonded with Masterbond using PZT 5H ceramics.

restricted to temperatures between  $15$  and  $45^\circ\text{C}$  for materials with low thermal expansion mismatch between the metal caps and the ceramic. For temperatures below  $15^\circ\text{C}$ , the decrease in displacement with temperature can be traced to the temperature dependence of the piezoelectric coefficient  $d_{31}$  [17].

With Masterbond it is possible to extend the temperature range of the cymbal actuator, Fig. 11. Under these circumstances, the temperature dependence of the net displacement is very close to that of the  $d_{31}$  coefficient of the ceramic. The dependence is higher for the more compliant metal endcaps. Exceptions to such behavior are observed for metals with higher thermal expansion coefficient than the ceramic.

Fig. 12 shows the measured curves for brass, kovar and tungsten endcaps bonded with Masterbond to several PZT ceramic types, along with the calculated data from Eq. (6) for kovar endcaps, Fig. 12(d). Based on these curves there are several ways of avoiding the temperature dependence of cymbal actuators:

(a) Reducing the temperature dependence of the radial coefficients of the PZT ceramic. If the bonding has no significant effect on the temperature characteristics and the stiffness of the metal is low, the thermal characteristics are controlled by the PZT ceramics, meaning that the cymbal works as a displacement amplifier. In this case, piezoelectric ceramics with low temperature dependence such as PZT 8D and PZT 5A are more useful over wide temperature ranges.

(b) Changing the cavity size: for brass endcaps, very low temperature dependence was observed for temperatures higher than  $40^\circ\text{C}$ . In such a case, the mismatch of thermal expansion coefficients between the metal endcaps and the ceramic produces a large positive thermally induced displacement. As a result, the cavity size is changing slowly in relation to the cavity depth. As the cavity depth increases, the displacement decreases [18]. Thus the net position of the actuator is continuously increasing because of the thermally induced displacement, even though the temperature dependence can be canceled over a limited temperature range.

(c) Using higher-stiffness metal: although the stiffness leads to a reduction in displacement, tungsten endcaps provide temperature-independent behavior. The slightly negative thermally induced displacement can easily be compensated. By utilizing multistack structures, it is possible to have very high displacement and negligible thermally induced displacement and temperature dependence.

Fig. 13 shows the measured temperature dependence of selected samples, taking into account both the net displacement and the thermally induced displacement. It can be seen that large displacements have been obtained without temperature dependence.

## 5. Conclusions

The properties and performance of ceramic-metal composites with  $2(0)-2-2(0)$  connectivity can be optimized through the selection of materials. Because of the composite structure, the metal endcaps amplify the displacement generated by the piezoelectric ceramic. The metal endcaps convert the transverse shrinkage of the ceramic into a longitudinal

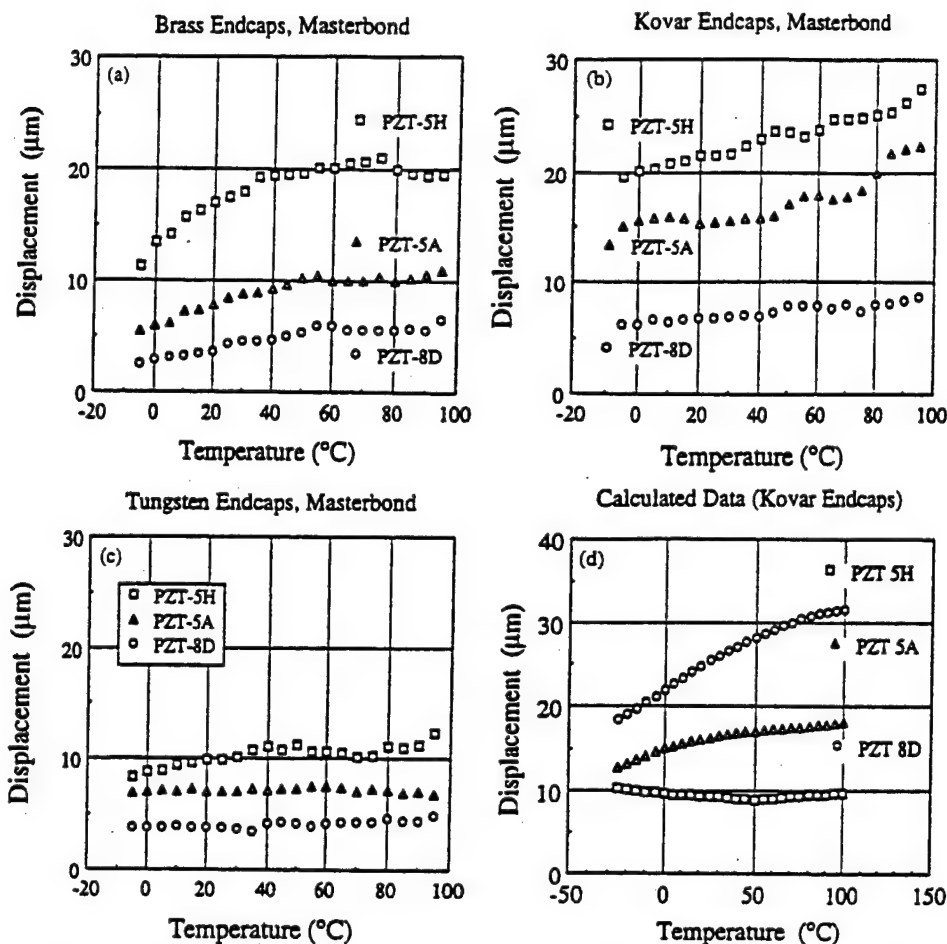


Fig. 12. Actuator net displacement as a function of temperature for cymbals bonded with Masterbond showing the behavior of different PZT types for brass (a), kovar (b) and tungsten (c) endcaps. (d) Calculated displacement (net displacement plus thermal expansion displacement) data for different PZT–kovar composites, electric field  $1 \text{ kV mm}^{-1}$ .

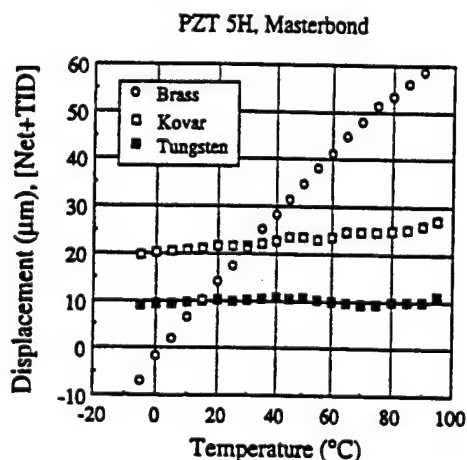


Fig. 13. Measured displacement temperature dependence of different cymbals bonded with Masterbond using PZT-5H type ceramic (net displacement plus thermally induced displacement).

displacement. The motion mechanism corresponds to a rotation of the metals endcap segment according to the simplified approach made. The higher the  $d_{31}$  of the PZT, the higher the displacement. The higher the Young's modulus of the metal, the lower the attained displacement. But, on the contrary, the

applicable maximum force increases with the Young's modulus of the metal endcaps and it seems to be independent of PZT ceramic type. Higher applicable force limits are reported (up to 85 N compared with the previous 20 N), based on more efficient stress-transfer bonding reached by the elimination of the curvature of the endcaps in the vicinity of the bonding area.

The thermal behavior of the cymbal actuator displacement depends on the thermal characteristics of the PZT ceramic element, particularly the  $d_{31}$  temperature behavior. The thermally induced displacement was also eliminated by using metals with similar thermal expansion coefficient to the ceramic, as it has been calculated that a higher cavity reduced such thermally induced displacement. Low or negligible temperature dependence of displacement in the cymbal actuator was achieved for metal endcaps with higher stiffness and lower thermal expansion coefficient than piezoelectric ceramics.

#### Acknowledgements

The authors would like to express their gratitude for the support from the following agencies and organizations:

Office of Naval Research Contract no. N00014-92 J 1510.  
National Science Foundation Grant no. DMR-9223847.  
Spanish Science Ministry (CICYT MAT94-807 and DGI-CYT PR94-028), Turkish Science and Technology Council (TUBITAK) and Middle East Technical University, Ankara.

## References

- [1] R.E. Newnham, Q.C. Xu and S. Yoshikawa, Transformed stress direction-acoustic transducer, US Patent No. 4 999 819 (12 March, 1992).
- [2] Q.C. Xu, A. Dogan, J. Tressler, S. Yoshikawa and R.E. Newnham, Ceramic-metal composite actuators, *Ferroelectrics*, 160 (1994) 337–346.
- [3] J.F. Fernandez, A. Dogan, J.F. Tressler, Q.M. Zhang and R.E. Newnham, Hollow piezoelectric composites, *Sensors and Actuators A*, 51 (1996) 183–192.
- [4] K. Onitsuka, A. Dogan, Q.C. Xu, J. Tressler, S. Yoshikawa and R.E. Newnham, Design optimization for ceramic-metal composite actuators (moonie), *Ferroelectrics*, 156 (1994) 37–42.
- [5] A. Dogan, S. Yoshikawa, K. Uchino and R.E. Newnham, The effect on the characters of the moonie transducer and reliability issue, *IEEE Trans. Ultrasonics, Ferroelectrics and Frequency Control*, Proc. V.II, France, 1994, pp. 935–939.
- [6] A. Dogan, Flexensional moonie and cymbal actuator, Ph.D. Thesis, The Pennsylvania State University, University Park, PA (1994).
- [7] A. Dogan, J.F. Fernandez, K. Uchino and R.E. Newnham, New piezoelectric composites actuator designs for displacement amplification, in G. Gusmano and E. Travesera (eds.), *Euroceramic* IV, Agenzia Polo Ceramico, Faenza, Italy, 1995, Vol. 4, pp. 1027–1032.
- [8] J.F. Tressler, A. Dogan, J.F. Fernandez, J.T. Fielding, K. Uchino and R.E. Newnham, Capped ceramic hydrophones, *Proc. IEEE Ultrasonic Symp.*, Seattle, WA, USA, 1995, pp. 897–900.
- [9] B. Koc, A. Dogan, J.F. Fernandez, R.E. Newnham and K. Uchino, Accelerometer application of the modified Moonie (Cymbal) transducer, *Jpn. J. Appl. Phys.*, 35 (1996) 4547–4549.
- [10] G.H. Haertling, Rainbow ceramics: a new type of ultra-high-displacement-actuator, *Am. Ceram. Soc. Bull.*, 73 (1994) 93–96.
- [11] F.P. Beer and E.R. Johnston, Jr., *Mechanics of Materials*, MacGraw Hill, New York, 1991.
- [12] Q.C. Xu, A.R. Ramachandran and R.E. Newnham, Resonance measuring technique for complex coefficients of piezoelectric composites, *J. Wave-Material Interaction*, 2 (1987) 105–122.
- [13] E.A. Brandes, *Smithell's Metals Reference Book*, Butterworth, New York, 6th edn., 1983.
- [14] Y.S. Touloukian, R.K. Kirby, R.E. Taylor and P.D. Desai, *Thermophysical Properties of Matter. The TPCR Data Series, Vol. 12: Thermal Expansions; Metallic Elements and Alloys*, JFI/Plenum, New York, 1975.
- [15] NIST Standard Reference Material 731, NIST, Gaithersburg, MD, June 1993.
- [16] K. Uchino, *Piezoelectric/Electrostrictive Actuators*, Morikita Publishers, Tokyo, 1986.
- [17] D. Berlincourt, Piezoelectric crystal and ceramics, in O.E. Mattiat (ed.), *Ultrasonic Transducer Materials*, Plenum Press, New York, 1971, pp. 63–124.
- [18] Q.C. Xu, S. Yoshikawa, J. Tressler and R.E. Newnham, Piezoelectric composites with high sensitivity and high capacitance for use at high pressures, *IEEE Trans. Ultrasonics Ferroelectrics and Frequency Control*, 38 (1991) 634–639.

# **APPENDIX 35**

# A piezoelectric pseudoshear multilayer actuator

Qing-Ming Wang<sup>a)</sup> and L. E. Cross

Intercollege Materials Research Laboratory, The Pennsylvania State University, University Park, Pennsylvania 16802-4800

(Received 9 February 1998; accepted for publication 2 March 1998)

A type of high strain piezoelectric ceramic actuator, namely, pseudoshear multilayer actuator, is described. In this structure, a stack of prepoled rectangular piezoelectric transducer ceramic sheets are conductively bonded at alternate ends, while the bottom layer bonded on a fixed base. When driven, alternate layers elongate or shrink in the same direction through converse piezoelectric effect, which results in the actuator structure developing a strong shear motion about the face perpendicular to the bonding direction. Experimental results indicate that more than 50  $\mu\text{m}$  displacement can be achieved from the top layer for an actuator consisting of 18 layers with dimensions of 25.57 mm  $\times$  4.02 mm  $\times$  0.51 mm ( $1 \times w \times t$ ). By reducing ceramic sheet thickness and using more layers, even large displacement can be obtained, and driving voltage can also be reduced while keeping the same field level. Nonlinear piezoelectric response under high driving field further enhances the displacement level. © 1998 American Institute of Physics. [S0003-6951(98)00418-5]

Piezoelectric actuators are usually classified into three categories: multilayer actuators, bimorph or unimorph benders, and flextensional composite actuators. Multilayer actuators, in which about 100 thin piezoelectric/electrostrictive ceramic sheets are stacked together with internal electrodes utilizing the longitudinal ( $d_{33}$ ) mode, are characterized by large generated force, high electromechanical coupling, high resonant frequency, low driving voltage, and quick response, but small displacement level ( $< 10 \mu\text{m}$ ).<sup>1</sup> On the other hand, bimorph or unimorph actuators consist of two thin ceramic sheets or one ceramic and one metal sheet bonded together with the poling and driving directions normal to the interface. When driving, the alternative extension and shrinkage of ceramic sheets due to transverse ( $d_{31}$ ) mode result in a bending vibration. Bimorph and unimorph actuators can generate a large displacement level but low electromechanical coupling, low resonant frequency, and low driving force. Flextensional composite actuator, "moonie",<sup>2,3</sup> consists of a piezoelectric or electrostrictive ceramic disk and metal end caps which act as a mechanical transformer converting and amplifying the lateral displacement of ceramic disk into axial motion. Medium displacement and force level can be obtained in moonie actuators.

Most recently developed cantilever monomorph, RAINBOW, and shear mode actuators<sup>4-7</sup> are basically modified unimorph actuators with advantage of simple monolithic structure by which bonding problems usually observed in bimorph-type actuators can be avoided. However, large displacement is achieved with sacrificing the generative force. In this letter, we report a new type of pseudoshear mode actuator which makes use of a composite structure assembled from thin sheet soft piezoelectric transducers (PZT) piezoelectric ceramics, poled in the usual direction normal to the major face of sheet and driven by electrodes upon the major faces.

In pseudoshear multilayer actuator structure,  $N$  layer

fully electroded piezoelectric ceramic plates are bonded together by a stiff conductive epoxy at alternate ends of the plate structure as depicted in Fig. 1(a). The bottom layer is bonded on fixed base with one end. The gaps between the nonbonded faces of the sheets are filled by thin plastic sheets or teflon coatings to stabilize the structure. All the ceramic plates have the same normal poling direction and they are connected electrically in parallel through the conductive epoxy bond line with the wires contacting alternate pairs of plates from each side. For PZTs, the piezoelectric  $d_{31}$  coefficient is negative. Tracing now the effect of a voltage applied between the two contact wires of sign shown in Fig. 1(b). The bottom plate is subjected to a field against the original poling direction, i.e., a negative field thus, since  $d_{31}$  is negative the resulting linear piezoelectric strain is

$$x_1 = -d_{31}(-E_3) = d_{31}E_3. \quad (1)$$

If  $L$  is the length dimension of ceramic stack, the elongation or shrinkage of each layer is

$$d_1 = d_{31}E_3L. \quad (2)$$

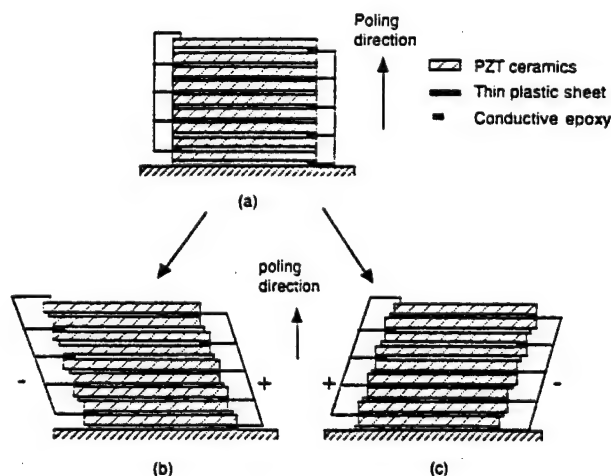


FIG. 1. Schematic drawing of pseudoshear actuator structure.

<sup>a)</sup>Electronic mail: qxw4@psu.edu

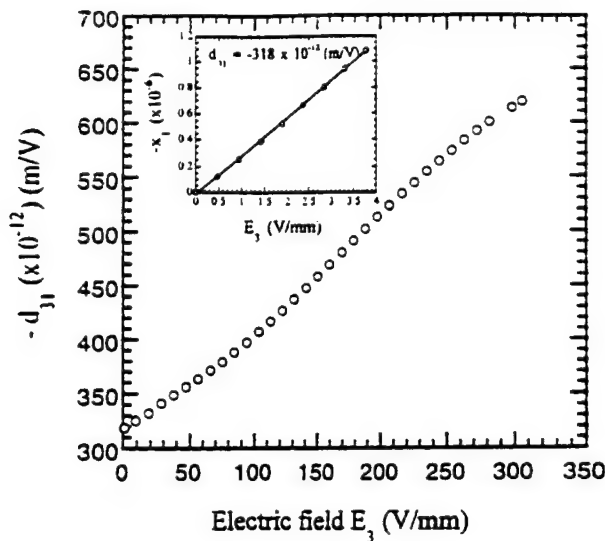


FIG. 2. Piezoelectric  $d_{31}$  coefficient as a function of bipolar ac electric field for soft PZT ceramics (Motorola 3203 HD).

Because ceramic plate are bonded at its right end, the left end is free and then moves to the left by a distance  $d_1$ .

For the second plate in the stack, however, a positive field is applied along the poling direction, thus plate 2 shrinks so that

$$d_2 = -d_{31}E_3L. \quad (3)$$

Now the right hand end of plate is free to move which will move a distance  $d_2$  also to the left, thus its total displacement, combining with plate 1, is  $d_1 + d_2$  to the left.

Obviously, each layer is carried by its following layer thus the direction of elongation and shrinkage of each layer are the same. Therefore the displacement of the upper layer is cumulative from its lower layers. For a stack of  $N$  plates, the total displacement of its top layer, with respect to base, is

$$d = d_1 + d_2 + \dots + d_N = Nd_{31}E_3L \quad (4)$$

at the free end, or

$$d = d_1 + d_2 + \dots + d_{N-1} = (N-1)d_{31}E_3L \quad (5)$$

at bonded end.

If the voltage is reversed to the stack as shown in Fig. 1(c), the actuator will now shear over upper surface moving to the right. Therefore under the ac field, this multilayer actuator vibrates similar to pure shear vibration can thus be called pseudoshear multilayer actuator.

From Eqs. (4) and (5), it can be found that the total displacement of the top layer depends on the number of ceramic layer  $N$ , the value of  $d_{31}$ , the magnitude of electric field  $E_3$ , and also the length of actuator  $L$ . It is interested to note that, due to  $E_3 = V/t$ , where  $V$  is the applied voltage and  $t$  is thickness of ceramic layer, the driving voltage can be reduced by reducing the thickness of ceramic layer while keeping the same field strength.

Assuming the space between each layers in the actuator stack is  $t_s$ , the total stack thickness will be  $(t+t_s)N$  and the shear angle or shear strain  $\delta$  will be

$$\delta = \frac{Nd_{31}E_3L}{(t+t_s)N} = \frac{d_{31}E_3L}{(t+t_s)}. \quad (6)$$

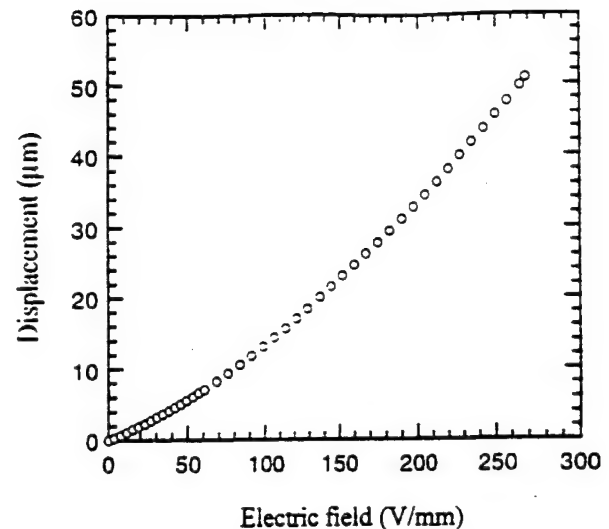


FIG. 3. Displacement as a function of electric field for a prototype pseudoshear actuator ( $N=18$ ,  $L=25.57$  mm,  $w=4.02$  mm,  $t=0.51$  mm).

since  $t \ll L$ , the stack can be designed to generate large shear angles.

From Eq. (6), we may introduce an effective shear coefficient  $d_{31}^e$  by comparing with pure shear strain,  $x_s = d_{15}E_3$ ,

$$d_{31}^e = \frac{d_{31}L}{t+t_s}, \quad (7)$$

which is a dimension-dependent coefficient.

To examine the performance of a pseudoshear actuator, an 18 layer stacked prototype actuator with dimensions of  $25.57$  mm  $\times$   $4.02$  mm  $\times$   $0.51$  mm ( $1 \times w \times t$ ) of each layer is prepared using commercial Motorola soft PZT (3203HD) ceramics. In the multilayer structure, all layers are aligned in the same poling direction. Silver epoxy (E-Solder<sup>®</sup> No. 3021 Conductive Adhesives, IMI Insulation Materials, Inc., New Haven, CT) was used to bond the alternative ends of ceramic sheets. Very fine copper wires were used to connect the electrodes in such a way that each layer was connected electrically in parallel. Thin plastic sheets of about  $0.1$  mm thickness or silicon grease were used to fill the gaps between each layer to stabilize the structure. A load of about  $1$  kg was applied on the top of multilayer structure when hardening the silver epoxy.

To characterize the actuator performance, the displacement of the top layer of pseudoshear actuator was measured as a function of driving electric field. The measurement setup and procedure were described in a previous letter.<sup>7</sup> To check the various vibration modes, impedance spectrum of actuator was measured by using an impedance/gain-phase analyzer (HP4194A, Hewlett Packard Co.).

It should be noted that for nonlinear piezoelectric materials such as PZTs, piezoelectric coefficient is electric field dependent. The data provided by material manufacturers are usually measured under weak field by resonance-antiresonance method, and thus are not applicable for the actuator performance evaluation because strong electric fields are usually applied to drive the actuators. Therefore, the piezoelectric  $d_{31}$  coefficient of Motorola PZT 3203HD ceramics was measured as a function of electric field. A rectangular sample with dimensions of  $38.0$  mm  $\times$   $12.5$  mm



$\times 0.5$  mm was used for this measurement. A sinusoidal driving field with frequency of 50 Hz is used to excite the sample. The effective  $d_{31}^e$  coefficient was obtained by  $d_{31}^e = x_1/E_3$ , here  $x_1$  is transverse strain under electric field  $E_3$ . The effective piezoelectric  $d_{31}^e$  coefficient as a function of electric field  $E_3$  is depicted in Fig. 2. It can be seen that due to its nonlinear ferroelectric nature,  $d_{31}$  is no longer a constant over the used electric field range for soft PZT ceramics. As the magnitude of applied electric field increases,  $d_{31}$  coefficient increases. The insert in Fig. 2 shows the transverse strain under weak electric field. It is clear that linear piezoelectric relation between strain and electric field,  $x_1 = d_{31}E_3$  is obeyed only at a rather low field level. The measured low field level  $d_{31}$  coefficient is  $-318 \times 10^{-12}$  m/V, which is in good agreement with the data provided by the manufacturer's data sheet,  $-320 \times 10^{-12}$  m/V, measured by resonance-antiresonance method.

It has been shown<sup>8,9</sup> that the nonlinear piezoelectric response in ferroelectric PZT ceramics under high driving field originates mainly from the motion of non-180° domain walls. Experimental results also showed that dielectric losses drastically increase with the amplitude of driving field, since the non-180° domain wall motion is inherently a lossy process. But no significant temperature increase was observed when frequency is far off the resonant frequency of the ceramic sample. So for off-resonant frequency driving, soft PZT can be driven under quite a high electric field level. However, the nonlinear piezoelectric response of PZT ceramics has to be considered in the actuator design.

Figure 3 shows the displacement as a function of electric field for the prototype pseudoshear actuator composed of 18 layer PZT ceramic sheets. More than 50  $\mu$ m shear displacement was obtained under a driving field of 270 V/mm. A nonlinear piezoelectric response under high electric field contributes significantly to the shear displacement. Considering the thickness of ceramic sheet and the space between layers ( $t + t_s = 0.61$  mm), we can calculate the effective piezoelectric  $d_{15}^e$  coefficient by using Eq. (7). Under weak field, since  $d_{31} = -318 \times 10^{-12}$  m/V, we have  $d_{15}^e = 13\,380 \times 10^{-12}$  m/V which is about 13 times higher than the shear mode piezoelectric coefficient  $d_{15}$  ( $= 1045 \times 10^{-12}$  m/V for soft PZT 3203HD) of the ceramic material. It is interesting to note that  $d_{15}^e$  is a dimension-dependent parameter. By using an even thinner ceramic sheet,  $d_{15}^e$  coefficient can be further increased. Since  $d_{31}$  increases with a driving field due to nonlinear piezoelectric response,  $d_{15}^e$  coefficient will also increase as the amplitude of applied ac field increases.

Frequency characteristics of pseudoshear actuator may be adduced from the impedance spectrum shown in Fig. 4. There is not any resonance observed below 1 kHz, indicating the displacement of pseudoshear actuator may have flat frequency responses in the low frequency range. Two weak resonances are evident near 1.33 and 3.0 kHz which are probably due to spurious bending modes. It was found that if a load was placed on the top of actuator, these two resonant modes were greatly reduced or even disappeared. By making more compact structure through better selection of the polymer filler material and better bonding processing, the two peaks could be eliminated. The resonance at 10 kHz is the first extended longitudinal mode which in pseudoshear con-

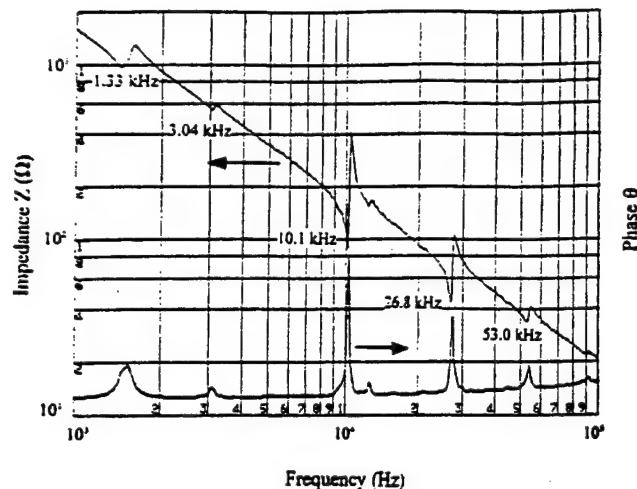


FIG. 4. Impedance and phase spectra for pseudoshear actuator in the frequency range of 1 to 100 kHz.

figuration will now represent the first effective shear mode. A second strong mode at 26.8 kHz is probably a shifted third harmonic. Weaker higher order modes are evident at 53 and 90.6 kHz.

In summary, a new type of piezoelectric actuator, namely, pseudoshear actuator is developed. Large displacement was obtained through this multilayer configuration. A nonlinear piezoelectric response further enhances the vibrational level of actuator. The frequency characteristics are also studied which indicated the resonant frequency of effective shear mode is much higher than that of the bending vibration mode of bimorph-type actuators. The pseudoshear actuator has the following advantages: (1) The actuator is assembled from thin sheet PZT already electroded and prepoled; (2) shear vibration is realized through  $d_{31}$  mode by applying ac voltage through the thickness direction so that high fields may be realized at low driving voltage; (3) the generative force is controlled by stiffness  $c_{11}$  which is larger than the shear stiffness  $c_{44}$ ; (4) the magnitude of shear can be controlled by the ratio of  $L/(t + t_s)$  and can be very large for thin sheets.

The pseudoshear mode actuator may have a very wide range of applications. The systems where it could replace conventional actuators would be linear and rotary motors, step and repeat (inchworm) type actuators, flow sensing and flow control, valving and pumping system, and many others.

<sup>1</sup>K. Uchino, Bull. Am. Ceram. Soc. 65, 647 (1986).

<sup>2</sup>Y. Sugawara, K. Onitsuka, S. Yoshikawa, Q. C. Xu, R. E. Newnham, and K. Uchino, J. Am. Ceram. Soc. 75, 996 (1992).

<sup>3</sup>Q. C. Xu, A. Dogan, J. Tressler, S. Yoshikawa, and R. E. Newnham, Ferroelectrics 160, 337 (1994).

<sup>4</sup>K. Uchino, M. Yoshizaki, and A. Nagao, Ferroelectrics 95, 161 (1994).

<sup>5</sup>Gene H. Haertling, Am. Ceram. Soc. Bull. 73, 93 (1994).

<sup>6</sup>Gene H. Haertling, Ferroelectrics 154, 101 (1994).

<sup>7</sup>Q.-M. Wang, B. Xu, V. D. Kugel, and L. E. Cross, Proceedings of the Tenth IEEE International Symposium on Applications of Ferroelectrics (unpublished), Vol. II, pp. 767-770.

<sup>8</sup>S. Li, W. Cao, R. E. Newnham, and L. E. Cross, Ferroelectrics 139, 25 (1995).

<sup>9</sup>S. Li, W. Cao, and L. E. Cross, J. Appl. Phys. 69, 7219 (1991).

# **APPENDIX 36**



# Resonance modes and losses in 1-3 piezocomposites for ultrasonic transducer applications

Xuechang Geng<sup>a)</sup> and Q. M. Zhang

Materials Research Laboratory and Department of Electrical Engineering, The Pennsylvania State University, University Park, Pennsylvania 16802

(Received 13 July 1998; accepted for publication 28 October 1998)

The article presents the results of a recent investigation on the ultrasonic performance of 1-3 piezocomposites. Using a guided wave approach, the electromechanical properties of the thickness resonance are modeled and the results are compared with the experimental data. The influence of various losses in a 1-3 composite on the dispersion curves and the quality factor for the thickness mode is examined. It is found that the reduction in the quality factor of a composite compared with piezoceramic is mainly due to the acoustic coupling between the two constituents. Even for a composite with the mechanical  $Q$  of the polymer higher than that of the ceramic, the mechanical  $Q$  of the composite is still lower than that of the ceramic except when the ceramic volume content is very low. Hence, in most of piezoceramic polymer composites, the mechanical  $Q$  of the ceramic phase plays a major role in determining the quality factor of a 1-3 composite transducer. For the lateral modes in a 1-3 composite, it is found experimentally that the frequencies of the two lowest lateral modes can be determined approximately by the shear wave velocity and the width of the polymer gap over a broad ceramic volume fraction range, suggesting that they correspond to the half-wave standing waves in the polymer gap. © 1999 American Institute of Physics. [S0021-8979(99)08603-X]

## I. INTRODUCTION

Piezoceramic polymer composites offer many advantages over single phase materials for many transducer applications such as underwater sonar, ultrasonic imaging for medical and NDE applications, and stress sensors.<sup>1,2</sup> The complementary properties of the polymer and ceramic phases in the electric and mechanical responses make it possible to tune the composite properties over a wide range. On the other hand, in order to fully make use of these advantages and to reduce the manufacture costs of composite, it is necessary and still a challenge to establish a quantitatively structure-property relationship which links various design parameters in the constituents to the final device performance and reveals new properties of composites that are absent in single phase materials.

In the past two decades, a great deal of effort has been devoted to analyze and model the transducer performance of piezocomposites.<sup>3-9</sup> The model (quasi-static model) developed by Smith and Auld<sup>3</sup> and Hashimoto and Yamaguchi<sup>4</sup> based on the isostrain and isostress concepts in treating the coupling between the constituent phases provided a qualitative prediction on the effective piezoelectric properties of 1-3 composites as a thickness resonator. It was shown from the model that the thickness coupling factor  $k_t$  of a composite can approach the longitudinal coupling factor  $k_{33}^I$  of the piezoceramic rod, which agrees with experiments for composites with a high aspect ratio  $d/t$ , where  $t$  is the thickness and  $d$  is the periodicity of the composites. Because of its simplicity, the quasi-static model offers a convenient means for a

quick estimation of the composite parameters. Auld *et al.* pointed out the existence of the stop band edge resonance in both 2-2 and 1-3 composites due to the periodic arrangement of the ceramic elements in these composites.<sup>5,6</sup> However, in order to address quantitatively many realistic issues of a composite material such as the influence of the aspect ratio and shape of the ceramic rod in a 1-3 composite on the performance, finite element method (FEM) is often used.<sup>7-9</sup>

More recently, based on the guided wave approach, an analytical model was developed which is capable of treating many practical issues related to the ultrasonic performance of a 2-2 composite. By combining this with the eigenmode expansion, the ultrasonic properties of a finite thickness 2-2 composite can be analyzed quantitatively and many new features were predicted and confirmed experimentally.<sup>10,11</sup> Clearly, the model results offer many new physical insights into the ultrasonic performance of a 2-2 piezocomposite. It is the purpose of this work to explore the possibility of using similar approach to 1-3 piezocomposites.

In this article, a simplified wave propagation model will be used to analyze the ultrasonic properties related to the thickness resonance of 1-3 composites and the results will be compared with experiment. Comparison will also be made with the quasi-static model to show the range of its validity. Since the mechanical  $Q$  of a composite is an important parameter in determining the bandwidth of the transducer made from it, experiment and model analysis are also made to show that the mechanical  $Q$  of a composite is not a simple extrapolation between the two end constituent phases (i.e., ceramic and polymer) and can be much smaller than those of both constituents. In addition, experimental results will be presented regarding the frequencies of the lateral modes and

<sup>a)</sup>Current address: Blatek, Inc. State College, PA 16801.

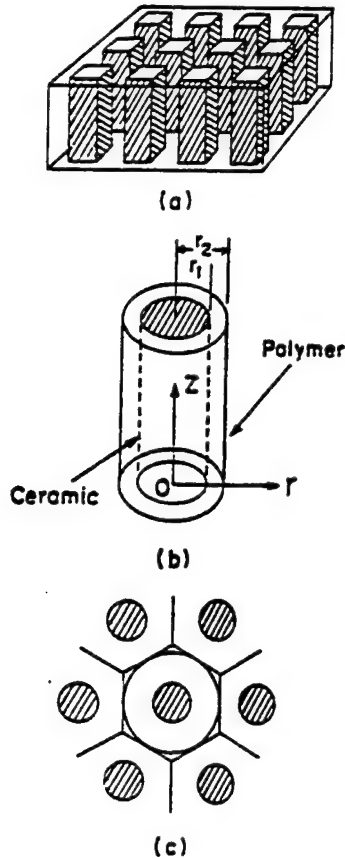


FIG. 1. (a) Schematic drawing of a 1-3 piezocomposite having a square unit cell. (b) A concentric unit cell and the coordinate system for a 1-3 composite ( $d=2r_2$ ). (c) Schematic drawing of a 1-3 composite with ceramic rods arranged in a hexagonal periodic array. A concentric unit cell may be used to approximate hexagonal unit cell as shown.

it will be shown that simple relationships exist between the frequencies positions of these modes and the parameters of the polymer matrix.

## II. SAMPLE PREPARATION

In order to compare the model results with experiment, 1-3 piezocomposites with different ceramic volume fractions were prepared by a dice and fill method. The ceramic used was the commercial PZT-5H disk and the polymer matrix was Spurr epoxy.<sup>12</sup> In the fabrication of 1-3 composites, PZT-5H ceramic disk was first diced in one direction periodically by Isomet 1000 dicing saw and the ceramic volume fraction is determined by the ratio of the kerf width/period. For example, for a 1-3 composite with 40.5% ceramic volume content, the periodicity is 1.024 mm and the kerf width is 0.355 mm. After the dicing, the sample was carefully cleaned by acetone, and the Spurr epoxy was then filled into the kerf. Any possible gas bubbles in the polymer were removed by placing the sample in a vacuum for more than an hour. The polymer matrix was then cured at 50°C in the oven for 8 h. After curing, the sample was cut in the perpendicular direction to the first cut with the periodicity and the kerf the same as the first cut, and then cleaned, filled with epoxy and cured. Because the ceramic may be partially de-poled in the process of cutting, curing and polishing, the final 1-3 composite was repoled in 70°C oil for 5 min under a 2

kV/mm dc electric field. Different thickness samples were used to vary the thickness resonance frequency and the electric impedance was measured by an HP 4194 Impedance Analyzer.

## III. WAVE PROPAGATION IN AN UNBOUNDED 1-3 PIEZOCOMPOSITE

In general, a 1-3 composite, such as shown in Fig. 1(a), has a three-dimensional structure and although its dynamic behavior can be treated using the approach in Refs. 13 and 14, the mathematics involved is quite complicated and cumbersome. To simplify the mathematics of the analysis, we will investigate the possibility of using the concentric unit cell Fig. 1(b), which is an approximation to the unit cell of a 1-3 composite having the ceramic rods arranged in a hexagonal lattice as schematically drawn in Fig. 1(c), to analyze the ultrasonic properties of a 1-3 composite at the thickness resonance. Such an approximation reduces the problem to a two-dimensional one which is much simpler and as will be shown in the article the model results on the thickness resonance compare quite well with experimental data.

The cylindrical coordinate system is chosen for the unit cell shown in Fig. 1(b) where the  $z$  axis is along the poling direction of the piezoceramic rod, the  $r$  axis is along the radial direction and the  $\theta$  axis is perpendicular to the  $r$ - $z$  plane, respectively. Because of the axial symmetry, the governing equations become<sup>15</sup>

$$\frac{\partial T_{rr}}{\partial r} - \frac{\partial T_{rz}}{\partial z} + \frac{1}{r}(T_{rr} - T_{\theta\theta}) = \rho \frac{\partial^2 u_r}{\partial t^2}, \quad (1a)$$

$$\frac{\partial T_{rz}}{\partial r} - \frac{T_{rz}}{r} - \frac{\partial T_{zz}}{\partial z} = \rho \frac{\partial^2 u_z}{\partial t^2}, \quad (1b)$$

$$\frac{\partial D_r}{\partial r} - \frac{1}{r}D_r + \frac{\partial D_z}{\partial z} = 0. \quad (1c)$$

The symbols adopted in this article are summarized as follows:  $T_{ij}$  and  $S_{ij}$  are the stress and strain tensor components,  $u_i$  is the elastic displacement vector,  $\rho$  is the density,  $D_i$  is the electric displacement vector, and  $E_i$  the electric field. The relevant material coefficients are:  $e_{ij}$  is the piezoelectric coefficient,  $c_{ij}$  is the elastic stiffness, and  $\epsilon_i$  the dielectric permittivity. Equation (1) holds for both polymer and piezoceramic phases.

The constitutive equations for the piezoceramic in the cylindrical coordinate system are

$$T_{rr} = c_{11}^E \frac{\partial u_r}{\partial r} + c_{12}^E \frac{u_r}{r} + c_{13}^E \frac{\partial u_z}{\partial z} - e_{31} E_z, \quad (2a)$$

$$T_{\theta\theta} = c_{12}^E \frac{\partial u_r}{\partial r} + c_{11}^E \frac{u_r}{r} + c_{13}^E \frac{\partial u_z}{\partial z} - e_{31} E_z, \quad (2b)$$

$$T_{zz} = c_{13}^E \frac{\partial u_r}{\partial r} + c_{13}^E \frac{u_r}{r} + c_{33}^E \frac{\partial u_z}{\partial z} - e_{33} E_z. \quad (2c)$$

$$T_{rz} = c_{44}^E \left( \frac{\partial u_r}{\partial z} + \frac{\partial u_z}{\partial r} \right) - e_{15}^E E_r, \quad (2d)$$

$$D_r = e_{15}^E \left( \frac{\partial u_r}{\partial z} + \frac{\partial u_z}{\partial r} \right) + \epsilon_{11}^E E_r, \quad (2e)$$

$$D_z = e_{31}^E \left( \frac{\partial u_r}{\partial r} + \frac{u_r}{r} \right) + e_{33}^E \frac{\partial u_z}{\partial z} + \epsilon_{33}^E E_z. \quad (2f)$$

For the polymer phase,  $e_{ki}$  in Eq. (2) is zero. The superscripts  $E$  and  $S$  indicate that the coefficients are under the constant electric field and constant strain conditions, respectively. Under the quasi-electrostatic approximation, the electric field  $E$  is related to the electrical potential  $\Phi$

$$\vec{E} = -\nabla\Phi. \quad (3)$$

Combining Eqs. (1), (2), and (3) yields differential equations governing the elastic displacement  $u_r$ ,  $u_z$ , and the electrical potential  $\Phi$  in the piezoceramic rod and in the polymer, respectively.<sup>11</sup> The general solutions for the piezoelectric active modes in the ceramic rod have the form:

$$[M_{ij}] = \begin{bmatrix} c_{33}^E \beta^2 + c_{44}^E h^2 - \rho \omega^2 & (c_{13}^E + c_{44}^E) h \beta & e_{33} \beta^2 + e_{15} h^2 \\ (c_{13}^E + c_{44}^E) h \beta & c_{11}^E h^2 + c_{44}^E \beta^2 - \rho \omega^2 & (e_{15} + e_{31}) h \beta \\ e_{33} \beta^2 + e_{15} h^2 & (e_{15} + e_{31}) h \beta & -(e_{11}^E h^2 + e_{33}^E \beta^2) \end{bmatrix}. \quad (5)$$

(where  $h$  is replaced by  $h_i^c$  for  $i = 1, 2$ , and  $3$ , respectively). The time-dependent term  $\exp(-j\omega t)$  is omitted in Eq. (4), where  $\omega$  is the angular frequency.<sup>11</sup>  $R_i^c$  are the coefficients to be determined from the boundary conditions.

Similarly, the solutions for the polymer phase can be obtained<sup>11</sup>

$$u_z^p = \sum_i f_i^p [R_i^p J_0(h_i^p r) + Q_i^p Y_0(h_i^p r)] \sin(\beta z),$$

$$u_r^p = \sum_i g_i^p [R_i^p J_1(h_i^p r) + Q_i^p Y_1(h_i^p r)] \cos(\beta z), \quad (6)$$

$$\Phi^p = [C_1^p J_0(h_3^p r) + C_2^p Y_0(h_3^p r)] \sin(\beta z),$$

where  $i = 1, 2$ , and the superscript  $p$  denotes the polymer. For a nonslippery interface between the ceramic and polymer,  $\beta$  in the polymer should be the same as that in the ceramic.  $Y_0$  and  $Y_1$  are the zeroth-order and first-order Hankel function.  $f_i^p$  and  $g_i^p$  are the cofactors of  $A_{k1}(i)$ ,  $A_{k2}(i)$  of Eq. (5) with all the material parameters replaced by those of polymer phase, and

$$(h_1^p)^2 = (k_L^p)^2 - \beta^2, \quad (h_2^p)^2 = (k_T^p)^2 - \beta^2, \quad \text{and} \quad (h_3^p)^2 = -\beta^2, \quad (7)$$

where  $k_L^p = \omega/\nu_L^p$ ,  $k_T^p = \omega/\nu_T^p$ ,  $\nu_L^p$  and  $\nu_T^p$  are the longitudinal and shear wave velocities in the polymer phase, respectively.  $R_i^p$ ,  $Q_i^p$ ,  $C_1^p$ , and  $C_2^p$  are the coefficients to be determined by the boundary conditions.

$$u_z^c = \sum_i R_i^c f_i^c J_0(h_i^c r) \sin(\beta z),$$

$$u_r^c = \sum_i R_i^c g_i^c J_1(h_i^c r) \cos(\beta z), \quad (4)$$

$$\Phi^c = \sum_i R_i^c r_i^c J_0(h_i^c r) \sin(\beta z),$$

where  $i$  runs from 1 to 3 and the superscript  $c$  denotes the ceramic.  $J_0$  and  $J_1$  are zeroth-order and first-order Bessel function.  $\beta$  is the wave vector component along the  $z$  direction ( $\beta = 2\pi/\lambda$ , where  $\lambda$  is the wavelength along the same direction) and  $h_i$  is the wave vector perpendicular to that direction. For each  $\beta$ , there are three  $h$ ,  $h_1^c$ ,  $h_2^c$ , and  $h_3^c$ , corresponding to the quasi-electromagnetic, quasi-longitudinal, and quasi-shear waves in the piezoceramic rod, respectively.  $f_i^c$ ,  $g_i^c$  and  $r_i^c$  are the cofactors of  $A_{k1}(i)$ ,  $A_{k2}(i)$ , and  $A_{k3}(i)$  of the determinant:

The expressions of the stresses and the electric displacement in the ceramic rod and the polymer phase can be obtained by substituting the equations of the elastic displacement and electric potential into the constitutive equations [Eq. (2) for the ceramic rod].<sup>11</sup>

The boundary conditions at the ceramic polymer interface ( $r = r_1$ ) are

$$u_r^c = u_r^p, \quad u_z^c = u_z^p, \quad T_{rr}^c = T_{rr}^p, \quad T_{rz}^c = T_{rz}^p, \quad (8a)$$

$$\Phi^c = \Phi^p, \quad D_r^c = D_r^p, \quad (8b)$$

and the symmetry conditions at  $r = r_2$  require

$$T_{rz}^p = 0, \quad u_r^p = 0, \quad D_r^p = 0. \quad (8c)$$

From Eq. (8), the relationship between  $\omega$  and  $\beta$ , the dispersion relations, can be determined. For each pair of  $\omega$  and  $\beta$ , the relationships among  $R_i^c$ ,  $R_i^p$ ,  $Q_i^p$ , and  $C_j^p$  [in Eqs. (4) and (6)] can be obtained.<sup>11</sup>

#### IV. EFFECTIVE ELECTROMECHANICAL PROPERTIES OF A 1-3 PIEZOCOMPOSITE

The longitudinal wave velocity of a 1-3 piezocomposite is determined from the dispersion curves using  $V_{ph} = \omega/\beta$ . Presented in Fig. 2(a) is the comparison of the theoretical and experimental results of the longitudinal wave velocity  $V^D$  as a function of  $d/t$  ( $t$  is the thickness of the composite and  $d = 2r_2$ , and at the thickness resonance  $\beta = 2\pi/\lambda = \pi/t$  for a 1-3 piezocomposite with 40% ceramic volume fraction. In this article, except otherwise specified, the composite

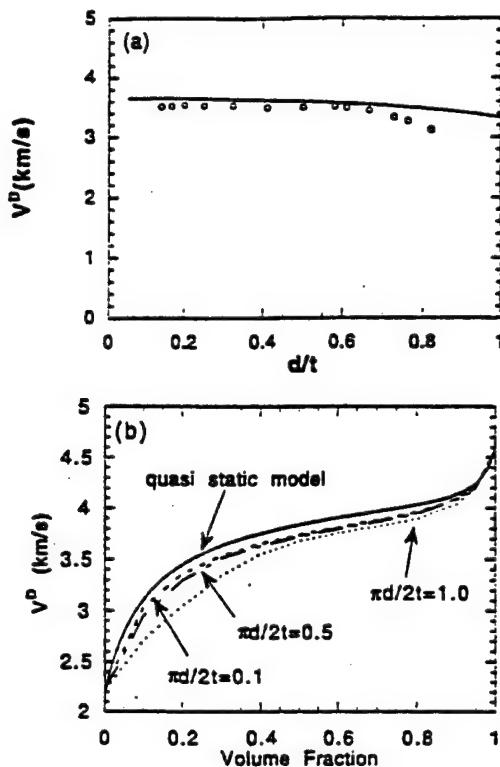


FIG. 2. (a) Longitudinal wave velocity of a 1-3 piezocomposite with 40% ceramic content as a function of  $d/t$ . The open circles are the experimental results and solid line is from the model. (b) The longitudinal wave velocity as a function of ceramic volume fraction for composites with different  $d/t$  derived from the model. For the comparison, the result from the quasi-static model is also included.

have PZT-5H as the piezoceramic and Spurr epoxy as polymer matrix.<sup>12</sup> The parameters of the PZT-5H piezoceramic and the Spurr epoxy are presented in Table I, where the real part of the material parameters is from Ref. 16. The experimental results are obtained by the resonance method using HP4194 Impedance Analyzer from 1-3 piezocomposite plates with different thickness  $t$  (the sample thickness  $t$  ranges from 0.5 to 5 mm) and  $V^D = 2 f_p t$  ( $f_p$  is the parallel resonance frequency). The agreement is very good for  $d/t$  less than 0.65. At  $d/t$  higher than 0.65, the theoretical results deviate from the experimental values, which is due to the concentric unit cell approximation used in the analysis which cannot treat the mode coupling correctly.

Shown in Fig. 2(b) is the dependence of the longitudinal wave velocity on ceramic volume fraction for a 1-3 piezocomposite with different ratio of  $d/t$ . The lowering of  $V^D$  for  $d/t=0.63$  shown at the low ceramic volume content region (at the ceramic volume content less than 40%) in the figure is due to the coupling of the thickness mode with the lateral mode. For composites with higher ceramic volume content, this coupling will occur at higher  $d/t$  and correspondingly, the lowering of  $V^D$  will occur at higher values of  $d/t$ . Away from the coupling region (in practical design, the frequency of the first lateral mode is chosen to be at twice that of the thickness mode),  $V^D$  exhibits very little dependence on  $d/t$  which is consistent with the data in Fig. 2(a) and earlier experiment results.<sup>17</sup> For the comparison,  $V^D$  from quasi-static model are also shown in Fig. 2(b).<sup>3,4</sup> And  $V^D$  derived

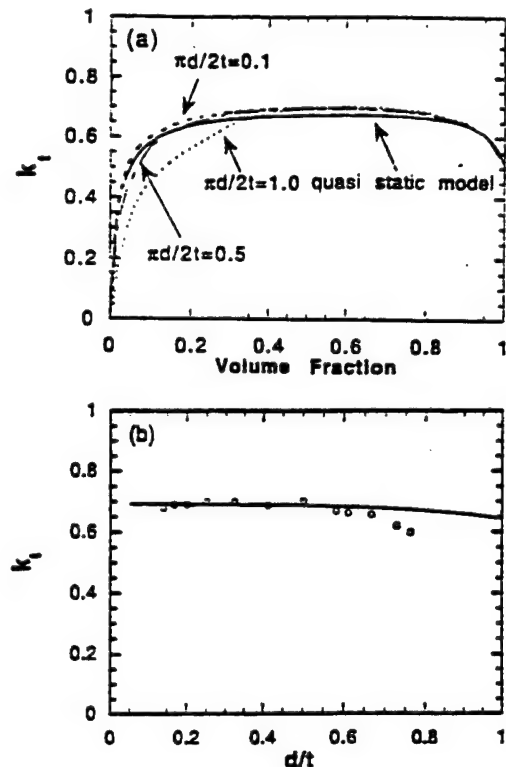


FIG. 3. (a) Electromechanical coupling coefficient  $k_t$  as a function of ceramic volume fraction for composites with different  $d/t$  derived from the model. For the comparison, the result from the quasi-static model is also included as the solid line. (b) The electromechanical coupling coefficient  $k_t$  of a 1-3 piezocomposite with 40% ceramic content as a function of  $d/t$ . The open circles are the experimental results and solid line is from the model.

from the quasi-static model is higher than that determined from this model and experimental data.

The thickness mode electromechanical coupling coefficient of a 1-3 piezocomposite is derived in the model from<sup>16</sup>

$$k_t^2 = 1 - \left( \frac{v_t^E}{v_t^D} \right)^2, \quad (9)$$

where  $v_t^E$  and  $v_t^D$  are the longitudinal wave velocity under constant  $E$  and constant  $D$  conditions, respectively. Presented in Fig. 3(a) is the dependence of  $k_t$  on ceramic volume fraction for a 1-3 piezocomposite with different  $d/t$ . Again, the reduction in  $k_t$  at the low ceramic volume fraction region for the curve with  $d/t=0.63$  is due to the coupling to the lateral mode. At  $d/t$  away from the coupling region,  $k_t$  exhibits very little dispersion. For the comparison, the results from the quasi-static model is also presented in the figure and  $k_t$  from the quasi-static model is less than that from this model even when  $d/t$  approaches zero, where the thickness of the composite is much larger than the period.

The thickness coupling factor for a 1-3 piezocomposite with 40% ceramic volume content was evaluated experimentally using the relation:<sup>18</sup>

$$k_t^2 = \frac{\pi f_s}{2 f_p} \tan \left( \frac{\pi f_p - f_s}{2 f_p} \right), \quad (10)$$

where  $f_s$  and  $f_p$  are the series and the parallel resonance frequencies of the 1-3 piezocomposite plate, respectively. The dependence of the theoretical and experimental electro-

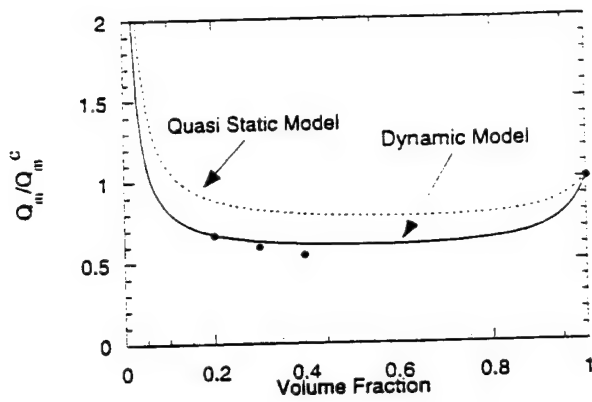


FIG. 4. Quality factor  $Q_m$  of 1-3 piezocomposites as a function of ceramic volume fraction.  $Q_m$  is evaluated at  $d/t=0.063$  and  $f=117$  kHz ( $\eta_{11}=20.7$  N/m<sup>2</sup>s and  $\eta_{44}=11.0$  N/m<sup>2</sup>s for the polymer).  $Q_m^c$  is the quality factor for the piezoceramic (poled PZT-5H). The result from the quasi-static model is included as the dashed line. The experimental data are represented as black dots.

mechanical coupling coefficient  $k$ , on the aspect ratio  $d/t$  is shown in Fig. 3(b) for composites with 40% ceramic content. The agreement between the two is excellent for  $d/t$  less than 0.65. At  $d/t$  above 0.65, the deviation of the theoretical value from the experimental one is due to the concentric unit cell approximation used in the model which cannot describe the mode coupling between thickness mode and lateral mode correctly.

## V. LOSSES IN 1-3 PIEZOCOMPOSITES

In the previous sections, the losses in the materials have not been included in the analysis. However, as has been demonstrated in many experiments, loss in a 1-3 piezocomposite is much higher and hence the mechanical  $Q$  is much lower than that in piezoceramic. Therefore, it is very important to include the losses in the analysis. For practical transducer applications, a material with a mechanical  $Q$  much lower than that of piezoceramics is desirable in order to broaden the transducer bandwidth.

In general, there are three types of losses in a piezoelectric material, i.e., mechanical loss, dielectric loss, and piezoelectric loss. In the polymer phase, there are only mechanical loss and dielectric loss. The losses in the ceramic phase can be expressed by complex constants.<sup>19</sup>

$$\begin{aligned} c_{ij}^E &= c_{ij}^{E'} + j c_{ij}^{E''}, \\ e_{ij} &= e_{ij}' + j e_{ij}'', \end{aligned} \quad (11)$$

$$\epsilon_{ij}^S = \epsilon_{ij}^{S'} - j \epsilon_{ij}^{S''}$$

and the losses in the polymer phase can be expressed as

$$c_{ij} = c_{ij}' + j c_{ij}'', \quad (12)$$

$$\epsilon = \epsilon' - j \epsilon''.$$

From the fact that the attenuation in piezoceramic is proportional to frequency, the imaginary part of the parameters in ceramic can be assumed constants.<sup>20</sup> While in the polymer phase, the main loss mechanism is due to viscosity, therefore,  $c_{ij}'' = \omega \eta_{ij}$ , where  $\eta_{ij}$  is the viscosity coefficient of the polymer.

The quality factor  $Q$  (or the mechanical  $Q$ ) for the thickness mode of a 1-3 piezocomposite is evaluated from the dispersion curves using the relation:

$$Q = \frac{\beta_r}{2\beta_i}, \quad (13)$$

where  $\beta_r$  and  $\beta_i$  are the real and imaginary part of the wave vector  $\beta$ , respectively. Presented in Fig. 4 is the  $Q$  of a 1-3 piezocomposite as a function of ceramic volume fraction evaluated at  $d/t=0.063$ . The loss parameters used in the calculation are those of PZT-5H for the ceramic phase and Spurr epoxy for the polymer (listed in Table I). Those parameters are obtained from several sources: the dielectric losses for the PZT-5H ceramic and the elastic losses in Spurr epoxy were measured here; the elastic losses and the piezoelectric losses for the PZT-5H ceramic are taken from Refs. 21 and 22. The elastic loss for the polymer is evaluated at 117 kHz which yields a mechanical  $Q=2.22 \times 10^3$  for the polymer (which seems to be very high, however, it was derived directly from measured viscosity coefficient  $\eta$  at 2.5 MHz). The mechanical  $Q$  in the polymer phase is inversely proportional to frequency while in the ceramic phase it is a constant.

The results in Fig. 4 show that the quality factor of a 1-3 piezocomposite is less than that of both the ceramic and polymer for the composites evaluated. For the comparison, the quality factor for the thickness mode of several 1-3 composites with different ceramic content and single phase PZT-5H ceramic plate was experimentally determined.<sup>18</sup> The experiment data are also presented in the figure which is consistent with the theoretical results. The result here is quite different from the real part of the elastic constant of a 1-3 composite which always lies in between the two end phases. This is also in contrary to the common belief that the low

TABLE I. Material parameters for the PZT-5H and Spurr epoxy used in the model calculation.

Ceramic: $c_{11}^E = 12.72 \times 10^{10} (1.0 + j 8.0 \times 10^{-3})$ N/m <sup>2</sup> , $c_{33}^E = 11.74 \times 10^{10} (1.0 + j 8.0 \times 10^{-3})$ N/m <sup>2</sup> , $c_{12}^E = 7.95 \times 10^{10} (1.0 - j 6.5 \times 10^{-3})$ N/m <sup>2</sup> , $c_{13}^E = 8.47 \times 10^{10} (1.0 + j 6.5 \times 10^{-3})$ N/m <sup>2</sup> , $c_{44}^E = 2.3 \times 10^{10} (1.0 + j 1.2 \times 10^{-3})$ N/m <sup>2</sup> ; $e_{11}^S = 1700 \epsilon_0 (1.0 - j 2.7 \times 10^{-3})$ , $e_{33}^S = 1470 \epsilon_0 (1.0 - j 2.7 \times 10^{-3})$ , $e_{31}^S = 23.09 (1.0 - j 5.4 \times 10^{-3})$ C/m <sup>2</sup> , $e_{15}^S = 17.0 (1.0 - j 5.0 \times 10^{-3})$ C/m <sup>2</sup> , $e_{31} = -6.6 (1.0 - j 7.2 \times 10^{-3})$ C/m <sup>2</sup> , $\rho^c = 7500$ kg/m <sup>3</sup> .	
Polymer: $c_{11}^p = 5.41 \times 10^9$ N/m <sup>2</sup> , $c_{44}^p = 1.307 \times 10^9$ N/m <sup>2</sup> , $\eta_{11} = 20.74$ N/m <sup>2</sup> s, $\eta_{44} = 11.0$ N/m <sup>2</sup> s; $\epsilon_{11}^p = 4.0 \epsilon_0$ , $\rho^p = 1100$ kg/m <sup>3</sup> .	



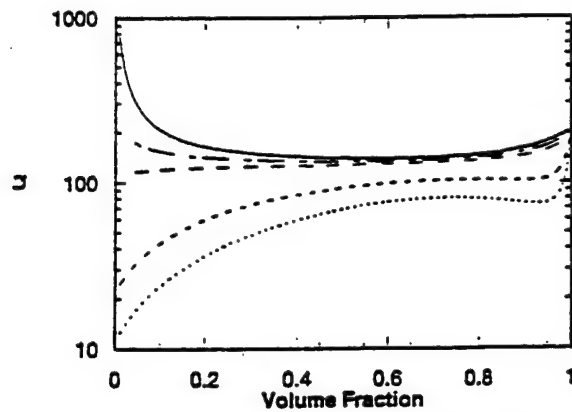


FIG. 5. Influence of elastic loss of polymer on the quality factor of a 1-3 piezocomposite as a function of ceramic volume fraction, where  $Q_p^D$  for each curve (from top to bottom) is 2220, 222, 111, 22.2, and 11.1, respectively. The losses for the ceramic phase is from depoled PZT-5H which piezoelectric coefficients are zero.

mechanical  $Q$  in a 1-3 composite is a result of the loss in the polymer phase. In fact, in the composite evaluated, the mechanical  $Q$  of the polymer phase (Spurr epoxy) is much higher than that of the piezoceramic, while the  $Q$  of the 1-3 composite is lower than that of the piezoceramic. The similar conclusion can also be obtained from the quasi-static model, which is presented in Fig. 4, where the quality factor is equal to  $1/\tan \delta$  of  $\bar{\epsilon}_{33}^D$  (the effective elastic constant of the composite at the constant electric displacement  $D$ ).

To examine whether the observed effect is due to the piezoelectric coupling, the quality factor for a 1-3 composite without piezoelectricity is also derived and the results are presented in Fig. 5 where the parameters are taken from Spurr epoxy and unpoled PZT-5H ceramic (no piezoelectric effect) and the mechanical  $Q$  of the ceramic is about 200. Apparently, the quality factor here is still less than that of both ceramic and polymer when the  $Q$  of the polymer phase is larger than that of the ceramic. On the other hand, when the  $Q$  of the polymer phase becomes smaller than that of the ceramic, the quality factor of the composite lies between that of the polymer and ceramic.

To elucidate how different losses of the ceramic phase in a composite influence the quality factor of the composite transducer, calculation is carried out for model composites with different losses in the ceramic. Presented in Fig. 6 are the results for a 1-3 piezoceramic composite in which the piezoceramic has dielectric loss only (no piezoelectric and elastic losses) and piezoelectric loss only (the dielectric and elastic losses are assumed to be zero). In both cases, the trend of quality factor with the ceramic volume fraction is quite similar to those in the pure elastic case as shown in Fig. 5. Apparently, through the piezoelectric coupling in the material, both the piezoelectric and dielectric losses reduces the mechanical  $Q$  of a 1-3 composite. It should be pointed out that in general, a piezoelectric loss may not imply a real energy loss. Although for the materials examined here, the piezoelectric loss reduces the mechanical  $Q$  of the thickness resonance mode, it can also be an energy gain in other cases which means an increase in the mechanical  $Q$ , as has been pointed out by Holland.<sup>21</sup>

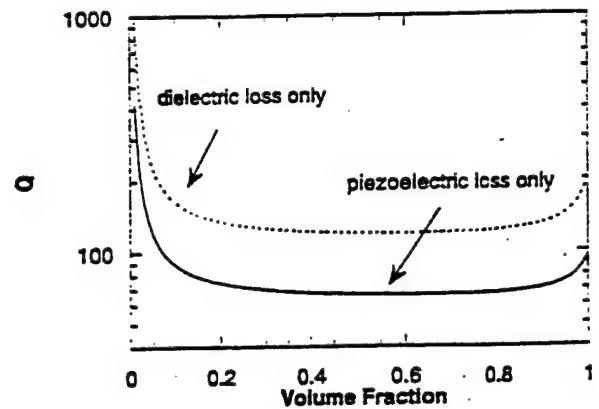


FIG. 6. Contribution of dielectric loss (no elastic and piezoelectric losses) and piezoelectric loss (no dielectric and elastic loss) of piezoceramic to the quality factor of a 1-3 piezocomposite as a function of ceramic volume fraction, where the  $\tan \delta$  of dielectric constant is 2% and the  $\tan \delta$  of the piezoelectric coefficient  $e_{ij}$  is 2%. The curves are evaluated at  $d/r=0.063$  and  $Q_p=2220$  for polymer.

Presented in Fig. 7(a) are the results when all the losses in a 1-3 composite are included (data in Table I), where the different polymer loss can be corresponding to different thickness resonance frequency. Since the elastic loss in a polymer increases linearly with frequency, different level of polymer loss may be obtained by using composite samples with different thickness mode resonance frequencies. It can

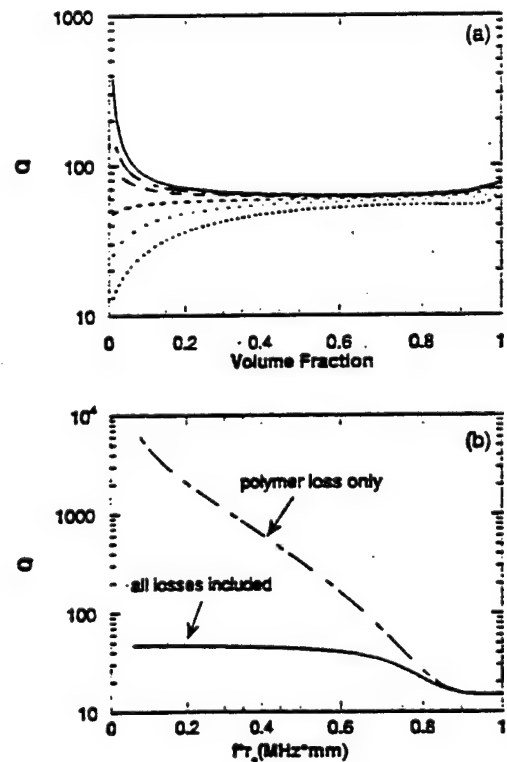


FIG. 7. (a) Quality factor of a 1-3 piezocomposite with both the elastic loss of the polymer and the elastic, dielectric, and piezoelectric losses of the piezoceramic, where the quality factor  $Q_p^D$  (polymer) for each curve (from the top to the bottom) is 2220, 222, 111, 44.4, 22.2, and 11.1, respectively. (b) Quality factor of a 1-3 composite with 40% ceramic content as a function of frequency when the loss is from the polymer only (dashed line) and when all the losses are included (solid line).

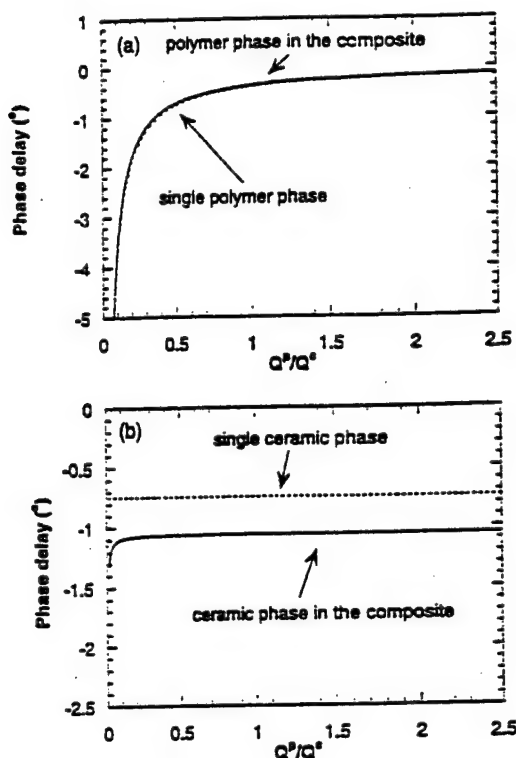


FIG. 8. (a) Comparison of the phase delay between the strain and stress in polymer as a single phase material (dashed line) and in composite (solid line). (b) Comparison of the phase delay between the strain and stress in ceramic as a single phase material (dashed line) and in composite (solid line). Apparently, by compositing, the phase delay in the polymer is reduced while in the ceramic, it is increased. The ceramic volume content is 10%.

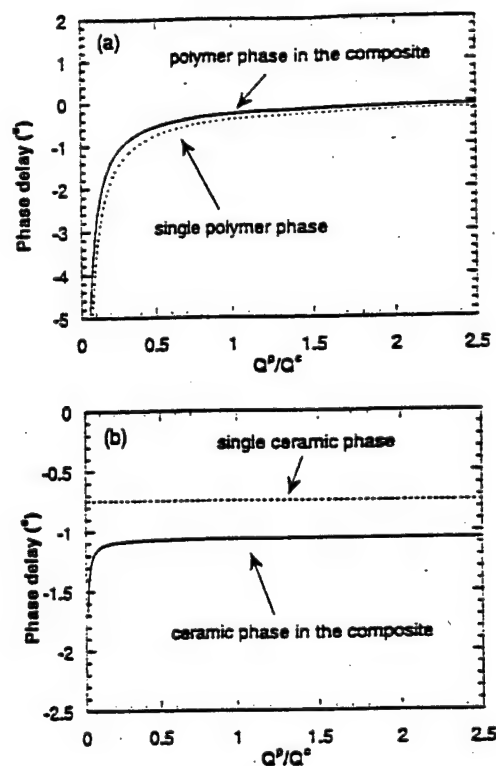


FIG. 9. (a) Comparison of the phase delay between the strain and stress in polymer as a single phase material (dashed line) and in composite (solid line). (b) Comparison of the phase delay between the strain and stress in ceramic as a single phase material (dashed line) and in composite (solid line). The ceramic volume content is 40%.

be seen that at high ceramic volume content (for example, >40%), the polymer loss does not have a significant effect on the quality factor of a composite transducer. For example, as the mechanical  $Q$  of the polymer is reduced from more than 2000 down to about 10, the  $Q$  of the composite changes only from about 63 to 47 for a composite of 40% ceramic volume content. On the other hand, the losses in the ceramic phase seem to play more important role in determining the mechanical  $Q$  of the composite. To illustrate that, in Fig. 7(b), the  $Q$  for a composite with losses from the polymer phase only, i.e., there is no loss in the piezoceramic, and for a composite with all the losses included is plotted as a function of frequency, where the ceramic volume content is 40% and the quality factor of the ceramic (PZT-5H) is 75. Since the quality factor is defined as the ratio of stored mechanical energy vs. mechanical energy loss in one cycle and as seen from Table I, the elastic constants of the ceramic are more than ten times higher than those of the polymer, only when the loss in the polymer becomes much higher than that of the ceramic, will it have significant effect on the quality factor of a piezocomposite, as shown in Fig. 7(b).

The acoustic coupling between the ceramic and polymer in a composite changes the phase relationship between the stress and strain in both phases. Shown in Figs. 8 and 9 are the phase angle  $\delta$  between the stress ( $T_{zz}$ ) and strain ( $S_{zz}$ ) along the  $z$  direction at the polymer center ( $r=r_2$ ) and ceramic rod center ( $r=0$ ) as a function of  $Q^p/Q^c$ , the ratio of the mechanical  $Q$  in the two phases. Two compositions are

examined, one with the ceramic content at 10% (Fig. 8) and the other at 40% (Fig. 9). In the figures, the dashed lines are the  $\delta$  in the single phase material and the solid lines are the  $\delta$  in the composites. Apparently, for the polymer phase, the  $\delta$  is reduced when the polymer is in the composite while for the ceramic, it is increased in the composite. Further more, the reduction in  $\delta$  in the polymer increases with ceramic volume content of the composite, and as shown in Fig. 10, for composites with ceramic volume fraction higher than

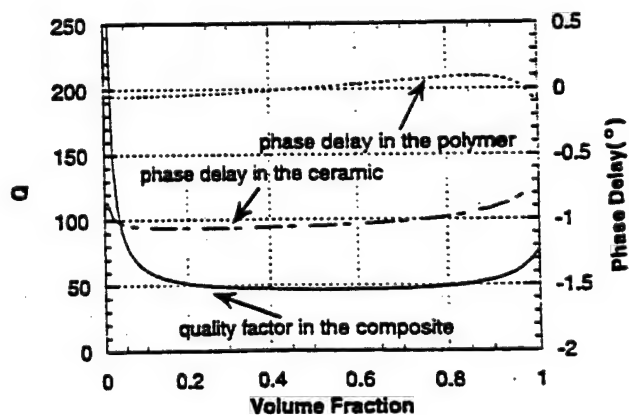


FIG. 10. Change of the phase delay  $\delta$  in the center of the polymer region and the center of the ceramic region of a composite as a function of the ceramic volume content. The polymer has a  $Q=2220$  and the calculation carried out at  $d/r=0.063$ . The corresponding quality factor of the composite is also included in the figure.

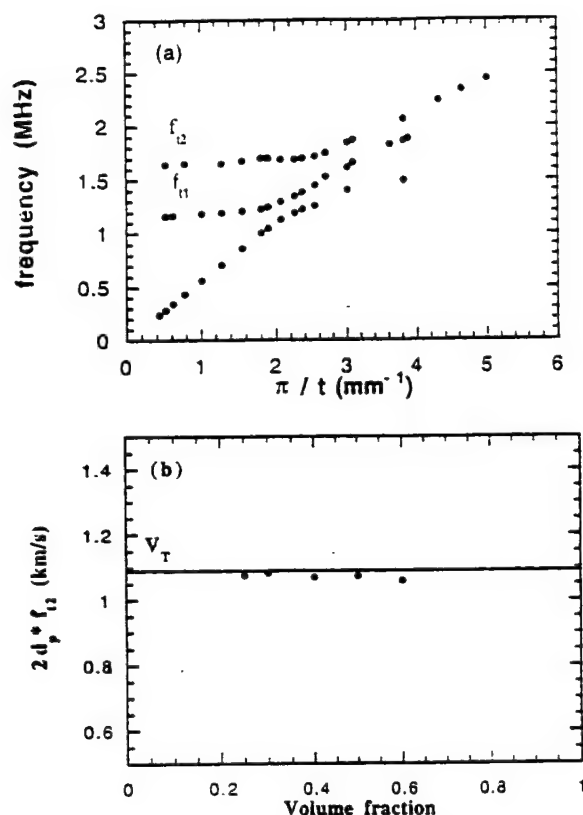


FIG. 11. (a) Experimental dispersion curves of a 40% 1-3 composite with a square unit cell. (b) Comparison between  $2d_p f_{12}$  (open circles, experimental data) and the shear wave velocity  $V_t$  of the polymer (solid line) for 1-3 composites with square unit cell with different ceramic volume fraction.

45%, the phase delay in the polymer even becomes positive. Hence the large increase in the  $\delta$  in the ceramic phase of the composite is the main reason causing the drop in the quality factor of composites since, as pointed out, the high elastic constants in the ceramic phase implies that in most cases, the loss in the ceramic region plays a dominant role in controlling the mechanical  $Q$  of the thickness mode of a composite.

## VI. DISPERSION CURVES AND THE LATERAL MODES IN 1-3 COMPOSITES

In designing 1-3 composites, the frequency of lateral modes with respect to the thickness mode is often a concern. In this section, the experimental results on the lateral modes from piezocomposites as schematically shown in Fig. 1(a) will be presented which reveal several relations between the frequency of these modes and the gap width and shear velocity of the polymer matrix.

Presented in Fig. 11(a) are the first three branches of the dispersion curves for a 1-3 composite with 40% ceramic volume fraction (thickness  $t$  from 0.6 to 8 mm and the polymer gap width  $d_p = 0.36$  mm). At small  $\pi/t$  limit, the first branch corresponds to the thickness resonance and the second and third branches are the two lateral modes  $f_{11}$  and  $f_{12}$ , respectively. It was found that at small  $\pi/t$ , the frequency of the second lateral mode  $f_{12}$  can be related to the polymer gap width  $d_p$  through

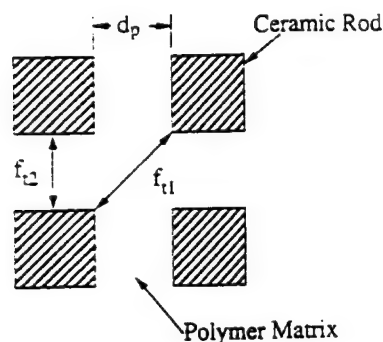


FIG. 12. Schematic of the lateral resonance modes in a 1-3 composite with square unit cell.  $f_{12} = V_t/2d_p$  and  $f_{11} = V_t/(2\sqrt{2}d_p)$ .

$$f_{12} = \frac{V_t}{2d_p} \quad (14)$$

where  $V_t$  is the shear velocity of the polymer phase. The result indicates that the second lateral mode can be viewed as a half-wave resonance in the polymer gap as depicted in Fig. 12. In addition, the frequency  $f_{11}$  (the first lateral mode) can be related to  $f_{12}$ .

$$f_{11} = f_{12}/\sqrt{2}$$

a relation which has been known previously.<sup>17</sup> This result suggests that the first lateral mode may correspond to a half-wave resonance across the diagonal direction as shown in Fig. 12. The interpretation here provides a much simpler and reasonable understanding on the nature of the lateral modes in a 1-3 composite and is consistent with the surface vibration profiles obtained from a laser probe reported in Refs. 17 and 23. As shown in Fig. 11(b), Eq. (14) is valid for 1-3 piezocomposites over a broad composition range as examined.

The results suggest that the lateral mode frequencies for 1-3 composites investigated here are determined mainly by the parameters of the polymer matrix: the shear wave velocity and the gap width. This is analogous to the behavior observed in 2-2 composites.<sup>11</sup> In addition, experiment was also conducted and result shows that  $f_{12}$  in Fig. 11(a) is nearly the same as the frequency of the first lateral mode in a 2-2 composite made with the same polymer and gap width (2-2 composite with 63% ceramic volume fraction). Hence, in analogy to 2-2 composites, because the elastic stiffness of the piezoceramic is much higher than that of the polymer, the ceramic can be viewed approximately as having stress free boundary condition and the polymer having fixed boundary condition (both  $u_3$  and  $u_1$  are zero at the interface). As has been demonstrated in our earlier paper,<sup>11</sup> this leads to the result that there are lateral resonance modes in a composite whose frequencies are determined mainly by the polymer gap properties.

## VII. SUMMARY

A dynamic model is derived for the analysis of the ultrasonic performance of 1-3 piezocomposites. To simplify the mathematics, 1-3 composites with the concentric unit cell was treated in the model which should closely resemble the



unit cell of a 1-3 composite with ceramic rods arranged in a hexagonal lattice. It is shown that the model can describe the thickness resonance of 1-3 composites quite well in the frequency range away from the mode coupling region. In addition, the lateral mode frequencies are examined experimentally and the data reveal that for 1-3 piezocomposites investigated (the elastic stiffness of the ceramic is much higher than that of polymer), the lateral mode frequencies are determined mainly by the polymer gap width and shear velocity. The result provides a useful guideline for the design of 1-3 composite transducers and is also important for the future development of theoretical models regarding the behavior of lateral modes in a 1-3 composite.

In the article, special attention is also paid to the losses in a 1-3 composite and it is found that the quality factor of the thickness mode for a composite is largely determined by the mechanical  $Q$  of the ceramic and its coupling to the polymer phase, which seem to be in contrary to the common belief that the low  $Q$  in a composite is due to the loss in the polymer. Even for a composite with the mechanical  $Q$  of the polymer larger than that of the ceramic, the quality factor (or mechanical  $Q$ ) of the composite is lower than both constituents. It is found that the phase delay between the strain  $S_{zz}$  and stress  $T_{zz}$  in the ceramic increases significantly in the composite compared with the single ceramic material, which is the main reason for the reduction of the quality factor  $Q$  in a composite. On the other hand, the coupling with the ceramic phase reduces the phase delay between the strain  $S_{zz}$  and stress  $T_{zz}$  in the polymer when compared with that in the single phase polymer. Due to the piezoelectric coupling, both the dielectric and piezoelectric losses affect the quality factor of a piezocomposite.

- <sup>1</sup>R. Newnham, *Annu. Rev. Mater. Sci.* **16**, 47 (1986).
- <sup>2</sup>W. A. Smith, *Proceeding of 1990 IEEE ISAF7*, Urbana, Illinois, 1990, p. 145.
- <sup>3</sup>W. A. Smith and B. A. Auld, *IEEE Trans. Ultrason. Ferroelectr. Freq. Control* **38**, 40 (1988).
- <sup>4</sup>K. Y. Hashimoto and M. Yamaguchi, *Proceedings 1986 IEEE Ultrasonics Symposium*, Williamsburg, VA, 1986, p. 697.
- <sup>5</sup>B. A. Auld, H. Kunkel, Y. A. Shui, and Y. Wang, *Proceedings of 1983 IEEE Ultrasonics Symposium* (Atlanta, GA, 1983), p. 554.
- <sup>6</sup>B. A. Auld, Y. A. Shui, and Y. Wang, *J. Phys. (Paris)* **45**, 159 (1984).
- <sup>7</sup>M. Yamaguchi, K. Y. Hashimoto, and H. Makita, *Proceedings of the 1987 IEEE Ultrasonics Symposium*, Denver, CO, 1987, p. 657.
- <sup>8</sup>J. A. Hossack and G. Hayward, *IEEE Trans. Ultrason. Ferroelectr. Freq. Control* **38**, 618 (1991).
- <sup>9</sup>A. Christine, H. Hennen, and J. N. Decarpigny, *J. Acoust. Soc. Am.* **94**, 621 (1993).
- <sup>10</sup>X. Geng and Q. M. Zhang, *Appl. Phys. Lett.* **67**, 3093 (1995).
- <sup>11</sup>X. Geng and Q. M. Zhang, *IEEE Trans. Ultrason. Ferroelectr. Freq. Control* **44**, 857 (1997).
- <sup>12</sup>PZT-5H is the trademark of Morgan Matroc, Inc. OH for one of its piezoceramics. Spurr epoxy is the trademark of Polysciences Inc., PA for one of its epoxy.
- <sup>13</sup>K. Nagaya, *J. Acoust. Soc. Am.* **67**, 2029 (1980).
- <sup>14</sup>H. S. Paul and M. Venkatesan, *J. Acoust. Soc. Am.* **85**, 163 (1989).
- <sup>15</sup>B. A. Auld, *Acoustic Fields and Waves in Solids* (Wiley, New York, 1973).
- <sup>16</sup>Q. M. Zhang and X. Geng, *J. Appl. Phys.* **76**, 6014 (1994).
- <sup>17</sup>T. R. Gururaja, W. A. Schulze, L. E. Cross, R. E. Newnham, B. A. Auld, and J. Wang, *IEEE Trans. Sonics Ultrason.* **SU-32**, 481 (1985).
- <sup>18</sup>IEEE Standard on Piezoelectricity, *ANSI/IEEE Std 176*, 1987.
- <sup>19</sup>R. Holland, *IEEE Trans. Sonics Ultrason.* **SU-14**, 18 (1967).
- <sup>20</sup>A. G. Evans, B. R. Tittman, L. Ahlberg, B. T. Khuri-Yakub, and G. S. Kino, *J. Appl. Phys.* **49**, 2669 (1978).
- <sup>21</sup>R. Holland, *Design of Resonant Piezoelectric Devices* (MIT, Cambridge, MA, 1969).
- <sup>22</sup>H. Wang, Q. M. Zhang, and L. E. Cross, *Jpn. J. Appl. Phys., Part 2* **32**, L1281 (1993).
- <sup>23</sup>Dominique Certon, O. Casula, F. Patat, and D. Royer, *IEEE Trans. Ultrason. Ferroelectr. Freq. Control* **44**, 643 (1997).

# **TRANSDUCER STUDIES**

**Frequency Agile  
Transducers**

# **APPENDIX 37**

# FLEXURAL PIEZOELECTRIC TRANSDUCERS WITH FREQUENCY-AGILITY OBTAINED VIA MEMBRANE LOADS

Chad A. Hébert\*  
Wyle Laboratories, El Segundo, CA

George A. Lesieutre†  
Penn State University, University Park, PA

## ABSTRACT

Broadband transducers find uses in many applications. One approach to increasing the bandwidth of a flexural transducer is to add damping to the device, usually decreasing its sensitivity. An alternative approach, useful in some applications, involves active tuning of the natural frequency of a high-sensitivity narrowband device. In this research, membrane loads were used to alter the natural frequencies and electromechanical coupling coefficients of three-layer (trilaminar) piezoelectric ceramic transducers. A coupling coefficient is a measure of the effectiveness with which a piezoelectric material or device converts electrical energy to mechanical energy or vice versa. Applying in-plane loads increased the effectiveness of the transducers by increasing their operating frequency range, while maintaining high coupling coefficients.

Two types of trilaminar flexural transducers were studied: beams and disks. The measured electrical impedance of individual devices was used to determine short and open circuit natural frequencies, and then coupling coefficients. In addition, finite element models were developed and used to predict the same quantities. Rotational springs were used in these models to account for non-ideal experimental boundary conditions, while reduction of the piezoelectric material coupling accounted for loss of performance due to stress depoling and aging. Good agreement between experimental data and theory was obtained.

Significant changes in natural frequencies, as well as increases in coupling coefficients were obtained for both beam and disk transducers. Experiments with the trilaminar beams yielded a 36% change in frequency, with an accompanying 38% increase in coupling coefficient. Experiments with the disks yielded a change in frequency of 13%, and an increase in coupling of 15%. These results demonstrated the feasibility of using membrane loads to improve the frequency agility of flexural piezo transducers.

\* Dynamics Engineer, Member.

† Assoc. Professor, Aerospace Eng'g., Assoc. Fellow.  
Copyright © 1999 by G.A. Lesieutre. Published by  
the American Institute of Aeronautics and Astronautics,  
Inc. with permission.

## INTRODUCTION

Piezoelectric transducers are electro-mechanical devices that convert electrical energy to mechanical energy or vice versa, and often operate over wide frequency ranges. Acoustic transducers of this type are usually tuned to a nominal design frequency. Designing these devices to span a larger range of frequencies while maintaining high sensitivity would greatly increase their utility.

Of particular relevance is the design and use of low frequency transducers. Several kinds of physical configurations have been used for low frequency transducers, including electromagnetic moving coils, flexensionals (Butler *et al.*, 1997) and flexural disks. One type of flexural transducer is the beam bimorph, in which the small nominal displacements of piezoelectric materials are greatly amplified by the bending motion of a beam. Such transducers have applications as sensors and actuators for motion and flow control. Another type of piezoelectric transducer is the flexural disk, with applications in the low frequency to ultrasonic ranges. As shown in Figure 1, examples of this type include sound generating buzzers and piezoelectric pumps (Waanders, 1991). The basic construction of a piezoelectric flexural disk involves two piezoceramic disks, each bonded to one side of a metal disk. Application of an electric field induces expansion on one side and contraction on the other, resulting in bending of the device.

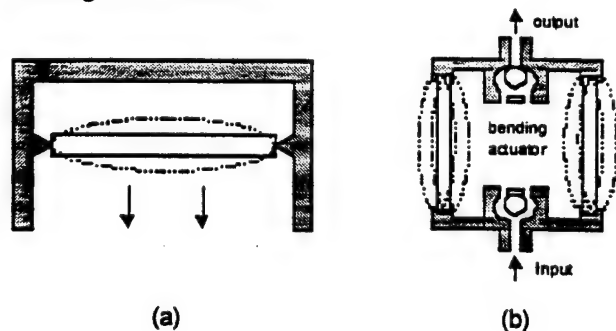


Figure 1: Sound Buzzer (a) and Pump (b) Applications

Several performance measures are important in the design of piezoelectric devices, including coupling coefficient, quality factor and bandwidth (Hughes,

1998). The device coupling coefficient affects the amount of electrical energy converted to mechanical or vice versa. An increase in coupling coefficient means, for example, that a sensor converts more of the energy in an imposed mechanical signal to electrical energy. The quality factor is related to the sensitivity of the device to harmonic signals at frequencies near its resonance frequency. With a high quality factor, a small input produces a large output. Bandwidth is the frequency range in which the sensitivity exceeds a nominal value, usually the half-peak power level near resonance. A common approach to increasing device bandwidth involves increasing damping, however, this decreases device sensitivity. Other issues include size, weight and cost.

The transducers discussed in the preceding are typically designed to operate over a specific frequency range and are usually not tunable. A tunable "frequency-agile" transducer could maintain high sensitivity at discrete frequencies over a broad design range, instead of low broadband sensitivity associated with a fixed design frequency. Such increased performance could perhaps reduce the amount of active material used in a device, thus decreasing its size, weight and cost.

Lesieutre and Davis (1997) recently investigated the use of membrane loads to alter the natural frequencies and coupling coefficients of trilaminar piezoceramic beams. The basic principle involves increasing or decreasing the lateral stiffness of a device using a tensile or compressive in-plane load, with resulting effects on device natural frequency and coupling coefficient. The work described herein verifies and extends their work, addressing trilaminar disks in addition to beams. In addition, improved models are presented, along with detailed consideration of experimental boundary conditions, stress depoling and aging of the piezoceramic material. Experiments and analytical results showed good agreement. The application of a compressive in-plane load to each type of device decreased its natural frequency and increased its coupling coefficient.

### MEASUREMENT OF DYNAMIC CHARACTERISTICS

Piezoelectric devices behave electrically as capacitors. Furthermore, the electrical impedance of a device can be used to effectively characterize device dynamic behavior. The impedance ( $Z$ ) of an electrical element, defined in Equation 1, is a complex, frequency-dependent quantity relating voltage and current (Cogdell, 1990). Figure 2 shows the magnitude of the electrical impedance of a typical piezoelectric flexural device.

$$Z(i\omega) = \frac{V(i\omega)}{I(i\omega)} \quad (1)$$

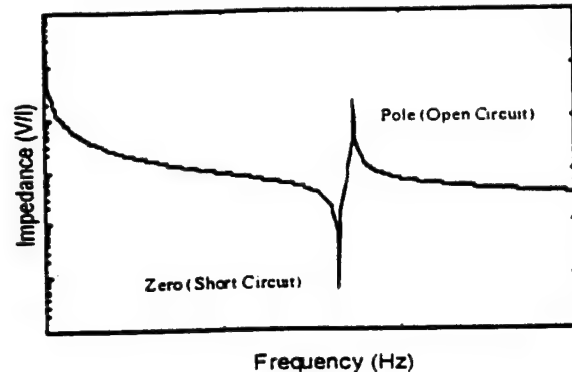


Figure 2: Impedance Magnitude vs. Frequency

The "zero" and "pole" in Figure 2 correspond to the natural frequencies of the device under short- and open-circuit conditions, respectively. A short-circuit condition corresponds to zero voltage across an electrical element and, from Equation 1, minimum impedance. An open-circuit condition corresponds to zero current and maximum impedance. (Johnson *et al.* 1992). The short- and open-circuit natural frequencies can be used to determine effective device coupling coefficients.

An HP 3563A Control Systems Analyzer was used to measure the electrical impedance of various devices. The analyzer produced a driving voltage ( $V_s$ ), while an op-amp circuit on a breadboard was used to convert the current signal to a voltage ( $V_o(I)$ ) (Davis and Lesieutre, 1998). The analyzer determined the impedance based on the two voltage signals.

### TRILAMINAR PIEZOCERAMIC BEAM

#### Modeling

A mathematical model of a trilaminar piezoceramic beam was developed for use in prediction of the behavior of the device under in-plane loads. Figure 3 shows such a beam. The main steps in the analysis were the use of an extended Hamilton's Principle to develop the differential equations and boundary conditions governing its lateral motion. This required the development and use of expressions for the kinetic and potential energies of the device. The effects of shear in the bond layer were considered and found to be negligible. Next, a beam finite element (Weaver and Johnston, 1984) was used to develop a discretized model of the device. The thesis by Hébert (1998) contains additional details of the analysis.



Figure 3: Trilaminar Beam with In-Plane Load

An eigenvalue problem for the natural frequencies and mode shapes of the device was then formulated, as shown in Equation 2. In Equation 2,

[M] is the mass matrix associated with the kinetic energy of the trilaminar beam, [K] is the stiffness matrix associated with the strain energy, and [K<sub>G</sub>] is the geometric stiffness matrix associated with the in-plane load P.

$$[(\mathbf{K}) - [\mathbf{K}_G(P)]] - \omega^2[\mathbf{M}]\{\mathbf{q}\} = \{0\} \quad (2)$$

This eigenvalue problem may be solved for the modal frequencies,  $\omega$ , of the device, under either short- or open-circuit conditions. For the short-circuit condition, the stiffness matrix is formed using the short-circuit elastic modulus of the piezoceramic material given by the manufacturer. For the open circuit condition, an open circuit modulus,  $E_{oc}$ , was calculated using Equation 3 (Crawley *et al.*, 1988), and used for that part of the device stiffness that can be affected by electrical boundary conditions. The 3-1 coupling coefficient of the piezoceramic material,  $k_{31}$ , governs electro-mechanical energy conversion in this device.

$$E_{oc} = \frac{E_{sc}}{1 - k_{31}^2} \quad (3)$$

The effects of the in-plane load on device natural frequency and coupling coefficient were described in terms of a non-dimensional buckling load, namely the ratio of the load to that required to produce buckling of the beam under short circuit conditions. The critical buckling load,  $P_{cr}$ , may be determined from the solution of another eigenvalue problem, as shown in Equation 4.

$$[(\mathbf{K}) - P_{cr}[\mathbf{K}_G(1)]]\{\mathbf{q}\} = \{0\} \quad (4)$$

## Experiments

The piezoceramic beams consisted of a top layer of piezoceramic, a middle layer of metal, and a bottom layer of piezoceramic. The piezoceramic used was APC 855 (American Piezo Ceramics International Ltd., 1997), and the metal was brass. Table 1 summarizes the pertinent geometric and material properties. The beam length was allowed to vary during the analysis to determine the effects of piezoceramic coverage. The exposed length of the brass beam on each side of the piezoceramic was kept consistent.

Table 1: Trilaminar Beam Geometric and Material Properties

	APC 855	Brass
Width (b)	0.0127 m	0.0127 m
Thickness (h)	5.08E-4 m	4.19E-4 m 6.35E-4 m
Length (l)	0.0635 m	Variable
Modulus ( $E_{sc}$ )	67.57E9 N/m <sup>2</sup>	105E9 N/m <sup>2</sup>
Density ( $\rho$ )	7500 kg/m <sup>3</sup>	8470 kg/m <sup>3</sup>
Coupling Factor ( $k_{31}$ )	0.39	

A method of supporting the beam while applying the in-plane load was devised by (Lesieutre and Davis, 1997). The ends of the brass beam were clamped between two aluminum supports and the screws tightened to prevent motion. A vise was then used to apply in-plane loads to the supports. The non-dimensional load ratio ( $P/P_{cr}$ ) was estimated from experimentally determined changes in short circuit natural frequency, as shown in Equation 5 (Lesieutre and Davis, 1997). In this equation,  $f_{\omega}$  is the natural frequency under the no-load condition.

$$\frac{P}{P_{cr}} = 1 - \left( \frac{f_z}{f_{z0}} \right)^2 \quad (5)$$

The coupling coefficient ( $k_{31}$ ) of the trilaminar piezoceramic beam at a given load was estimated from the short- and open-circuit natural frequencies ( $f_z$  and  $f_p$ ), as shown in Equation 6 (Lesieutre and Davis, 1997). The larger the separation between these two frequencies, the greater the device coupling coefficient.

$$k_{31}^2 = \frac{f_p^2 - f_z^2}{f_p^2} \quad (6)$$

*A priori* predictions did not agree well with experimental results: natural frequencies and coupling coefficients were too high. There were two primary reasons for this: non-ideal boundary conditions, and partial stress-depoling of the piezoceramic material under load.

In practice, the mechanical boundary conditions were softer than the classical clamped condition, but stiffer than simply-supported. Springs having finite rotational stiffness were added to the FEM model at the ends of the trilaminar beam, improving the agreement between predictions and experimental results for natural frequencies.

Measured coupling coefficients were initially lower than predicted, no matter what boundary conditions were assumed. Furthermore, for one specimen, coupling coefficients were observed to decrease in subsequent tests. A possible reason for such degradation was aging of the piezoelectric material. According to MIL-STD-1376, these piezoceramics degrade at a rate of about 2.5% per decade. Even with this correction, however, the predicted coupling coefficients were still significantly higher than measured.

Another possible explanation was stress depoling. Zhang *et al.* (1997) recently reported that PZT-5H, a piezoceramic material similar to APC 855, was found to be unsuitable for high stress applications due to its lack of dipole stability. Under compressive uniaxial stress ( $T_1$ ) greater than 50 MPa, there was a significant and permanent loss of performance. The major variable affected was the transverse electromechanical coupling factor ( $k_{31}$ ). Zhang *et al.*

(1997) reported a decrease in  $k_{11}$  from a value of 0.39 to 0.28 after partial stress depolarization had occurred.

Experiments on two trilaminar piezoceramic beams verified this behavior. One beam used APC 855 and the other used APC 850. These materials are similar to the PZT-5H and PZT-5A studied by Zhang *et al.* (1997). Figure 4 shows the effects of increasing compressive load for the trilaminar beam using APC 855. Increasing compressive stress in the piezoceramic on first loading significantly decreased device coupling coefficients relative to FEM predictions. Upon unloading, a permanent loss of performance was found. The results for APC 851 were similar, with a smaller reduction in coupling coefficient. Incorporating stress depoling and aging effects in the model greatly improved the agreement of predictions with experimental results.

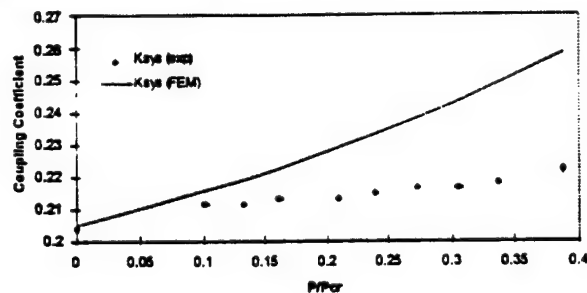


Figure 4: Effect of Initial Compressive Loading on Coupling Coefficient -APC 855

In practice, one way to avoid stress depoling problems is to scale the device dimensions so that the stresses needed to approach a significant fraction of the buckling load are well below those at which stress depoling occurs. Another is the use of a piezoceramic material that is less susceptible to depoling.

## Results

Figure 5 shows results for the dependence of the fundamental natural frequency of the trilaminar beam on load: the results verify the trends presented by Lesieutre and Davis (1997). Both open and short circuit frequencies decreased with increasing in-plane load, in good agreement with predictions of the modified finite element model. As shown in Figure 6, the device coupling coefficient increased with increasing in-plane load, in decent agreement with predictions. The maximum beam load ratio,  $P/P_{cr}$ , was 0.59, which decreased the frequency by 36% and increased the coupling coefficient by 38%.

### TRILAMINAR AXISYMMETRIC PIEZOCERAMIC DISK

The second type of device addressed was a trilaminar axisymmetric piezoceramic disk, as

illustrated in Figure 7. The planar coupling coefficient of the piezoceramic material,  $k_p$ , governs electro-mechanical energy conversion in this device. A finite element model was developed, and predicted changes in the natural frequencies and coupling coefficients due to in-plane loads were compared to those measured in experiments. Some of the practical challenges of implementing this concept were also explored.

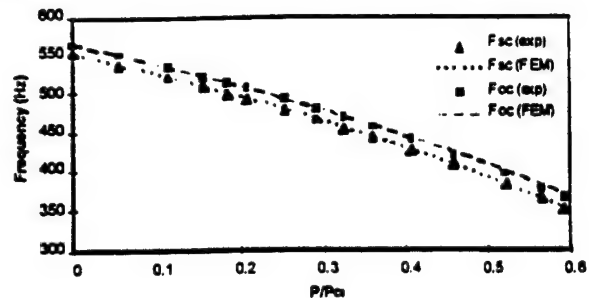


Figure 5: Frequency vs.  $P/P_{cr}$

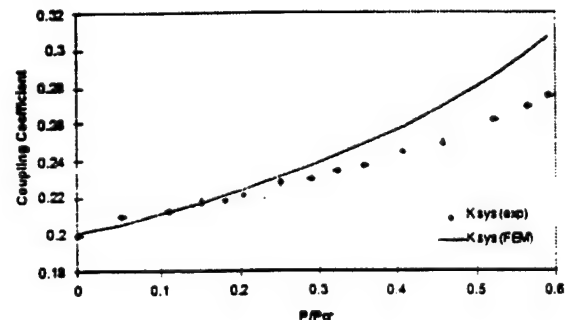


Figure 6:  $k_{ps}$  vs.  $P/P_{cr}$

## Modeling

A fully-coupled electromechanical finite element model of a trilaminar axisymmetric piezoceramic disk was developed and used to predict device behavior under uniform in-plane loads. Figure 8 shows the coordinate system and dimensions used in this analysis.

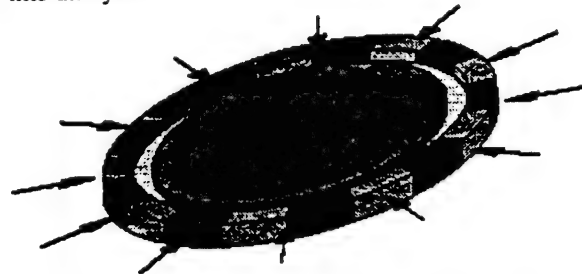


Figure 7: Trilaminar Axisymmetric Piezoceramic Disk

Equation 7 shows a condensed matrix version of one form of the constitutive equations for a linear



piezoelectric material (IEEE, 1988). In these equations  $T$  is the stress vector and  $S$  is the strain vector, while  $D$  is the electric displacement vector and  $E$  is the electric field vector. Stress and strain are related through  $c^E$ , the elastic coefficients at constant electric field. Electric displacement and electric field are related through  $\epsilon^S$ , the permittivities at constant strain. The parameters that couple the electro-mechanical properties of the material are  $e$ , the piezoelectric stress constants.

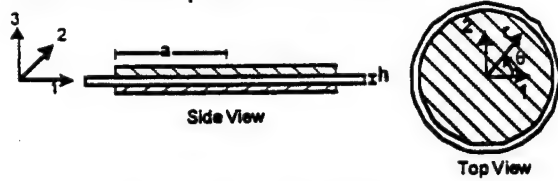


Figure 8: Coordinate System and Dimensions for Trilaminar Disk

$$\begin{Bmatrix} T \\ D \end{Bmatrix} = \begin{bmatrix} c^E & -e^t \\ e & \epsilon^S \end{bmatrix} \begin{Bmatrix} S \\ E \end{Bmatrix} \quad (7)$$

The strain, dielectric and kinetic energies of the device were developed in terms of derivatives of the displacement field, using the piezoelectric constitutive equations. Equations 8a and 8b show general and specific forms of the strain energy expression. In Equation 8,  $Y$  is the Young's modulus of the metal disk.  $Y_p$  is the short-circuit planar Young's modulus of the piezoceramic,  $h$  and  $h_p$  are the respective thicknesses, and the Poisson's ratios,  $\nu$ , are assumed to be the same. Equations 9a and 9b correspond to the dielectric energy. Equation 10 gives the kinetic energy of the device, while Equation 11 shows the virtual work associated with the in-plane load,  $N$ .

$$T = \frac{1}{2} \iiint_{\text{volume}} \rho(z) \left( \frac{\partial w}{\partial t} \right)^2 z r dr d\theta \quad (10)$$

$$U_{\text{strain}} = \frac{1}{2} \iiint_{\text{vol}} (T_r S_r + T_\theta S_\theta + T_{r\theta} S_{r\theta}) dz r dr d\theta \quad (8a)$$

$$U_{\text{strain}} = \frac{1}{2} \iint_{\text{area}} \left[ \left[ \frac{Y h^3}{12(1-\nu^2)} + \frac{Y_p}{12(1-\nu^2)} h_p (6h^2 + 12hh_p + 8h_p^2) \right] \left( \frac{1}{r^2} \left( \frac{\partial w}{\partial r} \right)^2 + \frac{2\nu}{r} \frac{\partial^2 w}{\partial r^2} \frac{\partial w}{\partial r} + \left( \frac{\partial^2 w}{\partial r^2} \right)^2 \right) \right. \quad (8b)$$

$$\left. + \left[ \frac{Y_p}{(1-\nu^2)} h_p E_3 d_{31} (h + h_p) (\nu + 1) \right] \left( \frac{\partial^2 w}{\partial r^2} + \frac{1}{r} \frac{\partial w}{\partial r} \right) \right] r dr d\theta$$

$$U_{\text{dielectric}} = \frac{1}{2} \iiint_{\text{vol}} (D_3 E_3) dz r dr d\theta \quad (9a)$$

$$U_{\text{dielectric}} = \frac{1}{2} \iint_{\text{area}} \left[ \left[ 2h_p \epsilon_{33} - 4 \frac{Y_p h_p}{(1-\nu)} d_{31}^2 \right] E_3^2 - \frac{Y_p h_p}{(1-\nu)} (h + h_p) d_{31} \left( \frac{\partial^2 w}{\partial r^2} + \frac{1}{r} \frac{\partial w}{\partial r} \right) E_3 \right] r dr d\theta \quad (9b)$$

$$U_{\text{geometric}} = \frac{1}{2} \iint_{\text{area}} N \left( \frac{\partial w}{\partial r} \right)^2 r dr d\theta \quad (11)$$

Based on an elastic annular finite element (Weaver and Johnston, 1984) and the energies determined in the preceding, the following set of coupled equations were formulated. Note that the voltage across the piezoelectric elements is a scalar quantity. Again, the thesis by Hébert (1998) contains additional details of the model.

$$[M]\{\ddot{q}\} + [K]\{q\} - [P]E_3 = \{f\} \quad (12)$$

$$[P]^t \{q\} + CE_3 = Q$$

The mass matrix  $[M]$  includes contributions to the kinetic energy from the brass and piezoceramic disks. The stiffness matrix  $[K]$  includes contributions to the strain energy from the brass and piezoceramic disks, as well as the geometric stiffness related to the in-plane load. The capacitance matrix  $[C]$  describes contributions to dielectric energy from the piezoelectric material. The piezoelectric coupling  $[p]$  matrix couples the transverse displacement and electric field. For this analysis, the mechanical force vector  $\{f\}$  was taken to be zero.

To model short-circuit conditions,  $\{E\}$  was set to zero in the first equation of Equation 12. To model open-circuit conditions,  $\{Q\}$  was set to zero in the second equation of Equation 12, which was then solved for  $\{E\}$  in terms of  $\{q\}$ , and substituted into the first equation. This led to an increase in stiffness as shown in Equation 13. In both the short- and open-circuit cases, an eigenvalue problem for natural frequencies was developed from the first equation.

$$[\Delta K] = [P][C]^{-1}[P]^t \quad (13)$$

As in the case of the beam, rotational springs were incorporated into the disk FEM model to adjust the boundary conditions, along with considerations for



the loss of performance of the piezoceramic material due to stress depoling and aging.

Table 2 summarizes the geometric and material properties for the disks considered. The thickness and radius of the brass disk were determined to optimize the zero load coupling coefficient (Hébert, 1998). A typical critical load for the disk specimens tested was  $7.56E4$  N/m

Table 2: Trilaminar Axisymmetric Disk Geometric and Material Properties

	APC 851	Brass
Radius (a)	0.0254 m 0.03175 m	0.0267 0.03342
Thickness (h)	3.81E-4 m	4.064E-4 m 6.35E-4m
Modulus (Y)	65.79E9 N/m <sup>2</sup>	105E9 N/m <sup>2</sup>
Density ( $\rho$ )	7700 kg/m <sup>3</sup>	8470 kg/m <sup>3</sup>
Poisson's' Ratio	0.3	0.34
Piezo Coeff. ( $d_{31}$ )	-185E-12 m/V	
Permittivity ( $\epsilon_{33}^T$ )	1.948E-8 F/m	

Figure 9 shows the predicted effects of in-plane loads on the short and open circuit natural frequencies. Clearly, the ability to apply both compressive and tensile loads would substantially increase the device frequency range.

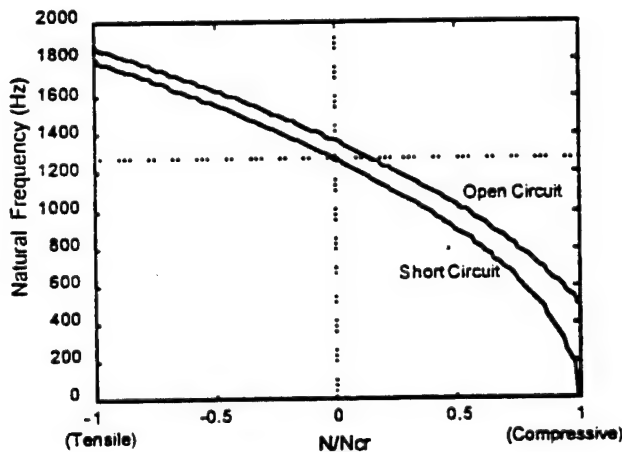


Figure 9: Disk Natural Frequency vs. In-plane Load

Figure 10 shows the predicted effect of in-plane load on device coupling coefficient. In principle, compressive loads can increase the coupling coefficient to a maximum value of 1.0 at the buckling load, while tensile loads decrease it. However, a tensile load may be useful for applications in which a large change in frequency is needed and a relatively small decrease in coupling coefficient can be tolerated.

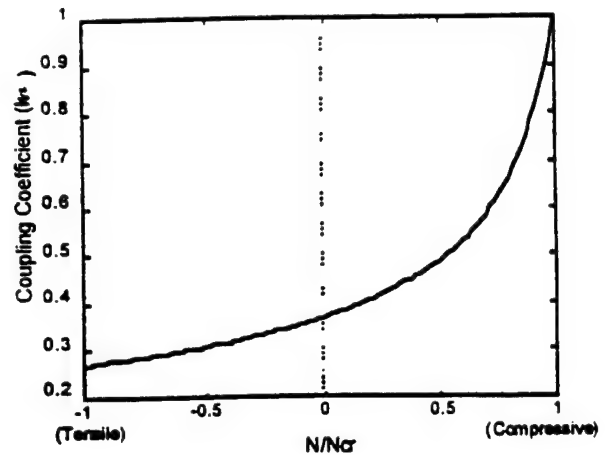


Figure 10: Coupling Coefficient vs. In-plane Load

## Experiments

Many tests addressed methods of load and boundary condition application, as detailed in (Hébert, 1998). The final configuration used for the trilaminar piezoceramic disk, shown in Figure 11, was a segmented ring with a notch on the inner edge, in conjunction with a circular clamp to provide the compressive in-plane load.

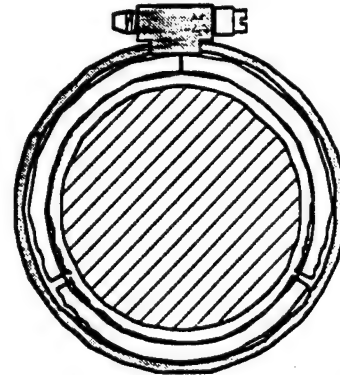


Figure 11: Experimental Configuration for Trilaminar Disk

Figure 12 shows the effects of compressive in-plane loads on electrical impedance. As compressive in-plane loads increased, frequencies decreased and coupling coefficients increased.

## Results

The experimental results that follow correspond to two different disk radii. All of the devices used piezoceramic disks  $3.81E-4$  m thick, and a ratio of piezoceramic radius to brass radius ( $a_p/a$ ) equal to 0.95. The first device tested had a piezoceramic disk radius of 0.0254 m and a brass thickness of  $4.064E-4$  m. Figure 13 shows the change in frequencies with

increasing compressive in-plane load, while Figure 14 shows the change in device coupling coefficients. An  $N/N_{cr}$  ratio of 0.23 resulted in a 13% change in frequency, and a 15% increase in device coupling coefficient.

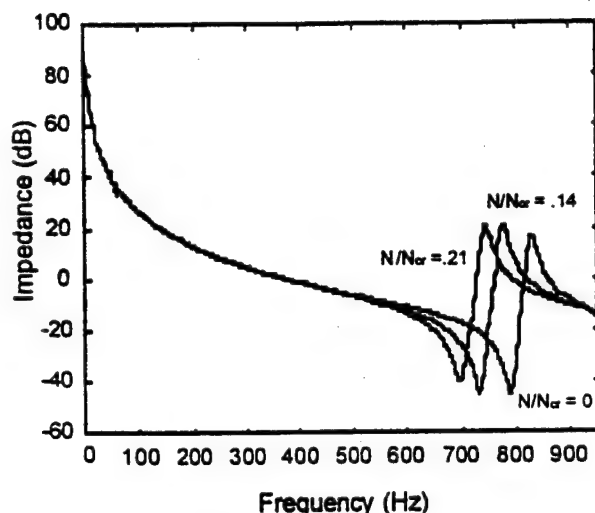


Figure 12: Effect of  $N/N_{cr}$  on Electrical Impedance

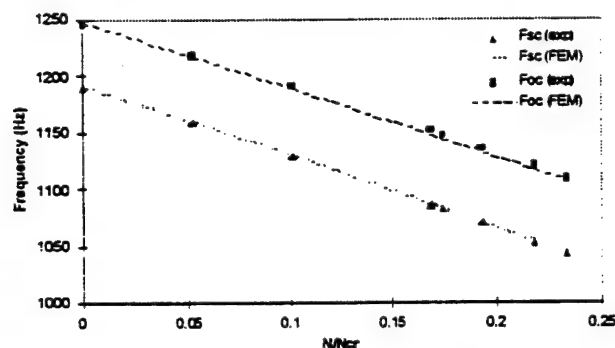


Figure 13: Frequency vs.  $N/N_{cr}$  - Piezo Radius = 0.0254m

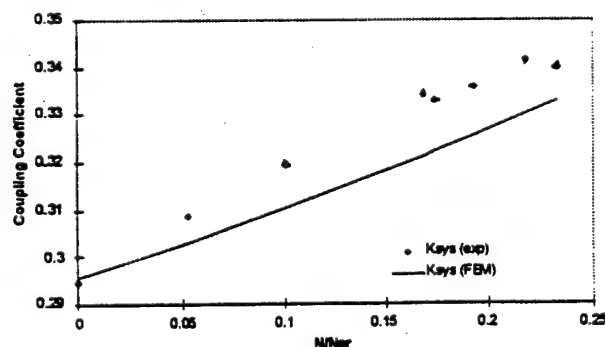


Figure 14:  $k_{ry}$  vs.  $N/N_{cr}$  - Piezo Radius = 0.0254m

The second device size had a piezoceramic disk radius of 0.03175 m and a brass thickness of  $4.064E-4$  m. The larger radius decreased the critical buckling load of the device to about  $4.84E4$  N/m. Figure 15 shows the changes in open and short circuit frequencies, while Figure 16 shows the changes in device coupling coefficient. An  $N/N_{cr}$  ratio of 0.22 resulted in a 12% frequency change, and an increase in coupling coefficient of 15%.

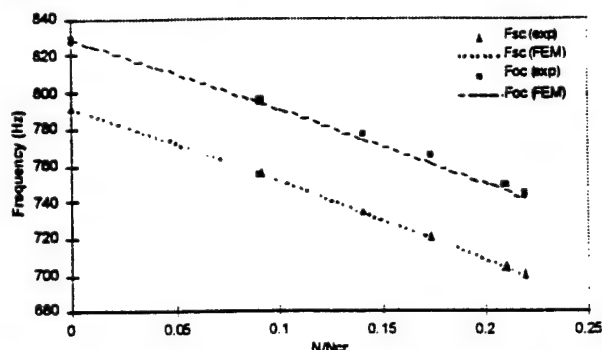


Figure 15: Frequency vs.  $N/N_{cr}$  - Piezo Radius = 0.03175m

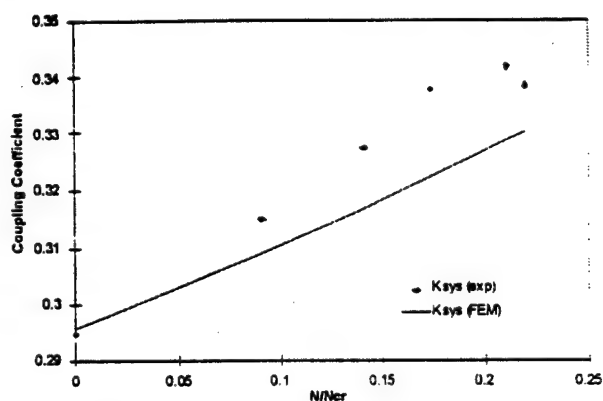


Figure 16:  $k_{ry}$  vs.  $N/N_{cr}$  - Piezo Radius = 0.03175m

## SUMMARY, CONCLUSIONS AND RECOMMENDATIONS

Piezoelectric transducers commonly operate over a fixed frequency range. Adding damping improves the bandwidth of such devices, but decreases their sensitivity. A frequency-agile transducer could be tuned to different frequencies to maintain high electro-mechanical energy conversion, instead of being locked into a fixed design frequency. Membrane loads were shown to change the natural frequency and coupling coefficients of trilaminar piezoceramic transducers.

The effects of compressive in-plane loads on the natural frequencies and coupling coefficients of trilaminar beams were investigated. Corrections to the FEM model related to boundary conditions and stress depoling significantly increased the accuracy of

predictions. Loads of 59% of the buckling load were successfully applied, corresponding to a frequency decrease of 36%, and a coupling coefficient increase of 38%.

Radial in-plane loads applied to trilaminar disks also changed their dynamic behavior significantly. Loads of 23% of the buckling load were applied successfully, corresponding to a frequency decrease of 13% and coupling coefficient increase of 15%.

In addition to increasing sensitivity, this approach could be used to reduce the size of low frequency flexural transducers. The radius of the device is proportional to the square root of the natural frequency. To decrease the frequency of the device, a larger radius is usually dictated. However, as shown in this work, compressive loads applied to a device can also reduce its natural frequency. Therefore, it might be possible to reduce size of a device while maintaining the lower frequency characteristic of a larger device. For example, a 25% reduction in natural frequency due to compressive loads, results in a device that could have a 15% smaller radius. This could decrease the size, weight, and cost of some piezoelectric transducers.

Many issues remain to be addressed. More effective ways to apply in-plane loads to disks are needed. This may involve new methods of applying the load, or a new transducer geometry, such as rectangular or hexagonal plates. Active control using piezoceramic or hydraulic load application devices could also improve device effectiveness. The dimensions of a real device would be sized so that the stresses at the buckling load were low relative to the depoling stress.

In-plane loads are capable of significantly changing the natural frequency and coupling coefficients of trilaminar devices. The use of such frequency-agile transducers may enable better performance in many applications.

## REFERENCES

- American Piezo Ceramics International Ltd., "Characteristics of our Piezoelectric Materials", Mackeyville, PA, 1997.
- Butler, S.C., Butler, J.L., Butler, A.L., and Cavanaugh, G.H., "A Low-Frequency Directional Flexensional Transducer and Line Array," *Journal of the Acoustical Society of America*, Vol. 102, No.1, pp. 308-314, July 1997.
- Cogdell, J.R., *Foundations of Electrical Engineering*, Prentice-Hall Inc., New Jersey, p. 130-151, 1990.
- Crawley, E.F., De Luis, J., Hagood, N.W., and Anderson, E.H., "Development of Piezoelectric Technology for Applications in Control of Intelligent Structures," *Proceedings of the 1988 American Control Conference*, Vol. 3, Atlanta, GA., June 15-17, 1988, pp. 1890-1896.
- Davis, C.L. and Lesieutre, G.A., "An Actively Tuned Solid State Vibration Absorber Using Capacitive Shunting of Piezoelectric Stiffness," *Journal of Sound and Vibration*, 1999 (accepted).
- Hébert, C.A., "Frequency-Agile Piezoceramic Transducers Obtained Through The Application of In-Plane Loads." M.S. thesis, Department of Aerospace Engineering, The Pennsylvania State University, 1998.
- Hughes, J., "Acoustic Transducers," *Journal of Physical Sciences*, Vol. , pp. , 1998.
- IEEE Standard on Piezoelectricity*, ANSI / IEEE Std. 176-1987, Institute of Electrical and Electronics Engineers, New York, 1988.
- Johnson, D.E., Johnson, J.R. and Hilburn, J.L. *Electrical Circuit Analysis*, Prentice-Hall Inc., New Jersey, pp. 23-66, 1992.
- Lesieutre, G.A., and Davis, C.L., "Can a Coupling Coefficient of a Piezoelectric Device be Higher Than Those of Its Active Material?," *Journal of Intelligent Material Systems and Structures*, Vol. 8, pp. 859-867, October 1997.
- Waanders, J.W., *Piezoelectric Ceramics Properties and Applications*, Philips Components, Eindhoven, The Netherlands, 1991.
- Weaver, Jr., W. and Johnston, P.R., *Finite Elements for Structural Analysis*, Prentice-Hall Inc., New Jersey, pp. 17-26, 222-226, 1984.
- Zhang, Q.M., Zhao, J., Uchino, K. and Zheng, J., "Change of the Weak-Field Properties of  $\text{Pb}(\text{ZrTi})\text{O}_3$  Piezoceramics With Compressive Uniaxial Stress and its Links to the Effect of Dopants on the Stability of the Polarizations in the Materials," *Journal Of Materials Research*, Vol. 12, No. 1, pp. 226-234, 1997.

# **APPENDIX 38**

# An actively-tuned solid state piezoelectric vibration absorber

Christopher L. Davis<sup>a</sup>, George A. Lesieutre<sup>b</sup>

<sup>a</sup>Smart Structures Technology, The Boeing Company, Seattle, WA 98032

<sup>b</sup>Department of Aerospace Engineering, The Pennsylvania State University, University Park, PA 16802

## ABSTRACT

A tunable solid state piezoelectric vibration absorber and an active tuning method were developed and demonstrated. A passive vibration absorber generally acts to minimize structural vibration at a specific frequency associated with either a tonal disturbance or the response of a lightly damped structural vibration mode. Because this frequency is rarely stationary in real applications, damping is usually added to ensure some level of effectiveness over a range of frequencies. Maximum response reductions, however, are achieved only if the absorber is lightly damped and accurately tuned to the frequency of concern. Thus, an actively-tuned vibration absorber should perform better than a passive one and, furthermore, could be made lighter. In its simplest form, a vibration absorber consists of a spring-mass combination. A key feature of the tunable vibration absorber described herein is the use of piezoelectric ceramic elements as part of the device stiffness. The effective stiffnesses of these elements was adjusted electrically, using a passive capacitive shunt circuit, to tune the resonance frequency of the device. The tuning range of the absorber is thus bounded by its short-circuit and open-circuit resonance frequencies. An alternative tuning approach might employ resistive shunting, but this would introduce undesirable damping. Another feature of the device is the ability to use the piezoelectric elements as sensors. A control scheme was developed to estimate the desired tuning frequency from the sensor signals, to determine the appropriate shunt capacitance, and then to provide it. The shunt circuit itself was implemented in ten discrete steps over the tuning range, using a relay-driven parallel capacitor ladder circuit. Experimental results showed a maximum 20 dB, and a 10 dB average improvement in vibration reduction across the tuning range, as compared to a pure passive absorber tuned to the center frequency, with additional benefit extending beyond the tuning range.

**Keywords:** passive vibration absorber, semi-active tuning, piezoelectric ceramic, capacitive shunting

## 1. INTRODUCTION

Vibration is an important aspect of many engineering systems, from machine tools to structure-borne noise in aircraft<sup>1</sup>. In most cases, such vibration is undesirable and requires attenuation. Attenuation techniques range in complexity from relatively simple narrow-band passive elastomeric vibration absorbers to fully active broad-band vibration control systems.

Passive attenuation methods represent an important class of approaches to the control unwanted structural vibrations<sup>2</sup>. One particular method of passive vibration suppression involves the use of passive vibration absorbers (PVAs). Passive vibration absorbers are conceptually simple devices consisting of a mass attached to a structure via a spring or via a parallel spring-damper combination. PVAs are commonly constructed of an elastomeric material sandwiched between the structure and an inertial (or proof) mass. The primary function of these devices is to increase the effective dynamic stiffness of a structure over a relatively narrow frequency band. Increasing the dynamic stiffness of a structure reduces its dynamic displacement (assuming the forcing level remains constant). In practice, PVAs are typically used to minimize vibration at a specific frequency associated with either a lightly damped structural mode or a tonal disturbance. The advantages of using vibration absorbers are low cost, low weight, and ease of attachment. The fact that a PVA may only be used effectively at a single frequency, however, can sometimes be a significant drawback.

---

Further author information:

G.A.L. (correspondence): Email: g-lesieutre@psu.edu; Telephone: 814-863-0103. Associate Professor.

C.L.D.: Email: christopher.l.davis@boeing.com; Telephone: 253-773-2036. Research Engineer.

While a common use of PVAs is to reduce vibration in tall buildings or towers<sup>1</sup>, they have also been successfully used in the aviation industry for some time. For example, the DC-9 for many years used a set of four PVAs attached to each engine pylon<sup>1</sup> to reduce aft cabin noise associated with the operating spool frequency of the engines. Similarly, both the Fokker F27 and the Saab 340<sup>5</sup> aircraft use PVAs attached directly to the fuselage frame to lower interior cabin noise levels.

In these applications, the absorbers provide considerable vibration attenuation at specific frequencies. Performance can be seriously degraded, however, if the disturbance source changes frequency. If this occurs, the PVA must be physically re-tuned to maintain optimal performance. Physically re-tuning the absorber is generally impractical. Thus, there is a need for vibration absorbers with tunable variable properties.

Active vibration absorbers (AVAs) are passive vibration absorbers with variable stiffness, mass, or damping properties. The advantage of using an AVA over a PVA is the tunability of the resonance frequency of the device. AVAs are commonly used to track frequency-varying disturbances or to increase the bandwidth of a vibration attenuation method. Recently, Northwest Airlines initiated plans to upgrade 173 of its DC-9s with active tuned mass absorbers built by Barry Controls<sup>6,7</sup>. Due to the increased weight and complexity of using AVAs, however, they have not generally found widespread use.

The goal of this research was to extend AVA technology by developing a tunable piezoceramic vibration absorber. The key aspects of a tunable vibration absorber are the method by which the stiffness or mass of the device is altered and the magnitude of the resulting change in frequency. Because it is generally more difficult to vary the mass of a device, focusing on how to incorporate a variable stiffness into the absorber is appropriate. Precisely how the stiffness may be changed is an important issue.

Piezoceramic materials offer an attractive solution to the variable stiffness problem, because these materials exhibit relatively strong coupling between electrical and mechanical behavior. Recently, the Center for Acoustics and Vibration at Penn State and PCB Piezotronics, Inc. were involved in the development of a piezoceramic inertial actuator (PIA)<sup>8</sup>. Part of the development research conducted by Penn State showed that a PIA, used passively, behaves like a passive vibration absorber<sup>9</sup>. The research presented here focused on developing a method for using such a PIA as an active vibration absorber.

## 2. BACKGROUND

A model was developed to improve insight into the effects of shunting a piezoceramic inertial actuator. First, a single degree-of-freedom (DOF) structure and absorber model were created. Next, the absorber model was modified to incorporate the effects of the piezoceramic forcing element of the inertial actuator. Finally, the electro-mechanical dynamics of the passively shunted piezoceramic were added to the model to capture the desired frequency dependent effects.

### 2.1 Vibration absorber/structure interaction

Consider a damped vibration absorber attached to a single DOF system, as shown in Figure 1. Let  $m_s$ ,  $k_s$ , and  $b_s$  represent the effective mass, stiffness, and damping of the structure respectively, and  $m_a$ ,  $k_a$ , and  $b_a$  represent the mass, stiffness, and damping of the absorber respectively.

First, consider the response of the structure only (*i.e.*, no absorber, just the base structure). The following linear equation of motion is readily found. (Note: unless otherwise stated, the damping terms  $b_s$  and  $b_a$  are considered small and ignored, to simplify analysis.)

$$m_s \ddot{x}_s = -k_s(x_s - x_{in}) \quad (1)$$

Assuming zero initial conditions, Eq. 1 may be transformed into the Laplace domain and expressed in transfer function form. Eq. 2 represents the ratio of the structural displacement,  $X_s$ , to the base disturbance displacement,  $X_{in}$ , or

$$\frac{X_s(s)}{X_{in}(s)} = \frac{k_s}{m_s s^2 + k_s} \quad (2)$$

The positive root of the denominator of Eq. 2 may be used to calculate natural frequency of the structure,  $\omega_s$ , namely

$$\omega_s = \sqrt{\frac{k_s}{m_s}} \quad (3)$$

Thus, when the structure is excited harmonically at a frequency  $\omega_s$ , it will resonate (i.e.,  $X_s$  will be large compared to  $X_{in}$ ).

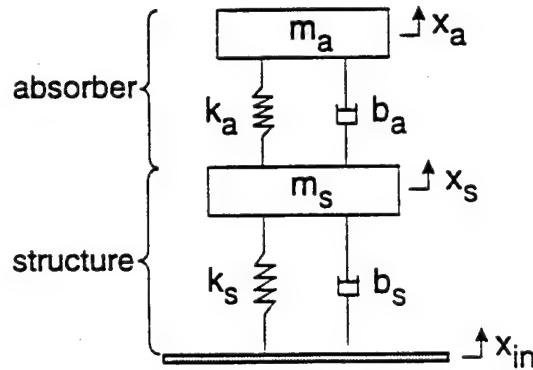


Figure 1. Passive vibration absorber attached to a single-DOF structure lumped parameter model

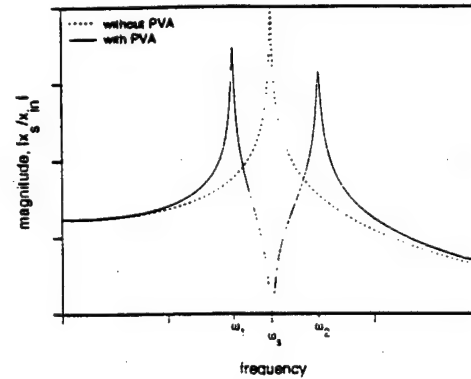


Figure 2. Sample frequency response functions for the single-DOF structure and the single-DOF structure with attached PVA

Next, consider the equations of motion for the coupled structure/absorber system shown in Figure 1, namely

$$m_a \ddot{x}_a = -k_a(x_a - x_s) \quad \text{and} \quad m_s \ddot{x}_s = -k_s(x_s - x_{in}) - k_a(x_s - x_a) \quad (4a, b)$$

Transforming Eqs. 4a and 4b into the Laplace domain and combining the results yields an expression for the structural displacement,  $X_s$ , in terms of the input disturbance displacement,  $X_{in}$ , or

$$\frac{X_s(s)}{X_{in}(s)} = \frac{k_s(m_a s^2 + k_a)}{m_s m_a s^4 + (m_a(k_s + k_a) + m_s k_a)s^2 + k_s k_a} \quad (5)$$

Eq. 5 describes the coupled dynamics of the structure/absorber system. Note that as with Eq. 2, the roots of the denominator of Eq. 5 are the poles of the coupled system and the roots of the numerator of Eq. 5 are the zeros of the coupled system. The frequencies of the poles ( $\omega_1$  and  $\omega_2$ ) and zero ( $\omega_{abs}$ ) of the coupled structure/absorber system are

$$\omega_{1,2} = \frac{\sqrt{2}}{2} \sqrt{\frac{m_a(k_a + k_s) + m_s k_a}{m_a m_s} \pm \sqrt{m_a k_a (m_a(k_a + 2k_s) + 2m_s k_a) + (m_a k_s + m_s k_a)^2}} \quad \text{and} \quad \omega_{abs} = \sqrt{\frac{k_a}{m_a}} \quad (6a, b)$$

Note that  $\omega_{abs}$  defines the frequency of minimum response of the coupled structure/absorber system, and is equal to the natural frequency of the (undamped) vibration absorber itself.

Consider now the structural frequency response function, both with and without an attached vibration absorber, due to an input displacement disturbance (see Figure 2). The response of the structure only (i.e., the magnitude of Eq. 2) is denoted by the dashed line in Figure 2. Notice the large structural response at the frequency  $\omega_s$ .



The solid line in Figure 2 shows the response of the structure with an attached vibration absorber that has a natural frequency,  $\omega_{abs}$ , equal to the natural frequency of the original structural mode,  $\omega_s$ . The response is reduced dramatically at the frequency of the original structural mode,  $\omega_s$ , and increased at frequencies both above and below the frequency of the original structural mode (*i.e.*, at the frequencies of the poles of the coupled system,  $\omega_1$  and  $\omega_2$ ).

From Eq. 5 and Figure 2, it is clear that the natural frequency of the absorber defines the frequency at which minimum structural response will occur. Upon closer inspection of the numerator of Eq. 5, it is also evident that the frequency of minimum structural response is solely a function of the absorber mass and stiffness. Thus it is possible in principle to reduce structural response at any disturbance frequency, provided the natural frequency of the absorber is equal to the disturbance frequency and the absorber is lightly damped. This idea will be used later when developing a tuning control strategy to maintain optimum absorber performance when subjected to a tonal disturbance frequency.

## 2.2 Vibration absorber frequency tuning via passive electrical shunting

With the knowledge that the natural frequency of the absorber defines the frequency of minimum structural response, the next step was to develop a method for changing the stiffness of the absorber in real-time to make the absorber tunable. Electrically shunting the actuator has the effect of changing the effective stiffness (and thus the natural frequency) of the device. A full description of the theory behind the shunting method for frequency tuning is presented in the conference paper by Davis, *et al.*<sup>10</sup> as well as the thesis by Davis<sup>11</sup> and is summarized here for completeness.

As mentioned previously, a vibration absorber may be modeled using lumped parameters such as a spring,  $k_a$ , and mass,  $m_a$  (Figure 3a). Similarly, an inertial actuator may be modeled as a spring-mass system with a forcing element,  $F_p$ , in parallel with the spring element,  $k_a$ , of the absorber (Figure 3b). Placing the forcing element of the inertial actuator (which has an associated effective stiffness) in parallel with the inherent structural stiffness of the absorber (Figure 3c) results in a net device stiffness that is the sum of the two stiffnesses.

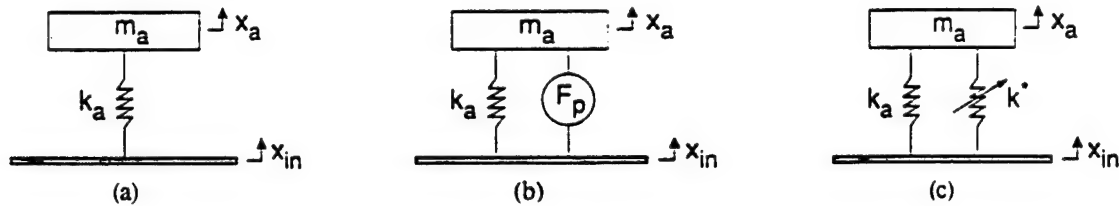


Figure 3. (a) Passive vibration absorber lumped parameter model. (b) Inertial actuator lumped parameter model. (c) Passively shunted inertial actuator lumped parameter model

Electrically shunting the piezoceramic forcing elements within a piezoceramic inertial actuator changes the effective stiffness of the piezoceramics. An expression was developed<sup>11</sup> for the effective stiffness,  $k^*$ , of the piezoceramic forcing element within the piezoceramic inertial actuator, namely

$$k^* = k^E \left( 1 + \frac{k_p^2}{1 - k_p^2 + \alpha(s)} \right) \quad (7)$$

where  $k^E$  is the effective short circuit piezoceramic stiffness,  $k_p$  is the piezoceramic planar electromechanical coupling coefficient,  $\alpha(s)$  is the nondimensional ratio of the electrical impedance of the piezoceramic (*i.e.*,  $1/sC_p^T$ , where  $C_p^T$  is the capacitance of the piezoceramic measured under constant stress) to the electrical impedance of the shunt circuit, and  $s$  is the Laplace parameter (*i.e.*,  $s = i\omega$  where  $\omega$  is radian frequency).

Regardless of the type of simple electrical shunt circuit (*e.g.*, resistor, capacitor, inductor), there are limits on the range of values  $k^*$  can take on. These limits are conveniently defined in terms of shunt circuit short- and open-circuit electrical impedances. When short circuited, the shunt impedance is effectively zero and Eq. 7 reduces to  $k^* = k^E$ . At open circuit, the



shunt impedance is effectively infinite and  $k^* = k^E(k_p^2 / (1 - k_p^2))$ . Thus the tunable range of  $k^*$  is limited by the value of the piezoceramic planar electromechanical coupling coefficient,  $k_p$ .

In the application described here, the value of  $k_p$  was approximately 0.6. For a device made solely of this type of piezoceramic material, the change in stiffness from short to open circuit could be as high as 56%, resulting in an almost 25% change in natural frequency. In practice, however, the stiffness of the piezoceramic is in parallel with the inherent mechanical stiffness of the actuator, and only some fraction of the net device stiffness may be changed due to electrical shunting.

Note that Eq. 7 may be complex depending upon the type of shunt circuit used (e.g., if a resistor is used as the shunt circuit). A complex stiffness would indicate that the device has mechanical properties similar to those of an anelastic material and therefore will add hysteretic damping effects to the system. In terms of vibration absorber performance, adding damping has the effect of increasing the response magnitude at the natural frequency of the absorber. Because the goal of this research was to maintain minimum structural response at  $\omega_{sh}$ , shunt circuits which added damping to the system were not considered.

An ideal capacitor is a purely reactive element (i.e., capacitors do not dissipate energy and thus provide no damping). The ratio of the effective tunable piezoceramic stiffness of a capacitively shunted piezoceramic element to the short circuit stiffness of the element is shown in Figure 4. Notice that for this case, the tuning ratio is the ratio of the shunt capacitance,  $C_{sh}$ , to the clamped capacitance of the piezoceramic. As illustrated in Figure 4, the tunable piezoceramic stiffness varies smoothly with increasing shunt capacitance. Also note that roughly a four-order-of-magnitude change in shunt capacitance is necessary to effectively change from open to short circuit (or vice versa).

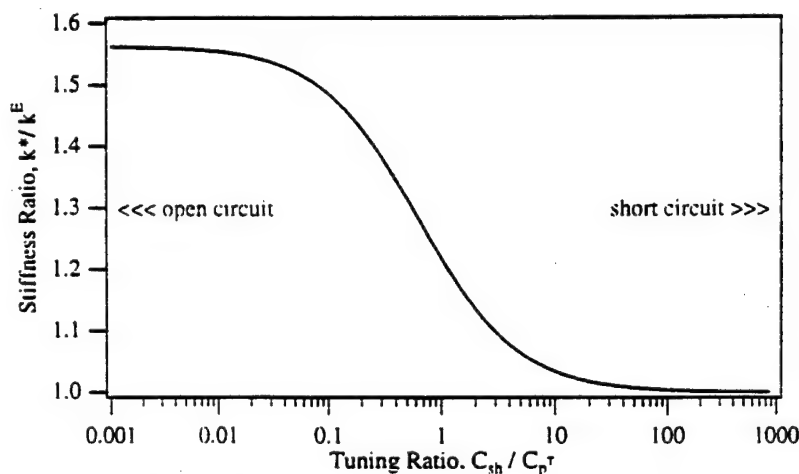


Figure 4. Effect of shunt capacitance on effective piezoceramic stiffness

As mentioned previously, the total stiffness of a piezoceramic vibration absorber is the sum of the effective tunable piezoceramic stiffness and the inherent stiffness of the device. The relative magnitudes of the two stiffnesses determines the net frequency change possible via electrical shunting. An experiment was conducted using a commercially available piezoceramic inertial actuator as a passive, electrically shunted vibration absorber. A schematic of the piezoceramic inertial actuator used for the experiments, PCB Model X712A02, is shown in Figure 5. The actuator (the lower flat cylinder in Figure 5) is approximately 2 inches in diameter and approximately 3/8 of an inch thick. The reaction mass is attached to the top of the actuator by a standard 10-32 threaded stud, making it relatively easy to coarsely tune the device by changing the mass. The base of the inertial actuator (hidden in Figure 5) also has a 10-32 threaded stud used for attaching the actuator to a structure.

The purpose of the experiment was to measure the natural frequency and modal damping ratio of the actuator under a variety of capacitive shunt conditions ranging between short and open circuit. In the experiment, the inertial actuator was attached to a shaker and accelerometers were used to measure both the input (i.e., the shaker) acceleration and the reaction mass acceleration. The ratio of the two acceleration measurements formed a frequency response function which was then curve fit to approximate the natural frequency and modal damping ratio of the actuator for a given shunt condition. The electrodes of

the inertial actuator were attached to a solderless breadboard where discrete values of capacitance could be used to shunt the device.

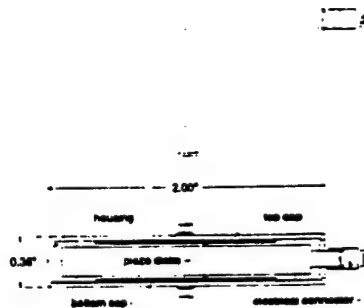


Figure 5. Schematic of the PCB Model X712A02 inertial actuator with 200g reaction mass

The results of the passive shunting experiment verified the ability to predictably tune the natural frequency of the piezoceramic vibration absorber between a short circuit natural frequency of 313 Hz and an open circuit natural frequency of 338 Hz. The resulting change in natural frequency was approximately 7.5% from short to open circuit. Next, a frequency tuning control method for the shunted piezoceramic vibration absorber was developed.

### 3. SEMI-ACTIVE PIEZOCERAMIC VIBRATION ABSORBER FREQUENCY TUNING CONTROLLER

The preceding section showed that it is possible to use a PIA as a passive vibration absorber and that such a PIA may be passively tuned with an external shunt circuit. In this section, the approach used to implement a semi-active tuning method is described.

#### 3.1 Concept

Consider a flexible structure with several well-spaced structural modes of vibration subjected to a tonal disturbance. Attaching a conventional passive vibration absorber to the structure, tuned to the tonal disturbance frequency, would reduce structural response at that frequency. Thus, as long as the disturbance frequency remained constant, a high level of attenuation would be achieved (*i.e.*, structural vibration would be minimized). If, however, the tonal disturbance frequency changed, performance would decrease (*i.e.*, the vibration level would increase). Therefore it is clearly beneficial to have a tunable vibration absorber and a tuning method to track a changing disturbance frequency and appropriately re-tune the frequency of the absorber.

Developing a tuning method for the PIA involved three steps: First, an appropriate system signal was identified, from which the desired tuning frequency could be estimated. The next step was to develop a method for actually estimating the frequency of structural vibration from the signal. The final step involved formulating a control scheme to determine and provide the proper shunt capacitance.

The concept of monitoring the disturbance frequency and tuning the absorber to maintain minimum structural response is illustrated in Figure 6. The upper plot represents broadband structural response for a structure both with and without an attached PIA vibration absorber. The highlighted area of the upper plot is enlarged in the lower portion of Figure 6 to show the transfer function zeros (or minima) created by the addition of a short circuit, shunted, and open circuit PIA to the structure.

First, consider the case when the piezoceramic element within the PIA is short circuited (indicated by the dashed line in the highlighted section in the lower plot of Figure 6). If a tonal disturbance acted on the structure at a frequency equal to  $f_{sc}$ , structural response would be minimal. If the disturbance frequency were to decrease while the PIA remained short circuited,

structural response would increase. Similarly, if the disturbance frequency were to increase to the frequency  $f_{oc}$ , while the piezo element remained short circuited, structural response would again increase. However, if the absorber were "re-tuned" by adjusting the electrical shunt impedance to an open circuit condition structural response would remain minimal. In addition, if the disturbance frequency were to fall anywhere between  $f_{sc}$  and  $f_{oc}$ , there exists a shunt impedance that will deliver minimum structural response.

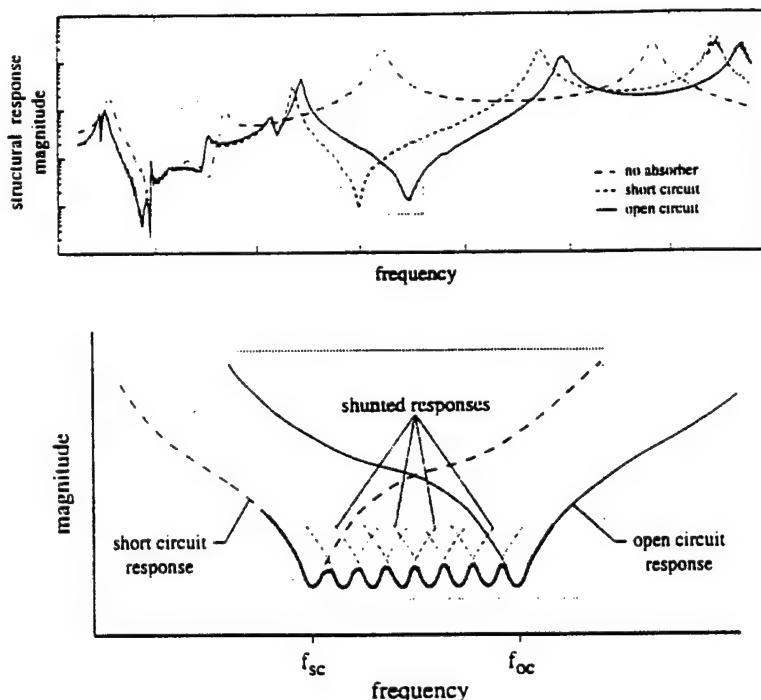


Figure 6. Conceptual tuned vibration absorber structural response

Consider the following situation: a structural mode is excited by a pure tone harmonic disturbance which varies in frequency by a few percent of some nominal frequency. In principle, a PIA-based vibration absorber could be added to the structure such that at a shunt tuning ratio of one, the natural frequency of the absorber would be equal to the nominal disturbance frequency (*i.e.*, the natural frequency of the absorber for a tuning ratio of one is half-way between  $f_{sc}$  and  $f_{oc}$ ). If sensing (in the form of determining the frequency of the disturbance), control (in the form of a command signal based on the sensed frequency to alter the electric shunt impedance), and actuation (in the form of a means to alter the electrical shunt condition) were provided, then minimum structural response could be maintained within the band defined between the open and short circuit frequencies.

The heavy solid line in Figure 6 illustrates the conceptual response of a discretely tuned PVA. In this illustration, the shunt capacitance does not vary smoothly between  $f_{sc}$  and  $f_{oc}$ , but instead is discretized. Thus, determining a means to estimate the disturbance frequency, choosing the correct value of shunt impedance based on the estimated frequency, and physically changing the shunt impedance are the main subject of the next section. Two important questions to be addressed are: 1) what sensor(s) could be used; and 2) once a sensed signal is acquired, how can frequency information be extracted from it?

### 3.2 Implementation

It is clearly desirable to try to use the fewest number of sensors in order to reduce control system complexity, weight, and power consumption. With this in mind, a method for sensing the tonal disturbance frequency based on the voltage produced by the piezoceramic within the PIA was developed.

Assuming a linear model for the coupled structure/PIA system, the voltage produced by the piezoceramic elements within the PIA is directly proportional to the piezoceramic strain and the shunt circuit electrical impedance. Thus, for an open circuit electrical PIA being forced near resonance, the piezo elements would be under considerable strain due to the motion of the

inertial mass (and corresponding small motion of the attached structure), producing considerable voltage. If, however, the PIA were short circuited, there would be effectively no measurable voltage across the terminals of the PIA. Instead, short-circuiting the device would produce a large current (for the same forcing conditions). Thus, because shunting the PIA can vary the electrical impedance of the device from nearly short circuit to nearly open circuit, using the electrical state of the piezoceramic to estimate vibration frequency can only be effective if both voltage and current are used as sensor variables.

For the prototype system described here, a control system was used in which the A/D conversion process required voltages within a prescribed range. Thus it was necessary to convert the PIA current to a corresponding voltage. The current estimation process was realized using an op-amp as an ideal current-to-voltage converter<sup>12</sup>.

The controller used for tuning the PIA is shown in Figure 7. The controller used two inputs and one output. The inputs were the PIA voltage,  $V_v$ , and the voltage proportional to the PIA current,  $V_i$ . The output was a voltage proportional to the tuning impedance of the shunt circuit. The main elements of the controller were: 1) the band-pass filters; 2) the frequency estimation logic; and 3) the control voltage calculation.

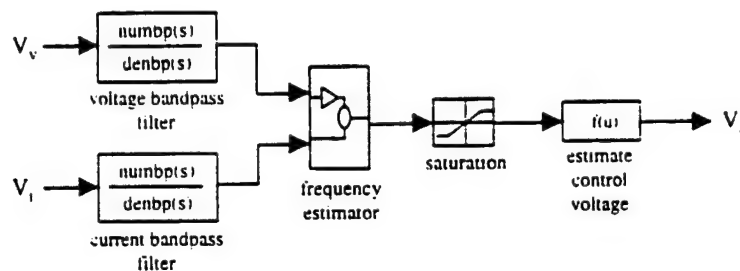


Figure 7. Control system block diagram

The band-pass filters removed any DC-component of the input signals and attenuated high frequency noise. The filters were second order with low and high cut-off frequencies of approximately 130 and 780 Hz respectively. Note that for the prototype system, the frequency range of interest (*i.e.*, the range of frequencies defined by the short and open circuit resonance frequencies of the PIA) was approximately 290 to 350 Hz. Thus the pass-band encompassed the range of interest well.

The filtered signals were next used to estimate the frequency of the tonal disturbance. For the prototype version, frequency estimation was done by the control computer. For increased performance, analog circuitry could be implemented in the form of a phase locked loop to convert the sensed voltages to a voltage proportional to frequency for use by the control system.

With a proper estimate for the frequency of vibration, the remaining task of the controller was to calculate an appropriate control voltage with which to vary the shunt impedance. Before the controller could be programmed, however, it was necessary to determine a method for physically altering the shunt capacitance. Recall that in Figure 2, the effective tuning ratio range for capacitive shunting is roughly 0.01 to 100 times the capacitance of the PIA measured at constant stress. The capacitance of the PIA measured at constant stress used in prototype system was approximately 0.072  $\mu\text{F}$ . Therefore, to tune the natural frequency of the PIA between  $f_{lc}$  and  $f_{hc}$ , a shunt capacitance range of roughly 0.7 nF to 7  $\mu\text{F}$  was required.

Variable capacitors do exist. However, the majority of variable capacitors have relatively small ranges (*e.g.*, even a range of 12 to 100 pF is not common) and must be tuned by physical means. Programmable capacitors also exist, but due to their added complexity and resistance, they were not considered for the prototype system. Instead, a "ladder" circuit of discrete capacitors wired in parallel was used to tune the PIA.

The effect of placing capacitors in parallel is a net capacitance equal to the sum of the individual capacitances. Figure 8 illustrates a conceptual shunt circuit with several parallel capacitors. If the frequency tuning band of the shunted PIA were discretized into a finite number of capacitive impedances, a control law could be developed to select a number of parallel capacitors whose sum would be the net electrical impedance needed to tune the actuator very close to the estimated disturbance frequency. Clearly, the number of discrete capacitance values used in a specific application will depend on the overall size of

the frequency tuning range, the intrinsic damping of the absorber, and the acceptable deviation from minimum response. Finer discretization of the tuning band will yield more uniformly low system response.

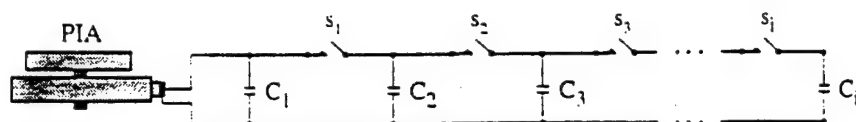


Figure 8. Conceptual "ladder" capacitive shunt circuit

Consider a discretized shunt circuit with 10 discrete capacitance levels ranging from approximately 0.7 nF to 7  $\mu$ F. Ideally, each discrete shunt capacitance will tune the PIA such that structural response will be a minimum for a prescribed frequency within the control bandwidth. Thus the tunable frequency band was divided into nine frequency bands between the short and open circuit natural frequencies of the PIA as shown in Figure 9.

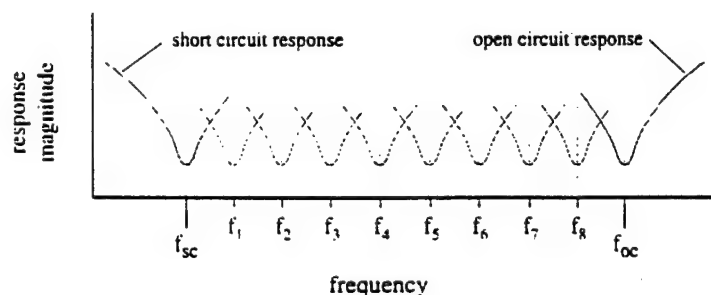


Figure 9. Frequency band shunt discretization

The frequencies at the minima of each frequency band (labeled as  $f_{sc}$ ,  $f_1$  through  $f_8$ , and  $f_{oc}$  in Figure 8) define frequencies at which the cumulative combinations of shunt capacitance prescribe the shunted natural frequency of the PIA. First, consider the open circuit shunt case. Open circuit corresponds to a very small (or zero) shunt capacitance. Thus if capacitor  $C_1$  in Figure 8 were very small (or removed) and all switches were open, the PIA would be in an approximately open circuit shunt condition (*i.e.*, the natural frequency of the PIA would equal  $f_{oc}$ ). Next, consider closing the switch  $s_1$  in Figure 8. The net capacitance of the shunt circuit increases to the sum of  $C_1$  and  $C_2$ . Conversely, the natural frequency of the PIA decreases to  $f_8$  (assuming  $C_1$  and  $C_2$  are chosen correctly). Similarly, closing switches  $s_1$  and  $s_2$  will increase the net shunt capacitance to the sum of the  $C_1$ ,  $C_2$ , and  $C_3$  and the PIA natural frequency (and thus the frequency of minimum structural response) will decrease to  $f_7$ . Closing all of the switches will increase the net shunt capacitance to the total of all of the capacitors in the ladder circuit. Thus, if  $C_1$  through  $C_i$  are chosen correctly, the sum of all the capacitors will be large enough to approximate a short circuit shunt condition (*i.e.*, the total parallel capacitance will be greater than or equal to  $100 \times C_p^T$ ). The question remains, however, as to how to open and close the switches in the ladder circuit.

The switches in the shunt circuit shown in Figure 8 determine the number of capacitors in parallel with the PIA. Ideally, these switches would operate in response to a prescribed signal from the control system. In doing so, however, the switches should not introduce any additional electrical impedance into the shunt circuit. A relay provides one possible solution to this problem.

The control voltage,  $V_c$ , shown in Figure 7, is used to turn the relays on in succession. Variable resistors wired between each relay driver circuit were adjusted such that for  $V_c=1V$ , relay #1 would turn "on" while the others would remain "off". For  $V_c=2V$ , relays #1 and #2 would turn "on" while the other relays would remain "off". Similarly, more relays would turn "on" while the remaining relays remained "off" for increasing integer voltage levels up to and including 9V. What remained was to program the control logic to output discrete integer voltage levels corresponding to desired shunt capacitance levels. Note that discrete voltage outputs were required to ensure the appropriate relays in the switching circuit were either "on" or "off".

Figure 10 illustrates the correlation between control voltage,  $V_c$ , PIA capacitive tuning ratio,  $\alpha$ , and the frequency of minimum structural response. From Figure 10 it is clear that, for a control voltage of 0V, no transistors are "on" and thus the PIA is shunted with one capacitor,  $C_1$ . As stated earlier, if  $C_1$  is sufficiently small (say approximately  $0.01 \times C_p^T$ ), the PIA will behave as if it were open circuited. For a control voltage of 1V, the first transistor turns "on" and the shunt capacitance is increased from  $C_1$  to the sum of  $C_1$  and  $C_2$ . If  $C_2$  equals  $0.1 \times C_p^T$ , the net tuning ratio would be approximately 0.11 and the natural frequency of the PIA and therefore the frequency of minimum structural response would be  $f_1$ .

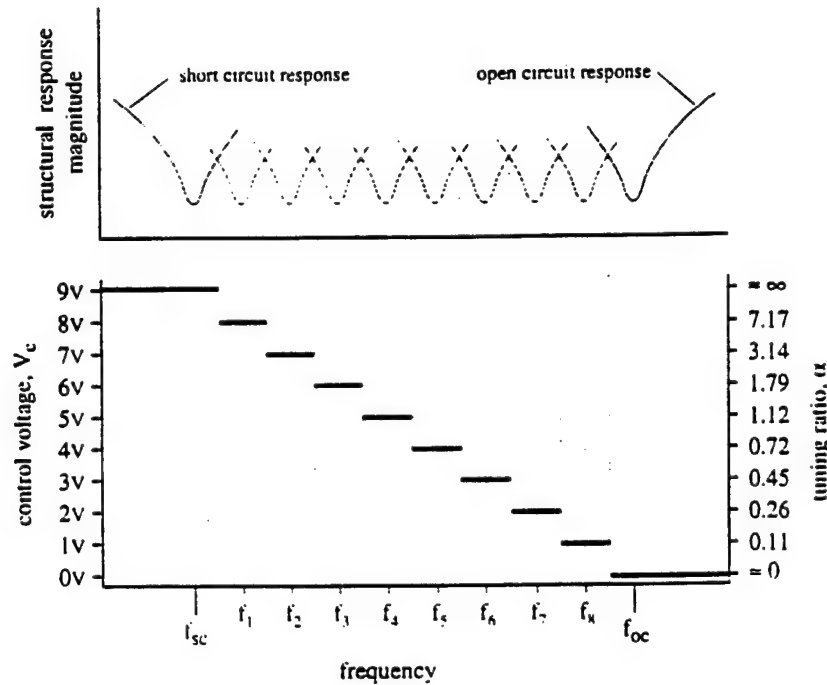


Figure 10. Control voltage to structural response correlation

As shown in Figure 10, varying the control voltage,  $V_c$ , from 0 to 9V changes the frequency of minimum structural response from approximately the open circuit natural frequency to approximately the short circuit natural frequency. Referring to the control system block diagram in Figure 6, the *estimate control voltage* block contains the code to convert the estimated disturbance frequency to an appropriate control voltage.

#### 4. TUNING CONTROL EXPERIMENTS

Several experiments were designed to evaluate the effectiveness of the tunable piezoceramic inertial actuator. In the experiments, a representative structure (a clamped-clamped beam) was driven with a tonal force disturbance. First, structural accelerance measurements were taken both with and without the passive PIA attached to the structure. Measurements in which the PIA was both short and open circuited were used to define the effective tuning bandwidth for the shunt control system. Finally, a sine sweep was used to vary the disturbance frequency from just below the PIA short circuit natural frequency to just above the PIA open circuit natural frequency for the short circuit, open circuit, and actively tuned cases.

Figure 11 shows the experimental setup for the semi-actively tuned PIA vibration absorber experiments. The representative structure was a  $0.913 \times 0.038 \times 0.006$  m aluminum beam rigidly fixed at both ends. An inertial actuator placed 10 cm from the left end of the beam was used to apply a disturbance force to the structure. The drive signal for the actuator was generated by a Hewlett Packard 3562A signal analyzer and amplified using a PCB/AVC high power charge amplifier. A dynamic force transducer placed between the actuator and the structure measured the force applied to the structure, while a high-sensitivity accelerometer located 30 cm from the right side of the beam measured the dynamic response of the beam at the location of the

PIA. Both the force transducer and the accelerometer signals were amplified via portable power units and then recorded by the HP signal analyzer. The analyzer was also used to process the force and acceleration signals to calculate acceleration FRFs.

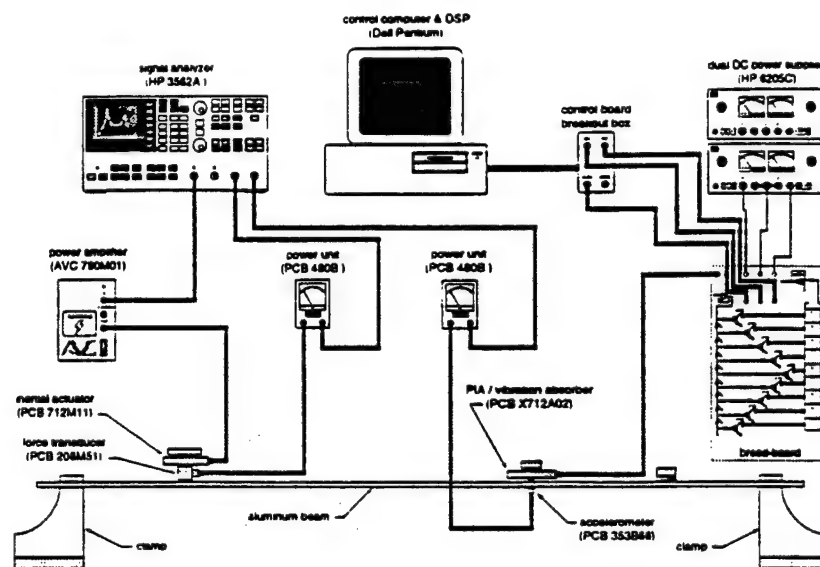


Figure 11. Semi-active tuned PIA vibration absorber experimental setup

Figure 12 shows the response of the system both with and without the PIA absorber attached to the clamped-clamped beam. The response of the system with no absorber attached has a prominent structural resonance at approximately 318 Hz. Clearly, the passive PIA significantly reduced the structural response in the neighborhood of the original structural resonance, and the frequency at which minimum structural response was obtained varied with the value of the electrical shunt.

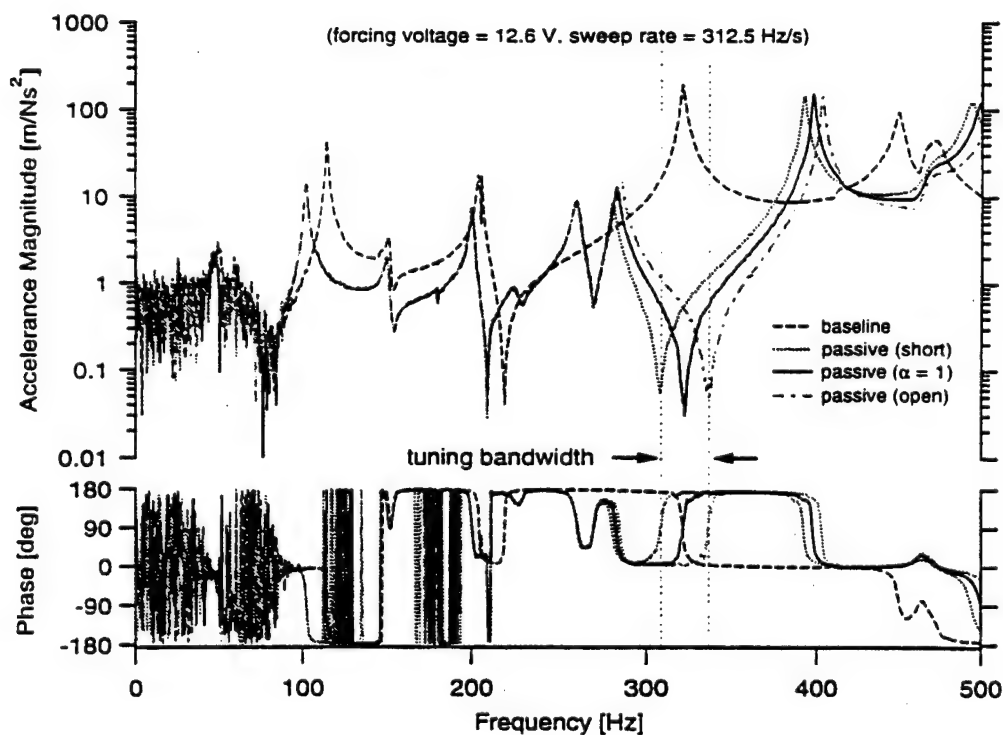


Figure 12. Structural acceleration for structure with PIA absorber



In addition to the open and short circuit measurements (i.e., measurements taken for tuning ratios of 0 and respectively), the acceleration was also measured for a tuning ratio of 1.0. The response for  $\alpha = 1$  defined the nominal or "control off" condition. In practice, a nominal disturbance frequency would be identified and the mass of the PIA would be selected such that for  $\alpha=1$ , minimal structural response would occur at the nominal disturbance frequency.

Next, the actuator was connected to the tuning circuit, which was implemented on an electronic breadboard. The breadboard was also connected to the real-time control computer to supply PIA voltage and PIA current estimates and receive shunt control voltages. The op-amps and relays used for the switching circuit were powered with Hewlett Packard DC power supplies.

The control computer used for the experiments was a 100 MHz Dell Pentium. The Pentium housed a dSPACE DS1102 Floating-Point Controller Board with Texas Instruments TMS320P14 processor chip. The two A/D channels of the controller board had an input voltage range of  $\pm 10V$  and used 16-bit converters. The D/A channel had an output voltage range of  $\pm 10V$  and used a 12-bit converter. MATLAB's Real-Time Workshop was used to translate a SIMULINK block diagram into C-code, then to invoke the TI C-compiler. The compiled C-code was then downloaded to the processor on the controller board. The controller was designed and set to sample at 10 kHz which adequately accommodated the simulation of the analog linear filters.

To gain a more accurate estimate of the passive and semi-active response of the system, swept sine measurements were made between 300 Hz and 350 Hz. Note that the sweep rate for the measurements was set sufficiently low to ensure that the filters within the controller had time to settle before the analyzer moved to the next frequency in the sweep.

Figure 13 illustrates the effects of using a semi-active piezoceramic vibration absorber on structural acceleration due to a varying-frequency tonal disturbance. The dotted line in Figure 13 is the passive structural acceleration (i.e., structural response with a constant  $\alpha = 1$ ). The solid line is the structural acceleration with the tuning controller turned on (i.e., structural response with a variable  $\alpha$ ). The changing discrete capacitances are evidently effective in increasing minimum acceleration over the previously defined tuning band. In addition, structural acceleration at frequencies below the short circuit frequency of the PIA and above the open circuit frequency of the PIA was improved.

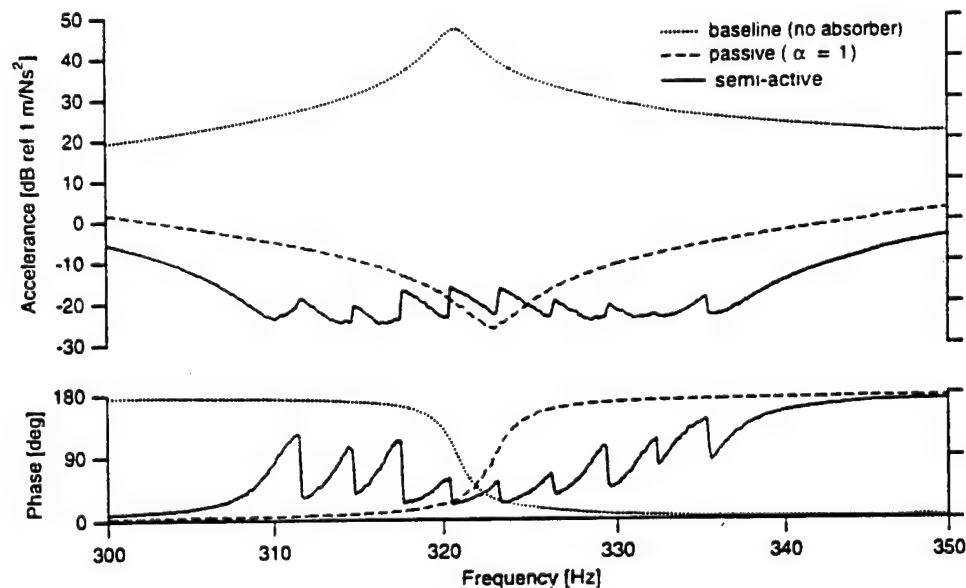


Figure 13. Actively tuned vs passive structural response

Figure 14 shows the difference (in dB) between the passive and active responses. Maximum increases in performance of about 20 dB occurred at both the short and open circuit PIA natural frequencies. On average, an approximately 10 dB increase in

performance was obtained over the frequency range shown ( $\pm 7\%$  change in frequency from the center frequency of 325 Hz). A slight decrease in performance, however, was observed in a small frequency range in the center of the tuning band. This was attributed to the fact that the discretized shunt capacitance was not quite equal to the PIA capacitance measured at constant stress (i.e.,  $\alpha = 1$ ) at the tuning band center frequency.

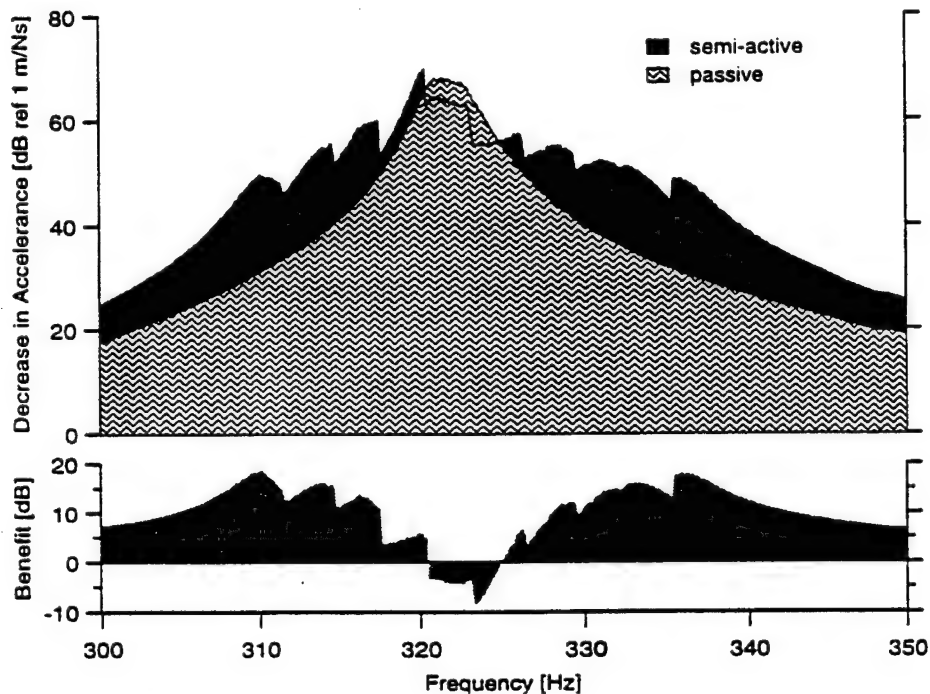


Figure 14. Active vs passive structural attenuation performance

Note that the speed of the control system was limited by the speed of the filters used in the control system. The electronics used to adjust the shunt capacitance operated very quickly compared to the filters. Thus, proper tuning was achieved as soon as the filters settled and the proper disturbance frequency was estimated. The rate of re-tuning due to a change in disturbance frequency was limited by the disturbance frequency estimation method. Small changes in disturbance frequency, less than about 11% of the tuning band, were effectively compensated in less than 60 milliseconds. Detecting, then completely switching the absorber from short to open circuit, or vice versa, required less than 250 milliseconds. A complete discussion of the effects of control speed as well as variations due to changing forcing amplitudes can be found in *A Tunable Piezoceramic Vibration Absorber*, Ph.D. thesis by Davis<sup>11</sup>.

## 5. CONCLUSIONS

A solid-state tunable semi-active piezoceramic vibration absorber was developed. Electrically shunting a piezoelectric inertial actuator with a capacitive electrical impedance changed a fraction of the effective net stiffness of the device, thus changing the device's natural frequency. The control system used to tune the PIA monitored the voltage and current produced by the device to estimate a tonal structural vibration frequency and in turn adjust the net discrete shunt capacitance appropriately.

The semi-active PIA absorber had a  $\pm 3.7\%$  tunable frequency band relative to the center frequency. Additional attenuation effects extended beyond  $\pm 7\%$  of the center frequency. Within the tuning band, increases in performance beyond passive performance were as great as 20 dB. In addition, the average increase in performance across the tunable frequency band was over 10 dB.

This combination of tunable vibration absorber and active tuning method has several features that distinguish it from, and give it potential advantages over, others described in the literature. First, it is a piezoelectric-based device. Second, it uses

capacitive shunting to accomplish an effective change in stiffness. Third, it is less complex than comparable devices, because it is completely solid-state. Fourth, it requires no additional sensors, as the voltage and current signals generated in the piezoelectric elements may be used directly. Fifth, it has relatively low power consumption relative to other PVA tuning methods: the electrical power required for shunt circuit switching is far less than the power required for driving stepper-motors or heating viscoelastic materials. Furthermore, the tuning controller was novel in that it could be implemented as a completely solid-state analog system. Achieving this would require performing the frequency estimation and control voltage calculation in hardware instead of software. Frequency estimation could be accomplished using a Phase-Locked Loop (PLL) circuit<sup>12,13</sup>. PLLs require little power, react quickly, and are commercially available in compact integrated circuit packages. The output of the PLL is a DC voltage directly proportional to frequency, thus making the control voltage calculation largely a matter of scaling.

## ACKNOWLEDGMENTS

This work was supported by the Office of Naval Research under MURI Grant N00014-96-1173 (Acoustic Transduction).

## REFERENCES

1. J.F. Unruh, "Structure-Borne Noise Control for Propeller Aircraft," *AIAA Journal of Aircraft*, Vol. 25, No. 8, pp 752-757, August 1988.
2. C.D. Johnson, "Design of Passive Damping Systems," *Journal of Vibration and Acoustics, Special 50th Anniversary Design Issue*, Vol. 117, pp 171-176, June 1995.
3. B.G. Korenev and L.M. Reznikov, *Dynamic Vibration Absorbers*, John Wiley & Sons, England, p 237-242, 1993.
4. E. Waterman, D. Kaptein, and S. Sarin, "Fokker's Activities in Cabin Noise Control for Propeller Aircraft," Proceedings of the SAE Business Aircraft Meeting & Exposition, SAE Paper No. 830736, 1983.
5. W. Halvosen and U. Emborg, "Interior Noise Control of the Saab 340 Aircraft," Proceedings of the SAE General Aviation Aircraft Meeting & Exposition, SAE Paper No. 891080, 1989.
6. M. Lavitt, "IPN International Product News: Active Absorbers Cancel Aircraft Engine Noise," *Aviation Week & Space Technology*, February 24, p. 68, 1997.
7. F. Fiorino, "Airline Outlook: DC-9 Noise Absorbers," *Aviation Week & Space Technology*, April 28, p. 15, 1997.
8. J. Dosch, G. Lesieutre, G. Koopmann, and C. Davis, "Inertial Piezoceramic Actuators for Smart Structures," Proc. of the Smart Structures and Materials 1995 Industrial and Commercial Applications of Smart Structures Technologies Conference, San Diego, CA, SPIE Vol. 2447, pp 14-25, 1995.
9. G. Lesieutre, G. Koopmann, and S. Yoshikawa, "High Power Density Piezoelectric Actuator for Noise and Vibration Reduction: Monthly Letter Status Report," NASA Contract NAS1-20205, AVC Instrumentation / PCB Piezotronics Subcontract 0001, Penn State University, July, 1995.
10. C. Davis, G. Lesieutre, and J. Dosch, "A Tunable Electrically Shunted Piezoceramic Vibration Absorber," *Proc. of the SPIE Smart Structures and Materials Passive Damping and Isolation Conference*, Vol. 3045, Paper 10, 1997.
11. C. Davis, "A Tunable Piezoceramic Vibration Absorber," Ph.D. Thesis, Department of Aerospace Engineering, The Pennsylvania State University, University Park, PA, December 1997.
12. P. Horowitz and W. Hill, *The Art of Electronics, Second Edition*, Cambridge University Press, Cambridge, U.K., p 184, 1994.
13. C. Niezrecki and H. Cudney, "Structural Control Using Analog Phase-Locked Loops," *Journal of Vibration and Acoustics*, Vol. 119, pp 104-109, January 1997.

# **APPENDIX 39**

## ACTIVE BROADBAND FORCE ISOLATION USING A FLEXURAL PIEZOELECTRIC INERTIAL ACTUATOR

Julien Bernard\*

George A. Lesieutre† and Gary H. Koopmann‡  
Penn State University, University Park, PA

### ABSTRACT

This research addressed the isolation of a payload subjected to a non-measurable broadband disturbance and rigidly mounted to either a rigid or flexible base. The work consisted of two parts: first, the modeling, design and realization of an actuator suitable for the application; and second, the design and implementation of a force feedback control system using the actuator. A flexural piezoceramic inertial actuator was used to generate reaction forces at the root of a double cantilever beam actuated in flexure by surface mounted piezoceramics. Necessary damping of the actuator itself was provided by a constrained layer damping treatment. Analytical and finite element models were developed and used to determine the effects of various design parameters on the actuator short-circuit dynamic stiffness and the blocked force frequency response functions. Using these models, an actuator, providing a minimum 0.03 N/V between 25 and 400 Hz, was designed and built.

Active force isolation experiments were conducted with the goal of minimizing the force transmitted to the base from 0 to about 100 Hz using force feedback. Controllers were designed using a variation of the LQG method. Fictitious disturbance and performance filters were appended to the physical plant models to account for the fact that the power spectral density of disturbances is usually band limited, and to ensure adequate roll-off of the controllers at high frequencies. In the rigid-base case, the best performance was a 6 dB average broadband reduction of the transmitted force between 20 and 110 Hz. In the flexible-base case, the best performance was a 2 dB average broadband reduction of the transmitted force between 20 and 90 Hz. The decrease in the level and the bandwidth of the reduction obtained in the flexible-base case can be attributed to additional phase delay of the secondary plant transfer function, as well as additional computer time delay.

\* Ph.D. candidate, Member.

† Assoc. Professor, Aerospace Eng'g., Assoc. Fellow.

‡ Professor, Mechanical Engineering.

Copyright © 1999 by G.A. Lesieutre. Published by the AIAA, Inc. with permission.

### INTRODUCTION

Vibration isolation problems involve a system comprising a payload, a mount, and a base [1]. In many applications, the payload is subjected to an external force or an acceleration, and generates a force at, and/or an acceleration of the base via the mount. The payload may be a vibrating machine of some kind, and the base, a car body, a ship hull, an aircraft fuselage or the floor of a building. The goal of an isolation system is to minimize the transmitted force and/or an acceleration over a specified frequency range.

To this end, passive active and hybrid techniques have been developed. The most commonly used passive technique, compliant mounts, present a risk of payload resonance, and do not offer any isolation below the first resonance frequency of the mount-payload system. The first problem is usually addressed by adding some damping to the mount, by using a viscoelastic material, a viscous damper, or an actuator with velocity feedback. The second problem often requires the use of an actuator in parallel or in series with the passive mount.

In some cases, such as a pipe containing a turbulent flow, the payload cannot tolerate any motion, and the mount must be rigid. Only active techniques, based on the application of a secondary force to the system, remain. Due to the rigidity of the system, the propagation delay between the disturbance and the output is generally very short. Feedforward control is then impractical and feedback control must be used. Active isolation techniques using feedback control avoid the risk of payload resonance, and theoretically allow for low frequency isolation. They present some limitations, however, such as the increased risk of instability in case of non-minimum phase systems, the trade-off between disturbance rejection and noise immunity, the controller contributions to the plant phase delay, and the inevitable modeling errors. Low and high frequency limits to active broadband isolation using feedback control, and a robust control design procedure based on the LQG method, are discussed in detail in [2].

Active isolation systems require several design decisions, including at least the following: the kind of actuator; the point of application of the secondary force

[1]; the control strategy (feedback or feedforward) [1]; the sensed variable(s) (interfacial force, base acceleration, payload acceleration, gap) [3, 4]; the control bandwidth (narrowband or broadband) [2, 5]; the control design methodology [2, 6]; and implementation of the controller(s). Good experimental results in active vibration isolation range from 16 to 20 dB for narrow band isolation [5, 7], and from 10 to 15 dB over a decade for broadband isolation [2, 8].

This research addressed the problem of active isolation of a payload subjected to a non-measurable broadband disturbance and rigidly mounted to either a rigid or a flexible base. The approach involved two parts: (1) the modeling, design and realization of a suitable actuator; and (2) the design, implementation, and evaluation of a robust force feedback control system. The performance of the active isolation system was evaluated using two different performance indices: the ratio of the closed loop to open loop force transmissibility, and the sensitivity transfer function.

### FLEXURAL PIEZOELECTRIC INERTIAL ACTUATOR

Piezoceramic actuators generally offer good force generation capability, high frequency bandwidth, and linearity of control. Available types of piezoceramic actuators include mainly longitudinal stack actuators ( $d_{31}$ ) and flexural actuators ( $d_{31}$ ). Stack actuators have been used successfully in hybrid isolation systems [9]. They can generate very high forces but have also very limited stroke [2]. For this reason they are more suitable if the base is rigid or slightly flexible. They are usually placed in parallel or in series with a passive isolation stage. In parallel, they have to overcome the stiffness of the mount. In series, they have to overcome the weight of the payload.

Flexural piezoceramic inertial actuators offer longer stroke, do not have to overcome the stiffness of the mount, or carry the weight of the payload. They are consequently more suitable than stack actuators in applications involving a flexible base, a rigid mount, and a heavy payload. However, they have some drawbacks: The larger stroke results in lower force than that provided by a stack actuator of the same volume. Also, the absence of a passive isolation stage results in very lightly damped actuator modes, which can themselves become unstable in closed loop conditions. It is necessary to add some passive damping to the system. In this research, a constrained layer damping treatment was used, improving the closed loop stability significantly.

Figure 1 shows a half symmetry drawing of the flexural piezoceramic inertial actuator used in this research. The main elements included a double cantilever base beam, piezoceramic plates bonded symmetrically on the top and the bottom surfaces of the beam, a reaction mass at each end of the beam, and a

fixture at its center to enable attachment to the external structure. The piezoceramics were used in the  $d_{31}$  mode, and bonded such that their inherent polarization was in the same direction. By applying the same electric field to the top and bottom plates, they experienced opposite deformations and generated a bending motion in the beam at the same frequency as the applied electric field. Assuming that the actuator was connected to a symmetric structure, *i.e.* that the angle of rotation at the attachment point remained zero, the actuator force was given by :

$$F(i\omega) = F_b(i\omega) - K_x^\infty(i\omega)X(i\omega) \quad (1)$$

where  $F(i\omega)$  is the effective force applied to the structure,  $X(i\omega)$  is the displacement at the point of attachment,  $F_b(i\omega)$  is the actuator blocked force, and  $K_x^\infty(i\omega)$  the actuator short circuit dynamic stiffness in the  $x$  direction. The blocked force is the force developed by the actuator when connected to an infinite impedance, *i.e.* when the displacement  $x$  is constrained to zero. The short circuit dynamic stiffness is the dynamic stiffness of the actuator when the electric field applied to the piezoceramics is zero. In the case of a non-symmetric structure, the actuation force would also depend on the rotation angle times the rotational dynamic stiffness of the actuator.

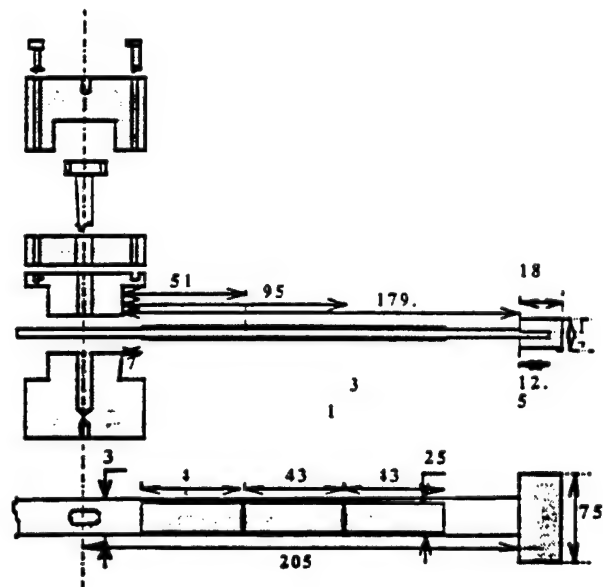


Figure 1. Geometry of the flexural piezoelectric inertial actuator (dimensions in mm)

### Modeling, design, and realization

Euler-Bernoulli analytical and finite element models of the actuator were developed and used to conduct three sets of parameter studies.

First, the effects of (1) the mass ratio and (2) the rotary inertia ratio (of the reaction mass to the base beam) on the natural frequencies of the base beam was studied. Clamped-free boundary conditions were adopted for the calculations since, in the subsequent experiments, the actuator would be connected either to a rigid or slightly flexible base. To a first approximation, assuming that the additional mass and stiffness due to the piezoceramics were negligible, these natural frequencies were also the resonance frequencies in the blocked force frequency response function. In a feedback control system, actuator resonances result in phase delays in the secondary plant transfer function, and increase the risk of instability. As shown in Figures 2 and 3, the first natural frequency of the base beam is primarily governed by the mass ratio, whereas the second natural frequency is sensitive mainly to the rotational inertia ratio. Using this insight, one can place the first and second natural frequencies almost independently, so that they do not interfere with the frequency spectrum of the disturbance.

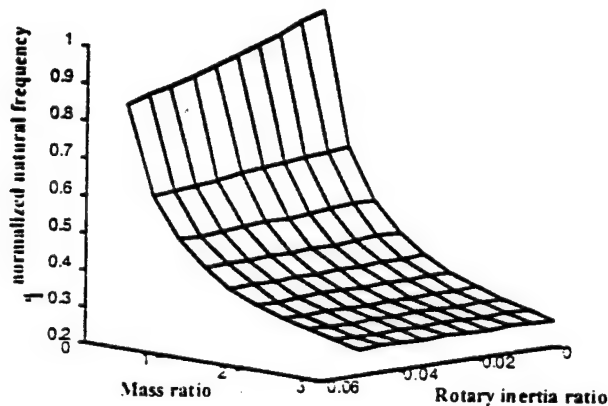


Figure 2: First normalized natural frequency versus mass and rotational inertia ratio

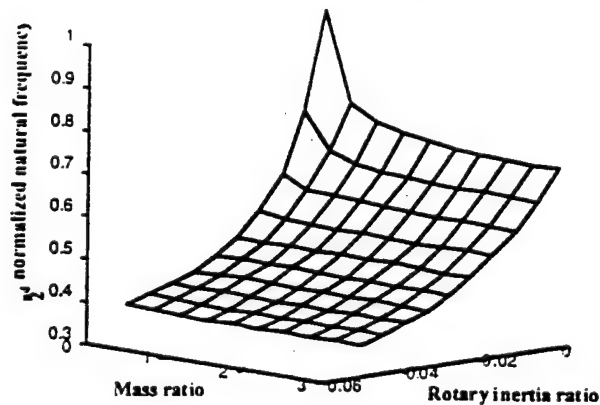


Figure 3: Second normalized natural frequency versus mass and rotational inertia ratio

Second, ways to improve the effectiveness of the piezoceramic actuator were investigated. Using an

Euler-Bernoulli model described in [10], the effect of the piezoceramic-to-beam thickness ratio on the normalized bending curvature (strain) was determined. For a given beam thickness, and for equal widths and Young's moduli, the optimal piezoceramic thickness was found to be about one third of the beam thickness. Then, using a finite element model, the effects of the aforementioned mass and rotational inertia ratios on the strain distributions of the first and second modes of the base beam in clamped-free boundary conditions was studied. Knowledge of the modal strain distributions was important because piezoceramics are most efficient in exciting a particular mode if placed in a region of high strain for that mode. The same phenomena were observed for the first and second mode, but to a larger degree for the second mode. As shown in Figure 4, the tip rotational inertia tends to shift the regions of high strains towards the free end. The tip mass tends to shift them back to their original position, but not as significantly. Consequently, if a large mass with small rotational inertia is chosen, the first natural frequency is reduced while keeping the second natural frequency high, and the regions of high strain are essentially unchanged.

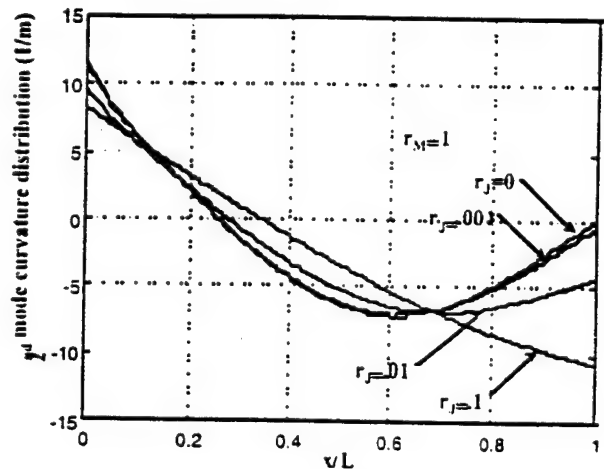


Figure 4: Strain distribution of the second mode for a fixed mass ratio and various rotational inertia ratios

Third, after selecting the geometry and the material properties of the actuator, the blocked force frequency response function was simulated using a finite element model. The possibility of increasing the force-delivering capability without changing the natural frequencies was investigated. This was accomplished by simultaneously increasing the thickness of the beam, the thickness of the piezoceramics, the tip reaction mass and rotational inertia, and the beam length. As shown in Figure 5, doubling and quadrupling the beam thickness increased the blocked force 80% and 460% respectively, at all frequencies.

A three step design procedure was then naturally deduced from these results. The first step was to determine the base beam and reaction masses



dimensions and material properties to obtain the desired natural frequencies in clamped-free boundary conditions. The second step was to determine the piezoceramic thickness and distribution so as to obtain the maximum curvature and to excite the desired modes. The third step was to change the size of the actuator without changing the natural frequencies (using the blocked force frequency response) until the desired level of blocked force was obtained, or until the constraints on the actuator size were reached.

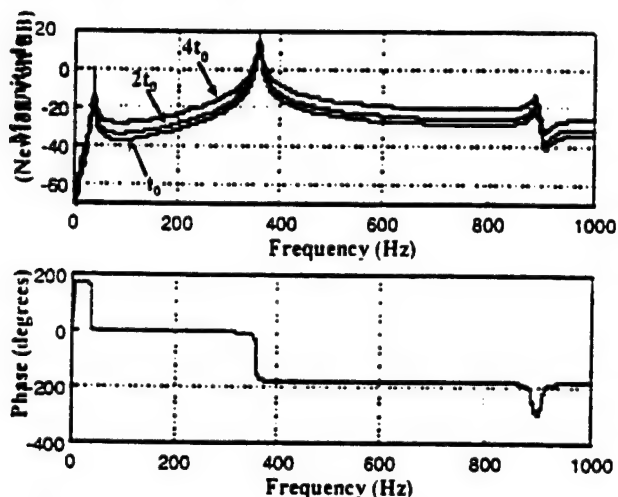


Figure 5. Simulated blocked force for various beam thicknesses and constant natural frequencies

Figure 6 shows an actuator mounted on a mass. The base beam was made of aluminum, the reaction masses of steel. APC 856 material was used for the piezoceramic plates. The dimensions of the base beam and reaction masses were chosen to place the first and second natural frequencies at about 35 and 300 Hz, respectively. The corresponding mass and rotational inertia ratios were 2.4 and 0.0078, respectively. The piezoceramic thickness was chosen to be one third of the beam thickness, and segmented piezoceramic plates were placed along the first three quarters of the beam. In the subsequent active control experiments, the disturbance power spectral density could be scaled so as not to exceed the maximum available force from the actuator. Hence, no attempt was made to maximize the blocked force. Once the dimensions were chosen, they were input to the finite element model and the Modal Strain Energy method [11] was used to predict the change in the modal damping ratios due to the addition of a constrained layer damping treatment.

#### Experimental characterization

The short circuit dynamic impedance and the blocked force frequency responses of the actuator were measured before and after the addition of the constrained layer damping treatment. For the measurement of the short circuit dynamic impedance, the piezoceramics

were short circuited. The experimental set-up included: an electromagnetic shaker driven by a random voltage signal to generate a force at the point of attachment of the actuator; a force transducer to measure the applied force; and a laser vibrometer to measure the velocity at the same point. For the measurement of the blocked force the set-up was even simpler: a large mass to be used as an infinite impedance; and a force transducer to measure the actuation force against the mass. These measurements were curve fit to obtain the change in the modal parameters of the first and second actuator resonance frequencies due to the constrained layer damping.

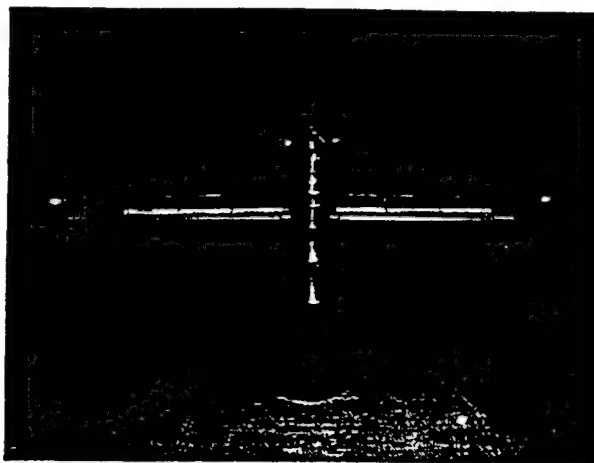


Figure 6: "Two arm" flexural piezoelectric inertial actuator mounted on a rigid mass

In the short circuit dynamic impedance measurement, the damping ratios increased by 1120% and 100% respectively, whereas the natural frequencies dropped by 1% and 8 % respectively. In the blocked force measurement, the damping ratios increased by 14% and 40% respectively, the first natural frequency remained unchanged and the second dropped by 6%.

Figures 7 and 8 show the blocked force frequency response before and after the application of the constrained layer damping treatment, from experimental measurement and simulation (only the undamped actuator blocked force was simulated). The first damping ratio and the second natural frequency change noticeably. However the level of the blocked force at non-resonant frequencies remained essentially unchanged. The actuator provides approximately 0.03 N/V between 50 and 250 Hz, i.e. about 9 N at the maximum driving voltage (300 V).

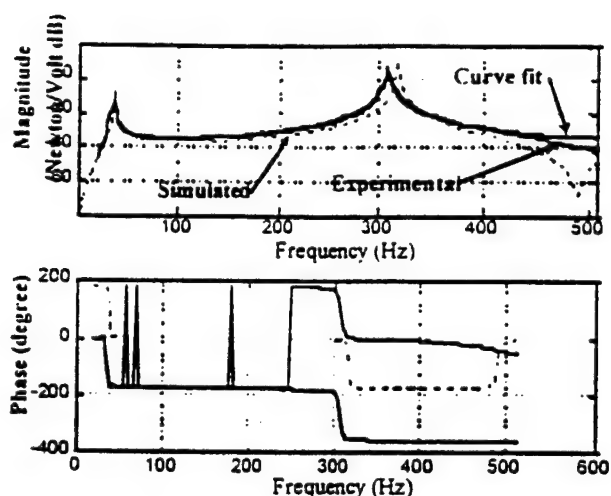


Figure 7. Experimental, simulated, and curve-fit blocked force of the actuator without CLD treatment

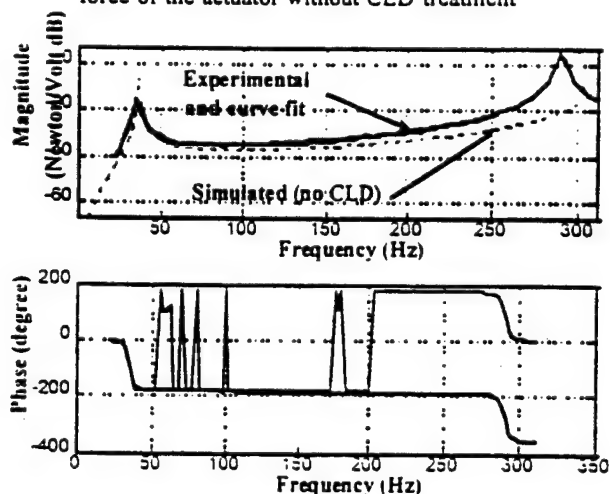


Figure 8. Experimental, simulated, and curve-fit blocked force of the actuator with CLD treatment

## CONTROL DESIGN METHODOLOGY

The problem addressed in this research can be represented by the block diagram shown on Figure 9. On this diagram,  $y$  is the sensor output giving the total force transmitted to the base,  $d$  is the sensor output giving the force transmitted to the base due to the disturbance,  $n$  is the sensor noise, and  $u$  the control input to the actuator.  $G_{yu}(s)$  is the actuator-sensor, or secondary plant, transfer function, and  $-K(s)$  the controller transfer function. In open loop conditions,  $Y(s)=D(s)$ . In closed loop conditions it is given by:

$$Y(s) = S(s)U(s) - 1(s)N(s) \quad (2)$$

$$S(s) = \frac{1}{1 + G_{yu}(s)K(s)} \quad (3)$$

$$T(s) = 1 - S(s) \quad (4)$$

$S(s)$  is called the sensitivity transfer function and  $T(s)$  the complementary sensitivity transfer function. For good disturbance rejection,  $S(s)$  should be small at some desired frequencies. As seen from Equation (4),  $T(s)$  will be large at these frequencies, resulting in high noise sensitivity. Since many disturbance spectra are limited in bandwidth, and since noise is usually a problem mainly at high frequencies, a trade-off between disturbance rejection and noise suppression is obtained by making  $K(s)$  large at low frequencies and small at high frequencies.

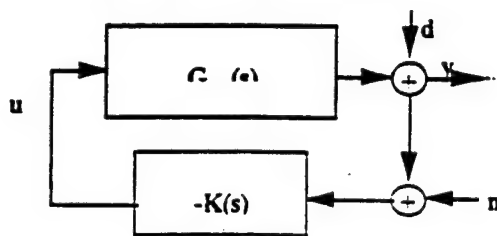


Figure 9. Block diagram representation of the regulation problem

The controllers were designed using a variation of the Linear Quadratic Gaussian (LQG) method. The LQG method is limited in that the disturbance input must be a zero mean gaussian white noise, and that no stability margins are guaranteed. To overcome these limitations, fictitious disturbance filters were appended to the physical system model before application of the LQG algorithm. The physical systems (rigid and flexible configurations) were described by state space equations of the form:

$$\dot{\underline{x}}(t) = A \underline{x}(t) + \underline{b}_u u(t) + \underline{b}_w w(t) \quad (5)$$

$$\underline{y}(t) = C \underline{x}(t) + \underline{d}_u u(t) + \underline{d}_w w(t) \quad (6)$$

where  $u$  is the control input,  $w$  the disturbance input,  $\underline{x}$  the vector of states,  $y$  the output and the measurement noise was temporarily ignored.  $A$ ,  $\underline{b}_u$ ,  $C$  and  $\underline{d}_u$  were determined by the system identification of the secondary plant transfer function.  $\underline{b}_w$ ,  $C$  and  $\underline{d}_w$  were arbitrarily set to 0 and 1, respectively. This assumption is appropriate in the rigid base case, in which the propagation delay between the disturbance input and the output is very short, but less justified in the flexible base case.

First, a fictitious disturbance filter was appended to the physical system, to account for the fact that the power spectrum density of the disturbance is likely to be band limited. Basically, the procedure consists in assuming that the power spectrum density of the disturbance  $w$  can be written as the square of a proper rational fraction polynomial  $H(s)$ . Using a property of linear systems,  $w$  can be viewed as the output of a linear system of transfer function  $H(s)$  to a zero mean gaussian white noise  $w_0$  of intensity  $W_0$ . In this research, the power spectrum density of  $w$  was

assumed to roll off as  $\omega^{-1}$ .  $H(s)$  was chosen to be a second order filter of static gain 1, undamped frequency  $\omega_n$ , and damping ratio  $\zeta_0$ . A state space representation for this filter was determined as:

$$\dot{\underline{x}}_w = \underline{A}_w \underline{x}_w + \underline{b}_{w_0} w_0 \quad (7)$$

$$w = \underline{C}_w \underline{x}_w + \underline{d}_{w_0} w_0 \quad (8)$$

Equations (7) and (8) were appended to Equations (5) and (6) to form an augmented system:

$$\dot{\underline{x}} = \begin{bmatrix} \underline{A} & \underline{b}_w \underline{C}_w & 0 \\ 0 & \underline{A}_w & 0 \end{bmatrix} \underline{x} + \begin{bmatrix} \underline{b} & 0 \\ 0 & \underline{b}_{w_0} \end{bmatrix} u + \begin{bmatrix} \underline{b}_d \underline{d}_w \\ \underline{b}_{d_0} \end{bmatrix} w_0 \quad (9)$$

$$y = [\underline{C} \quad \underline{d}_w \underline{C}_w] \underline{x} + \underline{d}_u u + \underline{d}_w \underline{d}_{w_0} w_0 \quad (10)$$

where the disturbance input  $w_0$  is a zero mean gaussian white noise, such that the condition for the application of the LQG method is satisfied. The introduction of the disturbance filter made it possible to obtain a low sensitivity transfer function in a limited bandwidth, and to keep the complementary sensitivity transfer function low above this bandwidth.

Secondly, a fictitious performance filter was appended to the augmented system to ensure adequate roll-off of the controllers at high frequencies. In the classical LQG method, the weight on the output,  $q$ , and the weight on the control input,  $r$ , are independent of frequency [12]. References [2] and [6] describe a procedure to make  $q$  frequency dependent, so as to penalize  $y$  only at certain frequencies. A fictitious output  $z$  is defined as the output of a linear system of transfer function  $F(s)$  to the physical output  $y$ . The LQG problem associated with the system of output  $z$  and constant weight  $q$ , is equivalent to the LQG problem associated with the system of output  $y$  and a frequency dependent weight  $q(i\omega) = q_1 F(i\omega)$ . To penalize  $y$  only in the low frequency range,  $F(s)$  was assumed to be a second order filter of static gain 1, undamped frequency  $\omega_1$ , and damping ratio  $\zeta_1$ . A state space representation of the performance filter, with a non zero measurement noise in the output equation, was determined:

$$\dot{\underline{x}}_z = \underline{A}_z \underline{x}_z + \underline{b}_z y \quad (11)$$

$$z = \underline{C}_z \underline{x}_z + \underline{d}_z y + \theta \quad (12)$$

Equations (11) and (12) were appended to Equations (9) and (10) to form the final augmented system:

$$\dot{\underline{x}} = \begin{bmatrix} \underline{A} & \underline{b}_w \underline{C}_w & 0 & 0 \\ 0 & \underline{A}_w & 0 & 0 \\ \underline{b}_z \underline{C}_z & \underline{b}_z \underline{d}_z \underline{C}_w & \underline{A}_z & \underline{b}_z \underline{d}_z \end{bmatrix} \underline{x} + \begin{bmatrix} \underline{b} & 0 \\ 0 & \underline{b}_{w_0} \\ 0 & 0 \end{bmatrix} u + \begin{bmatrix} \underline{b}_d \underline{d}_w \\ \underline{b}_{d_0} \\ 0 & 0 \end{bmatrix} w_0 + \theta \quad (13)$$

$$y = [\underline{C} \quad \underline{d}_w \underline{C}_w \quad \underline{C}_z \quad \underline{d}_z \underline{C}_w] \underline{x} + \underline{d}_u u + \underline{d}_w \underline{d}_{w_0} w_0 + \theta \quad (14)$$

The LQG algorithm was applied to the augmented system, and the combined observer-controller transfer function from  $z$  to  $u$  was obtained. The real feedback controller transfer function was recovered by:

$$\frac{U(s)}{Y(s)} = \frac{U(s)}{Z(s)} F(s) \quad (15)$$

Hence, roll-off of the controller transfer function at high frequencies is not only ensured by the presence of the fictitious filter in the plant transfer function, but also by multiplication by the performance filter transfer function. For the design of the controllers,  $\omega_0$ ,  $\omega_1$ , and  $\zeta_0$ ,  $\zeta_1$  were chosen to be equal to 800 rad/s and 0.7, respectively.

## ACTIVE FORCE ISOLATION EXPERIMENTS

Two active force isolation experiments were conducted. In the first experiment, the actuator was placed between an electromagnetic shaker (used as a disturbance source) and rigid mass. In the second experiment, it was placed between the shaker and a flexible fixed-fixed beam, as shown in Figure 10. The goal in both cases was to minimize the force transmitted to the base between 0 and 125 Hz using force feedback (i.e., the controller was designed to be most effective over this range). Theoretically, the actuator can always be designed such that its resonance frequencies are outside the frequency spectrum of the disturbance. In practice however, variation of the frequency spectrum of the disturbance may occur, resulting in the presence of one or more actuator resonances inside the range. To test the robustness of the active isolation system to this possibility, all experiments were conducted with a disturbance frequency spectrum ranging from 0 to 400 Hz, one that included the first two actuator resonance frequencies.

The forces at the shaker-actuator interface and the actuator-base interface were sensed by two PCB 208M51 force transducers. A Hewlett-Packard 35660A frequency analyzer was used to compute transfer functions for system identification and for performance assessment of the feedback control. The controller was

implemented digitally using a dSPACE digital signal processor board DS1102.

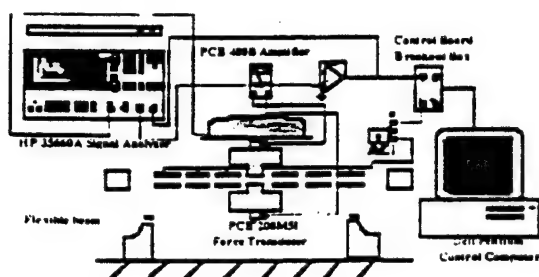


Figure 10. Experimental set-up of the flexible base active isolation experiment

The secondary plant, or actuator-sensor plant, was defined as the following: the power amplifier for the actuator, the actuator, the force transducer, the analog signal processing unit for the force transducer, and the power amplifier for the sensor. Additionally, a pure time delay accounting for the *estimated* computer time delay was included in the secondary plant transfer function.

The performance of the active isolation system was evaluated using two different primary plants (disturbance input to output): (1) the transfer function from the disturbance force, *i.e.* the force at the shaker-actuator interface, to the transmitted force, *i.e.* the force at the actuator-base interface, (force transmissibility); and (2) the transfer function from the voltage driving the shaker to the transmitted force. In both cases, the ratios of the closed loop to open loop primary plant transfer functions were used to evaluate the system. However, their significance and practical interest proved to be different.

Let  $Y_1$  be the output of the force sensor between the shaker and the actuator, and  $Y_2$  the output of the force sensor between the actuator and the base. The true performance of the active isolation system is given by the sensitivity transfer function, the ratio of the closed loop to open loop regulated output  $Y_2$ :

$$S(i\omega) = \frac{Y_2^{cl}(i\omega)}{Y_2^{ol}(i\omega)} \quad (16)$$

where  $^{cl}$  denotes closed loop quantities, and  $^{ol}$  open loop quantities

In the first case, the ratio of the closed loop to open loop primary plant transfer functions is the ratio of the closed loop to open loop force transmissibilities, and is defined by:

$$\frac{Y_2^{cl}(i\omega) Y_1^{ol}(i\omega)}{Y_1^{cl}(i\omega) Y_2^{ol}(i\omega)} = S(i\omega) \frac{Y_1^{ol}(i\omega)}{Y_1^{cl}(i\omega)} \quad (17)$$

A transmissibility ratio less than 1 means that the ratio of the transmitted force  $Y_2$  to the disturbance force  $Y_1$  has been decreased. This may be due either to a reduction of the magnitude of  $Y_2$ , or to an amplification of the magnitude of  $Y_1$ . The transmissibility ratio is equal to the sensitivity transfer function if and only if  $Y_1$  is the same in closed loop and open loop conditions at all frequencies. In open loop conditions, the motions of the shaker and the actuator are due to the disturbance force. In closed loop conditions, they are due to the superposition of the disturbance force and the actuator force. In practice, the motion of the shaker and the motion of the actuator due to the actuator force will be different, so that  $Y_1$  is necessarily different in closed loop and open loop conditions. The transmissibility ratio must be considered more as a conceptual way to assess the performance of the active isolation system, assuming that the disturbance source is able to generate a constant force.

In the second case, the ratio of the closed loop to open loop primary plant transfer functions is defined by:

$$\frac{Y_2^{cl}(i\omega) V^{ol}(i\omega)}{V^{cl}(i\omega) Y_2^{ol}(i\omega)} = S(i\omega) \frac{V^{ol}(i\omega)}{V^{cl}(i\omega)} \quad (18)$$

Provided that the same voltage is applied to the shaker in closed loop and open loop conditions, this ratio gives a direct measurement of the sensitivity transfer function, *i.e.* of the absolute reduction of the regulated output  $Y_2$  due to the active isolation system.

Three types of measurements were performed: (1) system identification, to get the secondary plant mathematical models; (2) open loop primary plant transfer functions; and (3) closed loop primary plant transfer functions for the two primary plants defined above, for various LQG design parameters. Then the ratios of the closed loop to open loop transfer functions were calculated to evaluate the performance of the active system.

## EXPERIMENTAL RESULTS

The transfer functions of the two secondary plants (rigid and flexible base configurations) were measured between 0 and 2 kHz. The data were curve fit using rational fraction polynomials [13] between 0 and 350 Hz, more than three times the desired control frequency range. For the rigid base case, the first two actuator modes were included, as shown in Figure 11, resulting in a fourth order mathematical model. For the flexible base case, the first two actuator modes and the first beam mode were included, as shown in Figure 12, resulting in a sixth order model.

As expected, the open loop transmissibility in the rigid case is nearly independent of frequency. The system behaves almost like a rigid mount, with the

disturbance force is equal to the transmitted force. The open loop transmissibility in the flexible case exhibits poles at 190 Hz and 320 Hz and a zero at 290 Hz. This zero corresponds to a resonance of the flexible base for which the mounting point is an antinode.

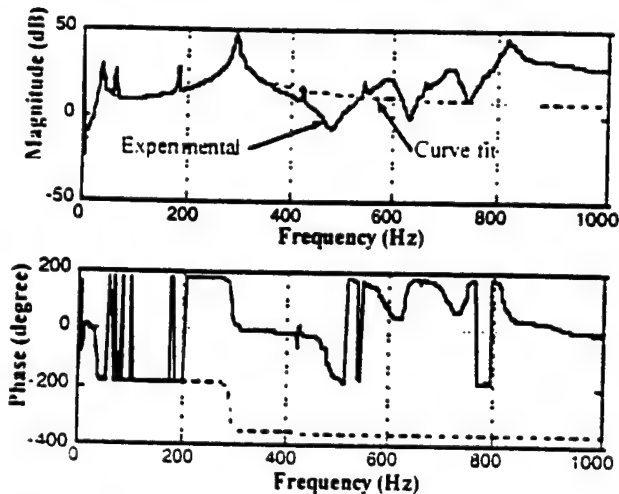


Figure 11. Rigid Base: experimental and mathematical secondary plant transfer function

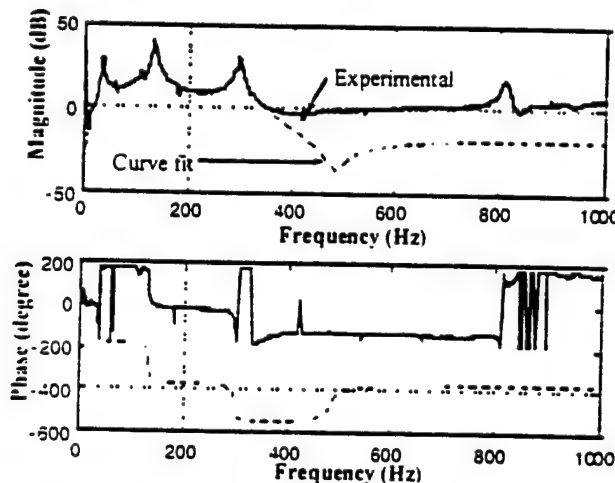


Figure 12. Flexible base: experimental and mathematical secondary plant transfer function

The open loop transfer functions from the voltage driving the shaker to the transmitted force in the rigid case exhibits a single pole at 40 Hz corresponding to the first resonance of the shaker and a zero at zero frequency. This zero is due to the fact that the shaker itself is an inertial device. The open loop transfer function in the flexible case exhibits poles at 40, 140 and 300 Hz and zeros at 0 and 290 Hz. The latter is due to a base resonance.

In the rigid base case, the isolation system was able to provide an average reduction of about 4.5 dB of the open loop transmissibility between 35 and 110 Hz. (35 Hz corresponds to the lowest actuator natural frequency.) Good coherence on the closed loop transmissibility below this frequency was difficult to

obtain. However, it is reasonable to believe that the closed loop transmissibility is close to the open loop transmissibility in this range, due to the lack of authority of the actuator below its first natural frequency.

In the flexible case, the isolation system was able to provide an average reduction of about 2.5 dB of the open loop transmissibility between 35 and 85 Hz. Reduction levels up to 15 dB were obtained between 120 and 250 Hz.

Figures 13 to 16 show the ratio of the closed loop to open loop transfer functions from the voltage driving the shaker to the transmitted force, in the rigid and flexible case, and for different values of  $q$  and  $W_0$ . Since the same voltage was used in closed loop and open loop, this ratio is also equal to the sensitivity transfer function.

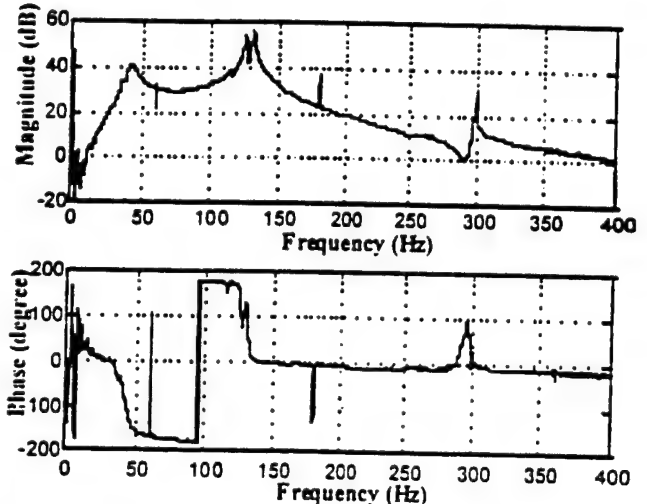


Figure 13. Rigid Base: Experimental sensitivity transfer function ( $q=100$ ):

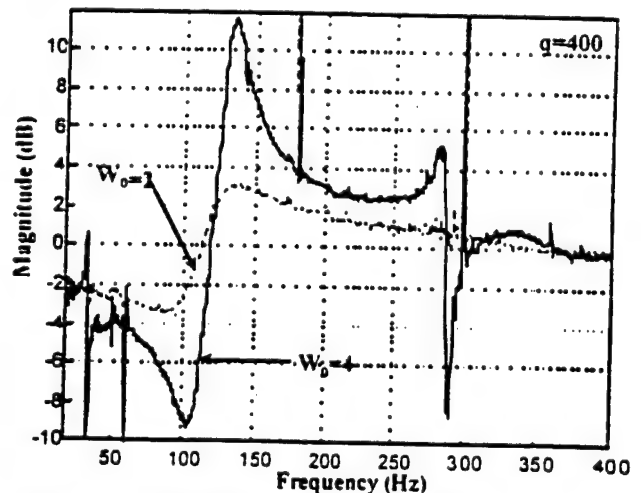


Figure 14. Rigid Base: Experimental sensitivity transfer function ( $q=400$ )

In the rigid base case, the isolation system was able to provide an average reduction of about 6 dB of



the transmitted force between 35 and 110 Hz. Reduction of about 2 dB was also obtained below the first actuator natural frequency, between 20 and 35 Hz.

In the flexible case, the isolation system was able to provide an average reduction of about 2 dB of the transmitted force between 20 and 90 Hz.

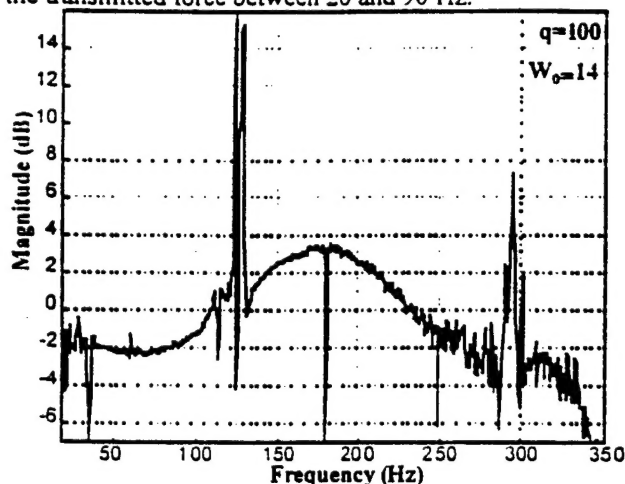


Figure 15. Flexible Base: Experimental sensitivity transfer function ( $q=100$ )

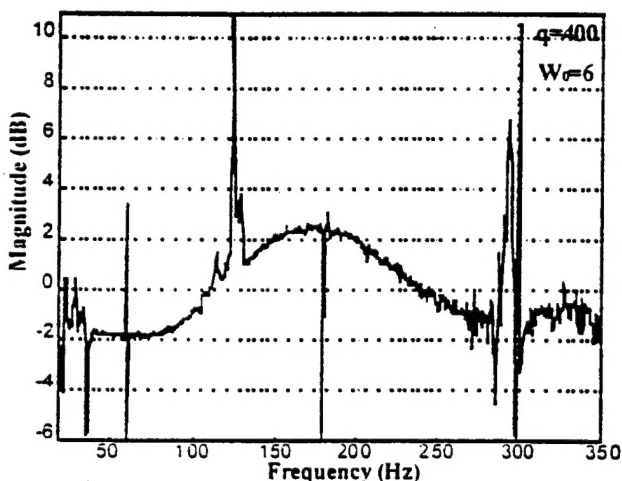


Figure 16. Flexible Base: Experimental sensitivity transfer function ( $q=400$ )

## Discussion

The interpretation of the transmissibility ratios is difficult because the transmissibility ratio is not directly related to the sensitivity transfer function (Equation (17)). Reductions of the force transmissibility may be due to either a reduction of the transmitted force, or an amplification of the disturbance force. In the case of the rigid base, transmissibility and sensitivity results show fairly good correlation. This suggests that the disturbance force is not modified significantly. In the case of the flexible base, the sensitivity results show that the transmitted force is increased between 120 and 250 Hz. The reduction of the transmissibility ratio over

this range is thus seen to be due to amplification of the disturbance force.

The interpretation of the sensitivity transfer functions focused on two aspects: the effect of the control design parameters  $q$  and  $W_0$  on the shape of the sensitivity transfer function; and the differences in the sensitivity transfer functions between the rigid and flexible cases.

The sensitivity transfer function is given by Equation (3). The poles of  $S(s)$ , also called optimal closed loop poles, are the zeros of  $1 + G_{yu}(s)K(s) = 0$ . The zeros of  $S(s)$  are the poles of  $G_{yu}(s)$  (open loop poles), and the poles of  $K(s)$ . Hence, a maximum should be observed at the optimal closed loop poles, and a minimum at the open loop poles and controller poles.

The effect of  $q$  on the shape of the sensitivity transfer function can be interpreted by assuming no modeling errors, i.e. that the states are perfectly estimated. The state equations of the system with perfect state feedback and no direct feedthrough of the input to the output are:

$$\dot{\underline{x}} = (\underline{A} - \underline{bK})\underline{\bar{x}} \quad (19)$$

where the controller gain  $K$  is given by:

$$\underline{K} = \underline{r}^{-1}\underline{b}_u'\underline{P} \quad (20)$$

and  $P$  satisfies the so-called Algebraic Riccati Equation:

$$\underline{P}\underline{A} + \underline{A}'\underline{P} - \underline{P}\underline{b}_u\underline{r}^{-1}\underline{b}_u'\underline{P} + \underline{Q} = 0 \quad (21)$$

where  $\underline{Q} = q\underline{C}'\underline{C}$ . The optimal closed poles in the case of pure state feedback are given by the equation:

$$1 + q \frac{a_2(s)a_2(-s)}{a_1(s)a_1(-s)} = 0 \quad (22)$$

where the weight on the control input is assumed to be 1,  $a_2(s)$  and  $a_1(s)$  are the numerator and denominator of the open loop transfer function  $G_{yu}(s)$ , respectively. For low values of  $q$ , the optimal closed loop poles are the stable open poles and the mirror images of the unstable ones. For high values of  $q$ , they tend towards the stable open loop zeros, the mirror images of the unstable ones, or towards infinity in the Butterworth pattern. Figures 17 and 18 show the loci of the optimal closed poles in the rigid and flexible case respectively.

In the rigid case, the poles corresponding to the first actuator resonance tend toward the double zero at the zero frequency, whereas the poles corresponding to the second actuator resonance tend toward a double real zero at about  $-2800 \text{ rad s}^{-1}$ . In the flexible case, the poles corresponding to the first actuator resonance also tend toward the double zero at the zero frequency. The poles corresponding to the first beam resonance tend

toward two real zeros at about -1400 and -2600  $\text{rd s}^{-1}$  respectively. The poles corresponding to the second actuator resonance tend toward two lightly damped zeros at about  $\pm 3000i$ . In both cases, the closed loop stability of first actuator mode is jeopardized by the non-minimum phase property of the plant transfer function, i.e. the presence of the double zero at the zero frequency. In the flexible base case, the closed loop stability of the second actuator mode is compromised due to the presence of the beam mode.

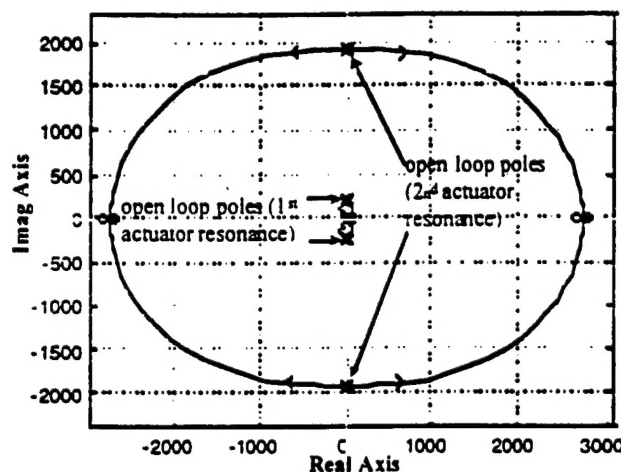


Figure 17. Rigid Base: loci of the optimal closed poles

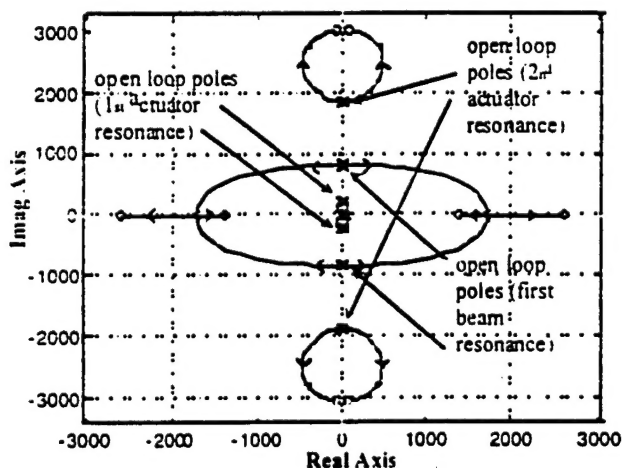


Figure 18. Flexible Base: loci of the optimal closed poles

To be consistent with the assumption of perfect state feedback, the theoretical results should be compared to the experimental results for which  $W_0$  is the highest. From the loci of the optimal closed loop poles, and from what was said about the poles and zeros of the sensitivity transfer function, pole-zero cancellation should occur at low values of  $q$ , and pole-zero separation should increase as  $q$  increases. This evolution can be observed experimentally in the rigid case, by comparing Figures 13 and 14 at about 25 and 290 Hz. Low stability margins in the flexible case did

not permit  $q$  to be increased sufficiently so that pole-zero separation occurs.

To interpret the effect of  $W_0$  on the shape of the sensitivity transfer function, the dynamics of the estimator must be taken into account. If no modeling errors are made on the system, the optimal poles are still given by Equation (22). However, the states will not be estimated instantaneously. The dynamics of the estimator can be represented by:

$$\dot{\tilde{x}} = (A - \underline{I}C)\tilde{x} \quad (23)$$

where  $\tilde{x}$  is the error on the states (difference between actual states and the estimated states),  $A$  the system evolution matrix,  $C$  the system output matrix, and  $\underline{I}$  the estimator gain.  $\underline{I}$  is given by:

$$\underline{I} = \Sigma C' \Theta^{-1} \quad (24)$$

where  $\Theta$  is the noise power spectrum density and  $\Sigma$  satisfies the so-called Filter Algebraic Riccati Equation (FARE):

$$\Sigma A + A' \Sigma - \Sigma C' \Theta^{-1} C \Sigma + W_0 = 0 \quad (25)$$

Taking the transpose of Equations (20), (21) and (22):

$$\dot{\tilde{x}}' = (A' - C' \underline{I}') \tilde{x}' \quad (26)$$

$$\underline{I}' = \Theta^{-1} C \Sigma' \quad (27)$$

$$\Sigma' A + A \Sigma' - \Sigma' C' \Theta^{-1} C \Sigma' + W_0' = 0 \quad (28)$$

The determination of the estimator gain becomes formally similar to the determination of the state feedback gain. In Equations (27) and (28),  $\Theta$  plays the same role as  $r$  in the state feedback gain design, and  $W_0$  the same role as  $q$ . Hence, conclusions can be drawn on the effect of  $W_0$  on the locations of the estimator poles for a fixed  $\Theta$ , by direct analogy with the effect of  $q$  on the optimal closed poles for a fixed  $r$ . In fact, the estimator poles are given by Figures 17 and 18, where increasing  $q$  just needs to be replaced by increasing  $W_0$ .

In the rigid case, the estimator poles corresponding to the first actuator resonance tend toward the zero frequency, and do not experience any significant change in damping. The estimator poles corresponding to the second actuator resonance decrease in frequency and become more damped. Hence, the rate of convergence of the error on the states associated with the second actuator mode is likely to increase as  $W_0$  increases.

In the flexible case, the estimator poles corresponding to the first actuator resonance follow the



same trend as in the rigid base case. The estimator poles corresponding to the beam resonance decrease in frequency and become more damped. The estimator poles corresponding to the second actuator resonance increase in frequency and, at first, increase in damping, then decrease again in damping. Hence, the rate of convergence of the error on the states associated with the beam mode is likely to increase as  $W_0$  increases. The rate of convergence of the error on the states associated with the second actuator mode first increases and then decreases again as  $W_0$  increases.

This trend can be observed experimentally in the rigid base case. Figures 13 and 14 show that increasing  $W_0$  increases the upper limit of the control frequency bandwidth, but also results in a higher peak sensitivity above the control frequency range. Again, low stability margins in the flexible case did not permit  $W_0$  to be increased sufficiently to observe its effect on the control frequency range.

Increasing  $q$  (because it results in higher controller gain) generally improves the level of reduction within a given bandwidth, and increasing  $W_0$  increases the control bandwidth. However, they also affect the sensitivity above the control bandwidth. This general phenomenon is a consequence of Bode's integral theorem [14], which states that the integral of the sensitivity over frequency is constant for a given plant.

In the preceding discussion, the mathematical model for the system was assumed to be perfect. However, modeling errors during the system identification are inevitable, so that the effective closed loop poles are not exactly given by the optimal closed loop poles.

Differences in the sensitivity transfer functions between the rigid and flexible cases, namely the decrease in the level of reduction and the upper limit of the control frequency range, can be attributed to: the additional plant phase delay due to the presence of additional resonances in the secondary plant transfer function, and additional computer time delay due to the higher complexity of the controller transfer function.

## CONCLUSIONS

The experiments demonstrated the ability of an active isolation system using a flexural piezoelectric inertial actuator to perform broadband isolation in the case of a payload rigidly mounted to a rigid or flexible base. In the rigid case, an average 6 dB reduction of the transmitted force between 35 and 110 Hz was obtained. In the flexible base case, an average reduction of 2 dB between 20 and 90 Hz was obtained. These results are not as good as those obtained in other studies of active broadband isolation [2,8]. This difference can be explained by two facts: (1) the experiments were conducted using a disturbance frequency spectrum including the first two actuator modes although, in

principle, the actuator could be designed to put at least one of these modes outside the disturbance spectrum; and (2) the actuator modes, by comparison to those of a hydraulic actuator like the one used in [2] or [8], are very lightly damped and, due to the double zero at the zero frequency (inherent to any inertial actuator), the first actuator mode can easily become unstable in closed loop conditions. This shows that the design of the actuator should focus on two main aspects: place as many actuator modes as possible outside the disturbance spectrum; and increase the damping of the actuator modes located inside the disturbance spectrum.

A constrained layer damping treatment was shown to significantly improve the damping of the actuator modes, however, not enough to provide the same stability as a hydraulic actuator [2,8], or as a hybrid mounting system with a damped passive isolation stage, such as shape memory alloys springs in parallel with a piezoelectric stack actuator [9]. Another difficulty in using a damping system that relies on deformations in the actuator itself is that the amount of added damping may be much lower in clamped root conditions than in free root conditions. This solution might not be suitable in the case of a rigid or slightly flexible base, as in the experiments conducted here. However, limitations inherent to feedback control, like the additional plant phase delay, are such that the isolation system is still more efficient for a rigid base than a flexible base.

The control design methodology used proved to be effective in dealing with the limitations of the actuator and the feedback control itself. Specifically, the use of fictitious disturbance and performance filters helped obtain the desired shape for the sensitivity transfer function while maintaining closed loop stability. The weight on the output,  $q$ , was found to govern pole-zero separation and thus the smoothness of the sensitivity transfer function. The power spectrum density of the fictitious white noise disturbance,  $W_0$ , was found to govern the upper limit of the control frequency range. Increasing both  $q$  and  $W_0$  was shown to increase the peak sensitivity above this frequency range.

A significant decrease in the level of isolation and its frequency bandwidth was observed in the case of the flexible base. This was mostly due to the additional beam mode, which tends to destabilize the second actuator mode in closed loop conditions, and to additional unmodeled computer time delay.

## RECOMMENDATIONS

Future work could be oriented in two main directions: plant design, and control system design. In the plant design, the amount of damping in the actuators appeared to be crucial in controlling the stability of the closed loop system. Techniques to increase more significantly the modal damping ratios

without reducing the force at non-resonant frequencies should be investigated. Resistively shunted piezoceramics [15] would be good candidates, as they provide most of their damping over a narrow frequency range. In the control system redesign, other robust control methods, such as  $H_\infty$ , could be tried. Mainly, some model of the physical path from the actuator to the force transducer at the shaker-actuator interface could be obtained, and included in the design of the controller.

#### ACKNOWLEDGMENTS

This work was supported by DARPA under the SAMPSON program.

#### REFERENCES

- Fuller, C. R., Elliott, S. J., Nelson, P. A., "Active Control of Vibration". Academic Press, 1996.
- Hyde, T. T., "An Experimental Study of Active Vibration Isolation", AIAA -97-1354, pp. 1763-1773.
- Blackwood, G. H., Von Flotow, A. H., "Active Control for Vibration Isolation despite Resonant Structural Dynamics : a Trade Study of Sensors, Actuators, and Configurations". 2<sup>nd</sup> Conference on Recent Advances in the Active Control of Sound and Vibrations 93. Technomic Press, 1993, pp. 482- 494.
- Hyde, T. T., "A Power Flow Approach to Active Isolation", AIAA-97-1156, pp. 301-311.
- Von Flotow, A. H., Sievers, L. A., Scribner, K. B., "Active Narrow Band Vibration Isolation of Machinery Noise from Resonant Substructures". ASME/Noise Control and Acoustics Division 90, Vol. 8, 1990, pp.101-111.
- Gupta, N. K., "Frequency-Shaped Cost Functionals : Extension of Linear-Quadratic-Gaussian Methods". *Journal of Guidance and Control*, Vol. 3, No. 6, Nov.-Dec. 1980, pp. 529-535.
- Jenkins, M. D., Nelson, P. A., Pinnington, R. J., Elliott, S. J., "Active Isolation of Periodic Machinery Vibrations". *Journal of Sound and Vibration*, Vol. 166, No.1, Sept 1993, p.117.
- Tanaka, N. and Kikushima, Y., "Rigid Support Active Vibration Isolation", *Journal of Sound and Vibration*, Vol. 125, No. 3, June 1988, pp. 539-553.
- Regelbrugge, M., Carrier, A., Dickson, W., "Cancelling Vibrations with Smart Materials: A Case Study", SPIE 1995, Vol. 2447, pp. 80-90.
- Crawley, E. F., and De Luis, Javier, "Use of Piezoelectric Actuators as Elements of Intelligent Structures", *AIAA Journal*, Vol. 25, No. 10, Jan. 1987, pp. 1373-1385.
- Nashif, A. D., Jones, D. I., Henderson, J. P., "Vibration Damping". John Wiley and Sons, 1985.
- Kailath, T., "Linear Systems". Prentice Hall, 1980.
- Richardson, M. H., Formenti, D. L., "Parameter Estimation from Frequency Response Measurements Using Rational Fraction Polynomials". Proceedings of the 2<sup>nd</sup> International Modal Analysis Conference, Orlando, FL, 1983.
- Zhou, K., "Essentials of Robust Control", Prentice Hall, 1998.
- Lesieutre, G. A., "Vibration Damping and Control Using Shunted Piezoelectric Materials", *The Shock and Vibration Digest*, Vol. 30, No. 3, May 1998, pp.187-195.